A theoretical and computational study of cavity formation in biological systems

Maximilian Jacob Kerr Winter

A thesis presented for the degree of
Doctor of Philosophy

The Francis Crick Institute
University College London
21/04/2021

0.1 Declaration

I, Maximilian Jacob Kerr Winter, confirm that the work presented in this thesis is my own. Where information has been derived from other sources, I confirm that this has been indicated in the thesis.

0.2 Abstract

In this thesis, I present my work on the emergence of self-organised structure within cellular systems, with a particular emphasis on the formation of fluid filled cavities. Self-organisation is a striking hallmark of living systems, and plays a particularly import role in developmental biology. To study such systems, I develop a novel hydrodynamic theory of cells in a background fluid of water and solutes. The solutes and water can move passively across the membrane of the cells. Furthermore, solutes can be actively transported in or out of the cell both isotropically and along a polar axis. Within this theory I demonstrate the existence of two potential mechanisms for cavity formation: spinodal phase separation driven by cell-cell adhesions, and an instability driven by active pumping of solutes into defects in the polarity field. This theory is general in scope, i.e. it is a framework to describe a variety of behaviours of any system consisting of adhering cells that can polarise and actively pump fluid.

I also present a study of a specific experimental system: mouse embryonic stem cell (mESC) aggregates. When grown from wild type cells, these aggregates form a spherical structure with cells polarised towards the centre. Fluid is pumped into the centre and a cavity opens. Such aggregates are the simplest example of mESC organoids that recapitulate key *in vivo* developmental processes *in vitro*. In order to quantify the growth of mESC aggregates, I develop an image segmentation and analysis pipeline. This pipeline allows me to extract meaningful, structured information from noisy 3D experimental time series data. In order to model the growth of mESC aggregates *in silico*, I develop a novel 2D model of polarised, deformable cells with continuous boundaries, called the Spline Model. Using the Spline Model as a prototype, I recapitulate key features of the experiments. Finally, I develop a 3D model of polarised, deformable cells. I demonstrate quantitative agreement between cell shapes produced by this model and in experiment. I study the dynamics of cell aggregates for the case where adhesion forces are coupled to apicobasal polarity, and make quantitative comparisons between these simulations and experiments. I find a positive correlation between the measured polarity of E-cadherin and predictions based on integration of extracellular matrix signalling. Furthermore, by coupling polarity to increased apical adhesion, I demonstrate the ability of extended cellular aggregates to undergo a transition to a compact state. When the coupling is removed, the transition no longer occurs. This behaviour is reminiscent of β1-KO cells, in which polarity alignment mechanisms are disrupted, that fail to form compact, organised aggregates.

0.3 Impact Statement

The work described in this thesis advances the fields of active matter hydrodynamics, biological image analysis, and tissue mechanics in a number of ways. The hydrodynamic theory presented in Chapter 4 is a significant addition to the growing field of active matter. It introduces several novel ideas (covered in more detail in the Discussion) to a growing subfield of physics trying to understand the behaviour of matter outside of thermodynamic equilibrium. My theory exists at the applied end of the spectrum of research in active matter, hence contributes to efforts to apply more theoretical developments in the field to a major class of active matter experiments,

namely aggregates of cells.

The novel computational tools I have built to analyse experimental movies of cell aggregates (Chapter 5), and simulate the mechanics of cell aggregates (Chapter 6), address ongoing obstacles to understanding the mechanics of cell growth and self-organisation. The analysis tools greatly simplify the quantification of complex, 3D time series data. The mechanical simulations include novel mechanisms for describing physics not easily included in existing computational models of cells. Both projects are quite general, and could be easily applied to a broad range of cell systems. Quantifying cellular systems and recapitulating them *in silico* is a common theme across many areas of biology, not just the embryonic stem cell aggregates I study in Chapter 7. As such, I hope my work will be impactful to many researchers in the biophysics community.

Beyond my own field of biophysics, my work contributes both to more distant academic communities and, through its contribution to medical research, society as a whole. The hydrodynamic theory of Chapter 4 describes a mixture of membrane bound vesicles in a binary fluid mixture. This could be applied to experimental systems in synthetic biology, where artifical "cells" are created by using lipid bilayers to compartmentalise chemical reactions. Furthermore, my theory could be applied to problems in chemical engineering involving mixtures of fluids with very different particle sizes, or to colloidal diffusion problems. These applications have wide ranging industrial applicability.

The broad theme of the work in this thesis is the study of tissue mechanics. The medical implications of this field are broad. Tumour metastasis, where growing cancer cells displace and then invade the surrounding healthy tissue, is one particularly impactful example. The question of whether a tumour will grow as a single colony or branch into many is partly down to the mechanics of growing tissues, and is a process that is not fully understood. Tissue mechanics also plays an important, and poorly understood, role in embryo development. Whether an embryo produced by IVF will implant successfully in the womb, or whether a zygote will divide to form twins, are important unanswered medical questions. The sort of quantitative, predictive methods described in this thesis may make a modest contribution towards answering them.

0.4 Breakdown of contributions

Chapters 1, 2, and 3 are entirely my own work. Chapter 4 is the work of my supervisor Prof. Guillaume Salbreux and myself. We were both involved in all aspects of the work. Chapter 5 is the work of Prof. Guillaume Salbreux, Dr. Alejandro Torres-Sanchéz, and myself. The theory of the Spline Model was developed by Prof. Salbreux and myself, and the source code was written by me. The Interacting Active Surfaces Model was developed by Dr. Torres-Sanchéz. Chapter 6 is the work of Ms. Antonia Weberling, Dr. Matteo Molé, Prof. Magdalena Zernicka-Goetz, Dr. Matthew Smith, Dr. Alejandro Torres-Sanchéz, Prof. Guillaume Salbreux, and myself. The project was conceptualised and planned by all of us. All experimental data was produced by Ms. Weberling and Dr. Molé under the supervision of Prof. Zernicka-Goetz. The Polar Interacting Active Surfaces Model was developed by Dr. Torres-Sanchéz and myself. The segmentation pipeline was developed by Dr. Smith and myself. The data analysis and comparison between simulations and experiments was done by me. Throughout the thesis I include more detailed attributes where appropriate.

0.5 Acknowledgements

First, I want to thank Guillaume Salbreux for his supervision and patient guidance. Guillaume contributed a great deal to my personal scientific development. Guillaume's curiosity, attention to detail and deep understanding of physics have been and will continue to be a great example for me. Without him this work would not have been possible.

I would also like to thank the members of my thesis committee, Buzz Baum, Nic Tapon, and Gunnar Pruessner, for their insight and guidance. I am grateful to all the students at the Francis Crick Institute, and the Institute for the Physics of Living Systems at UCL, for making such an exciting and supportive community. In particular, thank you Windie Hoefs for helping me with chemistry! Thank you to everyone who contributed to the Crick Physics Club, including Lars Hubatsch, Jamie Rickmann, Nuria Folguera Blasco, and many others.

During my PhD I have had the chance to work with many excellent biologists, from whom I learnt a great deal. For that I am grateful to Antonia Weberling, Matteo Molé, Marta Shahbazi, Christos Kyprianou, Neophytos Christodoulou, and Magdalena Zernicka-Goetz for all the insightful discussions, and exciting projects we started together.

I want to thank my friends and colleagues past and present from the Theoretical Physics of Biology Group at the Francis Crick Institute, namely Silvia Grigolon, Marc de Gennes, John Williamson, Luca Cocconi, Matthew Smith, Diana Khoromskaia, Alejandro Torres-Sanchéz, Andrea Cairoli, Maceo Joseph, Pragya Srivastava, Silvanus Alt, and Poulami Ganguly. Thank you all for everything you have done to contribute to my scientific development, as well as making these four and a bit years so fun. I want to thank Diana and Antonia (again) for their insightful and detailed feedback on my thesis. Furthermore, although I acknowledge their work in more detail throughout this thesis, Matthew Smith and Alejandro Torres-Sanchéz deserve special thanks for the many times they have helped me with computational problems.

Most importantly, I am deeply indebted to my family, and in particular my wife, Emily.

Contents

Chapter 1

Introduction

1.1 A physicist's perspective on morphogenesis

Morphogenesis, the umbrella term for the emergence of a structured, adult organism from a single fertilised egg cell, is the central object of study in developmental biology. The emergence of such a high degree of complexity and self-organisation from a simple starting point is a remarkable hallmark of life. Disentangling distinct processes from the more general term of 'morphogenesis' is an imprecise art, particularly given the complex feedbacks and interactions between different components in a growing embryo. However, in order for an adult organism to grow correctly, cells must reach the correct differentiated state, at the correct time and in the correct place. As such, developmental biology is particularly interested in cell fate specification [15], and tissue patterning [200] [111] [96].

Adult organisms are topologically complex, containing many enclosed cavities, networks of tubes, and often at least one hole through the entire body. In contrast, zygotes are topologically simple, as they are, to a good approximation, a ball. Consequently, topological transitions must play an important, and common, role in morphogenesis. Furthermore, the language of topology lends itself to the noisy and complex world of biology. Topologically identical objects can vary greatly in the details of their shape while maintaining a key property (e.g. genus). As such, a topological description captures the invariant (and hopefully important) nature of a system, while allowing a lot of flexibility in other parameters. This is reminiscent of embryogenesis: to be viable, it is necessary for a mouse embryo to develop a proamniotic cavity. However, exactly when and where the cavity forms, how many cells the embryo consists of at the time, or the precise shape and orientation of the cells can vary considerably. There is great variability in the dynamic trajectories of different components of a growing embryo, and yet a precisely organised adult organism eventually emerges. It is a challenge to the physicist to produce descriptions of biological systems that are quantitative and precise where necessary, but flexible otherwise.

The relationship between physics and biology is symbiotic. Biology provides a near endless variety of complex systems and phenomena that have no analogy in the non-living world. The study of morphogenesis is an excellent example of this: self-organisation, spontaneous symmetry breaking, and changes in topological state are all central concepts of physics, that play a key role in embryo growth. Similarly, physicists have made a significant contribution to biology. Two particularly prominent examples of theoretical contributions to biology from researchers in the mathematical sciences are Turing's description of how diffusion can counterintuitively drive pattern formation [200], and the neuronal action potential model of Hodgkin and Huxley [79]. Both examples demonstrate the power of systems of coupled differential equations to describe biological systems - an approach used heavily in this thesis. Despite being less mathematically

involved, Wolpert's French Flag Model of tissue patterning, and Thompson's On Growth and Form have both been influential in the subfield of biophysics applied to development [212] [193]. As well as theoretical contributions, physicists have played a crucial role both in developing modern experimental tools (e.g. super resolution microscopes [18] [161]), and in developing the computational and statistical techniques necessary to translate the increasingly large and complex datasets into meaningful insight. This wealth of high quality data forms the foundation upon which we can continue to build a body of theory to describe biology in a quantitative and predictive way.

In this thesis, I address the question of self-organisation both theoretically and computationally. Both approaches are inspired by the experimental work of the Zernicka-Goetz Group, at the University of Cambridge, on mouse embryology, mouse stem cell biology, and mouse embryonic organoids. In order to describe these systems, it was necessary to develop novel theoretical and computational tools to describe the intricate, 3D, cellular growth dynamics, and to develop image analysis tools capable of extracting quantitative information from noisy, complex data. The mouse stem cell systems I study maintain some of the simplicity of *in vitro* cell cultures, while displaying some of the self-organising behaviour of mouse embryos. As such they fulfil the maxim of being "as simple as possible, but no simpler".

Chapter 2

Cavity formation as a morphogenetic process

Cavity formation is a morphogenetic process that is particularly amenable to a physical analysis. It often has a simple and well defined geometry and topology, which can be can be recapitulated by cell models *in vitro*, and involves a combination of tissue and fluid mechanics. Across species, the formation of cavities is crucial during early development to ensure proper morphogenesis, and is typically crucial to the viability of the embryo. Here, I will concentrate only on mouse and human embryogenesis, and only on the early stages. In addition, I will also review the literature on cavity formation in cell culture and embryonic organoid systems, as these have proved to be very successful at isolating mechanisms of cavity formation, while maintaining some of the complexity of real embryos.

2.1 Mouse embryogenesis

Mus musculus, the laboratory mouse, is by far the most common model organism for studying mammalian development, thanks to its small size, fast reproduction rate, and similarity to humans. The mouse gestation period lasts 20 days, however here I will only consider the first 7 days up to gastrulation. In these 7 days, the embryo transitions from a single cell zygote to a blastocyst that implants in the maternal endometrium of the uterine wall. The blastocyst further develops into a gastrula containing three distinct embryonic tissue layers, as well as two extra-embryonic tissues, and becomes implanted in the maternal tissue of the uterine wall [16].

The pre-implantation embryo undergoes several major developmental changes. Upon fertilisation, the embryo undergoes a series of cleavage divisions while undergoing critical genetic and morphogenetic steps. At the 2 cell stage is the transition from maternal to zygotic transcription [218]. At the 8 cell stage, the embryo compacts and thereby specifies the first anatomically distinct cell populations, with some cells forming an outer layer, fully enclosing an inner group of cells. There follows a round of asymmetric cell divisions at the transition from the 8 to 16 cell stage, with some cells contributing both daughters to the outer layer, and some contributing one to the outer layer, and one to the inner [129]. The inner cells maintain pluripotency by the activity of the transcription factors OCT4, SOX2 and NANOG. The outer cells form the trophectoderm (TE), an extra-embryonic lineage that gives rise to the placenta [97] [218]. The final pre-implantation event is the formation of the blastocyst, where the embryo swells up and forms a fluid filled cavity. This cavity, the blastocoel, further segregates the pluripotent Inner Cell Mass (ICM) from the TE, and breaks the (approximate) spherical rotational symmetry of the embryo [55]. The blastocoel is formed by the external, polarised, cells of the TE pumping fluid into the centre of the embryo. This pumping process opens up microlumens along the in-

ner cell interfaces, which eventually drain into a single, large cavity, with the ICM on one side. The ICM then undergoes the second lineage segregation into the embryonic epiblast (EPI), which gives rise to the baby mouse, and the primitive endoderm (PE), which gives rise to the yolk sac [66]. The developmental steps the embryo undertakes from zygote to maturation of the blastocyst at E4.5 (Embryonic Day 4.5) are summarised in Fig. 2.1.

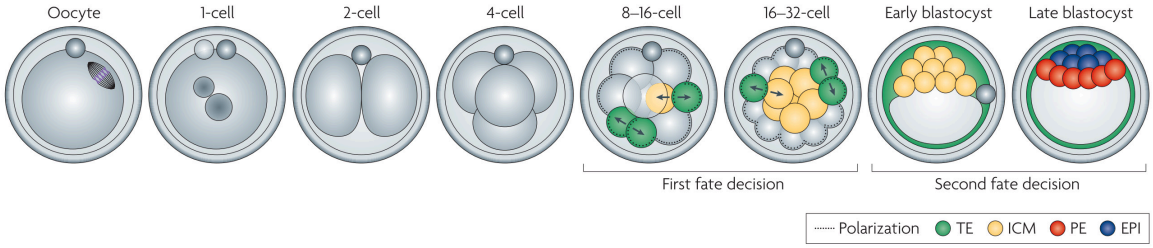

Figure 2.1: The development of a mouse embryo from Oocyte (unfertilised egg cell) to blastocyst, taken from Zernicka-Goetz et al. [218].

The next stage in mouse development is the implantation of the blastocyst into the maternal uterine wall [47]. During this process, the peri-implantation embryo undergoes significant morphological changes. The polar TE proliferates, and develops into the extra-embryonic ectoderm (ExE). Proliferation and invagination of the ExE causes the ExE and EPI to fill the blastocoel. The PE develops into the visceral endoderm (VE) and forms an epithelium surrounding the EPI and ExE. At the same time, the EPI cells transition from naive to primed pluripotency [175]. The EPI cells organise into a rosette, where the cells polarise with their apical domains pointed toward the centre of the EPI, forming a hedgehog defect-like structure [16]. The EPI cells then pump fluid into the centre of the rosette, which opens to form a cavity. A further cavity opens in the ExE, which then expands and fuses with the EPI cavity to form the pro-amniotic cavity [35]. This completes the transition of the embryo into an egg cylinder. The formation of these cavities by polar pumping of fluid overturned a previous hypothesis which held that apoptosis of cells in the centre of the embryo hollowed out the cavities. The apoptosis hypothesis was developed as a result of experiments on embryoid bodies, large aggregates of embryonic stem cells (ESCs), that do indeed form cavities in this way [38]. Bedzhov and Zernicka-Goetz [16] were able to directly observe the remodelling of the peri-implantation embryo *in vitro* by developing novel culturing techniques to simulate implantation [128]. By using a fluorescent cell death reporter, SYTOX, they observed the capability of EPI cells to form a cavity without apoptosis. Development of the peri-implantation embryo is summarised in Fig. 2.2.

The embryonic cells in the egg cylinder all belong to a single lineage, the epiblast, surrounded by the visceral endoderm. The final major event in the first 7 days of mouse development is gastrulation, where the epiblast differentiates into two lineages: the ectoderm and the mesoderm (which goes on to produce the definitive endoderm). Gastrulation initiates in the mouse embryo at the boundary between EPI and ExE cells, where a subpopulation of EPI cells express the signalling protein FGF and form the primitive streak [188]. The cells of the primitive streak undergo an epithelial-to-mesenchymal transition and start to migrate between the EPI and the VE. This process continues until there is a continuous cell layer, the mesoderm, lying between the ectoderm (EPI) and endoderm (VE) [77]. The mesoderm then gives rise to the definitive endoderm, resulting in the three germ layers of the adult mouse body: definitive endoderm,

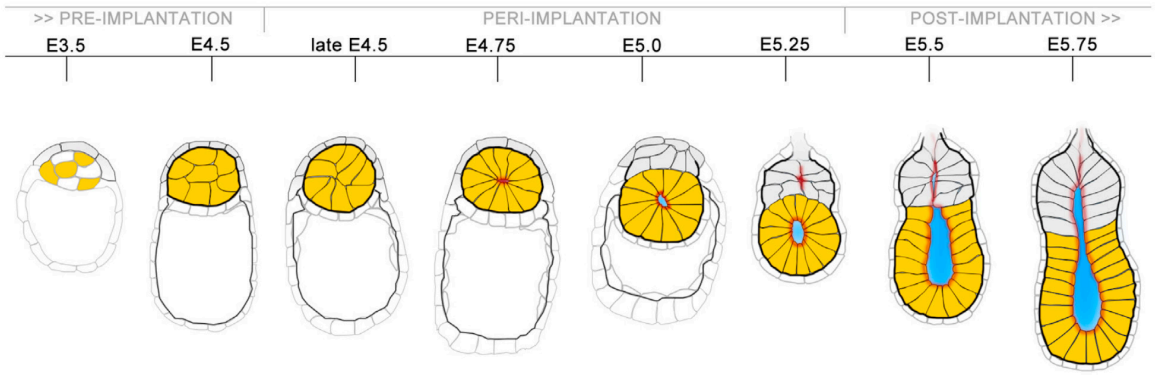

Figure 2.2: The development of a mouse embryo from blastocyst to egg cylinder, with EPI (yellow), ExE (grey) and VE (white), taken from Bedzhov and Zernicka-Goetz [16].

mesoderm and ectoderm [108]. It is a peculiarity of mouse development that the three cell lineages are inverted: ectoderm on the inside of the egg cylinder, and endoderm on the outside. The ectoderm goes on to differentiate into the skin and neural tube, the endoderm into the gut, and the mesoderm into muscles, bones and connective tissue. Gastrulation is a fundamental developmental milestone as it is the first major division of cell lineages within the body of the embryo, as opposed to the division of embryonic and extra-embryonic lineages that occurs pre-implantation.

2.2 Human embryogenesis

The study of human embryogenesis is beset by significantly more ethical and practical obstacles than that of the mouse, and consequently a less detailed picture is known. However, development up to the stage of the human blastocyst has been well studied, particularly in relation to *in vitro* fertilisation treatment [57]. Similar to mouse embryogenesis, the human embryo undergoes a series of cleavage divisions, which, after seven days, results in a blastocyst with the same structure as the mouse, and containing the same three lineages of EPI, TE and PE (called the hypoblast in humans) [21]. Although anatomically similar, Fogarty et al. have shown that genetic fate specification, controlled by OCT4, occurs earlier in human embryos than mice [63]. Studying human development beyond the blastocyst stage was previously based on the Carnegie Collection of Embryos [144]. However, post-blastocyst growth has recently been achieved *in vitro* by adaption of the culturing techniques of Morris et al. [128] [174]. The peri and post implantation human embryo is structurally quite different from the mouse, consisting of two lineages, the epiblast and hypoblast (equivalent of the mouse PE), surrounding the proamniotic cavity. This structure is shown in Fig. 2.3.

Compared with the mouse, very little is known about human gastrulation. Unlike the blastocyst, the gastrulating mouse and human embryos look very different, as shown in Fig. 2.4. Around day 9 an endodermal layer forms around the inside of the blastocyst. Some of these cells differentiate into mesoderm cells. A primitive streak forms, and mesodermal cells generated in the primitive streak replace some or all of the endoderm derived mesoderm [157]. Although we do not have a detailed picture of human gastrulation, the end result is an embryo with three embryonic cell lineages, the endoderm, ectoderm and mesoderm, encompassing two

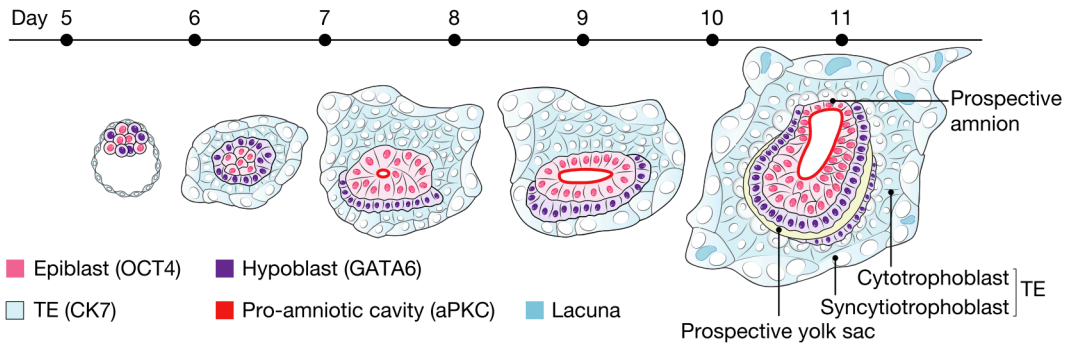

Figure 2.3: The development of the human embryo during the peri-implantation stage, taken from Shahbazi et al. [174].

cavities [188].

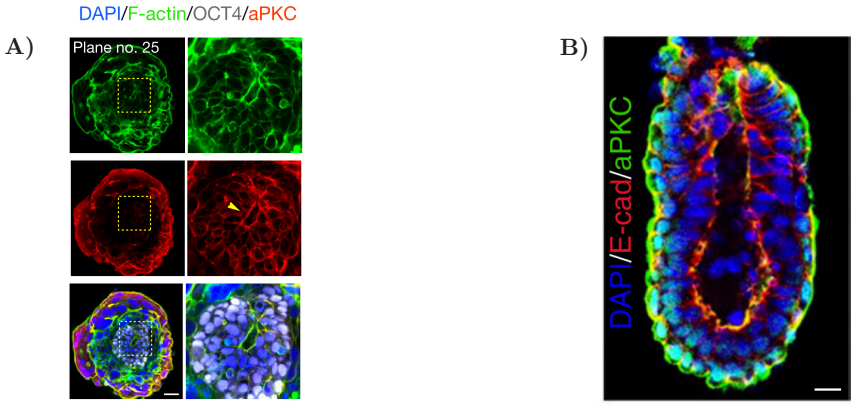

Figure 2.4: A) The human embryo at 11 days, before the onset of gastrulation [174]. B) The mouse embryo at 6 days, before the onset of gastrulation [35].

The formation of the blastocoel and proamniotic cavities are major events in the early development of mice and humans, allowing the embryo to specify cell fates, symmetry, and topology. This pattern is replicated across developmental biology where cavity forming events are common place. The vertebrate neural tube forms by both the folding of an epithelium, and the hollowing out of mesenchymal cells [110]; vascular lumens form as precursors to the heart in the zebrafish [84]; and a network of lumens gives rise to the Drosophila tracheal system [17]. These examples demonstrate not only the ubiquity of cavity formation, but also the wide range of mechanisms life has evolved to open up spaces within tissues. These include the folding of epithelia, hollowing out by apoptosis, organised polar pumping of fluid, and the hollowing of individual cells [111]. Disentangling these mechanisms is experimentally challenging as they are occurring inside delicate, growing embryos, often in conjunction with many other cellular processes. However, the recent development of complex organoids has become a powerful tool for studying cavity formation, and morphogenesis in general, in a controlled and isolated

environment.

2.3 Organoids

Culturing cells in isolation is common place in modern biology. However, the utility of cell culture in studying the self-organised complexity central to embryogenesis is limited. We are left with the difficult situation where an entire embryo is too complex to understand, whereas isolated cells are too simple to be of interest. An exciting middle ground between these two extremes has recently been developed in the form of organoids. Organoids are cell cultures, consisting of several cell types, that self-organise in such a way as to recapitulate at least some of the structure and function those cells exhibit *in vivo* [100]. In 1987, Li et al. observed that mouse mammary cells organise into ducts when cultured on a reconstituted basement membrane from Engelbreth-Holm-Swarm tumors [109]. Since then, more and more sophisticated structures have been grown. Sato et al. have grown gut organoids, that form budding crypts, with local stem cell populations at their tips, around a central lumen, as shown in Fig. 2.5 [167]. Takasato et al. have grown kidney organoids with early nephrons [192]. Both of these examples start with stem cells, in the case of Takasato et al. embryonic stem cells, that are then induced to differentiate into the correct cell types, thus highlighting the significant role fate specification plays in determining the structural organisation of the resulting tissue.

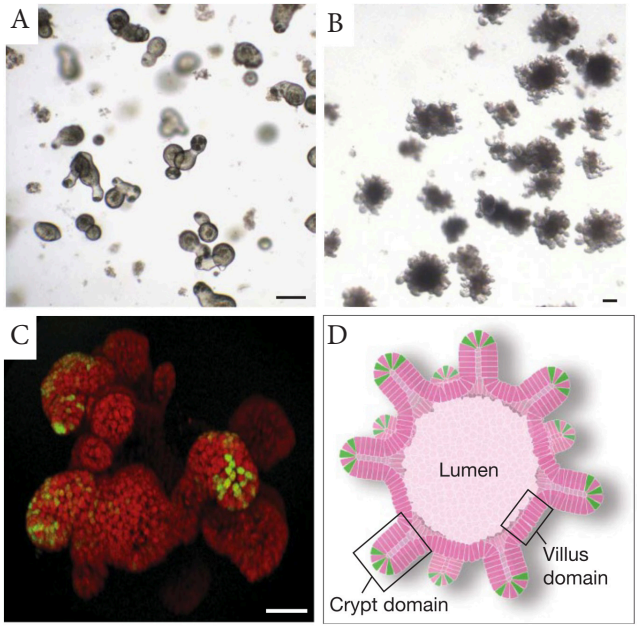

Figure 2.5: Gut organoids grown in culture for A) 5 and B) 14 days. C) A confocal image after 3 weeks. Stem cells are marked in green. D) A schematic demonstrating the structure of the organoid. These images were taken from Sato et al. [167].

Organoids have not only been shown to recapitulate *in vivo* structures, they also exhibit functional processes. Cerebral organoids are self-organising neuronal aggregates that recapitulate many of the structures seen in the mammalian brain, including networked neuron layers, genetically distinct forebrain regions, and enclosed cavities [154]. Cerebral organoids have been shown to generate spontaneous neuronal activity, that becomes synchronous across large populations of neurons. This neuronal activity is sufficient to induce contractions in connected

mouse muscle [67].

Organoids are proving to be valuable tools for studying morphogenetic processes in embryos. Culturing both human and mouse EPI stem cells in 3D matrigel can produce spherical aggregates that form a central rosette, which then forms a cavity, recapitulating the behaviour of EPI cells *in vivo* [174]. This system acts as a minimal model of morphogenesis: it consists of only one cell type, in a simple spherical geometry, and demonstrates a single morphogenetic process in isolation. Aggregates of EPI cells are not classed as organoids, however embryonic organoids can be grown by combining more cell types from the early embryo. Harrison, Sozen et al. have grown embryonic organoids by combining ESCs from the mouse EPI, and trophoblast stem cells from the ExE [74]. The resulting organoids recapitulate normal morphogenesis to a striking degree, as shown in Fig. 2.6. The two cell types segregate into an EPI-like region and an ExE-like region, cavities grow in each, and eventually fuse to form a proamniotic cavity. Furthermore, the organoids undergo the first stage of gastrulation, with a group of cells expressing mesoderm markers, hence breaking the rotational symmetry of the organoid. In Sozen et al., organoids grown from all three cell types of the post-implantation mouse embryo (EPI, ExE and PE) again form aggregates with very similar structure to natural embryos: two segregated regions of EPI and ExE cells, surrounded by an epithelium of PE. These organoids go further in the gastrulation process by exhibiting an epithelial-to-mesenchymal transition, and the growth of definitive endoderm [185]. Sozen et al. have also shown that organoids can be grown that mimic the mouse blastocyst, including all three cell types, that then undergo the peri-implantation remodelling of the embryo into an egg cylinder [186].

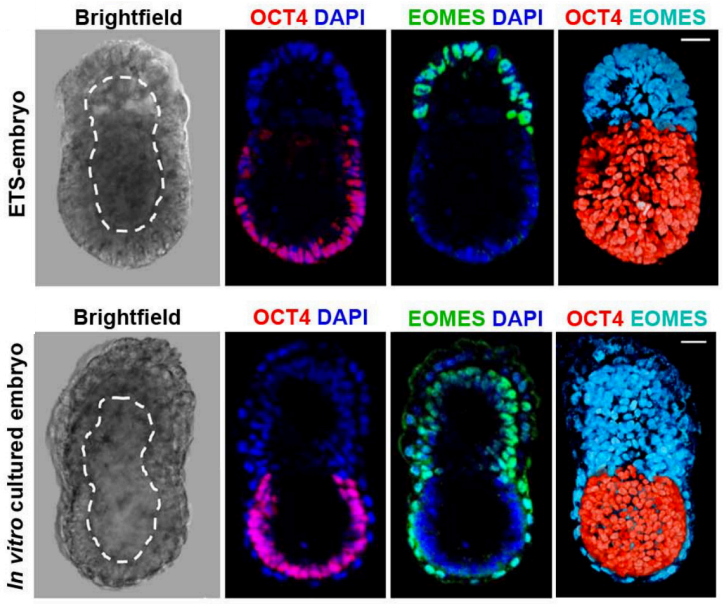

Figure 2.6: A comparison of embryonic organoids grown from two cell types (ETS-embryo, upper panel) and a post-implantation mouse embryo (lower panel), taken from Harrison, Sozen et al. [74].

Embryonic organoids provide a compelling new tool for investigating the causal mechanisms of embryogenesis. It is also an approach that chimes with that of physics: the embryo is broken down into its constituent parts, which can then be combined in ever more complex structures.

This hierarchical rebuilding of the embryo allows different morphogenetic mechanisms to be isolated, and hence addresses the question of what is a necessary and sufficient set of mechanisms for successful embryogenesis. Organoid experiments also highlight how complexity is an emergent, self-organised property of embryogenesis. This self-organisation is robust to the significant disruption to the normal developmental procedure caused by removing stem cells from an embryo and recombining them *in vitro*.

In this chapter I have briefly reviewed the literature on early mouse and human development. I have also reviewed the growing field of organoid research, with an emphasis on the recapitulation of mammalian developmental processes in embryonic organoids. In Chapter 4 I will detail my development of a theory of cavity formation in pumping cell aggregates, inspired by the pumping phenomena exhibited at various stages in the mouse embryo, and in EPI derived embryonic stem cell (ESC) aggregates. In Chapters 5 I will also present a computational study of the growth of ESC aggregates. But first, I will review the physics literature that provides the starting point for my own work.

Chapter 3

Continuum and computational models of biology

Biology offers a rich variety of systems, consisting of many microscopic, constituent particles, interacting with each other in a viscous, fluid environment, that broadly fall under the remit of fluid dynamics, thermodynamics and soft matter physics. The major departure of biophysics from these earlier fields of study is the role of out-of-equilibrium, or active, processes. Although such processes are not unique to the living world, they are ubiquitous in biology, and provide the driving force for much of the novel phenomena of life. Passive theories of complex systems still provide powerful tools to study biological systems, and key concepts such as coarse graining, order parameters, phase transitions and pattern forming instabilities are widely used in the study of active systems. In this chapter I will give a broad overview of the various elements of fluid dynamics, thermodynamics and soft matter physics that form the foundation of my work. As of yet, there is no unifying theory of active matter playing a role analogous to that of the Boltzmann distribution in equilibrium thermodynamics. Consequently, when describing the physics of living systems, a wide variety of methods and ideas are used. I will begin by reviewing the literature of passive soft matter systems.

3.1 Passive models of complex fluids

A single component, incompressible fluid can be described by the Navier-Stokes equation and incompressibility condition [32]

$$\rho D_t \mathbf{v} = \eta \nabla^2 \mathbf{v} - \nabla P + \nabla \cdot \sigma \tag{3.1}$$

$$\nabla \cdot \mathbf{v} = 0, \tag{3.2}$$

where $\mathbf{v}$ is the fluid velocity, ρ the density, η the viscosity, and P the pressure. It is convention to write any other forces (e.g. gravity) as the divergence of a stress, $\nabla \cdot \sigma$. $D_t = \partial_t + \mathbf{v} \cdot \nabla$ is the material time derivative, which includes the effect of quantities being advected by the fluid flow. These two equations, with a suitable set of boundary conditions, determines the 3 components of $\mathbf{v}$, and P. Implicit in this description is the assumption that the fluid can be coarse grained, i.e. that the microscopic velocities of the constituent particles can be averaged over volume elements that are large enough to contain many molecules. This average velocity, discretised over volume elements, can then be approximated by a continuous, smooth velocity field, $\langle \mathbf{v}_i \rangle \to \mathbf{v}$. Coarse graining replaces a large number of experimentally inaccessible microscopic variables, obeying highly stochastic dynamics, with a few macroscopic variables, obeying equations that are (hopefully) amenable to either analytical interrogation or efficient numerical integration. Typically, real life systems, and in particular biological systems, are more complicated than

that described by Eq. 3.1. In the following I will give an overview of a few common extensions to the Navier-Stokes equation.

3.1.1 Binary fluids

Binary fluid models have been used to describe a wide variety of systems, including polymer-solvent mixtures [62], colloidal suspensions [1], and biological tissues consisting of cells and interstitial fluid [166]. A binary fluid is a mixture of two fluid species, A and B. In order to describe the relative composition of the fluid, a macroscopic order parameter, ϕ, is defined as

$$\phi = \frac{\langle n_A - n_B \rangle}{\langle n_A + n_B \rangle}, \tag{3.3}$$

where $n_{A,B}$ are the number densities of the two species, and averages are taken over volume elements containing many particles [80]. This order parameter is conserved, hence obeys a continuity equation $\dot{\phi} = -\nabla \cdot \mathbf{J}$, for some current $\mathbf{J}$. The free energy of the system is a functional of the order parameter, $F[\phi]$. Although different authors use forms of the ϕ dynamics and free energy that differ in their details (e.g. to include size asymmetries [160], surface tensions [28], or hard sphere effects [105]), the archetypal binary fluid models are Model B and Model H [80]. The naming convention of Hohenberg and Halperin is not particularly informative or memorable, however Cates and Tjhung note that Model B is a diffusive theory driven by Brownian motion, and Model H is an extension of Model B including hydrodynamic effects, hence B for Brownian and H for Hydrodynamic.

Models B and H

Model B describes a binary fluid where there is no net flow, $\mathbf{v} = 0$. As such, the dynamics are governed by diffusion. The free energy is

$$F[\phi] = \int dV \left\{ \frac{\alpha}{2}\phi^2 + \frac{\beta}{4}\phi^4 + \frac{\kappa}{2}(\nabla\phi)^2 \right\}. \tag{3.4}$$

What is the justification for this free energy? The true free energy will be a function of the microscopic variables of the constituent particles. Coarse graining this function will in general be difficult or impossible. Instead, we can take a phenomenological approach, expanding the free energy as a power series in the order parameter, and including terms up to a particular order sufficient to describe the physics of interest. This approach is based on the concept of universality in statistical physics: the observation that close to critical points a wide range of systems, that differ from each other microscopically, behave in a similar way and can be described by order parameter expansions [61]. Such a phenomonological approach was used by Ginzburg and Landau [101] to describe superconductivity, and hence Eq. 3.4 is known as a Ginzburg-Landau, or just Landau, free energy. In the literature on binary fluid mixtures, the gradient term, $\frac{\kappa}{2}(\nabla\phi)^2$, is attributed to Cahn and Hilliard [28], and in this document I will refer to it as such. The parameters α and β describe a free energy density of the form shown in Fig. 3.1. The ground state of F can be shifted from 0, when $\alpha > 0$ and $\beta > 0$, to $\phi = \pm\sqrt{\frac{-\alpha}{\beta}}$, when $\alpha < 0$ and $\beta > 0$.

The exchange chemical potential, the change in free energy on the exchange of a B particle for an A particle, is defined

$$\mu = \frac{\delta F}{\delta \phi} = \alpha\phi + \beta\phi^3 - \kappa\nabla^2\phi. \tag{3.5}$$

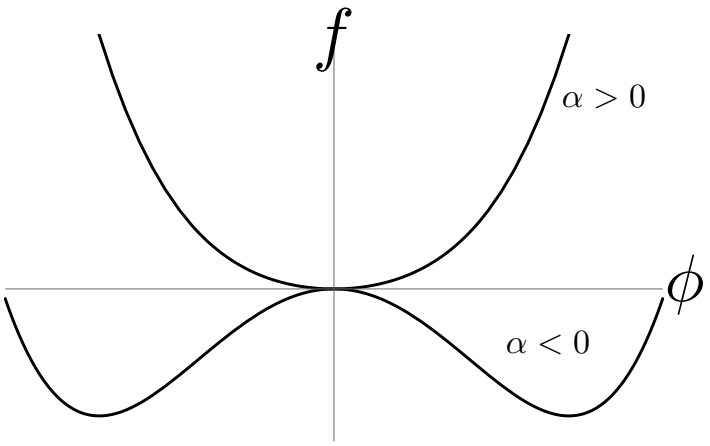

Figure 3.1: A schematic of the Landau free energy density, described in Eq. 3.4, where $F = \int f dV$. When $\alpha > 0$, the ground state is at $\phi = 0$. When $\alpha < 0$, the ground state is at $\phi = \pm\sqrt{\frac{-\alpha}{\beta}}$.

The order parameter current is taken to be linearly proportional to the gradient of the chemical potential, and hence the continuity equation for ϕ is

$$\partial_t \phi = -\nabla \cdot (-M \nabla \mu), \tag{3.6}$$

for some mobility M. The linear relationship between $\mathbf{J}$ and $\nabla\mu$ assumes gradients in the chemical potential are small, hence higher order terms allowed by symmetry (e.g. proportional to $\nabla^3\phi$) can be neglected. Eq. 3.5 and 3.6 form a closed set of equations for ϕ and constitute Model B.

The dynamics of Model B are driven solely by the diffusive processes described by the chemical potential. Model H is an extension of Model B that also includes fluid flows. As such, Eq. 3.5 and 3.6 must be supplemented by an equation for the fluid velocity $\mathbf{v}$. This is simply Eq. 3.1, with an additional force due to the order parameter ϕ (see Cates and Tjhung [32], Section 3.3 for more details). Consequently, Model H reads

$$\rho D_t \mathbf{v} = \eta \nabla^2 \mathbf{v} - \nabla P - \phi \nabla \mu \tag{3.7}$$

$$\nabla \cdot \mathbf{v} = 0 \tag{3.8}$$

$$D_t \phi = -\nabla \cdot (-M \nabla \mu) \tag{3.9}$$

$$\mu = \alpha\phi + \beta\phi^3 - \kappa\nabla^2\phi. \tag{3.10}$$

Binary phase separation

A central object of study in statistical physics is the phenomenon of phase transitions. Phase transitions constitute a macroscopic, qualitative, and typically dramatic change in the properties of a system, often with a corresponding change in the symmetry and structure [61]. A phase transition of particular relevance to biophysics, and which serves as an archetypal example, is

the phase separation of binary fluids. Listing again the equations of Model B,

$$\partial_t \phi = -\nabla \cdot \mathbf{J} \tag{3.11}$$

$$J = -M\nabla\mu = -M\nabla\frac{\delta F}{\delta \phi} \tag{3.12}$$

$$F = \int f dV = \int dV \left\{ \frac{\alpha}{2}\phi^2 + \frac{\beta}{4}\phi^4 + \frac{\kappa}{2}(\nabla\phi)^2 \right\}, \tag{3.13}$$

it is clear that the dynamics act to minimise the free energy along a steepest gradient trajectory. By varying the parameter α, F can transition from a state with a single minimum, to one with two minima, as shown in Fig. 3.1. As such, the system transitions from a single stable state, to two stable states as α crosses zero (a so called "quench"). The existence of this behaviour in Eq. 3.13 is, in part, the motivation for truncating the Landau free energy at $O(\phi^4)$. Physically, the transition from a single groundstate to two, corresponds to a binary fluid that initially exists in a mixed state of A and B molecules, spontaneously separating into two phases of A and B rich fluid, with order parameters ϕ_A and ϕ_B. At equilibrium, i.e. when the system exists in the global energy minimum, the two phases are balanced in their chemical potentials, and pressures. These two constrains are

$$\mu_A = \mu_B \tag{3.14}$$

$$f(\phi_A) - \phi_A\mu_A = f(\phi_B) - \phi_B\mu_B, \tag{3.15}$$

respectively [32]. There is a graphical interpretation of these constraints, which is that at equilibrium, the two phases exist on a common tangent line. Eq. 3.14 states the gradient of the free energy density is the same at phases ϕ_A and ϕ_B. Eq. 3.15 states that they have the same intercept of the f axis. The values of ϕ_A and ϕ_B that satisfy Eq. 3.14 and 3.15 are called the binodals.

Whether, and how, this separation can occur depends on the initial composition of the system. For $\alpha < 0$, consider the shape of the free energy about an initial composition $\phi = 0$. Thermal fluctuations will cause small scale inhomogeneities in ϕ, resulting in some regions with an excess of A, and some regions with an excess of B. The total free energy is then the sum of the free energies of these two regions, weighted by their relative abundance. The abundance of the two phases will be constrained by conservation of particle number. As such, the total free energy lies somewhere on a straight line connecting the two new phases. If the connecting line lies below the free energy curve, the phase separation is energetically favourable, and the phases will remain separate. There will follow a flux of A and B molecules into their respective regions, driven by an imbalance of chemical potentials and pressure, until ϕ_A and ϕ_B reach their binodal values, satisfying Eq. 3.14 and 3.15. This is the case for Region I in Fig. 3.2. The process of thermally driven local phase separation is called spinodal deomposition [27]. Outside of the binodals, the system cannot reduce its free energy by phase separation, and will remain in the initial mixed state. A system initialised in Region II of Fig. 3.2 lies within the binodals, but in a concave region of the free energy curve. Consequently, a line connecting two infinitesimally separated phases will lie above the free energy, but the overall free energy would be minimised by reaching the binodals. This scenario corresponds to a metastable state, where there is an energy barrier to phase separation. After some time, thermal fluctuations nucleate a phase separation above a critical size, which then progresses to the binodals. The boundary of Region II, the spinodal values of ϕ, are the points at which the curve becomes concave, i.e.

$$\frac{\partial^2 f}{\partial \phi^2} = 0. \tag{3.16}$$

Spinodal decomposition is the dominant mechanism of phase separation on short times, and results in a system that has separated A rich and B rich regions. The long time behaviour of this separated system is for matter to flow from the smaller separated regions to the bigger ones, by the mechanism of Ostwald ripening [205]. Variations on Model B spinodal phase separation have been applied to a wide variety of phase separating systems, including polymer melts [199] [43], metal alloys [127], and colloidal suspensions [11] [159], as well as serving as a basis for extensions to active fluids [194] [211].

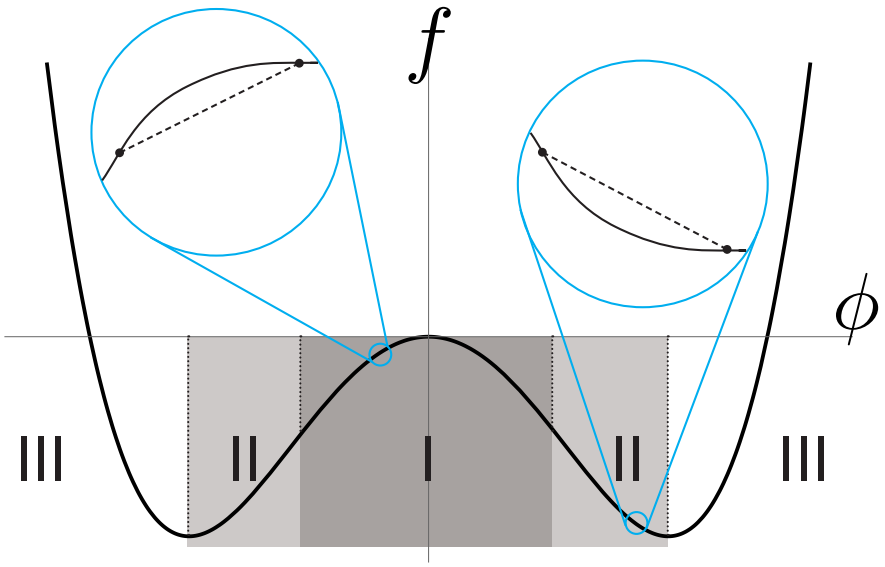

Figure 3.2: The phase separation behaviour is different in the three regions of this schematic free energy density. In Region I, the line connecting two phases lies below the free energy curve, hence local phase separation is energetically favourable. This region is unstable. In Region II, the connecting line lies above the free energy curve, hence local phase separation is unfavourable. However, the system can reduce its free energy by reaching the binodals, as such this region is metastable. Region III is stable, as the free energy cannot be reduced by phase separation.

Hard sphere models

More physically realistic models of single component and binary fluids have been developed by considering microscopic ensembles of hard spheres [12]. The entropy of hard sphere models is typically calculated by using a lattice based model as a way to enumerate the configurations of the system [160] [145]. Corrections to this idealised picture are then included by using various techniques to approximate the Virial expansion of real, or computer simulated, fluids [131]. The most popular of these theories is that of Carnahan and Starling [30] [121].

The behaviour of binary hard sphere models that are asymmetric, i.e. consisting of particles A and B that differ in size, has been studied in depth [64] [19] [106], in particular in relation to their tendency to phase separate via the Asakura-Oosawa effect [8] [107] [204]. This effect occurs in binary hard sphere mixtures with a diameter ratio less than about 0.2. Although there are no attractive forces in hard sphere models, once two of the larger particles get sufficiently close, the smaller particles are excluded from the volume in between. This results in a pressure imbalance between the inter-particle space and the surrounding medium, which pushes the two larger particles together.

3.1.2 Ternary and polydisperse fluids

A natural extension of the binary Models B and H is to include more fluid species. Ternary systems, consisting of three species, have been studied in the context of polymer melts (e.g. two polymer species and a solvent [95], or a polymer, solvent and non-solvent [195]), metal alloys [127], and as a simple test case for non-equilibrium thermodynamics [213] [124]. The free energy of multicomponent systems can be derived phenomenologically, similar to the binary case, Eq. 3.4, or by calculating the configurational entropy from lattice based models [208]. Including multiple species requires multiple order parameters, e.g. for a ternary fluid of A, B and C particles, we can use the volume fractions ϕ_A, ϕ_B and ϕ_C. Multiple chemical potentials can then be defined as

$$\mu_A = \frac{\delta F}{\delta \phi_A} \tag{3.17}$$

$$\mu_B = \frac{\delta F}{\delta \phi_B} \tag{3.18}$$

$$\mu_C = \frac{\delta F}{\delta \phi_C}. \tag{3.19}$$

For conserved particle numbers, A, B and C obey continuity equations of the form $\dot{\phi}_i = -\nabla \cdot \mathbf{J}_i$. Once again assuming a linear relationship between diffusive fluxes and gradients of chemical potential, the most general linear flux equations are

$$\begin{pmatrix} \mathbf{J}_A \\ \mathbf{J}_B \\ \mathbf{J}_C \end{pmatrix} = \mathbf{L} \begin{pmatrix} -\nabla \mu_A \\ -\nabla \mu_B \\ -\nabla \mu_C \end{pmatrix}, \tag{3.20}$$

where $\mathbf{L}$ is a matrix of diffusion coefficients. The off-diagonal elements of $\mathbf{L}$ correspond to cross coupling effects between the different chemical species. These cross diffusion effects are a novel feature of ternary and higher fluid mixtures, that are not present in the binary case. The fluxes are defined with respect to some reference frame. The reference frame can be defined such that one of the fluxes can be eliminated via the constraint

$$\sum_i a_i \mathbf{J}_i = 0, \tag{3.21}$$

for a choice of coefficients a_i [124]. Common reference frames are [94] [123] [213]:

- the centre of mass, or "mass fixed" frame. $a_i = m_i$, the mass of the particles. This is a reference frame being freely advected by the fluid.
- the rest frame of the solvent, or "solvent fixed" frame. $a_{\text{solvent}} = 1$ and $a_i = 0$ for all other species.
- the "volume fixed" frame. $a_i = v_i$, the volume of the particles. This corresponds to the experimental scenario of a container open at one end.

An alternative, though equivalent, framework of multicomponent diffusion is Maxwell-Stefan theory [22] [37]. In this framework, force balance equations are written between pairs of species. Consider a three component fluid, consisting of species with number density n_A, n_B and n_C. The force driving a flux of A is the gradient in the chemical potential of A. This force is balanced by friction between A and B, and between A and C, which is taken to be linear in the difference in velocities between the two species. The resulting force balance equation is

$$\frac{\nabla \mu_A}{RT} = -\frac{n_A j_B - n_B j_A}{n_A \bar{D}_{AB}} - \frac{n_A j_C - n_C j_A}{n_A \bar{D}_{AC}}, \tag{3.22}$$

where $\bar{D}_{ij}$ is the Maxwell-Stefan diffusion coefficient between species i and j. $\bar{D}_{ij}$ is inversely proportional to the friction between i and j.

Taking the number of distinct fluid species to infinity, we reach the polydisperse limit [183]. In polydisperse systems the individual fluid species are replaced by a distribution $\sigma(x)$ over the polydisperse variable, x. The free energy then becomes a functional of this distribution, $F[\sigma(x)]$. Polydispersity is exhibited in a number of experimental systems, and in a number of observables. Colloidal systems often contain a range of colloid sizes, that vary in an approximately continuous way [10], petrochemical processes produce hydrocarbons with a distribution of chain lengths [23], and copolymers can be made up of random sequences of two different monomers [49].

3.1.3 Liquid crystals

Increasing the number of fluid species is not the only way that fluids can become more complex than the situation described in Eq. 3.1. Liquid crystals are liquids made of molecules with complex shapes. Typical examples are polar liquid crystals, made up of molecules with a preferred direction, nematic liquid crystals, made up of molecules with a preferred orientation but not a distinct front and back, and hexatic smectic liquid crystals, made up of molecules which form layers, within which they have six fold rotational symmetry [45]. The concept of describing states of matter with underlying symmetry constraints has been borrowed extensively by the biophysics community to describe cellular chemical polarity patterns [147] [138], shape polarity patterns [75] [146], and locomotion [196] [14]. The study of the physics of liquid crystals is extensive, so I will restrict myself to considering only the polar case as this is most relevant to my own work.

The archetypal polar liquid crystal consists of polar molecules, i.e. molecules with a distinct head and tail, described by a vector $\mathbf{p}_i$ pointing from the tail to the head. Coarse graining such a fluid, the average molecular direction can be approximated with a continuous vector order parameter, $\mathbf{p}(\mathbf{r}) = \langle \mathbf{p}_i(\mathbf{r}_i) \rangle$, the polarity. How does $\mathbf{p}$ contribute to the free energy of the fluid? Let this contribution be F_p, and assume that F_p is a constant, that we can define as 0, when $\nabla \mathbf{p} = 0$. In the continuum limit, variations in $\mathbf{p}$ will occur across length scales much larger than the molecular scale, hence we can expand F_p about the uniform state in gradients of $\mathbf{p}$, resulting in the Frank free energy,

$$F_p = \int dV \left\{ \frac{K_1}{2} (\nabla \cdot \mathbf{p})^2 + \frac{K_2}{2} [\mathbf{p} \cdot (\nabla \times \mathbf{p})]^2 + \frac{K_3}{2} [\mathbf{p} \times (\nabla \times \mathbf{p})]^2 \right\}. \tag{3.23}$$

A detailed argument of why these are the lowest order terms allowed by symmetry is given in Section 3.1.2 of de Gennes and Prost [45]. The three Frank constants correspond to the three different deformation modes of splay (K_1), twist (K_2), and bend (K_3), shown in Fig. 3.3. A common simplification is to take these three constants to be equal, $K_1 = K_2 = K_3 = K$, resulting in

$$F_p = \int dV \left\{ \frac{K}{2} \partial_\alpha p_\beta \partial_\alpha p_\beta \right\}, \tag{3.24}$$

where the Einstein summation convention has been used for clarity.

Liquid crystals can form topological defects, where the polar order parameter is discontinuous. Example topological defects in a 2D polar fluid are shown in Fig. 3.4. Topological defects can be classified using the theory of homotopy groups applied to closed loops or surfaces enclosing the defects [119]. Loops that can be continuously deformed onto each other form a

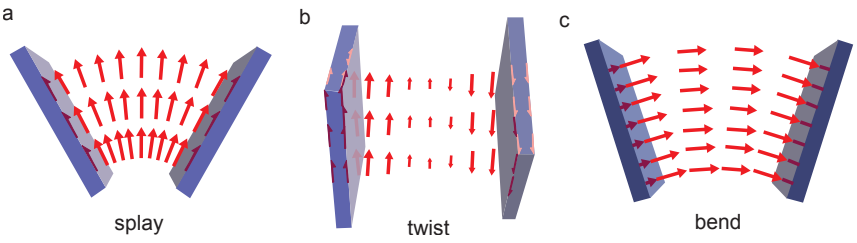

Figure 3.3: Polar fluid distortions in the splay, twist and bend configurations.

homotopy class. The complete set of homotopy classes for a particular system has a group structure, and is referred to as the fundamental group of the order parameter space. For a 2D polar fluid, with $|\mathbf{p}| = 1$, the order parameter space is the unit circle, which can be parameterised by an angle $\theta \in [0, 2\pi)$. Closed loops can go round the unit circle an integer number of times. Loops that go round the same number of times can be continuously deformed onto each other, and loops that go round different numbers of times cannot. As such, the number of times a loop goes round the unit circle, called the winding number, classifies loops into homotopy classes. The winding number is the number of times the polarity field undergoes a complete turn when traversing a loop around a defect in the physical space of the polar fluid. Topological defects play an important role in the mechanics of liquid crystals [176], as well as attempts to engineer them [132] [137], and it has been suggested that they play a role in the mechanics of polarised tissues [169] [52]. A wider range of defects are possible in 3D liquid crystals, including hedgehog defects and disclination loops [4]. Recent advances in microscopy and image segmentation have made possible the observation and classification of such defects experimentally [50].

Multiple fluid species, and anisotropic effects are just a handful of the ways in which the single component incompressible fluid of Eq. 3.1 has been extended to describe complex soft matter systems. However, fundamental to all of them is the assumption of thermodynamic equilibrium. The relaxation of this assumption is the major difference between living systems, and the systems that have traditionally been studied in soft matter and statistical physics. In the next section I will give a brief introduction to the physics of non-equilibrium, or active, matter.

3.2 Active matter

Thermodynamic equilibrium is defined as any state obeying detailed balance. For a set of microstates, where the probability distribution of state i is P_i, and the transition rate between state i and state j is ω_{ij}, detailed balance is defined as the condition

$$P_i \omega_{ij} = P_j \omega_{ji} \quad \forall i, j. \tag{3.25}$$

Systems in equilbrium obey the Boltzmann distribution

$$P(E_i) \propto e^{-\frac{E_i}{kT}}, \tag{3.26}$$

where $P(E_i)$ is the probability of the system occupying microstate i with energy E_i, k is the Boltzmann constant, and T the temperature [177]. Although the fields of thermodynamics, and later statistical physics, have been wildly successful at describing systems in equilibrium, they

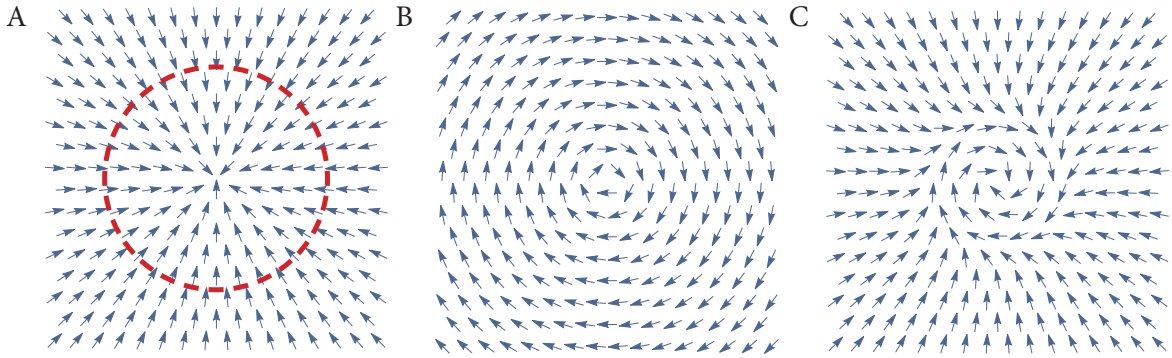

Figure 3.4: A) An example polar field with a +1 defect. Traversing the red path, the polar vector undergoes 1 full turn, hence the winding number is 1. B) Another example of a polar +1 defect. C) The smooth deformation of the first vector field onto the second. This is possible because they have the same winding number, hence belong to the same homotopy class.

are limited in their applicability to living organisms by the fact that life exists in a state out of equilibrium. Organisms continually absorb energy from their surroundings and convert it into mechanical and chemical work. At the cellular level this typically occurs by the hydrolysis of adenosine triphosphate (ATP) to adenosine diphosphate (ADP), releasing a few kT of energy [207]. It is also worth noting that there are non-living non-equilibrium systems, e.g. Janus particles, which are maintained out of equilibrium by a chemical bath [31], and the Earth's climate system, maintained out of equilibrium by the influx of solar radiation [115]. Active matter is the umbrella term applied to these non-equilibrium systems. Naturally, there is a great deal of interest in extending statistical physics to describe active matter [151] [34] [210] [136]. However, to date the only general theory of non-equilibrium thermodynamics is the near-to-equilibrium framework of Onsager [143].

3.2.1 Non-equilibrium physics

Equilibrium systems are defined by the property of detailed balance: the probability for a system to transition from microstate i to microstate j is equal to the transition probability from j to i. Much of the novel physics exhibited by living systems arises from the violation of this basic assumption. Providing a general description of non-equilibrium statistical systems is a major open problem. However, a broad class of non-equilibrium theories are derived from the work of Lars Onsager.

Onsager theory

The second law of thermodynamics states that the entropy of a macroscopic system cannot decrease,

$$dS \geq 0. \tag{3.27}$$

Furthermore, at equilibrium, $dS = 0$ [102]. The second law enforces a distinct arrow of time, in contrast to the time reversible microscopic dynamics of the constituent particles of the statistical system. The breaking of time reversal symmetry is recognised as a hallmark of active matter [136], and the rate at which entropy is produced as a measure of broken detailed balance [34]. Onsager's approach to non-equilibrium thermodynamics is to start with the known equilibrium state, then describe non-equilibrium states by a power series expansion about equilibrium in

some appropriate variables.

Dynamical equations for non-equilibrium processes can be derived by considering the rate of entropy production in a system. For a continuous system, the entropy density, s, obeys a continuity equation

$$\partial_t s + \partial_\alpha J^{\mathrm{s}}_\alpha = \sigma, \tag{3.28}$$

where J^{s}_α is a flux of entropy density, and σ an entropy source term. For an isolated, adiabatic system this equation reduces to

$$\partial_t s = \sigma \geq 0, \tag{3.29}$$

where the inequality is due to the second law of thermodynamics. Two assumptions are inherent in Eq. 3.28. Firstly, it is assumed that the entropy of an infinitesimal volume element can be written as a fraction of the total element, like sdV. This is justifiable if the volume elements of the continuous system are large enough to contain many microscopic particles. Secondly, it is assumed the volume elements are in a state of "local equilibrium", hence the entropy can be defined in the same way as for an equilibrium system. Mazur and de Groot show [46] that the entropy production rate can be written as a sum of pairs of thermodynamic fluxes and forces

$$\sigma = \sum_i J_i F_i, \tag{3.30}$$

where F_i are the thermodynamic forces. Both the forces and fluxes disappear at equilibrium. The fluxes can then be written as a series expansion about the equilibrium state in terms of the forces

$$J_i = \sum_j L_{ij} F_j, \tag{3.31}$$

where L_{ij} are the Onsager coefficients. L_{ij} obey the Onsager reciprocal relations $L_{ij} = L_{ji}$ (up to a change in sign that is not discussed here), and by the requirement that $\sigma \geq 0$, $L_{ii}L_{jj} \geq \frac{1}{4}(L_{ij} + L_{ji})^2$, where there is no sum over repeated indices.

What is the rationale for writing a series expansion of the fluxes in terms of thermodynamic forces? Consider the example of an incompressible ternary fluid, consisting of species A, B and C. The continuity equations are

$$\partial_t n_A = -\partial_\alpha j^A_\alpha \tag{3.32}$$

$$\partial_t n_B = -\partial_\alpha j^B_\alpha, \tag{3.33}$$

and C has been eliminated by incompressibility. j^A_α and j^B_α must be expressed as functions of n_a and n_B in order to form a closed set of equations. This can be achieved by writing $j^{A,B}_\alpha$ as a series expansion in a suitable set of variables, around a known state. In our case, the known state is that of thermodynamic equilibrium. Equilibrium in the ternary fluid is defined by the requirement that the chemical potentials for A and B are uniform,

$$\partial_\alpha \mu_A = 0 \tag{3.34}$$

$$\partial_\alpha \mu_B = 0. \tag{3.35}$$

As such, $\partial_\alpha \mu_A$ and $\partial_\alpha \mu_B$ suggest themselves as appropriate expansion variables as they are 0 at equilibrium, and small close to equilibrium. Hence, to linear order in gradients of the chemical potentials the fluxes are

$$j^A_\alpha = L_{00}\partial_\alpha \mu_A + L_{01}\partial_\alpha \mu_B \tag{3.36}$$

$$j^B_\alpha = L_{10}\partial_\alpha \mu_A + L_{11}\partial_\alpha \mu_B, \tag{3.37}$$

for some coefficients L_{ij}. Using the Einstein summation convention over Greek indices, the entropy production can be written

$$\sigma = -(\partial_\alpha \mu_A) j_\alpha^A - (\partial_\alpha \mu_B) j_\alpha^B, \tag{3.38}$$

i.e. as a sum of pairs of thermodynamic fluxes and forces. We can then identify $\partial_\alpha \mu_{A,B}$ as the conjugate thermodynamic forces to $j_\alpha^{A,B}$, and L_{ij} as the Onsager coefficients, obeying $L_{01} = L_{10}$. As long as the functions $\mu_{A,B}(n_A, n_B)$ are known, Eq. 3.32 and Eq. 3.33 can then be solved.

In general all fluxes can couple to all forces, potentially resulting in large constitutive equations. However, some couplings can be ruled out on symmetry grounds. Consider the entropy production of a generic system, with fluxes J_i, and forces F_i,

$$\sigma = \sum_i J_i F_i. \tag{3.39}$$

In general, there will be fluxes and forces of different tensorial order. The Curie Principle [40] states that for an isotropic system, there can be no couplings between fluxes and forces of different tensorial order. The general principle is described by Mazur and de Groot [46]. For brevity, the simplified case of scalar and vector forces is outlined here. Consider an entropy production rate

$$\sigma = J_s F_s + \mathbf{J}_v \cdot \mathbf{F}_v, \tag{3.40}$$

where J_s and F_s are scalars, and $\mathbf{J}_v$ and $\mathbf{F}_v$ are vectors. To linear order, the constitutive equations are

$$J_s = L_{ss} F_s + \mathbf{L}_{sv} \cdot \mathbf{F}_v \tag{3.41}$$

$$\mathbf{J}_v = \mathbf{L}_{vs} F_s + L_{vv} \mathbf{F}_v. \tag{3.42}$$

Any symmetry property of the system must leave the Onsager coefficients, L_{ij}, unchanged. An isotropic system has arbitrary rotational symmetry, hence L_{ij} will remain unchanged by an arbitrary rotation, $\mathcal{R}$. The scalar Onsager coefficients are trivially unchanged by a rotation. The vector coefficients must satisfy

$$\mathcal{R}\mathbf{L}_{sv} = \mathbf{L}_{sv} \tag{3.43}$$

$$\mathcal{R}\mathbf{L}_{vs} = \mathbf{L}_{vs}. \tag{3.44}$$

As $\mathcal{R}$ is an arbitrary rotation, these equations can only be satisfied by

$$\mathbf{L}_{sv} = \mathbf{0} \tag{3.45}$$

$$\mathbf{L}_{vs} = \mathbf{0}. \tag{3.46}$$

As such, the couplings between scalar and vector fluxes and forces disappear, and the constitutive equations simplify to

$$J_s = L_{ss} F_s \tag{3.47}$$

$$\mathbf{J}_v = L_{vv} \mathbf{F}_v. \tag{3.48}$$

The validity of Onsager's non-equilibrium approach has been verified experimentally in a wide range of systems [122] [123]. The existence of linear flux-force relations was known before Onsager in particular systems, e.g. Fick's law of diffusion, and Fourier's law of heat. Furthermore, reciprocal relations had also been observed before Onsager's theory, e.g. Lord Kelvin's observation of symmetric cross coupling between gradients of temperature and gradients of electrical potential difference [184].

Stochastic thermodynamics

In the past few decades significant work has been done to develop a rigorous basis for the thermodynamics of active matter, by considering the behaviour of meso- and microscopic systems along fluctuating trajectories in phase space [172] [36]. This emerging field is called stochastic thermodynamics, and has been applied to a range of non-equilibrium systems, e.g. a colloidal particle in a laser trap [87], and ATP driven biomolecules [171]. By considering a system with mesostates $\{I\}$, the entropy production rate, averaged over trajectories through the space of mesostates is [170]

$$\langle \dot{S}(t) \rangle = \sum_{I<J} \left(P_I(t) K_{IJ} - P_J(t) K_{JI} \right) \log \left(\frac{P_I(t) K_{IJ}}{P_J(t) K_{JI}} \right), \tag{3.49}$$

where $P_I(t)$ is the probability the system is in mesostate I at time t, and K_{IJ} is the transition rate from mesostate I to J. The mesostates are ordered chronologically along the trajectory, hence $I < J$ refers to states I that are visited prior to state J. Eq. 3.49 results in the second law of thermodynamics,

$$\langle \dot{S}(t) \rangle \geq 0, \tag{3.50}$$

as $(x - y)\log(x/y) \geq 0$ for all $x, y \geq 0$. Eq. 3.50 differs from the classical description of the second law as it recognises entropy only increases on average. At the level of individual trajectories, it is perfectly possible for thermal fluctuations to decrease the entropy of a system. Stochastic thermodynamics also provides a quantitative link between entropy production and the breaking of time reversal symmetry in non-equilibrium steady states. Denoting the probability of following a certain trajectory through the space of mesostates as $P(\mathcal{I})$, and the probability of following the trajectory traversing the same path but backwards in time as $P(\tilde{\mathcal{I}})$, the following condition holds [173]

$$\frac{P(\tilde{\mathcal{I}})}{P(\mathcal{I})} = e^{-\frac{\Delta S}{k}}, \tag{3.51}$$

where ΔS is the entropy produced along $\mathcal{I}$. Eq. 3.51 demonstrates that entropy producing (i.e. non-equilibrium) processes are far more likely to happen than their time reversed opposites.

Stochastic thermodynamics aims to understand the fundamental physics of active matter at a microscopic level. In parallel to this effort, many researches are studying the impact of including active terms in the dynamics of coarse grained, macroscopic variables, by developing hydrodynamic theories of active matter.

3.2.2 Hydrodynamic theories of active matter

Hydrodynamics, considering systems in the limit of long length scales and slow time scales, is a powerful tool in fluid dynamics and condensed matter physics. The most famous early examples of hydrodynamic theories in biophysics are the Vicsek Model [203], and its continuous counterpart, the Toner-Tu Model [196].

Vicsek Model

The Vicsek Model describes a set of self propelling particles, each with fixed speed $|\mathbf{v}_i| = v$. The model evolves by taking discrete timesteps. At each timestep, each particle adopts the average direction of motion of all other particles within some radius, plus a random directional

perturbation. In 2D, the direction of motion is described by a single angle, θ, and the update rule is written

$$\theta(t+1) = \langle\theta(t)\rangle_r + \Delta\theta. \tag{3.52}$$

$\Delta\theta$ is a random number drawn from a uniform distribution in $[-\frac{\eta}{2}, \frac{\eta}{2}]$, hence the parameter η acts qualitatively like a temperature. At zero fixed speed, this model reduces to the XY model of ferromagnets. At infinite fixed speed, the particles become completely mixed. However, at finite fixed speeds, Vicsek et al. computationally demonstrate interesting behaviour as a function of η. At high η, the system is mixed, and there is no net flow of particles. As η is decreased, the system undergoes a phase transition to a state where all particles are moving in the same direction. The direction of net motion is random, and spontaneously breaks the rotational symmetry of the initial condition. This result is significant as the 2D XY model does not exhibit such a transition, and indeed such a transition would be forbidden in equilibrium systems by the Mermin-Wagner theorem [120]. Consequently this is an example of a genuinely non-equilibrium phase transition. The average velocity of the particles is defined as

$$\mathbf{v} = \frac{1}{Nv}\sum_{i}^{N}\mathbf{v}_i. \tag{3.53}$$

Although the discretised velocities of the Viscek Model are not hydrodynamic variables, the average velocity is. The modulus of the average velocity is used as the order parameter of the phase transition.

The underlying mechanism of the Vicsek Model is very simple, yet it captures the key behaviour of flocking organisms: collective motion. A recent study of starling flocks in Rome has demonstrated that collective motion does indeed propagate through flocks by neighbour alignment, and that changes in direction are typically initiated by the more variable trajectories of birds at the edge of the flock [9].

Toner-Tu Model

The Toner-Tu Model is the continuum limit of the Vicsek Model. The particles (or birds, in the nomenclature of the paper) are described by a coarse grained number density ρ, which obeys the continuity equation

$$\partial_t\rho + \nabla\cdot(\rho\mathbf{v}) = 0, \tag{3.54}$$

i.e. birds are conserved. The flow field, $\mathbf{v}$, obeys the compressible fluid equation

$$\partial_t\mathbf{v} + (\mathbf{v}\cdot\nabla)\mathbf{v} = -\alpha\mathbf{v} - \beta|\mathbf{v}|^2\mathbf{v} - \nabla P + D_L\nabla(\nabla\cdot\mathbf{v}) + D_1\nabla^2\mathbf{v} + D_2(\mathbf{v}\cdot\nabla)^2\mathbf{v} + \mathbf{f}. \tag{3.55}$$

α and β are parameters from a Landau style free energy, where $\alpha > 0,\ \beta > 0$ describes a disordered phase with $\langle\mathbf{v}\rangle = 0$, and $\alpha < 0,\ \beta > 0$ describes an ordered phase with $|\langle\mathbf{v}\rangle| > 0$. P is the pressure of the system, and D_L, D_1 and D_2 are diffusion constants. $\mathbf{f}$ is a Gaussian random noise term. Toner and Tu demonstrate analytically that this system exhibits phase transitions that are different from the equilibrium XY model in dimensions less than 4, that the system undergoes spontaneous symmetry breaking in 2D, and that their equations describe a universality class to which the Vicsek model belongs.

3.2.3 Pattern formation

Pattern formation plays a central role in morphogenesis. Consequently, pattern forming, and more generally collective ordering, phenomena have been studied extensively by biophysicists. Phase transitions like those seen in the Toner-Tu Model, or Model B, can be thought of as the simplest form of collective ordering, where long range correlations dominate. However, to make an organism from a single cell, more complex spatial patterning is required.

Fluid instabilities

There are many different pattern forming mechanisms in fluid systems, which typically arise due to linear instabilities. Cross and Hohenberg [39] classify these instabilities into stationary and oscillatory, and Types I, II and III. Type I instabilities are unstable at zero wavevector, hence describe non-conserved variables. Type II instabilities have a band of unstable wavevectors starting at zero. Type III instabilities have a band of unstable wavevectors starting at some non-zero value, and hence have an associated characteristic length scale where exactly one mode is unstable. For example, the Rayleigh-Bénard instability occurs when a fluid in a gravitational field is heated from below. In this scenario, the governing equations are the Navier-Stokes equation, and a conservation law for heat, which have a Type I_s instability resulting in convection cells. The exact pattern of convection cells is determined by the parameters of the model (e.g. temperature gradient, buoyancy), and also the boundary conditions. Other commonly studied fluid pattern formation mechanisms are the Saffman-Taylor fingering instability along a fluid boundary [191], and front propagation in the Ginzburg-Landau equations [201].

Turing instabilities

The most famous example of pattern formation in biophysics, and one that was hypothesised very early on in the development of the field, is the Turing Instability [200]. Turing proposed a mechanism by which diffusion can drive an otherwise stable, homogeneous system into an unstable state. He proposes this mechanism as a specifically morphogenetic one, where two species of morphogen form a spontaneous pattern in order to organise a growing tissue. Consider two species of morphogen, X and Y, obeying the following dynamics:

$$\partial_t X = aX + bY + D_X \partial_\alpha^2 X, \tag{3.56}$$

$$\partial_t Y = cX + dY + D_Y \partial_\alpha^2 Y, \tag{3.57}$$

where D_X and D_Y are diffusion constants, and a, b, c, and d are parameters describing the chemical reactions between species X and Y. In the limit of no diffusion, this system is stable when $a + d < 0$ and $ad - bc > 0$. Introducing non-zero diffusion can then push the system into an unstable state when $(aD_Y + dD_X)^2 > 4D_X D_Y(ad - bc)$. This condition results in a Type III_s instability, hence there is a characteristic length scale associated with the Turing pattern. Turing patterns, and related reaction-diffusion instabilities, have had a major impact in developmental biology. Experimental examples of Turing and Turing-like mechanisms have been found in a wide range of contexts, including chemical reaction networks [54], bacterial populations [90], the growing mouse limb bud [153], and the early *C. elegans* embryo [70], to name a few. Example Turing patterns are shown in Fig. 3.5. Turing patterns result from Type III instabilities (both stationary and oscillatory) in the Cross and Hohenberg nomenclature, i.e. they exhibit a band of unstable wavenumbers. The onset of instability occurs at one non-zero critical wavenumber. This results in a pattern with a characteristic length scale.

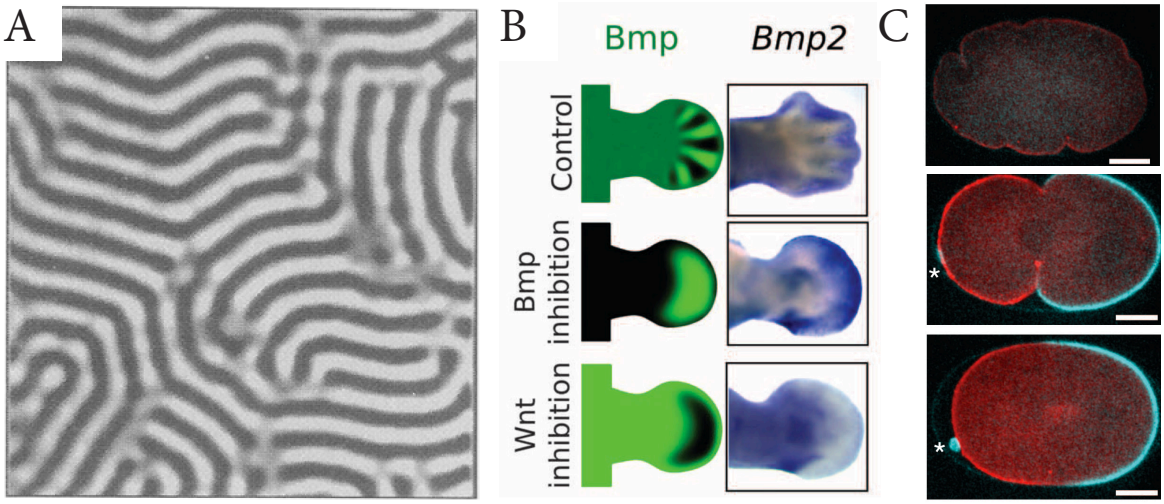

Figure 3.5: Examples of experimentally realised Turing patterns. A) A chemical reaction network, taken from Dulos et al. [54]. B) The BMP pattern in the mouse limb bud, taken from Raspopovic et al. [153]. C) The establishment of PAR polarity in the early *C. elegans* embryo, taken from Goehring et al. [70].

3.2.4 Active matter models of tissues

A major theme of recent biophysics research has been to apply theories of active matter to biological systems in greater and greater detail [113] [88]. Some models are quite general, e.g. Active Model B Plus [194], a non-equilibrium extension of the binary fluid Model B, whereas others contain more detailed descriptions of biological activity from the scale of proteins [99] to cells [149] to flocks of organisms [196]. Of particular interest to developmental biology are the cell cortex, made up of actin filaments and myosin motors, and tissues made up of collectively moving cells.

The acto-myosin cortex

The acto-myosin cortex is a force generating network of filamentous actin lying beneath the cell membrane. Stress in the network is generated by ATP driven myosin molecular motors. The actin filaments range in length from around 0.1 µm to 10 µm [148] and, with a persistence length of ≈15 µm [65], are stiff on cellular length scales. Due to the highly anisotropic shape of actin filaments, the actin cortex can be modelled as either an active nematic or active polar fluid depending on whether the actin fibres are aligned or not [98] [155]. Such a description can be made more realistic by taking into account the de/polymerisation kinetics between filamentous F actin and globular G actin monomers, and the presence of myosin motors, as in Kruse et al. [99], as well as the presence of a passive solvent, as in Joanny et al. [85], and Callan-Jones and Jülicher [29]. These active hydrodynamic theories of the cortex, and active gel physics in general [150], have been successfully applied to a variety of systems, for example: Joanny et al. [86] show that the structure of the cortex as a thin sub-membrane layer can be explained as the result of active wetting phenomena; Salbreux et al. use the theory of active nematics to describe the formation of a contractile actin ring during cytokinesis [165]; and Marth et al. [116] develop a model of cell motility by including bending rigidity.

Cells as an active fluid

Whereas the cortex determines mechanics at the scale of individual cells, morphogenesis typically takes place on the scale of tissues consisting of many cells. As such, there have been multiple examples of hydrodynamic descriptions of tissues. Cells can polarise, both in terms of their shape, and in terms of the distribution of chemicals within them, hence they can be described by active nematic, and active polar models [51]. The importance of topological defects in cell models has been emphasised by Beng Saw et al. [169], where they correlate defects with cell deaths and extrusions in epithelia. The interplay between the mechanical properties of cells, and their proliferation rates, as a driver of morphogenesis has been explored in e.g. Shraiman [179], Yeh and Chen [215], and Sarkar et al. [166]. Epithelial tissue dynamics has also been explored in detail by Popović et al. [149], where they include the novel contribution of topological rearrangements between neighbouring cells. Epithelia are particularly amenable to comparison between theory and experiment as they are essentially 2D, hence (comparatively) easy to image and analyse. In Merkel et al. [118], the deformation of an epithelium is quantitatively broken down into cellular growth, rotations, topological transitions and elongations. Active hydrodynamics has also been applied to the problem of cavity growth in Duclut et al. [53], where a spherical shell of polarised cells grows by active flows of fluid into the centre.

So far this chapter has summarised a range of ways in which relevant theory from fluid dynamics, soft matter, and statistical physics has proved relevant to, and formed a basis for, physical descriptions of biological systems. Analytical theories, and more specifically hydrodynamics, are powerful tools for predicting novel phenomena, and extending physical intuition. However, they tend to drastically simplify the complexity of real organisms, and in striving for generality tend to become less applicable to any one experimental system. In some ways this is a strength, but often a more detailed description of a specific situation is required. For this we must turn to computational methods. There is a vast literature on computational models in biology [168] [5] [125], so in the next section I will only consider common models in the subfield of tissue mechanics.

3.3 Computational models of tissues

Computational models of tissue mechanics aim to describe the dynamics of an aggregate of many cells with a simplified representation that is computationally tractable. Here I will give a brief overview of three common models: the Vertex Model, the Cellular Potts Model, and the Phase Field Model.

3.3.1 The Vertex Model

Vertex Models describe a tissue as a set of vertices and edges that partition the 2D plane into tessellating polygons [134] [59]. The positions of the vertices are then updated by calculating the forces acting on them due to pressure and line tension. This approach is particularly well suited to epithelia, which are close to 2D. The reduction of the tissue to a finite number of vertices allows the dynamics to be calculated efficiently. Alt et al. have generalised the Vertex Model to a 3D representation of the epithelium, with the constraint that the apical and basal surfaces have the same topology [5]. Generalising the Vertex Model further to generic (i.e. non-epithelial) 3D tissues has proven to be a significant challenge, due mainly to the wide variety of topological transitions that can take place between neighbouring polyhedra in 3D space [140] [76]. Although appropriate for confluent tissues, it is difficult to modify the Vertex Model for situations where lumens open. Furthermore, cell-cell adhesions are included implicitly in the

shared edge between neighbouring cells, which is a representation that does not lend itself to explicitly including adhesion mediated phenomena. The discrete nature of the Vertex Model representation makes it difficult to describe complex cell shapes, though a notable exception is the example of scutoids in curved epithelia described by Gomez-Galvez et al. [71]. The lack of smooth surface derivatives is an obstacle to including more complex active surface physics [164]. Despite these drawbacks, Vertex Models have been successful at describing tissue mechanics in a wide range of systems. Bielmeier et al. use a Vertex Model to describe cyst formation at the onset of cancer [20], Okuda et al. demonstrate the growth of 3D epithelial tubes [142], and Okuda et al. combine a Vertex Model with Turing Patterns to model a variety of morphogenetic processes [141].

3.3.2 The Cellular Potts Model

An alternative framework for tissue mechanics is the Cellular Potts Model [69]. The Cellular Potts Model is defined on an N dimensional square lattice, much like the Ising Model. One of a finite number of values is associated with each lattice site, representing a set of cellular species, and the extracellular medium. A free energy is defined for the lattice, describing cell-cell adhesions, line tensions, and pressure. Further complexity can be included, e.g. morphogen gradients, by adding terms to the system's Hamiltonian [41]. The dynamics are typically described by a Monte Carlo update algorithm, where lattice values are assigned a new, random value, and this change is accepted or rejected with a certain probability, dependent on the resulting change in free energy. The Cellular Potts Model is popular for a number of reasons: it is trivially generalised to 3D, Monte Carlo solvers are common, efficient, and well understood, and there is no need to explicitly include topological transitions. However, there is a disadvantage in that the dynamics are not the result of physical forces. The model does minimise its free energy, but the trajectory it takes is not the steepest gradient path. The Cellular Potts Model has been used by Graner and Glazier to model cell sorting by differential adhesion [72], by Marée et al. to model cell movement [114], and by Szabó to model cancer [190], to name but a few examples.

3.3.3 The Phase Field Model

The Phase Field Model describes cell boundaries as the level sets of a so called "phase field" [139]. Phase Field Models are common in materials science, where they are used to describe the dynamics of grain boundaries [187]. Dynamical equations for the evolution of the phase field include cell level processes like line tensions, adhesions and pressure. Multiple cell species can be included by using multiple phase fields. Generalisation of the model to 3D is trivial, and in contrast to the Cellular Potts Model, the dynamics are due to physical forces. Phase Field Models are a more recent introduction to the field of tissue mechanics than the Cellular Potts Model or Vertex Model, however they have been used to study cell migration by Najem et al. [135], and spindle positioning by Akiyama et al. [3]. There have also been extensions to the basic Phase Field Model to include auxiliary fields describing e.g. extracellular fluid with hydrodynamic reactions, or surface bound molecules [104]. Phase Field Models can be computationally expensive as the phase field equations are solved on the whole of a space filling grid in order to resolve mechanics that only occur at the cell surface. The abstraction of the cell surface as the level set of a higher dimensional function is also an obstacle to including more complex phenomena (e.g. diffusion of chemical species on the surface) and it remains to be seen whether this obstacle can be overcome.

3.4 Summary

In this chapter, I have summarised the existing literature on theoretical and computational work relevant to my own. Hydrodynamic theories of complex fluids (e.g. multi species fluid mixtures, or liquid crystals) have been extended to non-equilibrium scenarios by using Onsager's theory of non-equilibrium thermodynamics. This synthesis has resulted in a plethora of theories and models describing biology at scales ranging from individual proteins to flocks of organisms. The novel physics of these active matter system is beginning to be explored and understood in specific systems, though no general theory, analogous to equilibrium statistical physics, yet exists. The significant increase in modern computing power has opened the door for computational models of biological systems, which are becoming more and more complex and realistic. These models are still restricted to representations of tissues that are computationally efficient, and hence limited in their realism. However, they have been shown to demonstrate biologically relevant processes like tissue deformations and cell locomotion, and recent developments by Torres-Sánchez et al. on a continuous representation of cell surfaces provides an exciting step forward [197].

Chapter 4

The hydrodynamics of pumping cell aggregates

In this chapter I discuss our hydrodynamic theory of pumping cell aggregates. Our aim with this work was to describe cells in the hydrodynamic limit, with an emphasis on fluid pumping phenomena, and in the hope of ultimately describing the formation of a fluid filled cavity surrounded by tissue. In order to study the cavity forming behaviour of such cell aggregates, we begin by describing, in the continuum limit, a system consisting of cells, water and generic solute molecules.

4.1 Derivation of the hydrodynamic equations

4.1.1 Continuity equations

We consider a ternary fluid consisting of cells, water and solute molecules, as shown in Fig. 4.1. The solutes and water can pass through the cell membrane passively. Solutes can also be pumped across the cell membrane by active transport. This active pumping can occur both isotropically and along the polarity axis of the cell. As we are concerned with pumping phenomena, we treat the cells as simply a membrane bound volume containing a binary fluid of solutes and water. We neglect all other internal structure and complexity. By considering volume elements that are large enough to contain many cells, the cells, solutes, water, polarity and centre of mass velocity of the fluid can all be described by smooth, continuous fields.

In the following equations, n^{sm} denotes the number density of the solutes in the medium, n^{wm} the number density of water molecules in the medium, and $c(\mathbf{X})$ the number density of cells with some internal state variable $\mathbf{X}$. Note that n^{wm} is the number of water molecules in the medium of a volume element, divided by the volume of the volume element. The "local" number density of water in the medium is $\bar{n}^{\mathrm{wm}}$, i.e. the number of water molecules in the medium of a volume element, divided by the extra-cellular volume of the volume element. The volume of a water molecule is v^{w} and the volume of a solute molecule is v^{s}. We make the approximation that cells are entirely described by the state variable $\mathbf{X} = \{n^{\mathrm{s}}, n^{\mathrm{w}}, v^{\mathrm{c}}, \boldsymbol{\xi}\}$, where n^{s} and n^{w} are the total number of solute and water molecules in a cell, and v^{c} is the volume of the cell. The variable $\boldsymbol{\xi}$ quantifies the gradient of solutes in the cell, and is defined by taking the first term in a moment expansion of the solute density within the cell. Let N^{s} be the number density of solutes inside the cell. $\boldsymbol{\xi}$ is then defined as

$$\boldsymbol{\xi} = \frac{1}{v^{\mathrm{c}}} \int_{v^{\mathrm{c}}} (\mathbf{r} - \mathbf{r}^0) N^{\mathrm{s}} dV, \tag{4.1}$$

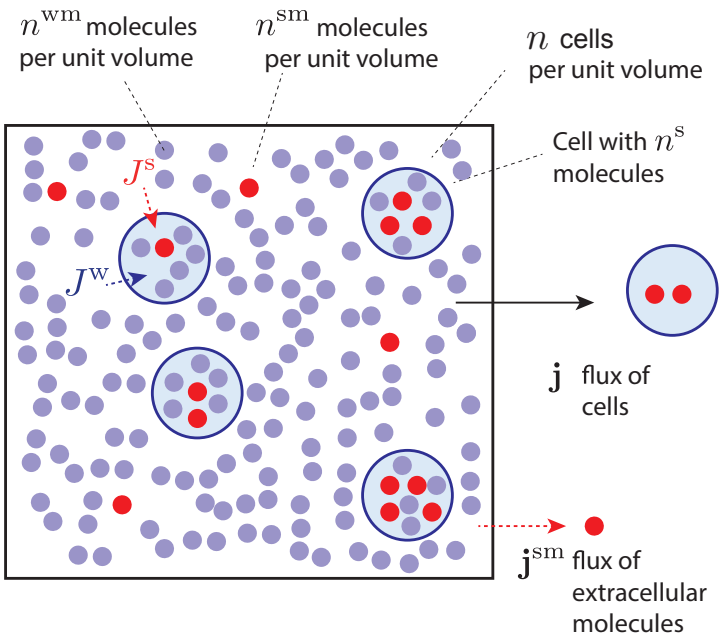

Figure 4.1
A ternary fluid consisting of cells, solutes (red) and water (blue).

where $\mathbf{r}$ is a point inside the cell, and $\mathbf{r}^0$ is the centre of the cell.

Throughout this chapter, greek indices are used to denote spatial coordinates. In the following, we use the Einstein summation convention over all repeated indices. For brevity, we use $\mathbf{n}$, $\mathbf{n}^{\mathrm{m}}$, $\boldsymbol{\nu}$ as vectorial notation for $\{n^{\mathrm{s}}, n^{\mathrm{w}}\}$, $\{n^{\mathrm{sm}}, n^{\mathrm{wm}}\}$, and $\{v^{\mathrm{s}}, v^{\mathrm{w}}\}$ respectively. With these conventions in place, the cells obey the following continuity equation,

$$\partial_t c + \partial_{n^{\mathrm{s}}}\left(J^{\mathrm{s}} c\right) + \partial_{n^{\mathrm{w}}}\left(J^{\mathrm{w}} c\right) + \partial_v\left(J^v c\right) + \partial_{\boldsymbol{\xi}}\left(\mathbf{J}^{\xi} c\right) + \partial_\alpha\left(V_\alpha c\right) = 0, \tag{4.2}$$

where V_α is the velocity of the cells. The continuity equation can be written more succinctly using the vector flux $\mathbf{J}^{\mathrm{X}} = \{J^{\mathrm{s}}, J^{\mathrm{w}}, J^{\mathrm{v}}, J^{\xi}_\alpha\}$, as

$$\partial_t c + \partial_{\mathbf{X}}\left(\mathbf{J}^{\mathrm{X}} c\right) + \partial_\alpha\left(V_\alpha c\right) = 0. \tag{4.3}$$

The solutes and water obey

$$\partial_t n^{\mathrm{sm}} + \partial_\alpha J^{\mathrm{sm}}_\alpha = -\int d\mathbf{X} J^{\mathrm{s}} c, \tag{4.4}$$

$$\partial_t n^{\mathrm{wm}} + \partial_\alpha J^{\mathrm{wm}}_\alpha = -\int d\mathbf{X} J^{\mathrm{w}} c. \tag{4.5}$$

The limits of the integrals are $\int d\mathbf{X} = \int_0^\infty dn^{\mathrm{s}} \int_0^\infty dn^{\mathrm{w}} \int_0^\infty dv \int_{-\infty}^\infty d\boldsymbol{\xi}$. For brevity these limits will not be written explicitly. J^{sm}_α, J^{wm}_α, and $V_\alpha c$ are the spatial fluxes of solutes, water and cells respectively. $J^{\mathrm{s}} c$ and $J^{\mathrm{w}} c$ are source terms in the solute and water continuity equations, describing solute and water molecules crossing the cell membrane. $J^{\mathrm{s}} c$ and $J^{\mathrm{w}} c$ also enter in the cell equation as fluxes in the (unnormalised) probability density c, i.e. when a solute leaves a cell with total internal solutes n^{s}, $c(n^{\mathrm{s}})$ decreases, unless a solute also leaves a cell with total internal solutes $n^{\mathrm{s}}+1$. The cell density must be positive, hence the fluxes $J^{\mathrm{s}} c$, $J^{\mathrm{w}} c$, $J^v c$ and $J^{\xi}_\alpha c$ vanish when $n^{\mathrm{s}} = 0$, $n^{\mathrm{w}} = 0$ or $v^{\mathrm{c}} = 0$. We also assume they vanish when $n^{\mathrm{s}} \to \infty$, $n^{\mathrm{w}} \to \infty$,

$v^{\mathrm{c}} \to \infty$, $\boldsymbol{\xi} \to -\infty$ or $\boldsymbol{\xi} \to \infty$.

The local total number density of cells is given by integrating over all cell states

$$n = \int d\mathbf{X} c(\mathbf{X}). \tag{4.6}$$

Using Eq. 4.2, the continuity equation for n is

$$\partial_t n + \partial_\alpha J_\alpha = 0, \tag{4.7}$$

with the total flux of cells

$$J_\alpha = n\langle V_\alpha \rangle = \int d\mathbf{X} V_\alpha c. \tag{4.8}$$

Here we have used the averaging operator for quantities that depend on the local density of internal cell states:

$$\langle f \rangle = \frac{\int d\mathbf{X} f(\mathbf{X}) c(\mathbf{X})}{n}. \tag{4.9}$$

Eq. 4.7 demonstrates that n is conserved, i.e. we do not include any birth or death processes for cells. The density of the fluid is

$$\rho = m^s n^{\mathrm{sm}} + m^{\mathrm{w}} n^{\mathrm{wm}} + \int dv^{\mathrm{c}} d\mathbf{n} (m^{\mathrm{s}} n^{\mathrm{s}} + m^{\mathrm{w}} n^{\mathrm{w}}) c, \tag{4.10}$$

where m^{s} and m^{w} are the mass of solute and water molecules respectively, and the centre of mass velocity is

$$u_\alpha = \frac{m^{\mathrm{s}} J_\alpha^{\mathrm{sm}} + m^{\mathrm{w}} J_\alpha^{\mathrm{wm}} + \int dv^{\mathrm{c}} d\mathbf{n} (m^{\mathrm{s}} n^{\mathrm{s}} + m^{\mathrm{w}} n^{\mathrm{w}}) V_\alpha c}{\rho}. \tag{4.11}$$

The density obeys the continuity equation

$$\partial_t \rho + \partial_\alpha (\rho u_\alpha) = 0. \tag{4.12}$$

The spatial fluxes in Equations 4.3 - 4.5 can be decomposed into centre of mass terms, and fluxes relative to the centre of mass:

$$V_\alpha = v_\alpha + u_\alpha, \tag{4.13}$$
$$J_\alpha = j_\alpha + u_\alpha n = (v_\alpha + u_\alpha) n, \tag{4.14}$$
$$J_\alpha^{\mathrm{sm}} = j_\alpha^{\mathrm{sm}} + u_\alpha n^{\mathrm{sm}} = (v_\alpha^{\mathrm{sm}} + u_\alpha) n^{\mathrm{sm}}, \tag{4.15}$$
$$J_\alpha^{\mathrm{wm}} = j_\alpha^{\mathrm{wm}} + u_\alpha n^{\mathrm{wm}} = (v_\alpha^{\mathrm{wm}} + u_\alpha) n^{\mathrm{wm}}, \tag{4.16}$$

where v_α, v_α^{sm} and v_α^{wm} are the velocity of cells, solute and water molecules relative to the centre of mass motion. Consequently, the continuity equations become

$$\partial_t c + \partial_\alpha (u_\alpha c) + \partial_{\mathbf{X}} \left(\mathbf{J}^{\mathrm{X}} c \right) + \partial_\alpha \left(v_\alpha c \right) = 0 \tag{4.17}$$

$$\partial_t n^{\mathrm{sm}} + \partial_\alpha (u_\alpha n^{\mathrm{sm}}) + \partial_\alpha (v_\alpha^{\mathrm{sm}} n^{\mathrm{sm}}) = -\int d\mathbf{X} J^{\mathrm{s}} c, \tag{4.18}$$

$$\partial_t n^{\mathrm{wm}} + \partial_\alpha (u_\alpha n^{\mathrm{wm}}) + \partial_\alpha (v_\alpha^{\mathrm{wm}} n^{\mathrm{wm}}) = -\int d\mathbf{X} J^{\mathrm{w}} c. \tag{4.19}$$

Substituting the relative fluxes j_α, $j_\alpha^{\rm sm}$, and $j_\alpha^{\rm wm}$ into the definition of u_α, Eq. 4.11, we deduce that they are not independent and verify the condition

$$n\langle(m^{\rm s}n^{\rm s}+m^{\rm w}n^{\rm w})\mathbf{v}\rangle + m^{\rm s}\mathbf{j}^{\rm sm} + m^{\rm w}\mathbf{j}^{\rm wm} = 0. \tag{4.20}$$

We further assume that the fluid inside and outside of cells is incompressible, such that

$$n^{\rm sm}v^{\rm s} + n^{\rm wm}v^{\rm w} + \int d\mathbf{X}v^{\rm c}c = 1 \tag{4.21}$$

$$n^{\rm s}v^{\rm s} + n^{\rm w}v^{\rm w} = v^{\rm c}. \tag{4.22}$$

The condition 4.21 results in a constraint on the divergence of the flow,

$$\partial_\alpha u_\alpha + \left(v^{\rm s} - \frac{m^{\rm s}v^{\rm w}}{m^{\rm w}}\right)\partial_\alpha\left(j_\alpha^{\rm sm} + \int d\mathbf{X}cn^{\rm s}u_\alpha\right) = 0, \tag{4.23}$$

where the second term depends on the difference in densities between solute and water molecules. What does this term represent intuitively? Consider the case where solute and water molecules have the same volume, but different masses. Enforcing Eq. 4.21, there can be a net flow of mass into or out of a region of pure water, and hence a non-zero divergence in u_α, if water and solute molecules swap places. When the density of water and solutes are approximated to be equal, we recover the familiar incompressibility condition $\partial_\alpha u_\alpha = 0$. Eq. 4.22 also results in the additional incompressibility constraint

$$J^{\rm v} = v^{\rm s}J^{\rm s} + v^{\rm w}J^{\rm w}, \tag{4.24}$$

i.e. cell volume changes are due to the movement of solutes and water across the membrane. Momentum is conserved, hence the centre of mass flow obeys

$$\partial_t(\rho v_\alpha) - \partial_\beta\sigma_{\alpha\beta}^{\rm tot} = 0 \tag{4.25}$$

where $\sigma_{\alpha\beta}^{\rm tot}$ is the stress tensor. In the low Reynolds number limit the inertial term can be neglected and this becomes

$$\partial_\beta\sigma_{\alpha\beta}^{\rm tot} = 0. \tag{4.26}$$

By averaging over c, we derive the following equations for the average number of solutes in a cell, the average cell volume, and the average $\boldsymbol{\xi}$,

$$\frac{d\langle n^{\rm s}\rangle}{dt} = \langle J^{\rm s}\rangle + \frac{\langle n^s\rangle}{n}\partial_\alpha u_\alpha - \frac{\partial_\alpha(\langle u_\alpha n^{\rm s}\rangle n)}{n} \tag{4.27}$$

$$\frac{d\langle v\rangle}{dt} = \langle J^{\rm v}\rangle + \frac{\langle v\rangle}{n}\partial_\alpha u_\alpha - \frac{\partial_\alpha(\langle u_\alpha v\rangle n)}{n} \tag{4.28}$$

$$\frac{d\langle\boldsymbol{\xi}\rangle}{dt} = \langle\mathbf{J}^\xi\rangle + \frac{\langle\boldsymbol{\xi}\rangle}{n}\partial_\alpha u_\alpha - \frac{\partial_\alpha(\langle u_\alpha\boldsymbol{\xi}\rangle n)}{n}. \tag{4.29}$$

In the above equations we have introduced the convected time derivative, $\frac{d}{dt} = \partial_t + u_\alpha\partial_\alpha$.

In order to solve the above continuity equations for cells, solutes, water and momentum density, it is necessary to derive expressions for the various fluxes involved. The processes driving these fluxes can be separated into passive and active terms. The passive processes can be described by considering an equilibrium description of the fluid. The active terms can be described near to equilibrium by using the theory of non-equilibrium thermodynamics to write a series expansion of the fluxes in terms of thermodynamic forces. We first consider the equilibrium case.

4.1.2 Thermodynamic equilibrium

The equilibrium processes can be described using classical thermodynamics, starting with the free energy of a ternary fluid of water, solutes and passive "cells". This passive limit is similar to synthetic biology experiments where enzymatic reactions take place within lipid vesicles [58] [78].

The free energy

We write the free energy of a volume $\mathcal{V}$ of this fluid as $F = \int_{\mathcal{V}} dV f^{\mathrm{tot}}$, with f^{tot} and f the free energy densities

$$f = \int d\mathbf{X} \left[f^{\mathrm{c}}(\mathbf{X}) + P^{\mathrm{c}}(\mathbf{n}\cdot\boldsymbol{\nu} - v^{\mathrm{c}}) \right] c + f^{\mathrm{F}}(n^{\mathrm{F}}) + f^{\mathrm{m}}(\mathbf{n}^{\mathrm{m}}, n, \langle v^{\mathrm{c}} \rangle) + P^{\mathrm{m}} \left(\mathbf{n}^{\mathrm{m}} \cdot \boldsymbol{\nu} + n\langle v^{\mathrm{c}} \rangle - 1 \right) \tag{4.30}$$

$$f^{\mathrm{tot}} = f + kT \int d\mathbf{X} c \ln\left(\frac{c}{n}\right). \tag{4.31}$$

$f^{\mathrm{c}}(\mathbf{X})$ is the free energy of an individual cell with internal state $\mathbf{X}$. P_c is the pressure in the cell, introduced as a Lagrange multiplier enforcing incompressibility of the intracellular fluid. f^{F} is the free energy associated with a fuel molecule (e.g. ATP) with number density n^{F}. Here we will simply write $f^{\mathrm{F}} = \Delta\mu n^{\mathrm{F}}$ where $\Delta\mu$, the change in free energy due to the hydrolysis of one ATP, is a constant in time and space. f^{m} is the contribution to the free energy density arising from mixing of cells and species in the medium, and interactions between cells. For simplicity we assume here that it depends on the average cell volume $\langle v^{\mathrm{c}} \rangle$ and total density n, rather than on the full cell density $c(\mathbf{X})$. Furthermore, we assume there are no interactions (e.g. electrostatic forces) between solute and water molecules. P^{m} is the extracellular pressure, enforcing incompressibility in the extracellular fluid. Finally, the term in $\sim c \ln c/n$ is an entropic term associated with the probability distribution c/n. The Gibbs entropy of a single cell drawn from the probability distribution c/n is $s^{\mathrm{cell}} = -k\frac{c}{n}\ln\left(\frac{c}{n}\right)$, hence the contribution to the free energy density of a volume element containing n cells is $-Tn\int d\mathbf{X} s^{\mathrm{cell}} = kT\int d\mathbf{X} c \ln\left(\frac{c}{n}\right)$.

We postulate the following simple form for the free energy of an individual cell,

$$f^{\mathrm{c}}(\mathbf{X}) = kT\left[n^{\mathrm{s}} \ln\left(\frac{n^{\mathrm{s}}}{n^{\mathrm{s}} + n^{\mathrm{w}}}\right) + n^{\mathrm{w}} \ln\left(\frac{n^{\mathrm{w}}}{n^{\mathrm{s}} + n^{\mathrm{w}}}\right)\right] + \frac{K}{2}\boldsymbol{\xi}^2 + f_0^{\mathrm{c}}(v^{\mathrm{c}}), \tag{4.32}$$

where the first term arises from the mixing entropy of an ideal solution of n^{s} solutes molecules and n^{w} water molecules [68]. In general the free energy of a cell will have some contribution from $\boldsymbol{\xi}$. For simplicity we only consider the lowest order term in an expansion in small $\boldsymbol{\xi}$, $\frac{K}{2}\boldsymbol{\xi}^2$. This term penalizes gradients of concentration in the cell. The third term contains additional contributions to the cell free energy. We assume that this contribution depends only on the cell volume v^{c}, e.g. arising from the surface tension of an idealised spherical cell.

We postulate the following free energy density of the extracellular medium f^{m}:

$$f^{\mathrm{m}} = kT\left(n^{\mathrm{sm}} \ln \frac{n^{\mathrm{sm}}}{n^{\mathrm{sm}} + n^{\mathrm{wm}}} + n^{\mathrm{wm}} \ln \frac{n^{\mathrm{wm}}}{n^{\mathrm{sm}} + n^{\mathrm{wm}}} \right) + kTn\tilde{Z}(\phi) + \frac{K^{\mathrm{c}}}{2}(\partial_\alpha n)^2. \tag{4.33}$$

where $\phi = n\langle v^{\mathrm{c}} \rangle$ is the cell volume fraction. The first term is a contribution coming from mixing of extracellular solutes and water. The second term corresponds to a contribution to

the free energy coming from the entropy of mixing and interactions of cells in the medium. $kT\tilde{Z}(\phi)$ is the excess free energy of a cell that was not already taken into account in f^{c}. The non-dimensional function $\tilde{Z}(\phi)$ satisfies $\tilde{Z}(\phi) = \ln\phi$ for $\phi \to 0$, such that the free energy reduces to the ideal gas entropy of mixing at infinite dilution. The precise form of $\tilde{Z}(\phi)$ away from the $\phi \to 0$ limit depends on the exact cell shapes and the nature of their interactions. To model the effect of inhomogeneities in the fluid, we follow the approach of Cahn and Hilliard [28], and include a term $\frac{K^{\mathrm{c}}}{2}(\partial_\alpha n)^2$ in the medium free energy, which penalises gradients in the cell density field.

What form can we hypothesise for the cellular contribution $\tilde{Z}(\phi)$? We obtain it from the following approximate calculation: We consider that cells are positioned on a lattice, where the volume of a lattice site is equal to the volume occupied by one water molecule. We assume that cells can take any shape but can not overlap. Starting with a volume V corresponding to a lattice of $M = V/v^{\mathrm{w}}$ sites, the number of ways $N = nV$ cells, each occupying $m = \langle v^{\mathrm{c}}\rangle/v^{\mathrm{w}}$ lattice sites, can be placed consecutively is $\Omega = M(M-m)(M-2m)...(M-(N-1)m)/(N!)$. By enumerating the microstates in this way we neglect jamming effects at high packing fraction, as well as the configurational entropy of individual cells that can take any shape. The contribution to the entropy density of mixing cells in the extracellular medium is then given in the large volume limit by $s = \frac{k}{V}\ln(\Omega) \simeq \frac{k}{\langle v^{\mathrm{c}}\rangle}\left[\phi\ln\left(\frac{\langle v^{\mathrm{c}}\rangle}{v^{\mathrm{w}}}\right) - \phi\ln\phi - (1-\phi)\ln(1-\phi)\right]$, where V is the total volume of the system and k the Boltzmann constant. A similar approach has been introduced to estimate the mixing entropy of macroemulsions [160]. A more detailed expression for the entropy of a liquid, modelled as an asymmetric binary hard sphere fluid, was derived by Carnahan and Starling by taking the equation of state of an ideal gas and adding an approximation of the Virial expansion [30, 12]. We have chosen not to use the more complicated Carnahan-Starling formula as it does not change the qualitative behaviour of the entropy [121], and we recognise that treating cells as hard spheres is itself an approximation. Consequently, the entropic contribution of cells to the free energy is

$$f^{\mathrm{entropic}} = \frac{kT}{\langle v^{\mathrm{c}}\rangle}\left[\phi\ln\left(\frac{v^{\mathrm{w}}\phi}{\langle v^{\mathrm{c}}\rangle}\right) + (1-\phi)\ln(1-\phi)\right] \tag{4.34}$$

Finally, adhesion forces are taken into account via a pairwise cell interaction term $-\frac{\epsilon\phi^2}{2\langle v^{\mathrm{c}}\rangle}$, where ϵ is the adhesion energy of a single cell-cell bond. Consequently, the function $\tilde{Z}$ is

$$\tilde{Z}(\phi) = \left(\ln\left(\frac{\phi v^{\mathrm{w}}}{v^{\mathrm{c}}}\right) + \frac{1-\phi}{\phi}\ln(1-\phi)\right) - \frac{\epsilon}{2kT}\phi, \tag{4.35}$$

and the free energy of the medium is

$$\begin{aligned} f^{\mathrm{m}} =& \frac{kT}{v^{\mathrm{s}}}\left(\phi^{\mathrm{sm}}\ln\frac{n^{\mathrm{sm}}}{n^{\mathrm{sm}}+n^{\mathrm{wm}}} + \frac{v^{\mathrm{s}}}{v^{\mathrm{w}}}\phi^{\mathrm{wm}}\ln\frac{n^{\mathrm{wm}}}{n^{\mathrm{sm}}+n^{\mathrm{wm}}}\right) + \frac{kT}{\langle v^{\mathrm{c}}\rangle}\phi\left(\ln\left(\frac{\phi v^{\mathrm{w}}}{v^{\mathrm{c}}}\right) + \frac{1-\phi}{\phi}\ln(1-\phi)\right) \\ & - \frac{\epsilon}{2kT}\phi + \frac{K^{\mathrm{c}}}{2}(\partial_\alpha n)^2. \end{aligned} \tag{4.36}$$

To compare the order of magnitude of different contributions to f^{m}, we note that the typical cell volume is $v^{\mathrm{c}} \approx 4\times10^3\,\mu\mathrm{m}^3$ and the molecular volume of water, $v^{\mathrm{w}} \approx 10^{-11}\,\mu\mathrm{m}^3$. Relevant biological solute volumes range from ions ($v^{\mathrm{s}} \approx 10^{-11}\,\mu\mathrm{m}^3$), to proteins ($v^{\mathrm{s}} \approx 10^{-6}\,\mu\mathrm{m}^3$, though this varies greatly between proteins and folding states). Therefore the term starting $kT/\langle v^{\mathrm{c}}\rangle$ is between 9 and 14 orders of magnitude smaller than the term starting kT/v^{s} (the logarithm of the large quantity $\frac{\langle v^{\mathrm{c}}\rangle}{v^{\mathrm{w}}}$ is still a relatively small number of order 1). This corresponds to our intuition that cells, being macroscopic objects, do not contribute a significant mixing entropy

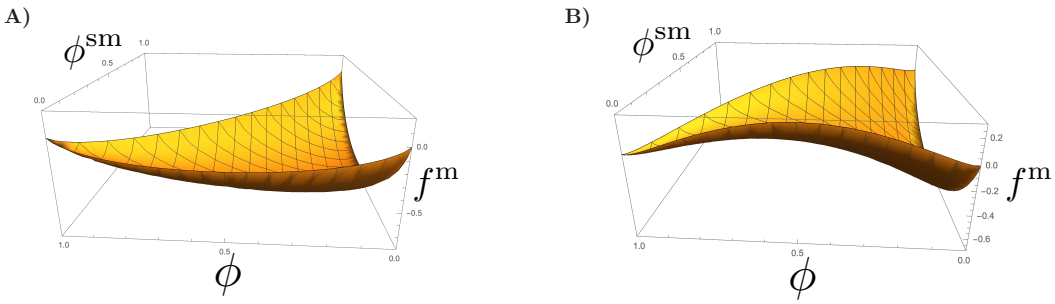

Figure 4.2
The free energy density surface of the passive, ternary system described in Eq. 4.64, with $\tilde{Z}(\phi)$ given by Eq. 4.35. The surface is shown below (A), and above (B), the critical adhesion energy Eq. 4.66. These plots were made with $v^{\mathrm{s}} = v^{\mathrm{w}}$ and unrealistic numerical values of the parameters for improved visualisation.

to the system. Nevertheless, we introduce this term here for completeness.

The form of $\tilde{Z}$ in Eq. 4.35 is only valid when ϕ is not close to 1. When the cells become densely packed, elastic effects will dominate over the balance of entropy and adhesion described above. As such, we will continue to work with the function $\tilde{Z}$, as opposed to the explicit expression in Eq. 4.35, where possible.

Chemical potentials and osmotic pressures

From the expression for the free energy density, Eq. 4.30, we introduce the chemical potentials associated to different concentrations as:

$$\mu \equiv \frac{\delta f}{\delta c} = f^{\mathrm{c}} + P_c(\mathbf{n}\cdot\boldsymbol{\nu} - v^{\mathrm{c}}) + P^{\mathrm{m}}v^{\mathrm{c}} + \frac{\partial f^{\mathrm{m}}}{\partial n} + \frac{v^{\mathrm{c}} - \langle v\rangle}{n}\frac{\partial f^{\mathrm{m}}}{\partial \langle v^{\mathrm{c}}\rangle} \tag{4.37}$$

$$\mu^{\mathrm{sm}} \equiv \frac{\partial f}{\partial n^{\mathrm{sm}}} = \frac{\partial f^{\mathrm{m}}}{\partial n^{\mathrm{sm}}} + P^{\mathrm{m}}v^{\mathrm{s}} \tag{4.38}$$

$$\mu^{\mathrm{wm}} \equiv \frac{\partial f}{\partial n^{\mathrm{wm}}} = \frac{\partial f^{\mathrm{m}}}{\partial n^{\mathrm{wm}}} + P^{\mathrm{m}}v^{\mathrm{w}}. \tag{4.39}$$

We denote $\Delta\mu \equiv \partial f^{\mathrm{F}}/\partial n^{\mathrm{F}}$, i.e. the difference in free energy between ATP and ADP. With the free energies f^{c} and f^{m} introduced in Eqs. 4.32 and 4.33, the explicit expressions for the chemical potentials are:

$$\mu^{\mathrm{sm}} = kT\ln\left(\frac{n^{\mathrm{sm}}}{n^{\mathrm{sm}} + n^{\mathrm{wm}}}\right) + P^{\mathrm{m}}v^{\mathrm{s}} \tag{4.40}$$

$$\mu^{\mathrm{wm}} = kT\ln\left(\frac{n^{\mathrm{wm}}}{n^{\mathrm{sm}} + n^{\mathrm{wm}}}\right) + P^{\mathrm{m}}v^{\mathrm{w}}\ , \tag{4.41}$$

and

$$\mu = kT\left\{n^{\mathrm{s}}\ln\left(\frac{n^{\mathrm{s}}}{n^{\mathrm{w}}+n^{\mathrm{s}}}\right)+n^{\mathrm{w}}\ln\left(\frac{n^{\mathrm{w}}}{n^{\mathrm{w}}+n^{\mathrm{s}}}\right)\right\}+\frac{K}{2}\boldsymbol{\xi}^2+f_0^{\mathrm{c}}(v^{\mathrm{c}})+P^{\mathrm{c}}(\mathbf{n}\cdot\boldsymbol{\nu}-v^{\mathrm{c}})+P^{\mathrm{m}}v^{\mathrm{c}}$$
$$+kT\left(\tilde{Z}+\frac{v^{\mathrm{c}}}{\langle v^{\mathrm{c}}\rangle}\phi\tilde{Z}'(\phi)\right)-K^{\mathrm{c}}\partial_\alpha^2 n \tag{4.42}$$

$$\mu^{\mathrm{tot}} = \mu + kT\ln\frac{c}{n}. \tag{4.43}$$

At equilibrium, the free energy is constrained by the condition of conservation of the number of molecules

$$\int_{\mathcal{V}} dV\left(\delta\mathbf{n}^{\mathrm{m}}+\int d\mathbf{X}\mathbf{n}\delta c\right)=0, \tag{4.44}$$

and the constraint of a fixed total number of cells $\int_{\mathcal{V}} dVn = N^{\mathrm{Tot}}$. Minimising the constrained free energy with respect to both c and $\mathbf{n}^{\mathrm{m}}$, and eliminating one Lagrange multiplier between the two results in the balance condition:

$$\mu^{\mathrm{tot}} = \boldsymbol{\mu}^{\mathrm{m}}\cdot\mathbf{n}+\lambda, \tag{4.45}$$

with λ the other Lagrange multiplier. Substituting Eqs. 4.40 and 4.41 for the chemical potentials in the medium, and Eq. 4.43 for the cell chemical potential, into Eq. 4.45 gives rise to the equilibrium distribution:

$$c = n\frac{\exp\left[-\frac{\mu-\boldsymbol{\mu}^{\mathrm{m}}\cdot\mathbf{n}}{kT}\right]}{\int d\mathbf{X}\exp\left[-\frac{\mu-\boldsymbol{\mu}^{\mathrm{m}}\cdot\mathbf{n}}{kT}\right]}, \tag{4.46}$$

where the Lagrange multiplier is absorbed into the normalisation condition in the denominator of Eq. 4.46.

It is informative to consider the limit where this distribution is narrowly peaked. In the limit $T\to 0$, the equilibrium value of $\mathbf{X}$ is found by minimizing $\mu-\boldsymbol{\mu}^{\mathrm{m}}\cdot\mathbf{n}$ with respect to v^{c}, $\mathbf{n}$, and $\boldsymbol{\xi}$:

$$\begin{aligned}\partial_v\mu &= 0\\ \partial_{\mathbf{n}}\mu &= \boldsymbol{\mu}^{\mathrm{m}}\\ \partial_{\boldsymbol{\xi}}\mu &= 0.\end{aligned} \tag{4.47}$$

As the contribution to the free energy from intra-cellular solute gradients is $\frac{K}{2}\boldsymbol{\xi}^2$, the third equation states that the intracellular gradient of solutes vanishes at equilibrium. Using the explicit expressions for the chemical potentials 4.40-4.43, the first two equilibrium conditions above can be written

$$P^{\mathrm{m}}-P^{\mathrm{c}} = -f_0^{\mathrm{c}\prime}(v^{\mathrm{c}})-kTn\tilde{Z}'(\phi) \tag{4.48}$$

$$P^{\mathrm{m}}-P^{\mathrm{c}} = \frac{kT}{v^{\mathrm{s}}}\left[\ln\left(\frac{n^{\mathrm{s}}}{n^{\mathrm{s}}+n^{\mathrm{w}}}\right)-\ln\left(\frac{n^{\mathrm{sm}}}{n^{\mathrm{sm}}+n^{\mathrm{wm}}}\right)\right] \tag{4.49}$$

$$P^{\mathrm{m}}-P^{\mathrm{c}} = \frac{kT}{v^{\mathrm{w}}}\left[\ln\left(\frac{n^{\mathrm{w}}}{n^{\mathrm{s}}+n^{\mathrm{w}}}\right)-\ln\left(\frac{n^{\mathrm{wm}}}{n^{\mathrm{sm}}+n^{\mathrm{wm}}}\right)\right]. \tag{4.50}$$

Eq. 4.48 corresponds to a mechanical balance equation. Modelling the cell as a sphere with surface tension γ, $f_0^c(v^{\mathrm{c}}) = \gamma(36\pi v^{\mathrm{c}2})^{\frac{1}{3}}$ and $f_0^{c\prime}(v^{\mathrm{c}}) = \gamma(4\pi/(3v^{\mathrm{c}}))^{\frac{1}{3}} = 2\gamma/r$ with r the cell radius. Therefore, this term corresponds to the Law of Laplace applied to a spherical surface

under tension, $P^{\mathrm{c}} - P^{\mathrm{m}} = 2\gamma H$, for mean curvature H. With a typical cell surface tension $\gamma \sim 10^2\,\mathrm{pN\,\mu m^{-1}}$ [60], and cell radius 10μm, the corresponding difference of pressure is ~ 20Pa. The second term corresponds to the effect of cell-cell interactions on the cell volume. In the dilute cell limit $\phi \to 0$, $\tilde{Z} \to \ln(\phi)$, and $\phi\tilde{Z}'(\phi) \to 1$ and the corresponding pressure correction is $kT/\langle v^{\mathrm{c}}\rangle$, of order $\sim 10^{-6}$Pa, and therefore generally negligible compared to other terms in the equation.

In the limit of dilute solutes in both the cell and the extracellular medium, $n^{\mathrm{sm}} \ll n^{\mathrm{wm}}$ and $n^{\mathrm{s}} \ll n^{\mathrm{w}}$, Eq. 4.50 further simplifies:

$$P^{\mathrm{m}} - P^{\mathrm{c}} \simeq kT\left(\frac{n^{\mathrm{sm}}}{1-\phi} - \frac{n^{\mathrm{s}}}{v^{\mathrm{c}}}\right). \tag{4.51}$$

This equation corresponds to the balance of hydrostatic and osmotic pressure across the cell interface, $P^{\mathrm{m}} - P^{\mathrm{c}} = \pi^{\mathrm{m}} - \pi^{\mathrm{c}}$, where

$$\pi^{\mathrm{m}} = kT\frac{n^{\mathrm{sm}}}{1-\phi}, \tag{4.52}$$

$$\pi^{\mathrm{c}} = \frac{kTn^{\mathrm{s}}}{v^{\mathrm{c}}}. \tag{4.53}$$

These expressions are in agreement with the van't Hoff law [202], as $\frac{n^{\mathrm{s}}}{v^{\mathrm{c}}}$ and $\frac{n^{\mathrm{sm}}}{1-\phi}$ are the local solute concentrations inside and outside of the cell.

Introducing polarity

In general, cells can polarise. Consequently we introduce the polarity field p_α, with free energy

$$F^{\mathrm{p}} = \int dV \left\{\frac{a}{2}p_\alpha^2 + \frac{b}{4}p_\alpha^4 + \frac{K^{\mathrm{p}}}{2}(\partial_\alpha p_\beta)^2\right\}, \tag{4.54}$$

where K^{p} is the Frank constant (here we approximate bend, twist and splay constants to be equal). The constants a and b determine the internal polarity dynamics of each cell. When $a, b > 0$, the ground state of an isolated cell is unpolarised. When $a < 0$, $b > 0$, the groundstate polarity vector has norm $|\mathbf{p}| = \sqrt{\frac{|a|}{b}}$, and the direction is unconstrained. b provides a non-linear penalty to polarising, hence limits the growth of polarised states. The molecular field, h_α, is defined

$$h_\alpha = -\frac{\delta F^{\mathrm{p}}}{\delta p_\alpha}. \tag{4.55}$$

The equilibrium stress

The equilibrium stress can be calculated from the Gibbs-Duhem relation. Perturbing the fluid with a uniform translation $\mathbf{x}' = \mathbf{x} + \delta\mathbf{x}$ results in a change of the free energy

$$\begin{aligned}\delta F = &\int_{\mathcal{V}} dV\left[\big[-\mu^{\mathrm{sm}}\partial_\alpha n^{\mathrm{sm}} - \mu^{\mathrm{wm}}\partial_\alpha n^{\mathrm{wm}} - \Delta\mu\partial_\alpha n^{\mathrm{F}} - \int d\mathbf{X}\mu^{\mathrm{tot}}\partial_\alpha c\big]\delta x_\alpha + h_\alpha(\partial_\beta p_\alpha)\delta x_\beta\right]\\ &+ \int_{\mathcal{S}} dS_\alpha\left[f^{\mathrm{tot}}\delta x_\alpha - \frac{\partial f}{\partial(\partial_\alpha p_\gamma)}(\partial_\beta p_\gamma)\delta x_\beta\right]\end{aligned} \tag{4.56}$$

The volume integral corresponds to the variation of F in $\mathcal{V}$, whereas the surface integral is due to the free energy density swept out by the volume when it is translated. Integrating by parts,

$$\delta F = \int_{\mathcal{V}} dV \Big[\big[(\partial_\alpha \mu^{\mathrm{sm}}) n^{\mathrm{sm}} + (\partial_\alpha \mu^{\mathrm{wm}}) n^{\mathrm{wm}} + (\partial_\alpha \Delta\mu) n^{\mathrm{F}} + \int d\mathbf{X} (\partial_\alpha \mu^{\mathrm{tot}}) c \big] \delta x_\alpha + h_\alpha (\partial_\beta p_\alpha) \delta x_\beta \Big] + \int_{\mathcal{S}} dS_\alpha \Big[\big(f^{\mathrm{tot}} - \mu^{\mathrm{sm}} n^{\mathrm{sm}} - \mu^{\mathrm{wm}} n^{\mathrm{wm}} - \Delta\mu n^{\mathrm{F}} - \int d\mathbf{X} \mu^{\mathrm{tot}} c \big) \delta_{\alpha\beta} - \frac{\partial f}{\partial(\partial_\alpha p_\gamma)} (\partial_\beta p_\gamma) \Big] \delta x_\beta \tag{4.57}$$

The work done on a fluid with equilibrium stress tensor $\sigma^{\mathrm{e}}_{\alpha\beta}$ undergoing a deformation described by sheer tensor $\partial_\alpha \delta x_\beta$ is [103] [32]

$$\begin{aligned} \delta F &= \int dV \sigma^{\mathrm{e}}_{\alpha\beta} \partial_\alpha \delta x_\beta \\ &= \int dS_\alpha \sigma^{\mathrm{e}}_{\alpha\beta} \delta x_\beta - \int dV \delta x_\beta \partial_\alpha \sigma^{\mathrm{e}}_{\alpha\beta}. \end{aligned} \tag{4.58}$$

By comparing Eq. 4.57 and Eq. 4.58, we can identify the equilibrium stress tensor

$$\sigma^{\mathrm{e}}_{\alpha\beta} = \left(f^{\mathrm{tot}} - \mu^{\mathrm{sm}} n^{\mathrm{sm}} - \mu^{\mathrm{wm}} n^{\mathrm{wm}} - \Delta\mu n^{\mathrm{F}} - \int d\mathbf{X} \mu^{\mathrm{tot}} c \right) \delta_{\alpha\beta} - \frac{\partial f}{\partial(\partial_\alpha p_\gamma)} (\partial_\beta p_\gamma) \tag{4.59}$$

$$= -P^{\mathrm{e}} \delta_{\alpha\beta} - \frac{\partial f}{\partial(\partial_\alpha p_\gamma)} (\partial_\beta p_\gamma), \tag{4.60}$$

where P^{e} is the equilibrium fluid pressure. The final term in Eq. 4.59 is a standard result from liquid crystal physics [45]. Evaluating Eq. 4.59 results in the equilibrium pressure:

$$P^{\mathrm{e}} = P^{\mathrm{m}} + kTnZ(\phi) - K^{\mathrm{c}} \left(\frac{(\partial_\alpha n)^2}{2} + n \partial_\alpha^2 n \right) - K^{\mathrm{p}} (\partial_\alpha p_\gamma)(\partial_\beta p_\gamma - \frac{1}{3} (\partial_\delta p_\gamma)^2) \ . \tag{4.61}$$

The first two terms correspond to the sum of the pressure in the medium P^{m}, and to an excess pressure that arises from cellular interactions. The function $Z(\phi) = \phi \tilde{Z}'(\phi)$ can be seen as the equation of state of the cellular aggregate. For translationally invariant systems, there can be no change in free energy due to the translation δx_α, hence $\delta F = 0$. This allows us to identify the Gibbs-Duhem relation from Eq. 4.57 as

$$-\partial_\beta \sigma^e_{\alpha\beta} = (\partial_\alpha \mu^{\mathrm{sm}}) n^{\mathrm{sm}} + (\partial_\alpha \mu^{\mathrm{wm}}) n^{\mathrm{wm}} + h_\beta \partial_\alpha p_\beta + (\partial_\alpha \Delta\mu) n^{\mathrm{F}} + \int d\mathbf{X} (\partial_\alpha \mu^{\mathrm{tot}}) c. \tag{4.62}$$

Spinodal phase separation

We discuss here whether the formation of a cavity in a tissue can be modelled as a phase separation event, similar to spinodal decomposition in binary fluid mixtures [27], where an initially uniform system transitions to cell dense (tissue) and cell poor (cavity) phases. To describe such a process, we consider apolar cells, that maintain a constant volume, v^{c}. Furthermore, the total number of cells, and the total number of extracellular solutes, is conserved. We then consider the stability of a homogeneous system with respect to perturbations in the cell and solute profiles. In this scenario, the free energy is

$$F = \int dV f^{\mathrm{m}} + \lambda^{\mathrm{sm}} \left(\int dV (1 - \phi) \bar{\phi}^{\mathrm{sm}} - v^{\mathrm{s}} N^{\mathrm{sm}} \right), \tag{4.63}$$

where $\bar{\phi}^{\mathrm{sm}} = \frac{n^{\mathrm{sm}} v^{\mathrm{s}}}{1-\phi}$ is the volume fraction of solutes in the extra cellular medium, N^{sm} is the total number of solutes in the extra cellular medium, and λ^{sm} is a Lagrange multiplier enforcing solute conservation. The medium free energy density, f^{m} (Eq. 4.33) can be written:

$$f^{\mathrm{m}} = -\frac{kT}{v^{\mathrm{s}}}(1-\phi)\left[\bar{\phi}^{\mathrm{sm}} \ln\left(1 + \frac{v^{\mathrm{s}}}{v^{\mathrm{w}}}\frac{1-\bar{\phi}^{\mathrm{sm}}}{\bar{\phi}^{\mathrm{sm}}}\right) + \frac{v^{\mathrm{s}}}{v^{\mathrm{w}}}(1-\bar{\phi}^{\mathrm{sm}}) \ln\left(1 + \frac{v^{\mathrm{w}}}{v^{\mathrm{s}}}\frac{\bar{\phi}^{\mathrm{sm}}}{1-\bar{\phi}^{\mathrm{sm}}}\right)\right] + \frac{kT}{v^{\mathrm{c}}}\phi\tilde{Z}(\phi) + \frac{K^{\mathrm{c}}}{2v^{\mathrm{c}2}}(\partial_\alpha \phi)^2. \tag{4.64}$$

Evaluating the equilibrium condition $\frac{\delta F}{\delta \bar{\phi}^{\mathrm{sm}}} = 0$ with the above free energy results in a $\bar{\phi}^{\mathrm{sm}}$ that is spatially uniform: solutes are homogeneously distributed in the extracellular medium. This is not unexpected as the solute contribution to f^{m} is entirely entropic, hence favours a maximally mixed state. Consequently, when considering the stability of the mixture, we can set $\bar{\phi}^{\mathrm{sm}}$ to a constant. Since the extracellular volume, $\int dV(1-\phi)$, is also fixed, the first term in Eq. 4.64 is also a constant. The free energy in Eq. 4.64 then reduces, up to a constant, to the last two terms in Eq. 4.64. Example free energy surfaces of the kind described by Eq. 4.64, are shown in Fig. 4.2. Enforcing a constant $\bar{\phi}^{\mathrm{sm}}$ is equivalent to considering the free energy along a line $\phi^{\mathrm{c}} = 1 - \frac{\phi^{\mathrm{sm}}}{\phi_0^{\mathrm{sm}}}$, for some constant $\bar{\phi}_0^{\mathrm{sm}}$. An example of the free energy along such a line is shown in Fig. 4.3. An instability of the homogeneous state arises when $\frac{\partial^2 f^{\mathrm{m}}}{\partial \phi^2} < 0$, i.e. there exists some concave region of the free energy curve. This condition corresponds to

$$Z(\phi) + \phi Z'(\phi) < 0\ , \tag{4.65}$$

with $Z(\phi) = \phi\tilde{Z}'(\phi)$.

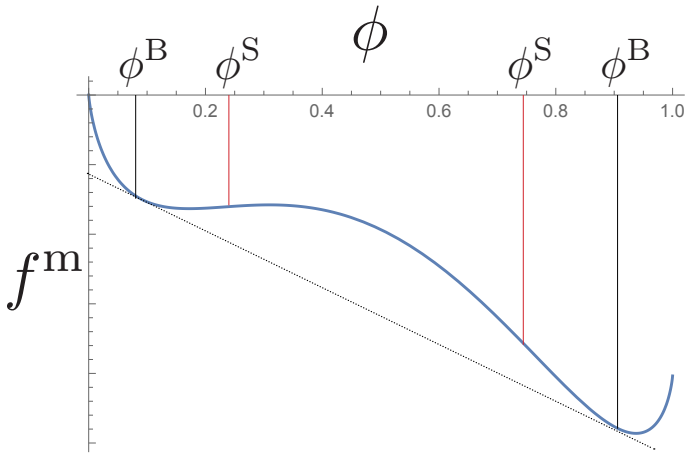

Figure 4.3
The free energy curve along a line $\bar{\phi}^{\mathrm{sm}} = \mathrm{const}$. The binodals, ϕ^{B}, lie on a common tangent. The spinodals, ϕ^{S}, are at the inflection points of the curve. This plot was made with $v^{\mathrm{s}} = v^{\mathrm{w}}$ and unrealistic numerical values of the parameters for improved visualisation.

Substituting the explicit expression for $\tilde{Z}$ in Eq. 4.35, the instability condition becomes

$$\epsilon > \epsilon^* = \frac{kT}{\phi(1-\phi)}. \tag{4.66}$$

How does this critical adhesion strength compare to biologically realistic adhesions? To estimate ϵ, we rely on previous studies of binding affinities and energy of homo and heterotypic

cadherin junctions [33, 91]. These studies estimate the number of cadherin dimers across a cell-cell junction at ~ 100, and the binding energy of a single cadherin bond $\sim 4 \times 10^{-20}$ J. Hence we obtain $\epsilon \sim 4 \times 10^{-18}$ J. The adhesion energy above which spinodal phase separation will occur is $\epsilon^* \approx 10^{-20}$J for $\phi = \frac{1}{2}$. We conclude that cadherin mediated adhesion is in principle large enough to overcome the entropic mixing of cells.

The phase separation of the system into cell rich and cell dense phases proceeds in a similar manner to standard binary fluid spinodal decomposition [32]. Below the critical adhesion energy, the curve is entirely convex, and hence stable. Above the critical adhesion energy, the curve develops two minima, a region becomes convex, and hence unstable. The binodals, ϕ^{B}, are the values of ϕ for the two separated phases that minimise the overall energy of the system, while satisfying the conservation of solutes and cells. They lie on a common tangent, as shown in Fig. 4.3. The spinodals are the inflection points of the curve, satisfying

$$\frac{\partial^2 f^{\mathrm{m}}}{\partial \phi^2} = 0. \tag{4.67}$$

Above the critical adhesion energy, the system can exhibit three different behaviours, depending on the initial proportions of cells and extra cellular fluid. For ϕ outside of the binodals, the system is stable, and will remain in a mixed state. Between the binodals and spinodals, the system is metastable and phase separation will progress via nucleation. Within the spinodals, it is energetically favourable for the fluid to locally separate into cell over-dense and cell under-dense regions, hence the system is unstable and undergoes spinodal phase separation. Although this analysis demonstrates that the system will phase separate for $\epsilon > \epsilon^*$, it does not address the timescale on which phase separation will occur. The speed of phase separation will be dealt with below when dynamic equations for the system are introduced.

4.1.3 Non-equilibrium phenomena

Entropy production and the Onsager theory of non-equilibrium thermodynamics

The previous analysis treated the system as a passive ensemble of solutes, water and vesicles in equilibrium. However, many biological processes occur out of equilibrium, driven by the hydrolysis of ATP. In order to describe these processes, we follow the formalism of non-equilibrium thermodynamics first proposed by Onsager [143], and widely used in the study of irreversible processes [46] [117] [83] and active matter [88] [113]. We start by deriving the rate of free energy production.

4.1.4 Free energy production

The free energy differential is

$$df^{\mathrm{tot}} = -\mu^{\mathrm{sm}} dn^{\mathrm{sm}} - \mu^{\mathrm{wm}} dn^{\mathrm{wm}} - \Delta\mu dn^{\mathrm{F}} - \int d\mathbf{X} \mu^{\mathrm{tot}} \delta c + h_\alpha dp_\alpha. \tag{4.68}$$

Including the rate of change of kinetic energy, the rate of change of the free energy reads

$$\frac{dF}{dt} = \int_{\mathcal{V}} dV \left[\frac{d}{dt}\left(\frac{1}{2}\rho u^2\right) + \mu^{\mathrm{sm}} \partial_t n^{\mathrm{sm}} + \mu^{\mathrm{wm}} \partial_t n^{\mathrm{wm}} + \Delta\mu \partial_t n^{\mathrm{F}} + \left(\int d\mathbf{X} \mu^{\mathrm{tot}} \partial_t c \right) - h_\alpha \partial_t p_\alpha \right]. \tag{4.69}$$

Using mass conservation (Eq. 4.12), force balance (Eq. 4.25), and performing an integration by parts, we find

$$\frac{dF}{dt} = \int_{\mathcal{V}} dV \Big\{ -(\tilde{\sigma}_{\alpha\beta} - \tilde{\sigma}^e_{\alpha\beta})\tilde{u}_{\alpha\beta} + (P - P^e)v_{\gamma\gamma} - h_\alpha \frac{Dp_\alpha}{Dt} + (\partial_\alpha \mu^{\rm sm}) j^{\rm sm}_\alpha + (\partial_\alpha \mu^{\rm wm}) j^{\rm wm}_\alpha - r\Delta\mu \\ + \int d\mathbf{X} c[(\partial_{n^{\rm s}}\mu - \mu^{\rm sm})\, J^{\rm s} + (\partial_{n^{\rm w}}\mu - \mu^{\rm wm})\, J^{\rm w} + (\partial_v \mu) J^v + (\partial_{\boldsymbol{\xi}}\mu)\cdot \mathbf{J}^\xi + (\partial_\alpha \mu^{\rm tot}) v_\alpha] \Big\} \tag{4.70}$$

where $\sigma_{\alpha\beta} = \sigma^{\rm tot}_{\alpha\beta} + \rho v_\alpha v_\beta$, and we have used the Gibbs-Duhem relation (Eq. 4.62). Furthermore, we have introduced the corotational time derivative

$$\frac{Dp_\alpha}{Dt} = \partial_t p_\alpha + u_\beta \partial_\beta p_\alpha + \omega_{\alpha\beta} p_\beta \ , \tag{4.71}$$

with $\omega_{\alpha\beta} = \frac{1}{2}(\partial_\alpha u_\beta - \partial_\beta u_\alpha)$ the antisymmetric part of the gradient of flow. In addition, $r = -\partial_t n^{\rm F}$ is the rate of consumption of the fuel molecule, and $\Delta\mu$ is the change in chemical potential between the fuel molecule and its products, which we have taken here to be uniform for simplicity. In the result above we do not write explicitly a surface term that would appear for the entropy production of a closed volume. The difference of non-equilibrium pressure $P = -\frac{1}{3}\sigma_{\gamma\gamma}$, and equilibrium pressure $P^e = -\frac{1}{3}\sigma^e_{\gamma\gamma}$, is coupled to the divergence of the flow $u_{\gamma\gamma} = \partial_\gamma u_\gamma$. The traceless symmetric part of the stress tensor $\tilde{\sigma}_{\alpha\beta} = \frac{1}{2}(\sigma_{\alpha\beta} + \sigma_{\beta\alpha}) - \frac{1}{3}\sigma_{\gamma\gamma}\delta_{\alpha\beta}$, relative to its equilibrium counterpart, is coupled to the traceless symmetric part of the gradient of flow, $\tilde{u}_{\alpha\beta} = \frac{1}{2}(\partial_\alpha u_\beta + \partial_\beta u_\alpha) - \frac{1}{3}u_{\gamma\gamma}\delta_{\alpha\beta}$. To arrive at the result above, we also have used that angular momentum conservation implies here [88]:

$$\sigma^a_{\alpha\beta} - \sigma^{e,a}_{\alpha\beta} = \frac{1}{2}(p_\alpha h_\beta - p_\beta h_\alpha) \tag{4.72}$$

where $\mathbf{A}^a$ denotes the antisymmetric part of the tensor $\mathbf{A}$.

The relative fluxes j_α, $j^{\rm sm}_\alpha$, $j^{\rm wm}_\alpha$ are not independent (Eq. 4.20). We use this constraint to eliminate the relative flux of water in the medium $j^{\rm wm}_\alpha$. Using the incompressibility conditions Eqs. 4.23 and 4.24 to eliminate the flow divergence $u_{\gamma\gamma}$ and the flux of water across cell membranes $J^{\rm w}$, we further obtain

$$\frac{dF}{dt} = \int_{\mathcal{V}} dV \Big\{ -(\tilde{\sigma}_{\alpha\beta} - \tilde{\sigma}^e_{\alpha\beta})\tilde{u}_{\alpha\beta} - h_\alpha \frac{Dp_\alpha}{Dt} - r\Delta\mu + \left(\partial_\alpha \left(\tilde{\mu}^{\rm sm} - \left(v^s - \frac{m^s v^w}{m^w}\right)(P - P^e)\right)\right) j^{\rm sm}_\alpha \\ + \int d\mathbf{X} c \Bigg[\left(\partial_{n^{\rm s}}\tilde{\mu} - \tilde{\mu}^{\rm sm} - \frac{v^{\rm s}}{v^{\rm w}}\partial_{n^{\rm w}}\tilde{\mu}\right) J^{\rm s} + \left(\partial_v \mu + \frac{\partial_{n^{\rm w}}\tilde{\mu}}{v^{\rm w}}\right) J^{\rm v} + (\partial_{\boldsymbol{\xi}}\mu)\cdot \mathbf{J}^\xi \\ + \left(\partial_\alpha \left(\tilde{\mu} - \left(v^{\rm s} - \frac{m^{\rm s} v^{\rm w}}{m^{\rm w}}\right)(P - P^e) n^{\rm s}\right)\right) v_\alpha \Bigg] \Big\}, \tag{4.73}$$

where again we do not write surface terms after performing an integration by parts. Finally, this expression can be written in a compact form as

$$\frac{dF}{dt} = \int_{\mathcal{V}} dV \Big\{ -(\tilde{\sigma}_{\alpha\beta} - \tilde{\sigma}^e_{\alpha\beta})\tilde{u}_{\alpha\beta} - h_\alpha \frac{Dp_\alpha}{Dt} + (\partial_\alpha \bar{\mu}^{\rm sm})\, j^{\rm sm}_\alpha - r\Delta\mu \\ + \int d\mathbf{X} c \Big[-\Delta\mu^{\rm s} J^{\rm s} - \Delta\Pi J^{\rm v} - \chi_\alpha J^\xi_\alpha + (\partial_\alpha \bar{\mu})\, v_\alpha \Big] \Big\}, \tag{4.74}$$

where we have defined $\boldsymbol{\chi} = -\partial_{\boldsymbol{\xi}}\mu$. We have also introduced the effective chemical potentials

$$\bar{\mu}^{\rm sm} = \mu^{\rm sm} - \frac{m^{\rm s}}{m^{\rm w}}\mu^{\rm wm} - \left(v^s - \frac{m^s v^w}{m^w}\right)(P - P^e), \tag{4.75}$$

$$\bar{\mu} = \mu + kT \ln\frac{c}{n} - \frac{m^{\rm s} n^{\rm s} + m^{\rm w} n^{\rm w}}{m^{\rm w}}\mu^{\rm wm} - \left(v^s - \frac{m^s v^w}{m^w}\right)(P - P^e) n^{\rm s}, \tag{4.76}$$

and the effective chemical potential difference and pressure

$$\Delta\mu^{\rm s} = \partial_{n^{\rm s}}\mu - \mu^{\rm sm} - \frac{v^{\rm s}}{v^{\rm w}}(\partial_{n^{\rm w}}\mu - \mu^{\rm wm}), \tag{4.77}$$

$$\Delta\Pi = \partial_v\mu + \frac{\partial_{n^{\rm w}}\mu - \mu^{\rm wm}}{v^{\rm w}} \ . \tag{4.78}$$

In the limit of dilute solutes in the cells and in the extracellular medium, the effective chemical potential and effective pressure difference have the form:

$$\Delta\mu^{\rm s} \simeq kT \ln\left(\frac{v^{\rm c} n^{\rm sm}}{n^{\rm s}(1-\phi)}\right), \tag{4.79}$$

$$\begin{aligned}\Delta\Pi &\simeq kT\left(\frac{n^{\rm s}}{v^{\rm c}} - \frac{n^{\rm sm}}{1-\phi}\right) - kTn\tilde{Z}'(\phi) - f_0^{\rm c\prime}(v^{\rm c}) \\ &= \Delta P - \Delta\pi \ .\end{aligned} \tag{4.80}$$

where ΔP is the equilibrium difference of pressure between the medium and fluid inside the cells, as defined in Eq. 4.48; and $\Delta\pi = \pi^{\rm m} - \pi^{\rm c}$ with $\pi^{\rm m}$ amd $\pi^{\rm c}$ the osmotic pressure in the extracellular medium and in the cell, as defined in Eq. 4.53-4.52. It is convenient to introduce the local concentration of solutes in the cell, $\bar{n}^{\rm s} = n^{\rm s}/v^{\rm c}$, and in the medium $\bar{n}^{\rm sm} = n^{\rm sm}/(1-\phi)$. In Eq. 4.80, we have identified $\pi^{\rm c} = kT\bar{n}^{\rm s}$ and $\pi^{\rm m} = kT\bar{n}^{\rm sm}$ as the osmotic pressures in the cell and in the medium, as given by the van't Hoff law.

The first four terms in Eq. 4.74 are standard pairs of fluxes and forces which appear in hydrodynamic theories of active polar fluids [88]. They describe, respectively, dissipation associated to the fluid deformation, changes in the polar order, flux of solutes and consumption of the fuel molecule. The last term, which integrates over the distribution of cell states $\mathbf{X}$, describes dissipation associated to changes in the number of solutes, cell volumes, and internal solute gradients within the fluid, and to the flow of cells across fluid elements.

4.1.5 Constitutive equations

From the expression for the rate of change of the free energy, we identify the generalised thermodynamic flux/force pairs:

Flux	Force
$\tilde{\sigma}_{\alpha\beta} - \tilde{\sigma}^e_{\alpha\beta}$	$\tilde{u}_{\alpha\beta}$
$\frac{Dp_\alpha}{Dt}$	h_α
$j^{\rm sm}_\alpha$	- $\partial_\alpha\bar{\mu}^{\rm sm}$
r	$\Delta\mu$
v_α	-$\partial_\alpha\bar{\mu}$
$J^{\rm s}$	$\Delta\mu^{\rm s}$
J^v	$\Delta\Pi$
J^ξ_α	χ_α

Writing the fluxes as a power series expansion of the forces to linear order, we obtain the following set of constitutive equations:

$$\tilde{\sigma}_{\alpha\beta} - \tilde{\sigma}^e_{\alpha\beta} = 2\eta\tilde{u}_{\alpha\beta} + \nu_1\widetilde{[p_\alpha h_\beta]} + q_{\alpha\beta}\zeta\Delta\mu - \nu^{\rm sm}\widetilde{[p_\alpha\partial_\beta\bar{\mu}^{\rm sm}]} + \int d\mathbf{X}\left[-\nu^{\rm c}(\mathbf{X})\widetilde{[p_\alpha\partial_\beta\bar{\mu}^{\rm c}]} + \nu^{\rm s}(\mathbf{X})q_{\alpha\beta}\Delta\mu^{\rm s} + \nu^{\rm v}(\mathbf{X})q_{\alpha\beta}\Delta\Pi + \nu^{\xi}(\mathbf{X})\widetilde{[p_\alpha\chi_\beta]}\right] \quad (4.81)$$

$$\frac{Dp_\alpha}{Dt} = \frac{1}{\gamma_1}h_\alpha - \nu_1 p_\beta\tilde{u}_{\alpha\beta} + \lambda p_\alpha\Delta\mu + \kappa^{\rm sm}\partial_\alpha\bar{\mu}^{\rm sm} + \int d\mathbf{X}[\kappa^{\rm c}(\mathbf{X})\partial_\alpha\bar{\mu}^{\rm c} + \kappa^{\rm s}(\mathbf{X})p_\alpha\Delta\mu^{\rm s} + \kappa^{\rm v}(\mathbf{X})p_\alpha\Delta\Pi + \kappa^{\xi}(\mathbf{X})\chi_\alpha] \quad (4.82)$$

$$j^{\rm sm}_\alpha = -\gamma^{\rm s}\partial_\alpha\bar{\mu}^{\rm sm} + \nu^{\rm sm}p_\beta\tilde{u}_{\alpha\beta} + p_\alpha\lambda^{\rm sa}\Delta\mu - \kappa^{\rm sm}h_\alpha + \int d\mathbf{X}[-\Lambda^{\rm sm,c}(\mathbf{X})\partial_\alpha\bar{\mu}^{\rm c} + \Lambda^{\rm sm,s}(\mathbf{X})p_\alpha\Delta\mu^{\rm s} + \Lambda^{\rm sm,v}(\mathbf{X})p_\alpha\Delta\Pi + \Lambda^{\rm sm,\xi}(\mathbf{X})\chi_\alpha] \quad (4.83)$$

$$v_\alpha = -\gamma(\mathbf{X})\partial_\alpha\bar{\mu}^{\rm c} - \nu^{\rm c}(\mathbf{X})p_\beta\tilde{u}_{\alpha\beta} + p_\alpha\lambda^{\rm ca}(\mathbf{X})\Delta\mu - \kappa^{\rm c}(\mathbf{X})h_\alpha - \Lambda^{\rm sm,c}(\mathbf{X})\partial_\alpha\bar{\mu}^{\rm sm} + \Lambda^{\rm c,s}(\mathbf{X})p_\alpha\Delta\mu^{\rm s} + \Lambda^{\rm c,v}(\mathbf{X})p_\alpha\Delta\Pi + \Lambda^{\rm c,\xi}(\mathbf{X})\chi_\alpha \quad (4.84)$$

$$J^{\rm s} = \Lambda^{\rm s}(\mathbf{X})\Delta\mu^{\rm s} - \nu^{\rm s}(\mathbf{X})q_{\alpha\beta}\tilde{u}_{\alpha\beta} + \Lambda^{\rm sa}(\mathbf{X})\Delta\mu + \kappa^{\rm s}(\mathbf{X})p_\alpha h_\alpha - \Lambda^{\rm c,s}(\mathbf{X})p_\alpha\partial_\alpha\bar{\mu}^{\rm c} - \Lambda^{\rm sm,s}(\mathbf{X})p_\alpha\partial_\alpha\bar{\mu}^{\rm sm} + \Lambda^{\rm s,v}(\mathbf{X})\Delta\Pi + \Lambda^{\rm s,\xi}(\mathbf{X})p_\alpha\chi_\alpha \quad (4.85)$$

$$J^{\rm v} = \Lambda^{\rm v}(\mathbf{X})\Delta\Pi - \nu^{\rm v}(\mathbf{X})q_{\alpha\beta}\tilde{u}_{\alpha\beta} + \Lambda^{\rm va}(\mathbf{X})\Delta\mu + \kappa^{\rm v}(\mathbf{X})p_\alpha h_\alpha - \Lambda^{\rm c,v}(\mathbf{X})p_\alpha\partial_\alpha\bar{\mu}^{\rm c} - \Lambda^{\rm sm,v}(\mathbf{X})p_\alpha\partial_\alpha\bar{\mu}^{\rm sm} + \Lambda^{\rm s,v}(\mathbf{X})\Delta\mu^{\rm s} + \Lambda^{\rm v,\xi}(\mathbf{X})p_\alpha\chi_\alpha \quad (4.86)$$

$$J^{\xi}_\alpha = \Lambda^{\xi}(\mathbf{X})\chi_\alpha - \nu^{\xi}(\mathbf{X})p_\beta\tilde{u}_{\alpha\beta} + \Lambda^{\xi a}(\mathbf{X})p_\alpha\Delta\mu + \kappa^{\xi}(\mathbf{X})h_\alpha - \Lambda^{\rm c,\xi}(\mathbf{X})\partial_\alpha\bar{\mu}^{\rm c} - \Lambda^{\rm sm,\xi}(\mathbf{X})\partial_\alpha\bar{\mu}^{\rm sm} + \Lambda^{\rm s,\xi}(\mathbf{X})p_\alpha\Delta\mu^{\rm s} + \Lambda^{\rm v,\xi}(\mathbf{X})p_\alpha\Delta\Pi \quad (4.87)$$

$$r = \Lambda\Delta\mu - \zeta q_{\alpha\beta}\tilde{u}_{\alpha\beta} + \lambda p_\alpha h_\alpha - \lambda^{\rm sa}p_\alpha\partial_\alpha\bar{\mu}^{\rm sm} + \int d\mathbf{X}\big[-\lambda^{\rm ca}(\mathbf{X})p_\alpha\partial_\alpha\bar{\mu}^{\rm c} + \Lambda^{\rm sa}(\mathbf{X})\Delta\mu^{\rm s} + \Lambda^{\rm va}(\mathbf{X})\Delta\Pi + \Lambda^{\xi a}(\mathbf{X})p_\alpha\chi_\alpha\big]. \quad (4.88)$$

Here we have introduce the nematic tensor $q_{\alpha\beta} = p_\alpha p_\beta - \frac{1}{3}p_\gamma p_\gamma\delta_{\alpha\beta}$. $\tilde{A}$ denotes the traceless, symmetric part of a tensor A. These constitutive equations are linear flux-force relationships that can be written $J_m = O_{mn}F_n$ for fluxes J_m and forces F_m. They can be split into dissipative and reactive parts, $J_m = O^{\rm d}_{mn}F_n + O^{\rm r}_{mn}F_n$. The dissipative couplings are between fluxes and forces with opposite time reversal symmetry, and obey $O^{\rm d}_{mn} = O^{\rm d}_{nm}$. These terms contribute to entropy production. The reactive couplings are between fluxes and forces with the same time reversal symmetry, and obey $O^{\rm r}_{mn} = -O^{\rm r}_{nm}$ [88]. All coupling constants are, in principle, functions of the variables n, $n^{\rm sm}$, $\langle n^{\rm s}\rangle$, $\langle v^{\rm c}\rangle$, and p_α, characterising the state around which the non-equilibrium theory is expanded. In addition, some coupling constants depend on the cell state $\mathbf{X}$; here this dependency has been made explicit. However, the Onsager theory places no constraints on how the coupling constants depend on the state variables.

In the above, all possible linear couplings between fluxes and forces have been written, resulting in equations which contain a large number of terms and coupling coefficients. Furthermore, the assumption of being near to equilibrium that enforces the Onsager symmetry relations is not necessarily appropriate for biological cells. Therefore, we propose constitutive equations which retain specific couplings, guided by the physical process of cell aggregation, and we make a number of simplifications: we consider flows occurring at low

Reynolds number. We restrict ourselves to a strongly peaked cell distribution $c(n^{\mathrm{s}}, n^{\mathrm{w}}, v^{\mathrm{c}}, \boldsymbol{\xi}) = n\delta(n^{\mathrm{s}} - \langle n^{\mathrm{s}}\rangle)\delta(v^{\mathrm{c}} - \langle v^{\mathrm{c}}\rangle)\delta(n^{\mathrm{w}} - \langle n^{\mathrm{w}}\rangle)\delta(\boldsymbol{\xi} - \langle\boldsymbol{\xi}\rangle)$, where $\langle n^{\mathrm{s}}\rangle$, $\langle n^{\mathrm{w}}\rangle$, $\langle v^{\mathrm{c}}\rangle$ and $\langle\boldsymbol{\xi}\rangle$ are the average number of internal solutes, water molecules, cell volume, and intracellular solute gradient, and n is the total cell number density, in a given volume element (we now drop the $\langle\cdot\rangle$ notation for convenience). Contributions from the entropic term $\sim c\ln c$ are also neglected. We further consider that the fuel chemical potential $\Delta\mu$ is uniform in space.

We write constitutive equations for the deviatoric stress tensor and polarity dynamics, analogous to the theory of active fluids [85]:

$$\tilde{\sigma}_{\alpha\beta} - \tilde{\sigma}^{e}_{\alpha\beta} = 2\eta\tilde{u}_{\alpha\beta} + 2\eta\tilde{v}_{\alpha\beta} + \zeta\Delta\mu q_{\alpha\beta} \tag{4.89}$$

$$\frac{Dp_\alpha}{Dt} = \frac{1}{\gamma_1}h_\alpha - \kappa\partial_\alpha n \tag{4.90}$$

where η is the fluid viscosity, $\zeta\Delta\mu q_{\alpha\beta}$ is the active anisotropic stress, $1/\gamma_1$ describes dissipation associated to polarity changes, and κ is a coupling between the gradient of cell density and polarity. Here we do not enforce the Onsager symmetry relations, as these equations describe cellular processes which we do not expect to be close to equilibrium. Equation 4.89 describes the contribution to the stress tensor from the passive shear viscosity, η, and from an active stress due to the polarity. We assume that viscous stresses arise mostly within cells, and therefore have introduced the tensor $v_{\alpha\beta} = \frac{1}{2}(\partial_\alpha v_\beta + \partial_\beta v_\alpha)$; such that $u_{\alpha\beta} + v_{\alpha\beta}$ is the gradient of flow in the cell phase. Eq. 4.90 describes the evolution of the polarity. The molecular field, h_α, acts to minimise the polarity free energy in Eq. 4.54. The coupling constant κ determines the response of the polarity to gradients in the cell density n, which will be particularly strong at tissue boundaries.

We next write three constitutive equations for the rate of change of the cell state variables:

$$J^{\mathrm{s}} = \Lambda^{\mathrm{s}}\Delta\mu^{\mathrm{s}} + \Lambda^{\mathrm{sa}}\Delta\mu \tag{4.91}$$

$$J^{\mathrm{v}} = v^{\mathrm{s}}J^{\mathrm{s}} + \Lambda^{\mathrm{w}}\Delta\Pi + \Lambda^{\mathrm{wa}}\Delta\mu \tag{4.92}$$

$$J^{\xi}_{\alpha} = \Lambda^{\xi}\chi_\alpha + \Lambda^{\mathrm{sm},\xi}\partial_\alpha\bar{\mu}^{\mathrm{sm}} \tag{4.93}$$

Eq. 4.91 describes the movement of solutes across the membrane by passive and active transport, with Λ^{s} the passive membrane permeability to solutes. $\Delta\mu^{\mathrm{s}} \simeq kT\ln\frac{\bar{n}^{\mathrm{sm}}}{\bar{n}^{\mathrm{s}}}$, where the approximation is in the limit of dilute solutes, is the driving thermodynamic force for the passive movement of solutes across the membrane due to any imbalance of chemical potentials inside and outside of the cell. A membrane permeability coefficient λ_m can be defined for a given species by relating the flux of molecules through the membrane J_m to the difference of concentration across the membrane Δc, $J_m = \lambda_m\Delta c$. What are the typical values of this quantity? The permeability of an artificial lipid bilayer is $\lambda_m = 10^{-10}\,\mu\mathrm{m\,s^{-1}}$ [214]. The permeability of real cell membranes is greatly increased by the presence of ion channels. Cahalan et al. state that single ion channels typically transport more than 10^6 molecules per second [26], and Ritchie et al. report sodium channel densities of $\approx 200\,\mu\mathrm{m^{-2}}$ [156]. For a cell of radius $10\,\mu\mathrm{m}$, this results in an order of magnitude estimate of $\lambda_m \approx 1\,\mu\mathrm{m\,s^{-1}}$. At the other end of the size spectrum, proteins are transported in and out of the cell by exocytotic vesicles. Sheetz et al. report the rate at which material is added to the cell membrane by vesicles is $1\,\mu\mathrm{m^2\,s^{-1}}$ [178]. Proteins in the cell can have a typical radius of 10 nm (e.g. ATP-ase [130]), vesicles have a typical radius of a few hundred nanometres [189], and vesicles typically contain between 1 and 10 proteins [133]. Consequently, approximately 10 proteins leave the cell by exocytosis per second, corresponding to $\lambda_m = 10^{-8}\,\mu\mathrm{m\,s^{-1}}$. Consequently, values for λ_m are in the range $10^{-8} - 1\,\mu\mathrm{m\,s^{-1}}$. For a spherical cell the coefficient Λ^{s} is related to the membrane

permeability coefficient (at small difference of concentration across the cell membrane) through $\Lambda^{\mathrm{s}} kT/\bar{n}^{\mathrm{s}} = 4\pi R^2 \lambda_m$; hence $\Lambda^{\mathrm{s}} kT/\bar{n}^{\mathrm{s}} \sim 10^{-5} - 10^{3} \mu\mathrm{m}^3/\mathrm{s}^{-1}$ with $R = 10\mu\mathrm{m}$. $\Lambda^{\mathrm{sa}}\Delta\mu$ is the flux describing active transport of solutes across the cell membrane.

Equation 4.92 describes changes in volume due to the flux of solutes and water across the membrane, where we have followed the incompressible decomposition of volume change 4.24. For $\Delta\mu = 0$, the flux of water is driven by the balance of hydrostatic pressure, ΔP, and osmotic pressure, $\Delta\pi$, with $\Delta\Pi = \Delta P - \Delta\pi$. The difference in pressure between the extracellular medium and the cell, ΔP, is the result of both passive surface tension and bulk effects. The coefficient Λ^{w} is related to the permeability to water of the cell membrane, L_p, for a spherical cell with radius R by $\Lambda^{\mathrm{w}} = 4\pi R^2 L_p$. With $L_p \sim 10^{-6}\,\mu\mathrm{m\,s^{-1}\,Pa^{-1}}$ [56], one obtains $\Lambda^{\mathrm{w}} \sim 10^{-3}\,\mu\mathrm{m^3\,s^{-1}Pa^{-1}}$. In the non-equilibrium case, the flux of water across the membrane gains an active contribution $\Lambda^{\mathrm{va}}\Delta\mu$, coming for instance, from the tension in the actomyosin cortex.

We then consider constitutive equations for the cell and solute velocities $\mathbf{v}$ and $\mathbf{v}^{\mathrm{sm}}$. We first split the total solute velocity into three parts, arising respectively from passive motion of solutes in the extracellular medium, passive motion of solutes through cells, and active pumping by cells:

$$v_\alpha^{\mathrm{sm}} = v_\alpha^{\mathrm{sm0}} - \frac{\phi\Lambda^{\mathrm{sm},\xi}}{n^{\mathrm{sm}}}\left(\partial_\alpha \bar{\mu}^{\mathrm{sm}} + \frac{kT}{K\bar{n}^{\mathrm{sm}} v^{\mathrm{c}\frac{2}{3}}}\chi_\alpha\right) + \lambda^{\mathrm{sa}}\Delta\mu n p_\alpha. \tag{4.94}$$

For a cell with an internal solute concentration gradient there will be more solutes passing through the membrane on one side of the cell than the other. This flux is described by the term in $\Lambda^{\mathrm{sm},\xi}$. The exact form of this term is chosen so as to reproduce the diffusion equation in $\bar{n}^{\mathrm{sm}}$ in the limit of infinitely permeable cells, as detailed in Section 4.2.3. We have taken the flux due to active pumping proportional to the density of cells performing active pumping, and to the amount of external solutes available for pumping. $\lambda^{\mathrm{sa}}\Delta\mu$ is a characteristic velocity of pumping per cell. We expect $\lambda^{\mathrm{sa}} n^{\mathrm{sm}}\Delta\mu \sim rJ$ with r a characteristic cell size and J a characteristic molecular secretion rate. A typical length scale is $r \sim 10\mu\mathrm{m}$, and there is a wide range of typical secretion rates, $J \sim 1{-}10^9$ molecules/s [73, 93]; hence $\lambda^{\mathrm{sa0}} n^{\mathrm{sm}}\Delta\mu \sim 10{-}1{\times}10^{11}\mu\mathrm{m/s}$.

In principle, a similar decomposition can be written for the cell flux and solute flux; although we assume here that the active contribution to these two fluxes can be neglected. Then to determine the cell flux, water flux, and the passive part of the solute flux we follow an approach similar to the Maxwell-Stefan constitutive equations for a multicomponent system. The Maxwell-Stefan framework is an alternative to the Onsager approach of writing all possible couplings between diffusion fluxes and gradients in chemical potentials, like so $j_\alpha^i = L_{ij}\partial_\alpha \mu^j$. The disadvantage of using the Onsager coefficients, L_{ij}, is that although they are functions of the variables of the system, we have no information about what those functional relationships look like. Maxwell-Stefan allows us to relate diffusion constants to friction forces between the fluid species.

We start by considering the balance of forces between the divergence of the stress in the three

fluid components, and the friction between them. Hence we write, at low Reynolds number:

$$n\partial_\alpha\mu + h_\beta\partial_\alpha p_\beta + \phi\partial_\alpha(P-P^e) - \partial_\beta\tilde{\sigma}_{\alpha\beta} = -n\bar{\phi}^{\rm sm}\xi^{\rm s}\left(v_\alpha - v_\alpha^{\rm sm0}\right) - n(1-\bar{\phi}^{\rm sm})\xi\left(v_\alpha - v_\alpha^{\rm wm}\right) \ , \tag{4.95}$$

$$n^{\rm sm}\partial_\alpha\mu^{\rm sm} + (1-\phi)\bar{\phi}^{\rm sm}\partial_\alpha(P-P^e) = -n\bar{\phi}^{\rm sm}\xi^{\rm s}\left(v_\alpha^{\rm sm0} - v_\alpha\right) - n^{\rm sm}(1-\bar{\phi}^{\rm sm})\xi^{\rm sw}\left(v_\alpha^{\rm sm0} - v_\alpha^{\rm wm}\right) \ , \tag{4.96}$$

$$n^{\rm wm}\partial_\alpha\mu^{\rm wm} + (1-\phi)(1-\bar{\phi}^{\rm sm})\partial_\alpha(P-P^e) = -n(1-\bar{\phi}^{\rm sm})\xi\left(v_\alpha^{\rm wm} - v_\alpha\right) - n^{\rm sm}(1-\bar{\phi}^{\rm sm})\xi^{\rm sw}\left(v_\alpha^{\rm wm} - v_\alpha^{\rm sm0}\right) \ , \tag{4.97}$$

where $\bar{\phi}^{\rm sm} = \frac{v^{\rm s}n^{\rm sm}}{v^{\rm s}n^{\rm sm}+v^{\rm w}n^{\rm wm}}$ is the volume fraction of solutes in the extracellular medium. Here we have introduced 3 friction coefficients between system components: ξ is the friction coefficient between cells and solvent (here water), $\xi^{\rm s}$ between cells and solutes, and $\xi^{\rm sm}$ between solutes and solvent. The left hand sides are driving force densities which can be written as $-\partial_\beta\sigma^{\rm c}_{\alpha\beta}$, $-\partial_\beta\sigma^{\rm sm}_{\alpha\beta}$, and $-\partial_\beta\sigma^{\rm wm}_{\alpha\beta}$; the gradients of stress in cells, solutes and water. The driving force density for cells $-\partial_\beta\sigma^{\rm c}_{\alpha\beta}$ is opposed by friction against cell motion relative to water (with friction coefficient per cell $(1-\bar{\phi}^{\rm sm})\xi$) and against cell motion relative to solutes (with friction coefficient per cell $\xi^{\rm s}\bar{\phi}^{\rm sm}$). Similarly, the driving force density for solutes $-\partial_\beta\sigma^{\rm s}_{\alpha\beta}$ is opposed by friction against the motion of solutes relative to the cells, and friction against the motion of solutes relative to water (with friction coefficient per solute molecule $(1-\bar{\phi}^{\rm sm})\xi^{\rm sm}$). The order of magnitude of friction coefficients is discussed in Section 4.2.2.

In the equations above we have assumed that the non-equilibrium force densities $h_\beta\partial_\alpha p_\beta$ and $\partial_\beta\tilde{\sigma}_{\alpha\beta}$ arise only within the cells, as motion in the extracellular environment is assumed to occur only through passive effects. Adding up Eqs. 4.95-4.97 leads to cancellation of the left-hand side due to the Gibbs-Duhem relation (Eq. 4.62) and force balance (Eq. 4.25) at low Reynolds number; and the friction terms on the right-hand side also cancel in this summation. As a result one of the 3 equations can be removed, and we choose here to eliminate the equation for the solvent flux Eq. 4.97. Using the condition for mass conservation of fluxes (Eq. 4.20) to eliminate the solvent velocity $\mathbf{v}^{\rm wm}$, Eqs. 4.95 and 4.96 allow us to determine the cell and solute velocities $\mathbf{v}$ and $\mathbf{v}^{\rm sm}$. This is done in Eqs. 4.108 and A.8.

An additional constitutive equation can be written for the fuel consumption rate r, which we do not discuss here. The total pressure P is fixed by the incompressibility condition 4.23.

In the following, we make additional simplifying assumptions. We take the limit where solutes are dilute both inside the cells and in the extracellular medium, $n^{\rm sm} \ll n^{\rm wm}$ and $n^{\rm s} \ll n^{\rm w}$. We also assume that the solutes and water have the same mass density, $v^{\rm s}/v^{\rm w} = m^{\rm s}/m^{\rm w}$. Consequently, the incompressibility condition reduces to the familiar expression $\partial_\alpha u_\alpha = 0$. With these simplifications the effective chemical potentials of solutes and cells defined in Eqs. 4.75 and 4.76 take the form:

$$\bar{\mu}^{\rm sm} \simeq kT\ln\frac{n^{\rm sm}v^{\rm w}}{1-\phi} \ , \tag{4.98}$$

$$\bar{\mu} \simeq kT\left(n^{\rm s}\ln\frac{v^{\rm w}n^{\rm s}}{v^{\rm c}} + \frac{v^{\rm c}n^{\rm sm}}{1-\phi} + \tilde{Z}(\phi) + \frac{v^{\rm c}}{\langle v^{\rm c}\rangle}\phi\tilde{Z}'(\phi)\right) + f_0^c(v^{\rm c}) + \frac{K}{2}\boldsymbol{\xi}^2 - K^{\rm c}\partial_\alpha^2 n \ . \tag{4.99}$$

and the gradients of cell and solute chemical potentials entering Eqs. 4.95 and 4.96 read:

$$\partial_\alpha\mu = v^{\rm c}\partial_\alpha P^{\rm m} + kT\phi\left(2\tilde{Z}'(\phi) + \phi\tilde{Z}''(\phi)\right)\frac{\partial_\alpha n}{n} + kT\phi\left(\tilde{Z}'(\phi) + \phi\tilde{Z}''(\phi)\right)\frac{\partial_\alpha v^{\rm c}}{v^{\rm c}} \ , \tag{4.100}$$

$$\partial_\alpha\mu^{\rm sm} = v^{\rm s}\partial_\alpha P^{\rm m} + \frac{kT(1-\phi)}{n^{\rm sm}}\partial_\alpha\frac{n^{\rm sm}}{1-\phi} \ . \tag{4.101}$$

To summarise, in the dilute limit, and assuming the mass densities of solutes and water are equal, the constitutive equations are

$$\tilde{\sigma}_{\alpha\beta} - \tilde{\sigma}^e_{\alpha\beta} = 2\eta\tilde{u}_{\alpha\beta} + 2\eta\tilde{v}_{\alpha\beta} + \zeta\Delta\mu q_{\alpha\beta} \tag{4.102}$$

$$\frac{Dp_\alpha}{Dt} = \frac{1}{\gamma_1}h_\alpha - \kappa\partial_\alpha n \tag{4.103}$$

$$J^{\rm s} = \Lambda^{\rm s}\Delta\mu^{\rm s} + \Lambda^{\rm sa}\Delta\mu \tag{4.104}$$

$$J^{\rm v} = v^{\rm s}J^{\rm s} + \Lambda^{\rm w}\Delta\Pi + \Lambda^{\rm wa}\Delta\mu \tag{4.105}$$

$$J^\xi_\alpha = \Lambda^\xi\chi_\alpha + \Lambda^{{\rm sm},\xi}\partial_\alpha\bar{\mu}^{\rm sm} \tag{4.106}$$

$$v^{\rm sm}_\alpha = v^{\rm sm0}_\alpha - \frac{\phi\Lambda^{{\rm sm},\xi}}{n^{\rm sm}}\left(\partial_\alpha\bar{\mu}^{\rm sm} + \frac{kT}{K\bar{n}^{\rm sm}v^{\rm c\,\frac{2}{3}}}\chi_\alpha\right) + \lambda^{\rm sa}\Delta\mu n p_\alpha \tag{4.107}$$

$$\begin{aligned} v^{{\rm sm},0}_\alpha =& \frac{v^{\rm c}(1-\phi)(\xi^{\rm sw}v^{\rm c} - \xi^{\rm s}v^{\rm s})}{\xi(\xi^{\rm s}\phi v^{\rm s} + v^{\rm c}\xi^{\rm sw}(1-\phi))}\left[n\partial_\alpha\mu + h_\beta\partial_\alpha p_\beta + \phi\partial_\alpha(P - P^e) - \partial_\beta\tilde{\sigma}_{\alpha\beta}\right] \\ & - \frac{1-\phi}{n^{\rm sm}\left[\xi^{\rm sw}(1-\phi) + \xi^{\rm s}\phi\frac{v^{\rm s}}{v^{\rm c}}\right]}\left[n^{\rm sm}\partial_\alpha\mu^{\rm sm} + (1-\phi)\bar{\phi}^{\rm sm}\partial_\alpha(P - P^e)\right] \end{aligned} \tag{4.108}$$

$$\begin{aligned} v_\alpha =& -\frac{(1-\phi)}{n\xi}\left[n\partial_\alpha\mu + h_\beta\partial_\alpha p_\beta + \phi\partial_\alpha(P - P^e) - \partial_\beta\tilde{\sigma}_{\alpha\beta}\right] \\ & + \frac{v^{\rm s}\phi(1-\phi)(\xi - \xi^{\rm s})}{\xi n\left[\xi^{\rm s}\phi v^{\rm s} + v^{\rm c}\xi^{\rm sw}(1-\phi)\right]}\left[n^{\rm sm}\partial_\alpha\mu^{\rm sm} + (1-\phi)\bar{\phi}^{\rm sm}\partial_\alpha(P - P^e)\right] \end{aligned} \tag{4.109}$$

4.2 Solving the hydrodynamic equations

We now use the constitutive equations above to solve the hydrodynamic equations in various scenarios.

4.2.1 The Young-Laplace Law for a spherical shell of cells

We first consider the scenario of a spherical shell of cells enclosing a fluid filled cavity. It is well known that there is a pressure imbalance between the inside and outside of a bubble or cavity in a fluid, due to the coupling of surface tension to curvature [44]. For a spherical cavity of radius R and surface tension γ, the Laplace pressure is

$$\Delta p = p_{\rm external} - p_{\rm internal} = -\frac{2\gamma}{R}. \tag{4.110}$$

This quantity plays an important role in the growth and persistence of a cavity. How does it arise in our theory? Consider a spherical shell of cells, of thickness $2d$, with radius R

$$\phi(r) = \begin{cases} 0 & \text{if } r < R - d \\ \phi_0 & \text{if } R - d < r < R + d \\ 0 & \text{if } r > R + d \end{cases} \tag{4.111}$$

and a spherically symmetric polarity field $\mathbf{p} = p\hat{\mathbf{r}}$. If there is no flow of cells, the stress tensor can be written

$$\sigma_{\alpha\beta} = \sigma^{\rm e}_{\alpha\beta} + \sigma^{\rm a}_{\alpha\beta} = \begin{pmatrix} -P^{\rm e} + \frac{2\zeta\Delta\mu p^2}{3} & 0 & 0 \\ 0 & -P^{\rm e} - \frac{\zeta\Delta\mu p^2}{3} & 0 \\ 0 & 0 & -P^{\rm e} - \frac{\zeta\Delta\mu p^2}{3} \end{pmatrix}, \tag{4.112}$$

where $\sigma^{\mathrm{e}}_{\alpha\beta} = -P^{\mathrm{e}}\delta_{\alpha\beta}$ is the passive, equilibrium stress calculated with the Gibbs-Duhem relation, and $\sigma^{\mathrm{a}}_{\alpha\beta}$ is the active part of the stress from Eq. 4.89. We set the norm of the polarity to 1, and the ϕ dependence of ζ to $\zeta(\phi) = -\phi\zeta^0$, for positive ζ^0. This form of ζ represents some active stress generating contractile tension in the shell of cells, e.g. by intercellular adhesions. The force balance equation, $\partial_\beta \sigma^{\mathrm{tot}}_{\alpha\beta} = 0$, in the $\hat{\mathbf{r}}$ direction is

$$\frac{d}{dr}\left(-P^{\mathrm{m}} - \frac{2}{3}\zeta^0\Delta\mu\phi\right) = \frac{2\zeta^0\Delta\mu\phi}{r}. \tag{4.113}$$

Integrating over the shell of cells results in

$$\Delta P = -\frac{4\zeta^0\Delta\mu d\phi_0}{R}, \tag{4.114}$$

where $\Delta P = P^{\mathrm{e}}(r > R+d) - P^{\mathrm{e}}(r < R-d) = P^{\mathrm{m}}(r > R+d) - P^{\mathrm{m}}(r < R-d)$. This is the familiar Young-Laplace Law, with active surface tension $2\zeta^0\Delta\mu d\phi_0$.

At steady state, the difference in pressure across the spherical shell is balanced by an imbalance of osmotic pressure, due to differences in solute concentration inside and outside of the shell. Although the solutes are being actively transported across the shell by the cells, the water flows by passive osmosis. Hence we can apply the equilibrium constraint on the chemical potential of water, $\partial_\alpha \mu^{\mathrm{wm}} = 0$. In spherical polar coordinates this reads

$$\frac{d}{dr}(kT\log(1-\bar{\phi}^{\mathrm{sm}}) + P^{\mathrm{m}}v^{\mathrm{w}}) = 0. \tag{4.115}$$

Integrating over the shell, we recover (in the dilute limit $\bar{\phi}^{\mathrm{sm}} << 1$) the balance of osmotic and hydrostatic pressure

$$kT\frac{\Delta\phi^{\mathrm{sm}}}{1-\phi^{\mathrm{c}}} = v^{\mathrm{s}}\Delta\Pi = v^{\mathrm{w}}\Delta P^{\mathrm{m}}, \tag{4.116}$$

as expected from the van't Hoff law [202].

4.2.2 Passive, apolar, impermeable cells

Here we assume that cells are passive and apolar, are impermeable to solutes and water ($\Lambda^{\mathrm{s}} = \Lambda^{\mathrm{w}} = \Lambda^{\mathrm{sm}\xi} = 0$) and have a fixed volume v^{c} (Fig. 4.4). We then take $\Delta\mu = 0$, such that the force balance equation 4.25, constitutive equation 4.89 and incompressibility condition give $\partial_\alpha u_\alpha = 0$ and $P = \partial_\alpha v_\alpha$.

Using the balance equations for the number of cells and extracellular solutes, Eqs. 4.3 and 4.4, together with the constitutive equations 4.95 and 4.96 and the expression for the equilibrium pressure 4.61, we obtain (details of this calculation are given in Appendix A.1):

$$\frac{dn}{dt} = -\partial_\alpha(nv_\alpha) \tag{4.117}$$

$$\frac{dn^{\mathrm{sm}}}{dt} = -\partial_\alpha j^{\mathrm{sm}}_\alpha \tag{4.118}$$

$$v_\alpha - \frac{1-\phi}{\phi}\frac{\eta v^{\mathrm{c}}}{\xi}\left(\frac{4}{3}-\phi\right)\partial^2_\beta v_\alpha = -D(1-\phi)^2 z(\phi)\frac{\partial_\alpha n}{n} - D^{\mathrm{s}}v^{\mathrm{s}}\left(\frac{\xi^{\mathrm{s}}}{\xi}-1\right)(1-\phi)\partial_\alpha\left(\frac{n^{\mathrm{sm}}}{1-\phi}\right) \tag{4.119}$$

$$j^{\mathrm{sm}}_\alpha = -D^{\mathrm{s}}(1-\phi)\partial_\alpha\left(\frac{n^{\mathrm{sm}}}{1-\phi}\right) + n^{\mathrm{sm}}D^{\mathrm{s}}\frac{\xi^{\mathrm{sw}}v^{\mathrm{c}} - \xi^{\mathrm{s}}v^{\mathrm{s}}}{\xi}\Bigg((1-\phi)z(\phi)\partial_\alpha n - \frac{\eta}{kT}\left(\phi - \frac{4}{3}\right)\partial^2_\beta v_\alpha\Bigg) \tag{4.120}$$

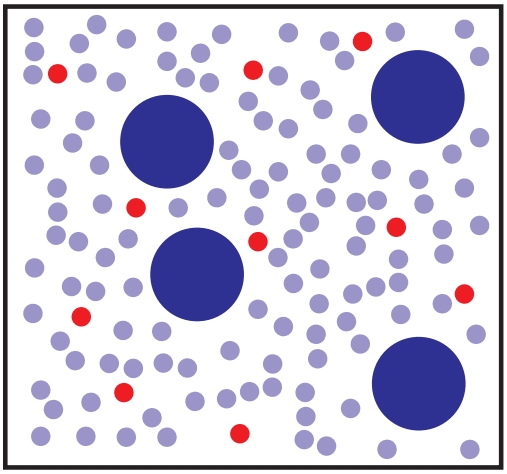

Figure 4.4
A schematic of passive, apolar, impermeable cells.

where we have introduced the single cell diffusion coefficient $D = kT/\xi$, the solute diffusion coefficient $D^{\mathrm{s}} = kT/\left(\xi^{\mathrm{sw}} + \frac{\phi\xi^{\mathrm{s}}v^{\mathrm{s}}}{(1-\phi)v^{\mathrm{c}}}\right)$, the non-dimensional modified compressibility factor $z(\phi) = Z(\phi) + \phi Z'(\phi)$ and we have set $K^{\mathrm{c}} = 0$ for this section. The function $z(\phi)$ satisfies $z(0) = 1$, corresponding to the limit of infinite cell dilution. Several points can be drawn from these equations.

First, a permeation length $\ell_p = \sqrt{\left(\frac{4}{3} - \phi\right)(1-\phi)\eta v^{\mathrm{c}}/(\xi\phi)}$ appears. What does this correspond to intuitively? Consider moving a cell through the fluid at a constant velocity. The motion of the cell would cause a distortion of the fluid that decays over length scales $\sim \ell_p$. Its value strongly depends on the cell volume fraction ϕ, as we expect that η depends strongly on ϕ. For $\phi \to 0$, we expect $\eta \sim \phi^2$, corresponding to the probability of two cells coming into contact, and therefore the permeation length goes to 0. In that case dissipation is dominated by relative motion between cells and the fluid, rather than by relative motion between cells. In the converse limit where $\phi \to 1$, we expect that relative flows with velocity of magnitude v between cells and the solvent, occuring on the intercellular distance ℓ, will result in a total force $\sim 4\pi r^2 v^{\mathrm{c}}\eta^{\mathrm{w}}/\ell$ on the surface of the cell. Therefore, the friction coefficient $\xi \sim r^2\eta^{\mathrm{w}}/\ell$ where $\ell/r \sim (1-\phi)/3$ for spherical cells of radius r; so that $\xi \sim r\eta^{\mathrm{w}}/(1-\phi)$. Therefore in this limit $\ell_p \sim \ell\sqrt{\eta/\eta^{\mathrm{w}}}$. Even if ℓ is small, this distance can become large if the cellular viscosity is high. Taking as a typical order of magnitude in a dense tissue $\ell \sim 100\,\mathrm{nm}$, $\eta^{\mathrm{w}} \sim 10^{-3}\,\mathrm{Pa\,s}$, and $\eta \sim 10^3\,\mathrm{Pa\,s}$ [126], one finds $\ell_p \sim 100\,\mu\mathrm{m}$, of the order of about 10 cells.

Second, we can consider the linear stability of a system of impermeable cells. Here we expand Eqs. 4.117-4.120 around a homogeneous state. We denote n, n^{sm} the homogeneous density of cells and solutes and δn, δn^{sm} perturbations from this density. We perform a Fourier transform in space of these perturbations, with $\delta\tilde{n}(\mathbf{q}) = \int d\mathbf{x}\delta n e^{-i\mathbf{q}\cdot\mathbf{x}}$ and $\delta\tilde{n}^{\mathrm{sm}}(\mathbf{q}) = \int d\mathbf{x}\delta n^{\mathrm{sm}} e^{-i\mathbf{q}\cdot\mathbf{x}}$.

Truncating to linear order in the perturbations, we obtain:

$$\partial_t \delta\tilde{n} = -\frac{q^2}{1+\ell_p^2 q^2}\left[D(1-\phi)^2 z(\phi)\delta\tilde{n} - D^{\rm s} v^{\rm s} n\left(\frac{\xi^{\rm s}}{\xi}-1\right)\delta\tilde{n}^{\rm sm}\right] \tag{4.121}$$

$$\partial_t \tilde{n}^{\rm sm} = -q^2\left[D^{\rm s}\delta\tilde{n}^{\rm sm} + n^{\rm sm} D^{\rm s}\frac{\xi^{\rm sw}v^{\rm c} - \xi^{\rm s}v^{\rm s}}{\xi(1-\phi)}\left(z(\phi)(1-\phi)^2\delta\tilde{n} + O(q^2)\right)\right] \tag{4.122}$$

These equations are linearly unstable for $z(\phi) < 0$. This instability is of Type II according to the Cross and Hohenberg classification [39], i.e. there exists a band of unstable wavevectors starting at $q^2 = 0$. The instability corresponds to the spinodal decomposition instability discussed in Section 4.1.2 and Eq. 4.66. In this case we had $z(\phi) = 1 - \frac{\epsilon}{kT}\phi(1-\phi)$, corresponding to Eq. 4.35, i.e. the cells contribute to the free energy an entropic mixing term, and an adhesion energy. We can now estimate the growth rate of this instability. Writing Eq. 4.121 with homogeneous solutes,

$$\partial_t \delta\tilde{n} = -\frac{D(1-\phi)^2\left(1-\frac{\epsilon}{kT}\phi(1-\phi)\right)q^2}{1+\left(\frac{4}{3}-\phi\right)\frac{1-\phi}{\phi}\frac{\eta v^{\rm c}}{\xi}q^2}\delta\tilde{n}. \tag{4.123}$$

Well above the instability threshold ($\epsilon >> \epsilon^*$), a perturbation of size L (where L is sufficiently large) grows in a time $\tau \sim L^2 kT/(D\epsilon(1-\phi)^3\phi)$; taking the diffusion coefficient of cells in the dilute limit $\phi \to 0$, $D = kT/(6\pi r\eta^{\rm m})$ with r the cell radius and $\eta^{\rm m}$ the extracellular medium viscosity, $\tau \sim 6\pi(L/r)^2 r^3\eta^{\rm m}/(\epsilon(1-\phi)^3\phi)$. With $L/r = 10$, $r \sim 10\,\mu$m, $\phi = 1/2$, $\eta^{\rm m} \sim 10^{-3}\,$Pa s and $\epsilon \sim 4\times10^{-18}\,$J (section 4.1.2), this corresponds to $\tau \sim 1$ hour, a timescale compatible with biological developmental processes. We conclude that passive spinodal decomposition driven by cell-cell adhesion could, in principle, drive cell aggregation. This timescale however diverges for $\phi \to 0$ (dilute cell limit) and for $\phi \to 1$ (dense cell limit); in which case stability is restored.

Third, we study the effect of gradients of solutes on the cell number density. We consider a cell moving in a solute gradient. According to Eq. 4.119, the cellular velocity is then given by

$$v_\alpha = -D^{\rm s} v^{\rm s}\left(\frac{\xi^{\rm s}}{\xi}-1\right)\partial_\alpha n^{\rm sm}, \tag{4.124}$$

where we have neglected the cell viscosity term η as we are working in the limit $\phi \to 0$. This corresponds to a process of diffusiophoresis, whereby colloid particles move in a concentration gradient [6]. This contribution vanishes for $\xi^{\rm s} = \xi$. This is to be expected since no cell motion should occur from a solute gradient if the solute molecules have the same physical properties as the solvent molecules. In the limit of isolated spherical cells of radius r and dilute extracellular solutes, $\bar{\phi}^{\rm sm} \to 0$, the friction coefficients $\xi \to 6\pi r\eta^{\rm w}$ and $(1-\bar{\phi}^{\rm sm})\xi + \bar{\phi}^{\rm sm}\xi^{\rm s} \to 6\pi r\eta^{\rm m}$ with $\eta^{\rm w}$ the viscosity of pure water and $\eta^{\rm m}$ the viscosity of the extracellular solution. The ratio $\xi^{\rm s}/\xi - 1 = (\eta^{\rm m} - \eta^{\rm w})/(\eta^{\rm w}\bar{\phi}^{\rm sm}) \equiv [\eta^{\rm m}]$ is the intrinsic viscosity of the solution, and is generally positive [7]; implying that cells move against the solute gradient. For the special case where solutes are spherical particles of radius a, sufficiently large compared to water molecules, the friction coefficient of solutes in water is $\xi^{\rm sw} = 6\pi a\eta^{\rm w}$ and the intrinsic viscosity is $\frac{5}{2}$ [162]. With these relations, the cellular velocity given in Eq. 4.124 becomes $-10kTa^2/(18\eta^{\rm w})\,\partial_\alpha n^{\rm sm}$, which agrees with results on diffusiophoresis by steric interactions, up to a numerical prefactor [6]. To estimate the order of magnitude of this velocity, we can consider a gradient of macromolecules of size $\sim$ 5nm (a typical protein size), and a gradient of 10mM across a cell size $2r = 20\,\mu$m; we find a velocity of $1\,\mu\mathrm{m\,h^{-1}}$.

In the converse limit $\phi \to 1$, the velocity of a "flock" of cells depends strongly on the friction coefficient between cells and solutes $\xi^{\rm s}$. Assuming the distance between cells is still large

compared to the size of a single solute, $a \ll \ell$, and no specific intercellular structures such as tight junctions stop solutes from moving in the extracellular fluid, one still has $\xi^{\mathrm{s}} = \xi(1+[\eta^{\mathrm{m}}])$. Evaluating the ratio in the denominator of D^{s} with the expressions for ξ^{s} and ξ^{sw} above, we find $\frac{\phi\xi^{\mathrm{s}}v^{\mathrm{s}}}{(1-\phi)\xi^{\mathrm{sw}}v^{\mathrm{c}}} \sim \frac{a^2}{\ell^2}$ which is small. Hence $D^{\mathrm{s}} \approx \frac{kT}{\xi^{\mathrm{sw}}}$, as in the $\phi \to 0$ case, and $|\mathbf{v}| \approx 1\,\mu\mathrm{m\,h}^{-1}$ still applies.

Finally, we consider the case where tight junctions or other intercellular structures impede the movement of solutes past the cells. This corresponds to $\xi^{\mathrm{s}} \to \infty$, hence $D^{\mathrm{s}} \to 0$, and $|\mathbf{v}| \to 0$, as expected.

4.2.3 Passive, apolar, infinitely permeable cells

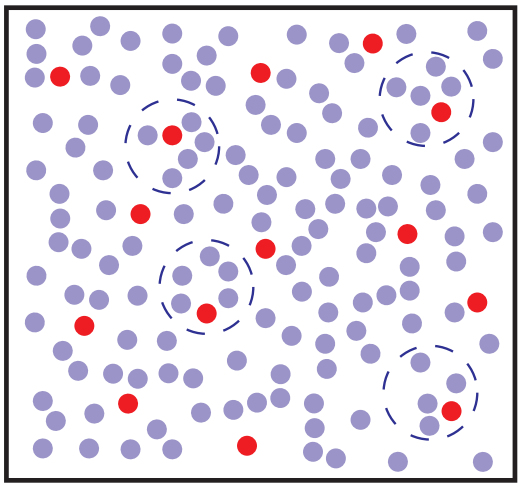

Figure 4.5
A schematic of passive, apolar, infinitely permeable cells. The solutes and water behave as if the cells were not there.

In this Section we consider the simple case where cells behave as passive apolar objects ($\Delta\mu = 0$, $\mathbf{p} = 0$), that on hydrodynamic length scales are uniformly distributed in space, and are also infinitely permeable (Fig. 4.5). In this case we expect solutes to diffuse as if the cells were absent. The dynamics of internal solutes, internal solute gradients, and external solutes are

$$\frac{dn^{\mathrm{s}}}{dt} = \Lambda^s kT \ln\left(\frac{\bar{n}^{\mathrm{sm}}}{\bar{n}^{\mathrm{s}}}\right) - \frac{\partial_\alpha(\langle u_\alpha n^{\mathrm{s}}\rangle n)}{n}, \tag{4.125}$$

$$\frac{d\xi_\alpha}{dt} = \Lambda^{\xi}\chi_\alpha + \Lambda^{\mathrm{sm},\xi}\partial_\alpha\bar{\mu}^{\mathrm{sm}} - \frac{\partial_\beta(\langle u_\beta\xi_\alpha\rangle n)}{n}, \tag{4.126}$$

$$\frac{dn^{\mathrm{sm}}}{dt} = -\partial_\alpha\left\{-D^{\mathrm{s}}(1-\phi)\partial_\alpha\bar{n}^{\mathrm{sm}} - \phi\Lambda^{\mathrm{sm},\xi}\left(\partial_\alpha\bar{\mu}^{\mathrm{sm}} + \frac{kT}{K\bar{n}^{\mathrm{sm}}}\chi_\alpha\right)\right\} - n\Lambda^s kT\ln\left(\frac{\bar{n}^{\mathrm{sm}}}{\bar{n}^{\mathrm{s}}}\right). \tag{4.127}$$

Once again, we consider the evolution of perturbations about a steady state ($n^{\mathrm{s}} = n^{\mathrm{s},0} + \delta n^{\mathrm{s}}$ etc.), and truncate to linear order. It is instructive to write the equation in ξ_α as a sum of bulk

and boundary terms, like so

$$\partial_t \delta\xi_\alpha = \frac{\Lambda^{\mathrm{sm},\xi} kT}{\bar{n}^{\mathrm{sm}}} \left(\partial_\alpha \delta\bar{n}^{\mathrm{sm}} - \frac{\delta\xi_\alpha}{v^{\mathrm{c}\frac{2}{3}}} \right) - \left(\Lambda^\xi K - \frac{\Lambda^{\mathrm{sm},\xi} kT}{\bar{n}^{\mathrm{sm}} v^{\mathrm{c}\frac{2}{3}}} \right) \delta\xi_\alpha \tag{4.128}$$

Taking the limit $\Lambda^{\mathrm{s}} \to \infty$, $\Lambda^{\mathrm{sm},\xi} \to \infty$ and $\Lambda^\xi \to \infty$, while keeping $\Lambda^\xi K - \frac{\Lambda^{\mathrm{sm},\xi} kT}{\bar{n}^{\mathrm{sm}} v^{\mathrm{c}\frac{2}{3}}}$ finite, Eq. 4.125 implies $\delta\bar{n}^{\mathrm{s}} = \delta\bar{n}^{\mathrm{sm}}$, and Eq. 4.126 implies $\delta\xi_\alpha = v^{\mathrm{c}\frac{2}{3}} \partial_\alpha \delta\bar{n}^{\mathrm{sm}}$. The equation in n^{sm} becomes

$$\partial_t \delta n^{\mathrm{sm}} = \left[D^{\mathrm{s}}(1-\phi) + \phi v^{\mathrm{c}\frac{2}{3}} \left(\Lambda^\xi K - \frac{\Lambda^{\mathrm{sm},\xi} kT}{\bar{n}^{\mathrm{sm}} v^{\mathrm{c}\frac{2}{3}}} \right) \right] \partial_\alpha^2 \delta n^{\mathrm{sm}} + \phi v^{\mathrm{c}\frac{2}{3}} \partial_t \partial_\alpha^2 \bar{n}^{\mathrm{sm}}. \tag{4.129}$$

In the hydrodynamic limit, gradients in $\bar{n}^{\mathrm{sm}}$ occur on length scales much greater than $v^{\frac{1}{3}}$, hence the final term can be neglected. Identifying the relationship between Λ^ξ, $\Lambda^{\mathrm{sm},\xi}$, and D^{s},

$$\Lambda^\xi K - \frac{\Lambda^{\mathrm{sm},\xi} kT}{\bar{n}^{\mathrm{sm}} v^{\mathrm{c}\frac{2}{3}}} = \frac{D^{\mathrm{s}}}{v^{\mathrm{c}\frac{2}{3}}}, \tag{4.130}$$

we recover the solute diffusion equation, as expected:

$$\partial_t \delta n^{\mathrm{sm}} = D^{\mathrm{s}} \partial_\alpha^2 \delta n^{\mathrm{sm}}. \tag{4.131}$$

This result justifies the form of the passive flux of solutes through cells given in Eq. 4.94.

4.2.4 Cell volume regulation

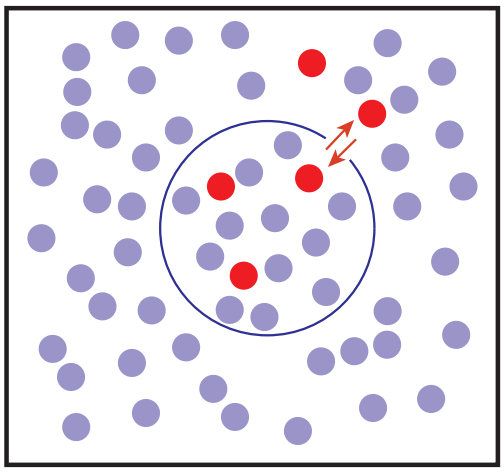

Figure 4.6
A schematic of a cell actively pumping solutes across its membrane in order to maintain its volume.

Here we discuss a cell volume regulation mechanism represented by the coefficients Λ^{s}, Λ^{w}, Λ^{sa}, shown in Fig. 4.6. We assume that cells actively pump solutes in order to maintain their cell volume [25]. This process reflects physiological observations of cell regulatory volume increase and decrease, whereby cells react to a change in extracellular osmolarity by pumping ions to

restore their volumes, on a time scale of roughly 10 minutes. We assume that this behaviour can be captured by postulating the following relation for the active solute flux $\Lambda^{\mathrm{sa}}\Delta\mu$:

$$\Lambda^{\mathrm{sa}} = -\Lambda^{\mathrm{sa0}}(v^{\mathrm{c}} - v^{\mathrm{T}}) \tag{4.132}$$

with v^{T} the target volume and $\Lambda^{\mathrm{sa0}} > 0$.

We consider the situation where the cell density n and extracellular solute density n^{sm} are fixed, and we also assume that cells are not polarized, $p_\alpha = 0$. The remaining equations for the cell volume and number of cell solutes read:

$$\frac{dn^{\mathrm{s}}}{dt} = \Lambda^{\mathrm{s}} kT \ln \frac{\bar{n}^{\mathrm{sm}}}{\bar{n}^{\mathrm{s}}} - \Lambda^{\mathrm{sa0}}(v^{\mathrm{c}} - v^{\mathrm{T}})\Delta\mu \tag{4.133}$$

$$\frac{dv}{dt} = \Lambda^{\mathrm{w}} \left(kT\left(\bar{n}^{\mathrm{s}} - \bar{n}^{\mathrm{sm}}\right) - \frac{2\gamma}{R} \right) + v^{\mathrm{s}}\Lambda^{\mathrm{s}} kT \ln \frac{\bar{n}^{\mathrm{sm}}}{\bar{n}^{\mathrm{s}}} - v^{\mathrm{s}}\Lambda^{\mathrm{sa0}}(v^{\mathrm{c}} - v^{\mathrm{T}})\Delta\mu. \tag{4.134}$$

The surface tension, γ, contains both active and passive contributions. In the regime $\Lambda^{\mathrm{sa0}} = 0$ where the cell does not perform volume regulation, there exist no steady states for $\gamma \neq 0$. When we neglect the surface tension (as is biologically realistic) the steady-state is set by $\bar{n}^{\mathrm{s}} = \bar{n}^{\mathrm{sm}}$, i.e. equal concentrations of solutes in the cell and in the extracellular medium. In that case the volume of the cell is set by the initial condition.

Now considering the realistic regime for biological cells where the contribution of cell surface tension $2\gamma/R$ can be neglected, and $\Lambda^{\mathrm{sa0}} \neq 0$, a steady-state equilibrium is reached for $\bar{n}^{\mathrm{s}} = \bar{n}^{\mathrm{sm}}$, $v^{\mathrm{c}} = v^{\mathrm{T}}$. A sudden small change in external osmolarity $\bar{n}^{\mathrm{sm}} + \delta\bar{n}^{\mathrm{sm}}$ away from this steady state gives rise to a linear response described by:

$$\partial_t \delta n^{\mathrm{s}} = \Lambda^{\mathrm{s}} kT \left(\frac{\delta\bar{n}^{\mathrm{sm}}}{\bar{n}^{\mathrm{sm}}} - \frac{\delta\bar{n}^{\mathrm{s}}}{\bar{n}^{\mathrm{s}}} \right) - \Lambda^{\mathrm{sa0}}\delta v^{\mathrm{c}}\Delta\mu \tag{4.135}$$

$$\partial_t \delta v^{\mathrm{c}} = \Lambda^{\mathrm{w}} kT \left(\delta\bar{n}^{\mathrm{s}} - \delta\bar{n}^{\mathrm{sm}}\right) - v^{\mathrm{s}}\Lambda^{\mathrm{sa0}}\delta v^{\mathrm{c}}\Delta\mu, \tag{4.136}$$

where we have neglected the logarithmic contribution to Eq. 4.134. In Cadart et al. [25], cells are subjected to an osmotic shock that increases their volume by approximately 30%. The active volume control response is measured and found to have a typical relaxation time of approximately 10 minutes. This measurement allows the value of $\Lambda^{\mathrm{sa0}}\Delta\mu$ to be estimated from the linear response time of Eqs. 4.133 and 4.134. In the strong volume control limit, $\Lambda^{\mathrm{sa0}} >> \Lambda^{\mathrm{s}}$, this results in $\Lambda^{\mathrm{sa0}}\Delta\mu = 10^{26}\,\mathrm{m}^{-3}\,\mathrm{s}^{-1}$. How does this value compare to known pumping rates? Considering only the dominant active pumping term, the active flux of solutes in response to a 30% increase in volume is

$$-\Lambda^{\mathrm{sa0}}\Delta\mu(v^{\mathrm{c}} - v^{\mathrm{T}}) \approx -10^{10}\,\mathrm{s}^{-1}. \tag{4.137}$$

For comparison, Grosell reports a Na^+ pumping flux of approximately $10^{-6}\,\mathrm{mol\,m^{-2}\,s^{-1}}$, which corresponds to a pumping rate of of $10^9\,\mathrm{s}^{-1}$ for a spherical cell of radius $10\,\mu\mathrm{m}$ [73]. From this we conclude that the assumption of strong volume control is reasonable. We do not consider the effect of impermeant solutes within the cell. This is in contrast to the Pump and Leak Mechanism (PLM) [198] [92]. In the PLM, the osmotic pressure generated by impermeant solutes is countered by the active transport of Sodium and Potassium ions by the Na^+/K^+ ATP-ase pump.

4.2.5 Instability of active, polar aggregates

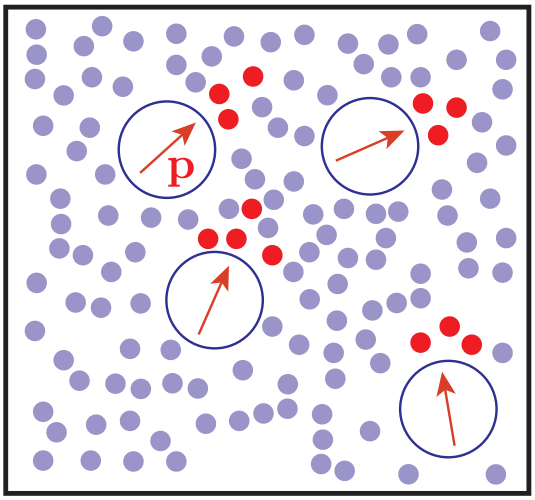

Figure 4.7
A schematic cells actively pumping solutes along their polar axis.

In this section we consider whether the system is unstable with respect to the polar, active pumping of solutes. First, it is convenient to write the dynamic equation for ξ_α in terms of boundary and bulk effects, like so

$$J^{\xi}_{\alpha} = \frac{\Lambda^{\mathrm{sm},\xi} kT}{\bar{n}^{\mathrm{sm}}} \left(\partial_\alpha \bar{n}^{\mathrm{sm}} - \frac{\xi_\alpha}{v^{\mathrm{c}\,\frac{2}{3}}} \right) - \frac{D^{\mathrm{s}}}{v^{\mathrm{c}\,\frac{2}{3}}} \xi_\alpha. \tag{4.138}$$

Using the explicit form of $\tilde{Z}(\phi)$ given in Eq. 4.35 (mixing entropy and adhesion), and again making the simplification that the mass density of solutes and water are equal, the hydrody-

namic equations for cells, cell volume, internal and external solutes, and polarity, are

$$\frac{dn}{dt} = -\partial_\alpha(nv_\alpha) \tag{4.139}$$

$$\frac{dv}{dt} = \Lambda^{\mathrm{w}}\left(kT\left(\bar{n}^{\mathrm{s}} - \bar{n}^{\mathrm{sm}}\right) - kTn\tilde{Z}'(\phi) - f_0^{\mathrm{c}\prime}(v^{\mathrm{c}}) + \frac{\Lambda^{\mathrm{wa}}}{\Lambda^{\mathrm{w}}}\Delta\mu\right) + v^{\mathrm{s}}\Lambda^{\mathrm{s}}kT\ln\frac{\bar{n}^{\mathrm{sm}}}{\bar{n}^{\mathrm{s}}} - v^{\mathrm{s}}\Lambda^{\mathrm{sa0}}(v^{\mathrm{c}} - v^{\mathrm{T}})\Delta\mu \tag{4.140}$$

$$\frac{dn^{\mathrm{s}}}{dt} = \Lambda^{\mathrm{s}}kT\ln\frac{\bar{n}^{\mathrm{sm}}}{\bar{n}^{\mathrm{s}}} - \Lambda^{\mathrm{sa0}}(v^{\mathrm{c}} - v^{\mathrm{T}})\Delta\mu \tag{4.141}$$

$$\frac{d\xi_\alpha}{dt} = \frac{\Lambda^{\mathrm{sm},\xi}kT}{\bar{n}^{\mathrm{sm}}}\left(\partial_\alpha\bar{n}^{\mathrm{sm}} - \frac{\xi_\alpha}{v^{\mathrm{c}\frac{2}{3}}}\right) - \frac{D^{\mathrm{s}}}{v^{\mathrm{c}\frac{2}{3}}}\xi_\alpha \tag{4.142}$$

$$\begin{aligned}\frac{dn^{\mathrm{sm}}}{dt} =& \partial_\alpha\left(-n^{\mathrm{sm}}v_\alpha^{\mathrm{sm0}} + \phi\Lambda^{\mathrm{sm},\xi}\left(\partial_\alpha\bar{\mu}^{\mathrm{sm}} + \frac{kT}{K\bar{n}^{\mathrm{sm}}v^{\mathrm{c}\frac{2}{3}}}\chi_\alpha\right) - \lambda^{\mathrm{sa0}}\Delta\mu nn^{\mathrm{sm}}p_\alpha\right)\\ &- \Lambda^{\mathrm{s}}nkT\ln\frac{\bar{n}^{\mathrm{sm}}}{\bar{n}^{\mathrm{s}}} + \Lambda^{\mathrm{sa0}}(v^{\mathrm{c}} - v^{\mathrm{T}})n\Delta\mu\end{aligned} \tag{4.143}$$

$$\frac{Dp_\alpha}{Dt} = -\frac{1}{\tau_p}p_\alpha - \frac{b}{\gamma_1}p_\beta p_\beta p_\alpha + K\partial_\beta^2 p_\alpha - \kappa\partial_\alpha n \tag{4.144}$$

$$\begin{aligned}v_\alpha^{\mathrm{sm},0} =& \frac{v^{\mathrm{c}}(1-\phi)(\xi^{\mathrm{sw}}v^{\mathrm{c}} - \xi^{\mathrm{s}}v^{\mathrm{s}})}{\xi(\xi^{\mathrm{s}}\phi v^{\mathrm{s}} + v^{\mathrm{c}}\xi^{\mathrm{sw}}(1-\phi))}\left[n\partial_\alpha\mu + h_\beta\partial_\alpha p_\beta + \phi\partial_\alpha(P - P^e) - \partial_\beta\tilde{\sigma}_{\alpha\beta}\right]\\ &- \frac{1-\phi}{n^{\mathrm{sm}}\left[\xi^{\mathrm{sw}}(1-\phi) + \xi^{\mathrm{s}}\phi\frac{v^{\mathrm{s}}}{v^{\mathrm{c}}}\right]}\left[n^{\mathrm{sm}}\partial_\alpha\mu^{\mathrm{sm}} + (1-\phi)\bar{\phi}^{\mathrm{sm}}\partial_\alpha(P - P^e)\right]\end{aligned} \tag{4.145}$$

$$\begin{aligned}v_\alpha =& -\frac{(1-\phi)}{n\xi}\left[n\partial_\alpha\mu + h_\beta\partial_\alpha p_\beta + \phi\partial_\alpha(P - P^e) - \partial_\beta\tilde{\sigma}_{\alpha\beta}\right]\\ &+ \frac{v^{\mathrm{s}}\phi(1-\phi)(\xi - \xi^{\mathrm{s}})}{\xi n\left[\xi^{\mathrm{s}}\phi v^{\mathrm{s}} + v^{\mathrm{c}}\xi^{\mathrm{sw}}(1-\phi)\right]}\left[n^{\mathrm{sm}}\partial_\alpha\mu^{\mathrm{sm}} + (1-\phi)\bar{\phi}^{\mathrm{sm}}\partial_\alpha(P - P^e)\right]\end{aligned} \tag{4.146}$$

Note that the non-linear terms from Eqs. 4.27 - 4.29 have been neglected, as they do not affect the linear stability. The parameter $\tau_p = \frac{\gamma_1}{a}$ is the autonomous relaxation time of the polarity field. In order to simplify the equations we take the limit of strong cell volume control. The limit of strong volume control corresponds to Λ^{s}, Λ^{sa0}, Λ^{w}, $\Lambda^{\mathrm{sm},\xi} \to \infty$. This results in $\bar{n}^{\mathrm{s}} = \bar{n}^{\mathrm{sm}}$, $v^{\mathrm{c}} = v^{\mathrm{T}}$, and $v^{\mathrm{c}\frac{2}{3}}\partial_\alpha\bar{n}^{\mathrm{sm}} = \xi_\alpha$. By taking this limit we can exploit a separation of timescales between the variables n^{s} and v^{c}, which equilibriate quickly, and the slow dynamics of n, n^{sm}, and p_α. Eq. 4.143, the dynamics of the solutes in the medium, can be rewritten as

$$\begin{aligned}\frac{d}{dt}\left(n^{\mathrm{sm}} + nn^{\mathrm{s}} - \phi\partial_\alpha\xi_\alpha\right) =& -\partial_\alpha\left\{n^{\mathrm{sm}}v_\alpha^{\mathrm{sm0}} + \lambda^{\mathrm{sa0}}nn^{\mathrm{sm}}\Delta\mu p_\alpha - \frac{\phi D^{\mathrm{s}}}{v^{\mathrm{c}\frac{2}{3}}}\xi_\alpha + n^{\mathrm{s}}\phi v_\alpha\right\}\\ &+ \phi v_\alpha\partial_\alpha n^{\mathrm{s}} + \partial_\alpha\xi_\alpha\partial_\beta(\phi v_\beta).\end{aligned} \tag{4.147}$$

This eliminates all terms in the permeabilities that we take to infinity. Perturbing about a steady state, truncating to linear order in the perturbations, and lowest order in q^2, the hydrodynamic equations become

$$\partial_t\delta\tilde{n} = -zD(1-\phi)^2q^2\delta\tilde{n} + D^{\mathrm{s}}v^{\mathrm{s}}n(1-\phi)\left(\frac{\xi^s}{\xi} - 1\right)q^2\delta\tilde{n}^{\mathrm{sm}} \tag{4.148}$$

$$\begin{aligned}\partial_t\delta\tilde{n}^{\mathrm{sm}} =& \left\{D^{\mathrm{s}}z\phi^{\mathrm{sm}}(1-\phi)\frac{\xi^{\mathrm{sw}}v^{\mathrm{c}} - \xi^{\mathrm{s}}v^{\mathrm{s}}}{v^{\mathrm{s}}\xi} + n^{\mathrm{s}}zD(1-\phi)^2\right\}q^2\delta\tilde{n}\\ &- \left\{1 - n^{\mathrm{s}}nv^{\mathrm{s}}(1-\phi)\left(\frac{\xi^{\mathrm{s}}}{\xi} - 1\right)\right\}D^{\mathrm{s}}q^2\delta\tilde{n}^{\mathrm{sm}} + \lambda^{\mathrm{sa0}}nn^{\mathrm{sm}}\Delta\mu\delta\tilde{\rho}\end{aligned} \tag{4.149}$$

$$\partial_t\delta\tilde{\rho} = -\frac{1}{\tau^{\mathrm{p}}}\delta\tilde{\rho} - Kq^2\delta\tilde{\rho} + \kappa q^2\delta\tilde{n}. \tag{4.150}$$

where $\tilde{\rho}$ is the Fourier transform in space of $\partial_\alpha p_\alpha$. Note that more details of this calculation are given in Appendix A.2. The first two terms of Eq. 4.148 and Eq. 4.149 correspond to cross diffusion between cells and solutes. The third term in Eq. 4.149 is the flux of actively pumped solutes. The first term in Eq. 4.150 is the relaxation of the polarity to its unpolarised groundstate, the second term is the Frank term which encourages alignment in the polarity field, and the third term is the response to gradients in the cell number density.

Choosing parameters such that the system is spinodally stable (i.e. there is no instability due to the cross diffusion of cells and solutes), an instability arises at sufficiently high λ^{sa0} (see Appendix A.2). This instability corresponds to the mechanism shown in Fig. 4.8. Inhomogeneities in the cell density field induce perturbations in the polarity field, as described by the final term in Eq. 4.150. The cells then actively pump solutes along their polarity axes, as described by the final term in Eq. 4.149. The resulting flux of solutes, and osmotic flows of water, into topological defects in the polarity field force a flow of cells out of these regions due to incompressibility. Consequently the inhomogeneity of the cell density is increased, and a feedback loop is established. This mechanism of positive reinforcement results in a fluid filled cavity surrounded by a cell-dense tissue phase, with the cells polarised toward the centre of the cavity. The instability is Type II, i.e. there exists a band of unstable wavevectors starting at 0.

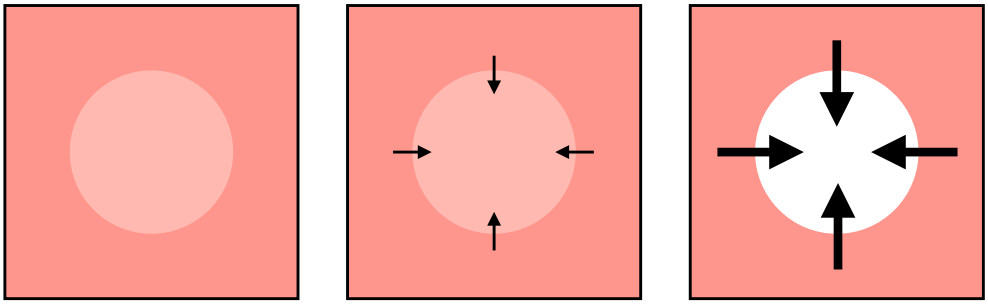

Figure 4.8
A schematic of the polar pumping instability. Inhomogeneities in the cell density induce a topological defect in the polarity field. Active pumping of solutes, and the resulting osmotic flows of water drive cells out of the central region, which in turn reinforces the inhomogeneity of the cell density.

Eqs. 4.148-4.150 become unstable when

$$\lambda^{\mathrm{sa0}}\Delta\mu > \left(\frac{1}{\tau^{\mathrm{p}}} + Kq^2\right)\frac{\Phi}{\kappa}, \tag{4.151}$$

where

$$\Phi = \frac{z(\phi)}{v^{\mathrm{s}}n^2n^{\mathrm{sm}}\left(\frac{\xi^{\mathrm{s}}}{\xi}-1\right)}\Bigg\{D(1-\phi)\left[1-n^{\mathrm{s}}nv^{\mathrm{s}}(1-\phi)\left(\frac{\xi^{\mathrm{s}}}{\xi}-1\right)\right] - v^{\mathrm{s}}n\left(\frac{\xi^{\mathrm{s}}}{\xi}-1\right)\left[D^{\mathrm{s}}\phi^{\mathrm{sm}}(1-\phi)\left(\frac{\xi^{\mathrm{sw}}v^{\mathrm{c}}-\xi^{\mathrm{s}}v^{\mathrm{s}}}{\xi v^{\mathrm{s}}}\right)+n^{\mathrm{s}}D(1-\phi)^2\right]\Bigg\} \tag{4.152}$$

There are various points we note about the form of Eqs. 4.151 and 4.152. First, $z > 0$ corresponds to a spinodally stable system. Consequently, a positive pumping rate is necessary

to induce an instability, as expected. Secondly, the pumping rate at which the system becomes unstable diverges for $\xi^{\mathrm{s}} = \xi$, as this limit corresponds to the solutes and water being physically indistinguishable. Thirdly, it becomes increasingly difficult for the system to become unstable as q^2 increases. This is because K penalises gradients in the polarity field.

For a more intuitive interpretation of this stability criterion, we relate Eq. 4.151 to an approximate solute pumping rate per cell by considering the pumping flux j^{p}_α in response to a step function tissue boundary. Neglecting the Frank term, the polarity dynamics are $\partial_t p_\alpha = \frac{-1}{\tau^{\mathrm{p}}} p_\alpha - \frac{\kappa}{v^{\mathrm{c}}} \partial_\alpha \phi$. The polarity, $\bar{p}$, induced by a 1D tissue boundary that goes from $\phi \approx 1$ to $\phi \approx 0$ across a length scale of one cell is

$$\bar{p} = \frac{\kappa \tau^{\mathrm{p}}}{{v^{\mathrm{c}}}^{\frac{4}{3}}}. \tag{4.153}$$

The flux of solutes pumped by a single cell is $\sigma |\mathbf{j}^p| = \sigma \lambda^{\mathrm{sa0}} \Delta\mu n n^{\mathrm{sm}} \bar{p} = N^{\mathrm{p}}$, where σ is the cross sectional area of the cell. Hence,

$$N^{\mathrm{p}} = \frac{\pi \lambda^{\mathrm{sa0}} \Delta\mu n n^{\mathrm{sm}} \kappa \tau^{\mathrm{p}}}{{v^{\mathrm{c}}}^{\frac{2}{3}}}. \tag{4.154}$$

To evaluate N^{p} we must make some choices about parameter values. Reasonable particle volumes and diffusion constants are given in Table 4.1. The diffusion constants are calculated using the Stokes-Einstein relation. We choose $\xi^{\mathrm{s}} = 3\xi$, corresponding to the viscosity quoted by Applebey [7] for a solute:water ratio of 1:9. ξ and ξ^{sw} are evaluated using the Stokes-Einstein relation as $\xi = 6\pi\eta^{\mathrm{w}} {v^{\mathrm{c}}}^{\frac{1}{3}}$ and $\xi^{\mathrm{sw}} = 6\pi\eta^{\mathrm{w}} {v^{\mathrm{s}}}^{\frac{1}{3}}$. We choose the incompressibility factor $z = 0.1$, where $z > 0$ is the boundary of spinodal stability. The volume fractions are chosen to be $\phi = 0.5$, $\phi^{\mathrm{sm}} = 0.1$, $\bar{\phi}^{\mathrm{s}} = \bar{n}^{\mathrm{s}} v^{\mathrm{s}} = 0.1$. Consequently, in the limit $q^2 \to 0$, we get

$$N^{\mathrm{p}} > \frac{\pi n n^{\mathrm{sm}} \Phi}{{v^{\mathrm{c}}}^{\frac{2}{3}}} \approx 10^9\,\mathrm{s}^{-1}. \tag{4.155}$$

Grosell reports a Na^+ pumping flux of approximately $10^9\,\mathrm{s}^{-1}$ for a spherical cell of radius 10 µm [73]. Consequently, the single cell pumping rate above is at the upper end of biological plausibility.

Parameter	Value
v^{c}	$10^{-15}\,\mathrm{m}^3$
v^{s}	$10^{-29}\,\mathrm{m}^3$
D	$10^{-14}\,\mathrm{m}^2\,\mathrm{s}^{-1}$
D^{s}	$10^{-10}\,\mathrm{m}^2\,\mathrm{s}^{-1}$
η^{w}	$10^{-3}\,\mathrm{Pa\,s}$

Table 4.1

It is to be expected that the onset of instability occurs at relatively high pumping rates, as this calculation was performed with a low concentration of solutes and a system that is only half filled with cells. I expect N^{p} to fall as ϕ increases, as it should be easier for cells to form a cavity by active pumping in a dense tissue. This can be seen in the form of Eq. 4.152, where Φ decreases if D decreases, as would be expected at high cell volume fraction. In order to realistically evaluate Φ as $\phi \to 1$, we would need to hypothesise a new form for z, as the treatment of cells as large, deformable particles floating in a binary mixture of solutes and water would no longer be valid.

4.2.6 Summary

In this chapter we have derived a hydrodynamic theory of cells, in a background fluid of solutes and water. We study the equilibrium behaviour of this system by writing down the free energy, and minimising it subject to particle conservation constraints. From this analysis we deduce the system exhibits spinodal phase separation above a critical cell-cell adhesion strength. To study the non-equilibrium behaviour, we derive constitutive equations for the various fluxes in the system. These constitutive equations allow us to write down and solve hydrodynamic equations for the dynamics of the system. We demonstrate a number of results.

First, a spherical shell of cells surrounding a fluid filled cavity reproduces the Young-Laplace Law, with an active surface tension. Second, we derive diffusion constants for the case of impermeable cells. This allows us to calculate a spinodal phase separation time of roughly 1 hour, which is biologically plausible. Third, we demonstrate that in the limit of infinitely permeable cells, we recover the diffusion equation of solutes in a background of water, as expected. Fourth, we demonstrate that cells can control their volume by actively pumping solutes across their membranes. This results in a volume response to an osmotic shock on a timescale of roughly 10 minutes. Finally, we demonstrate the existence of a Type II instability due to the active pumping of solutes by cells along their polar axes. This instability allows an initially uniform system to evolve into cell dense (tissue) and cell poor (cavity) phases, and occurs at biologically plausible pumping rates.

Chapter 5

Quantifying the growth of mouse stem cell aggregates

Aggregates of mouse embryonic stem cells, when grown *in vitro*, recapitulate key morphogenetic processes. The simplest example of such a system is described by Shahbazi et al. [175]. In this work, a single cell is taken from the mouse epiblast, and grown for up to 72 hours. The resulting cells grow into a spherical aggregate, a spheroid, form a rosette where all of the cells polarise towards the centre, and eventually pump fluid into the centre to form a cavity. Examples of the resulting spheroids are shown in Figure 5.1.

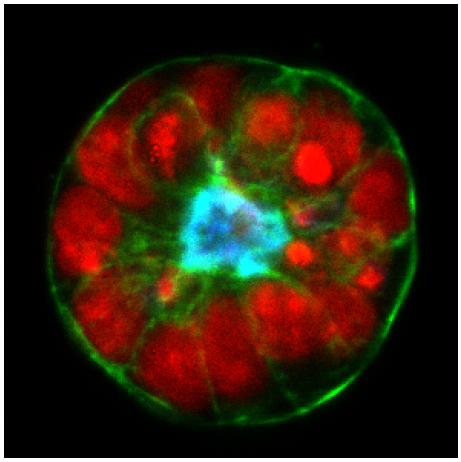

Figure 5.1: Example spheroids grown from a single epiblast cell. F-actin is shown in green, DAPI in red, and podocalyxin in blue [209].

More complex aggregates, so called embryonic organoids, can be grown by combining more cell types. In Harrison et al., cells from the epiblast and extra-embryonic trophoblast are combined to form aggregates that are structurally similar to post implantation embryos [74]. In Sozen et al., cells from the epiblast, trophoblast and extra-embryonic endoderm are combined to form embryonic organoids [185]. Both examples undergo the rotational symmetry breaking that is a hallmark of gastrulation, with the organoids in Sozen et al. also undergoing an epithelial to mesenchymal transition. These organoid systems demonstrate the remarkable self-organising capabilities of embryonic stem cells. They are also an excellent reductionist tool for studying embryo development, allowing us to separate the embryo into its constituent parts, then observe structure emerging as we recombine them.

In my work, I have focused on the simplest example of *in vitro* morphogenesis: the formation of rosettes, and hence cavities, in aggregates of ESCs taken from the mouse epiblast. I contrast

these growth processes with the failure of rosette formation in β1-integrin knock outs. As the formation of a cavity is straightforward once a rosette has formed, I focus on the transition from a single cell to a rosette. The study of these spheroids has been done in collaboration with the group of Prof. Magdalena Zernicka-Goetz. The experiments that provided data for my work were performed by Ms. Antonia Weberling and Dr. Matteo Mòle. Ms. Weberling and Dr. Mòle have produced movies of spheroid growth from a single cell for 24-48 hours. They have used both wild type cells, and β1-KO cells. β1-KOs do not express the protein β1-integrin, a key component in the correct positioning of the apicobasal axis [112]. As shown in Figure 5.2, β1-KOs fail to form rosettes. In this chapter I will describe my work quantifying and contrasting the growth of WT and β1-KO mESC aggregates, with a particular emphasis on rosette formation.

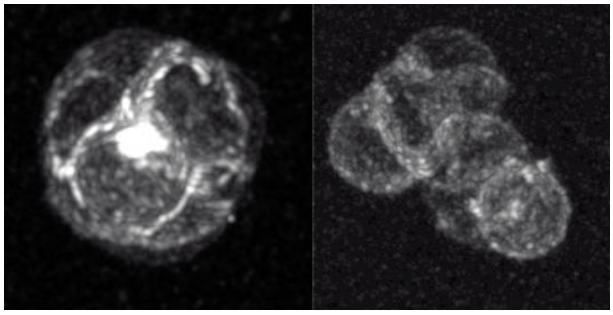

Figure 5.2: Examples of the resulting aggregates from WT (left) and β1-KO (right) cells. The fluorescence is E-cadherin. The WT cells form a clear rosette, with their apical polarity vectors forming a hedgehog defect. The β1-KO cells fail to form a rosette [209].

5.1 Segmentation pipeline

The raw data produced by the Zernicka-Goetz Group is in the form of 3D movies, produced by confocal microscope, where fluorescent tags have been attached to either E-cadherin or F-actin. In order to segment the cells both proteins are viable, though E-cadherin gives cleaner cell boundaries. A typical movie is shown in the upper panels of Figure 5.6. In order to quantify the growth and rearrangements of the cells in these movies I have developed a movie segmentation pipeline in collaboration with Dr. Matthew Smith. Dr. Smith has developed Convolutional Neural Networks (CNNs), based on the U-Net architecture [158], that apply a distance transform to the raw movies. The value of a distance transformed image at any point is the distance from that point to the nearest cell membrane. The CNNs also mask the aggregate, i.e. voxel values outside of the aggregate are set to 0. The effect of this transformation is shown in Figure 5.3. A noisy and complicated image of cells is replaced by a distance transform consisting of a few well separated regions of high intensity. The CNNs were trained on a dataset of segmentations I produced using the active mesh plug-in described below, which were converted to ground truth distance transforms by an exhaustive search algorithm. Although the dataset presented in this thesis (4 E-cadherin WT movies, 2 F-actin WT movies, and 3 β1-KO movies) appears small, the distance transform is a pixel-wise mapping. Each movie contains many pixels from which the distance transform value can be measured, hence a deep learning approach was viable.

I then segment the distance transformed movies using the active mesh ImageJ plugin described in Smith et al. [181] and Smith et al. [182]. The active mesh plugin works by placing

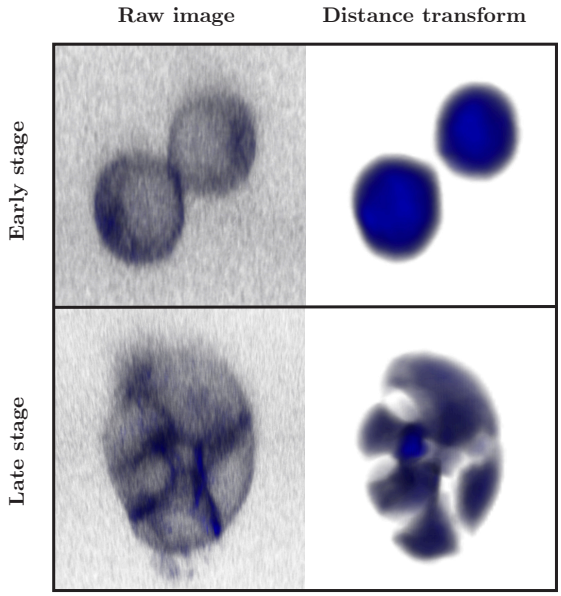

Figure 5.3: An example demonstrating the effect of the distance transform. Complex and noisy raw data is transformed into a simplified, cleaner, representation [180].

an approximately spherical mesh in the centre of a cell. The mesh is then deformed so as to minimise an energy that is the sum of internal and external components. The external energy is taken to be the negative of the pixel intensities at each vertex of the mesh. Consequently, it is energetically favourable for the mesh to colocalise with regions of high intensity. The internal energy describes line tensions between all neighbouring vertices, and a pressure that expands the mesh. The effect of evolving the vertex positions according to an energy minimisation routine is demonstrated in Figure 5.4. The balance of external energy, pressure and surface tension causes the mesh to deform onto the surface of the cell, while maintaining a degree of smoothness.

The boundary of the distance transformed regions is only an approximation of the cell surface. Consequently, in the final segmentation step I take the meshes that have deformed onto the distance transform, and deform them onto a blurred version of the original image. This process is demonstrated in Figure 5.5.

The segmentation process can be summarised as follows:

1. Distance transform the raw movies
2. Deform meshes onto the distance transform
3. Deform meshes onto the raw movies

Using the CNNs to apply the distance transform reduces the time it takes to segment a 300 frame movie from approximately 22 hours to 6 hours. A typical WT movie and segmentation are shown in Figure 5.6. A typical β1-KO movie and segmentation are shown in Figure 5.7. The failure of rosette formation in the β1-KO is clear. It is also important to note that the fluorescence of β1-KOs is significantly worse than WTs. Futhermore, β1-KOs suffer a far higher rate of cell death. As such, accurate β1-KO segmentations are much harder to produce than WTs.

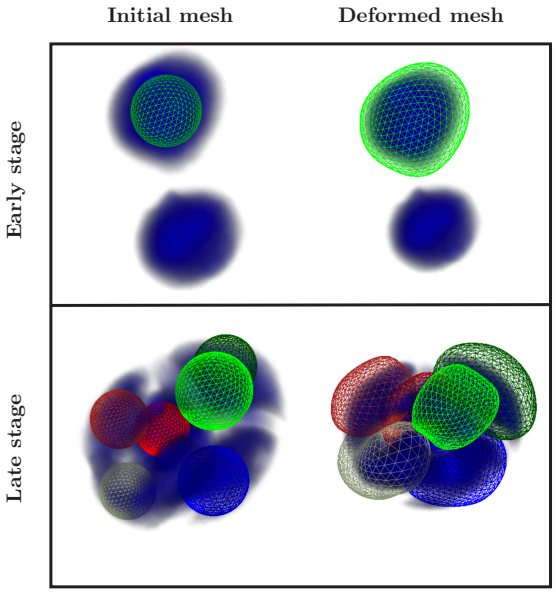

Figure 5.4: An example demonstrating the effect of the active mesh plugin. A spherical mesh is initialised at the centre of each cell. In the distance transformed image, the boundary of the cells has the lowest intensity. Consequently, the external energy of the mesh is inverted, and the mesh deforms towards regions of low intensity, i.e. the boundaries of the cells [181].

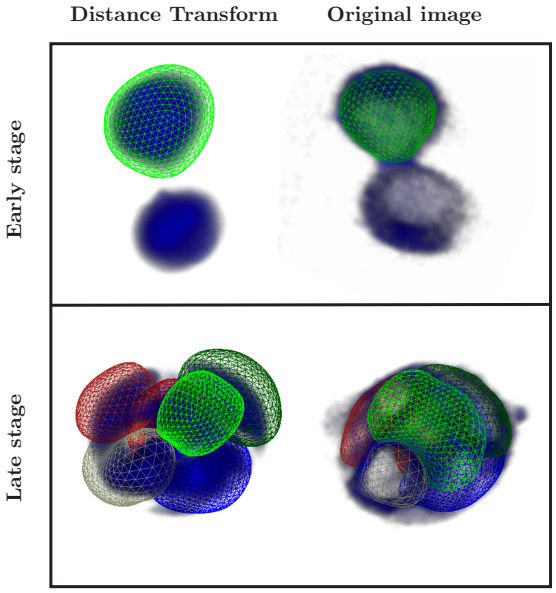

Figure 5.5: An example demonstrating meshes that have been deformed to the distance transform of an image (left) and then to the image itself (right).

The resulting segmentations are stored as meshes, i.e. lists of vertices, edge connections, and triangle connections, within a custom python class, `track`. A `track` consists of a list of consecutive meshes, tracking a particular cell over its lifetime. These meshes are then passed

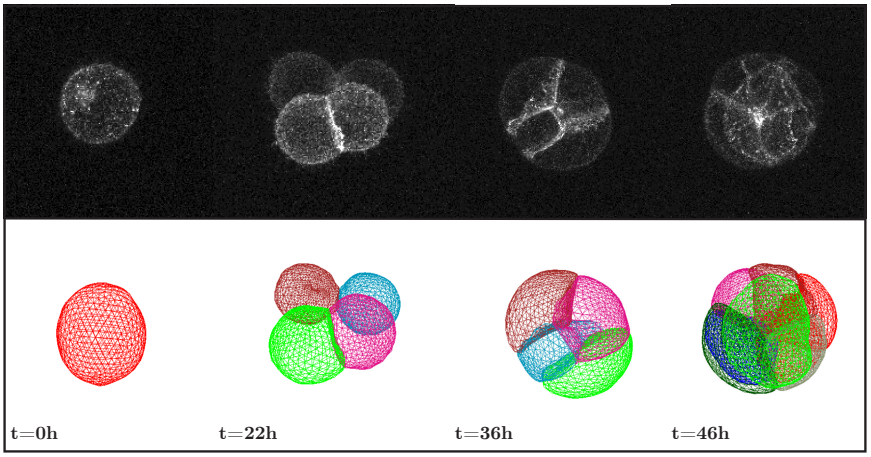

Figure 5.6: A typical WT movie. Top panels: maximum intensity projections of E-cadherin. Bottom panels: the resulting segmentation.

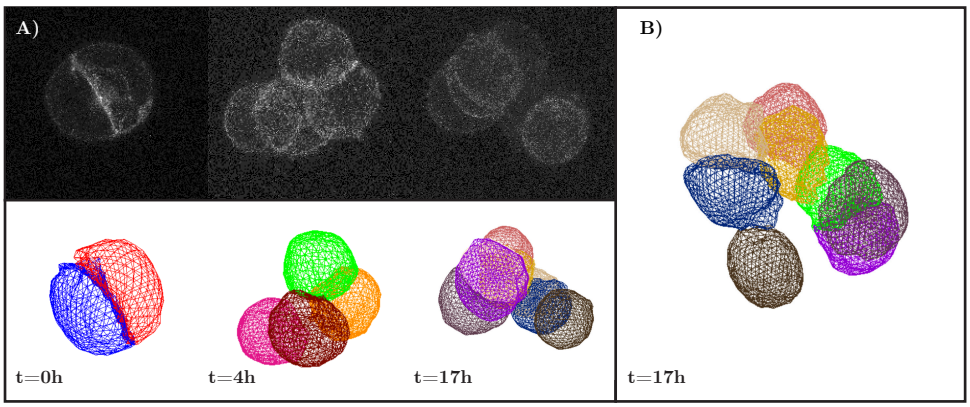

Figure 5.7: A typical β1-KO movie. A) Top panels: maximum intensity projections of E-cadherin. Bottom panels: the resulting segmentation. B) The segmentation at 17 hours, rotated to clearly display the failure of rosette formation.

to a suite of analysis tools I wrote in Python. This mesh representation of the cell surfaces is both memory efficient and convenient for calculating the variety of variables described in the next section.

5.2 Data quantification and analysis

In segmenting movies of aggregate growth, my goals were threefold. First, I aimed to extract quantitative insight from the raw experimental movies. Second, I aimed to quantitatively describe the growth of a single cell into a rosette, and compare this with the failure of rosette formation in β1-KOs. Third, I wanted to gain insight, and justification, for design decisions I made while developing the computational model of cell aggregate growth described in Chapter 6. The growth of an aggregate can be quantified with a number of meaningful variables. Some are descriptors of the state of the cells, either individually or as an aggregate. Others are par-

ticularly useful for distinguishing between the rosette forming behaviour of WT cells, and that of β1-KOs. My dataset of segmentations consists of 6 WT movies, of which 4 form rosettes within the timeframe of the movie, and 3 β1-KOs.

5.2.1 Cell volume

Plots of the evolution of cell volume in representative WT and β1-KO examples are shown in Figure 5.8. These demonstrate that both WT and β1-KO cells approximately double their volume over their lifetimes. Furthermore, cell cycle times are closely synchronised between cells. Further plots are shown in Fig. C.1.

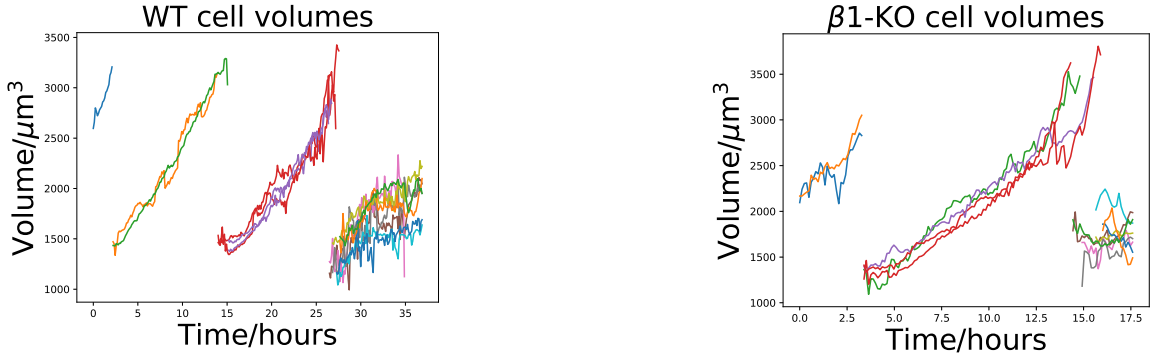

Figure 5.8: Representative examples of the evolution of cell volume in WT (left) and β1-KO (right) cells.

5.2.2 Sphericity

The sphericity of a 3D object is a measure of its deviation from a sphere. It is calculated as the ratio of the surface area of a sphere with the same volume as the object, to the surface area of the object itself.

$$\Psi = \frac{\pi^{\frac{1}{3}}(6V)^{\frac{2}{3}}}{A} \tag{5.1}$$

where Ψ is the sphericity, V the volume, and A the surface area of the object. A sphere has $\Psi = 1$, whereas a cube has $\Psi = (\frac{\pi}{6})^{\frac{1}{3}} \approx 0.806$. Some example cells with varying sphericities are shown in Fig. 5.9.

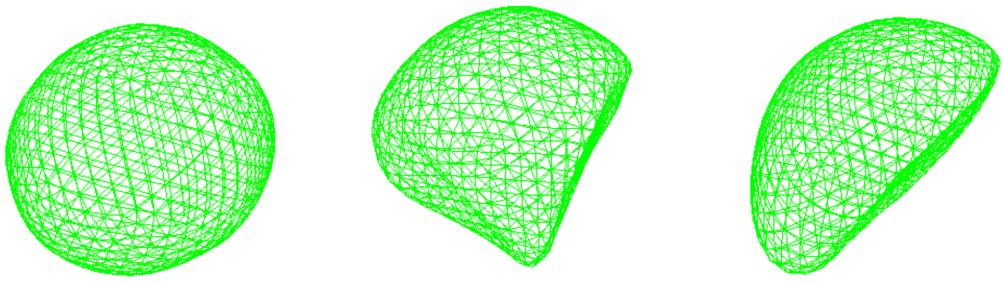

$\Psi = 0.99$ $\Psi = 0.92$ $\Psi = 0.88$

Figure 5.9: Examples of cells with differing sphericities.

Plots of the evolution of cell sphericity in representative WT and β1-KO examples are shown in Figure 5.10. The WT cells are initially very close to spheres. However, as they form a close packed aggregate, and ultimately a rosette, the cells deform away from spheres and their sphericity falls. No such transition occurs for the β1-KOs as they do not form close packed aggregates or rosettes. Further plots are shown in Fig. C.2.

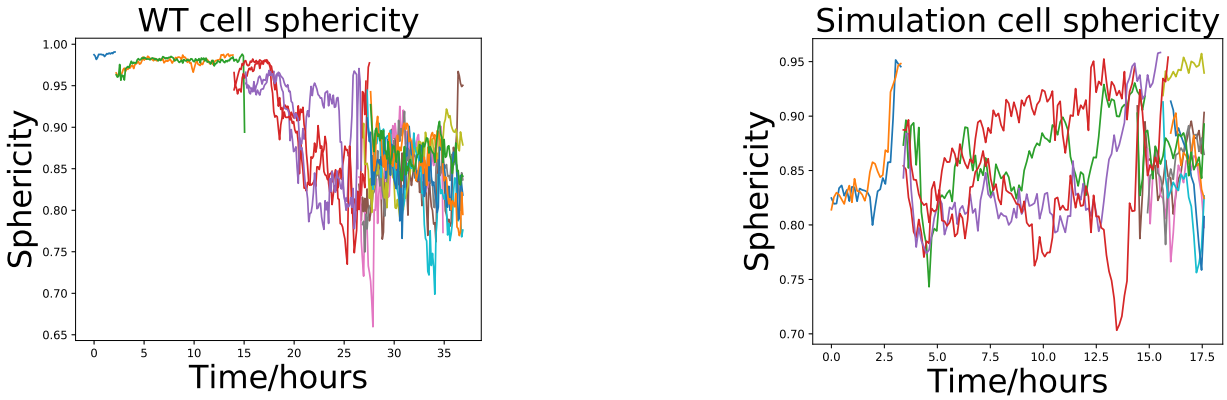

Figure 5.10: Representative examples of the evolution of cell sphericity in WT (left) and β1-KO (right) cells.

5.2.3 Division symmetry

A measure of the symmetry of cell divisions is the ratio of the volumes of the two daughter cells, $\frac{v_1 - v_2}{v_1 + v_2}$, where $v_1 < v_2$. Schematics of a symmetric, and an asymmetric division are shown in Fig. 5.11. The distribution of this variable, for WTs and β1-KOs, is shown in Figure 5.12. Divisions tend to be close to symmetric, and there is no significant difference between the two cell populations.

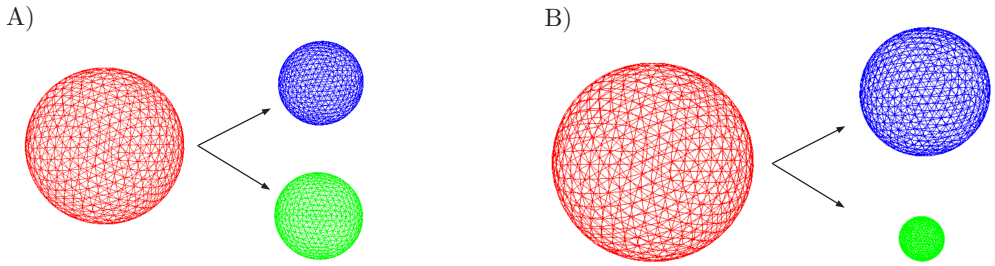

Figure 5.11: A) A schematic of a symmetric division. Both daughters have equal volume. B) A schematic of an asymmetric division, where one daughter is larger than the other.

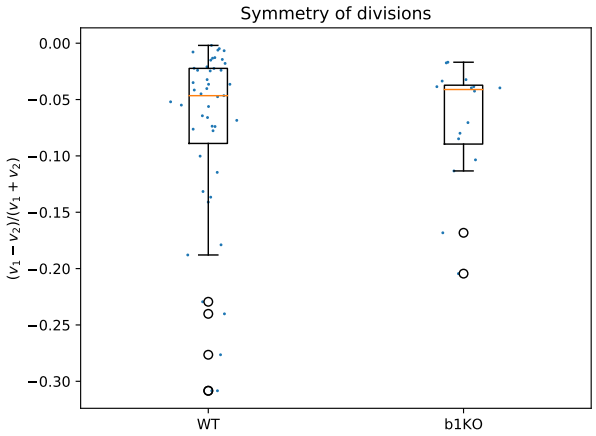

Figure 5.12: The asymmetry in daughter cells with volumes v_1 and v_2, where $v_1 < v_2$.

5.2.4 Division orientation

Are there correlations between the orientation of division from one generation to the next? In order to answer this question the angle of the division normal was measured with respect to the line connecting the centre of the aggregate to the centre of the dividing cell, as demonstrated in Fig. 5.13.

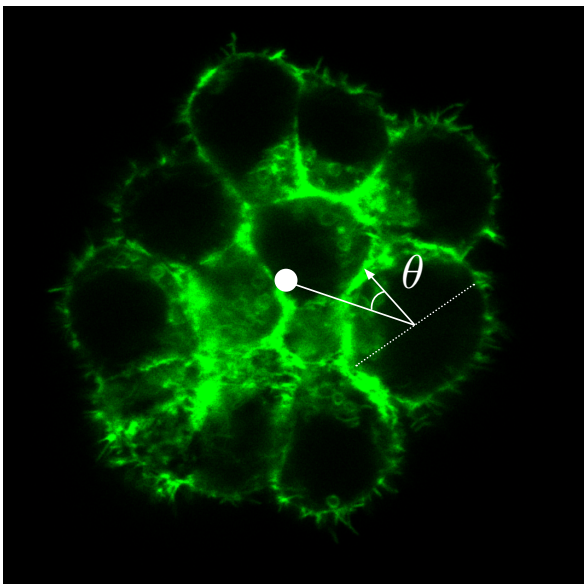

Figure 5.13: A schematic showing the division angle, θ, between the normal of the division plane (dotted line) and the line connecting the centre of the aggregate with the centre of the dividing cell (white line).

This angle is compared between mother and daughter cells in Fig. 5.14. There is no clear correlation. With WT movies, there is enough data to split the divisions between the 2 cell to 4 cell transition, and the 4 cell to 8 cell transition. Again, there is no obvious structure in either population, as shown in Fig. 5.15. However, there is a bias in division angles towards 90°. The distribution of division angles for WT and β1-KO movies is shown in Fig. 5.16. The count of division angles is divided by $\sin(\theta)$ in Fig. 5.16 (which comes from integrating over the ϕ direction), resulting in a normalised count that is proportional to the probability density function of the division angle. There is a clear bias towards cells dividing around 90°, though interestingly this bias exists for both WT and β1-KO movies, so does not explain their different end states.

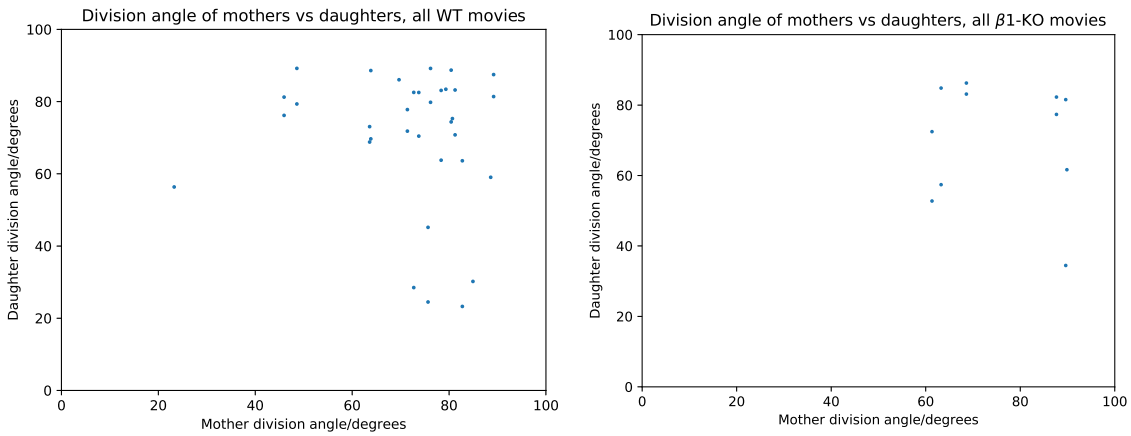

Figure 5.14: The division angle of daughter cells vs the division angle of their mother, for WT (left) and β1-KO (right) movies. The division angle is the angle between the normal of the division plane and the line connecting the centre of the aggregate to the centre of the dividing cell.

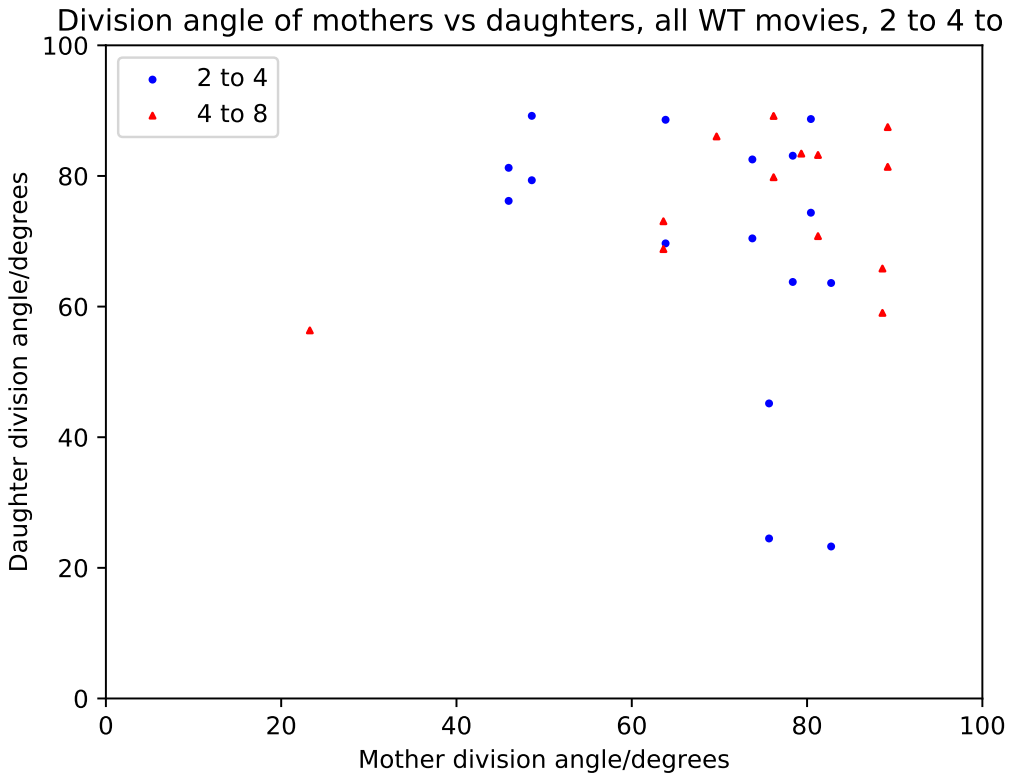

Figure 5.15: The division angle of daughter cells vs the division angle of their mother. The blue dots correspond to pairs of cells where the mother is one of the two cell stage cells. The red triangles correspond to pairs of cells where the mother is one of the four cell stage cells.

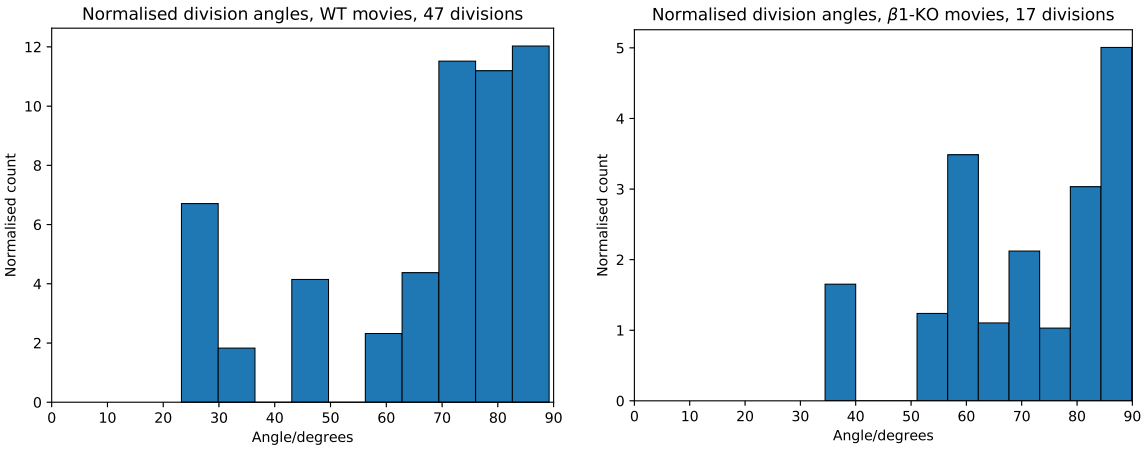

Figure 5.16: The distribution of division angles for WT (left) and β1-KO (right) movies. The actual count of division angles is divided by $\sin(\theta)$, resulting in a normalised count that is proportional to the probability density.

5.2.5 Number of neighbours

Two cells are defined as neighbours if any of their vertices lie within a cutoff radius r^{c} of each other, as demonstrated in Fig. 5.17. The dependence of the neighbour count on r^{c} is shown for a particular aggregate in Fig. 5.18. The optimum choice of r^{c} is subjective. However, we conclude from Fig. 5.18 that it should be between 0.01 and 0.1 of the cell diameter (taken to be the longest axis of the cell), hence we choose $r^{\mathrm{c}} = 0.05$ of the cell diameter.

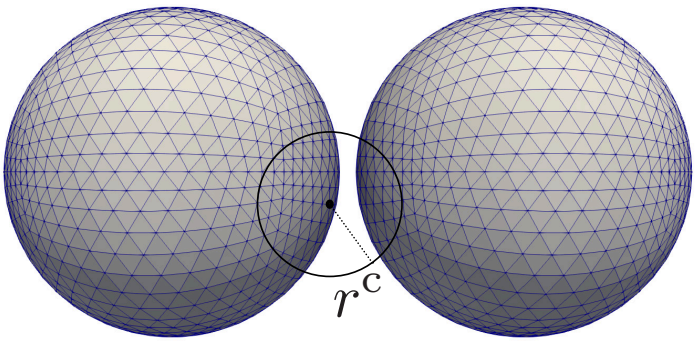

Figure 5.17: Two cells are neighbours if any of their vertices lie within r^{c} of each other.

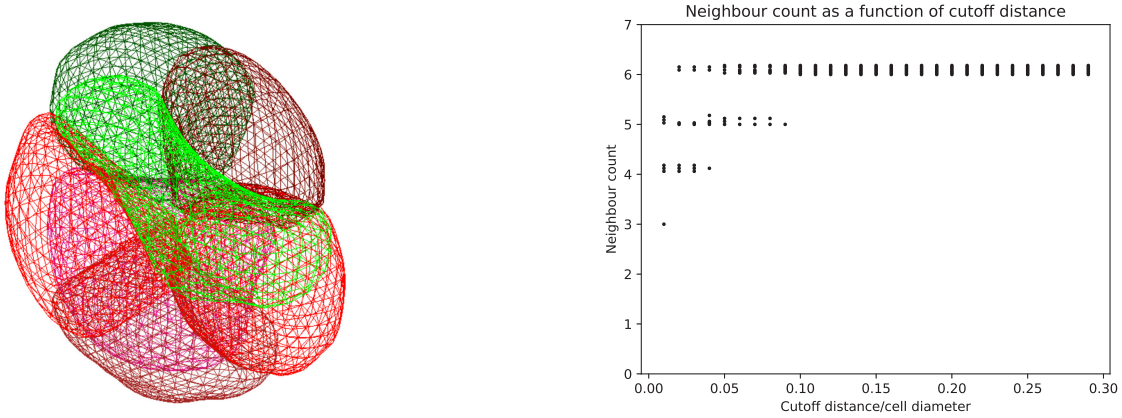

Figure 5.18: The sensitivity of the neighbour count to the cutoff radius, for the meshes shown on the left.

Plots of the number of neighbours of each cell in representative WT and β1-KO examples are shown in Figure 5.19. As a WT cell grows into a rosette, each cell gains a large number of neighbours (typically 4 or more). Cells with very few neighbours are rare. In contrast, β1-KO cells typically have fewer neighbours, and cells with < 2 neighbours are common. The presence of β1-KO cells with few neighbours is a result of the extended, branching structures β1-KOs form, e.g. in Fig. 5.7. Fig. 5.19 is a good example of the power of our 3D segmentation and analysis pipeline. Cell neighbour count is a conceptually simple variable that is almost impossible to measure from 2D representations of the experimental data, but easy to measure with segmented meshes. Further plots are shown in Fig. C.3.

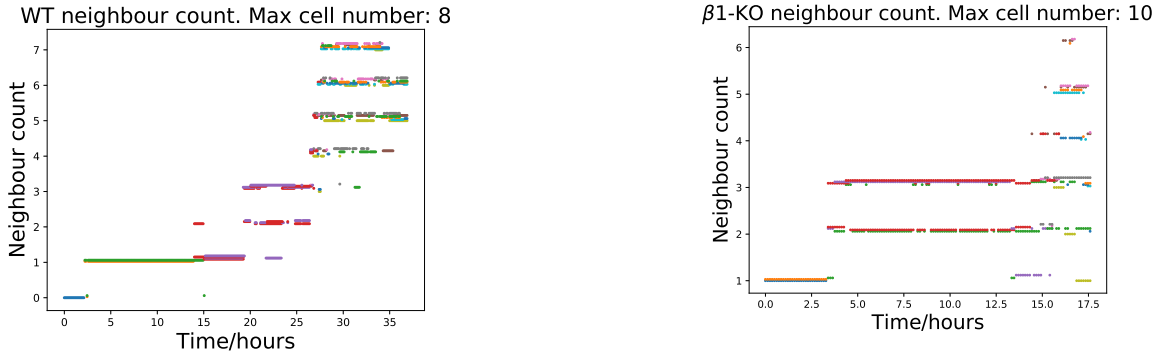

Figure 5.19: The number of neighbours each cell has as a function of time.

5.2.6 Ratio of areas

An important characteristic of a rosette is the large interfaces between neighbouring cells. The interfacial area is defined as any region of the cell surface within some cutoff length of any other cell. A schematic of this is shown in Fig. 5.20.

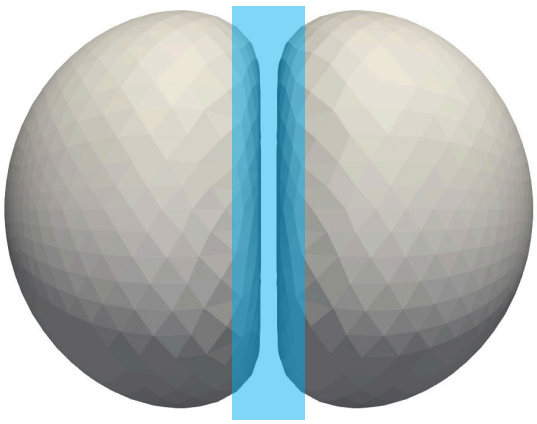

Figure 5.20: Φ is the ratio of the interfacial area (blue) to the total area of the cell.

Plots of the ratio of interface area to total area are shown for four movies of rosette formation in Fig. 5.21. In three of the four movies the interface area increases. In the fourth movie (bottom right), the cells have an unusually large interface at the 2 cell stage, and an unusually loose packing up to the 8 cell stage. I expect the ratio would increase at later times, however due to photobleaching it becomes difficult to segment the movie beyond the timepoints shown. Plots of this ratio for three β1-KO movies are shown in Fig. 5.22. In none of these movies does the ratio increase.

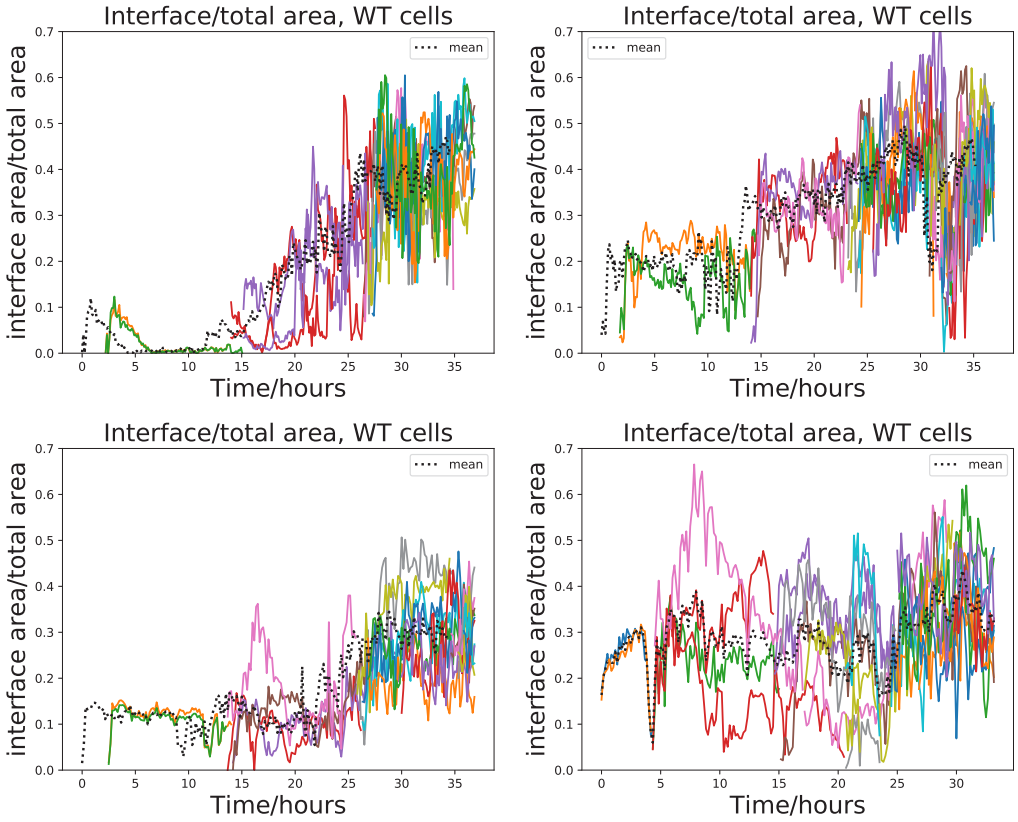

Figure 5.21: The ratio of interface area to total area for WT movies that form rosettes.

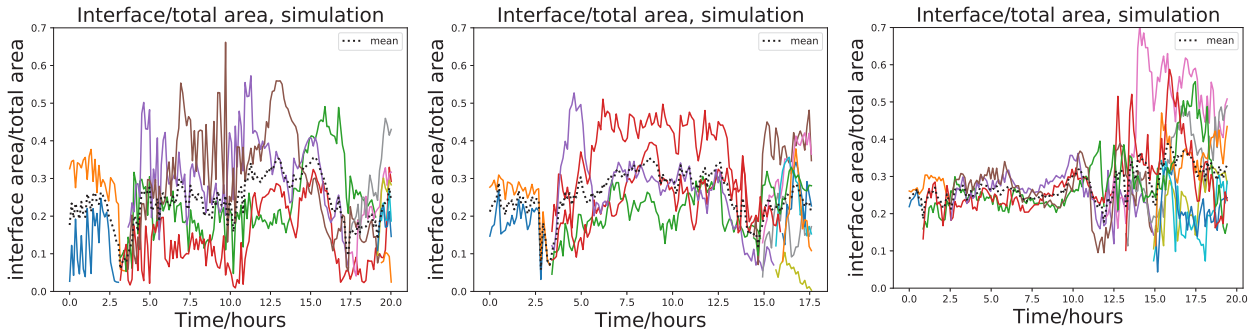

Figure 5.22: The ratio of interface area to total area for β1-KO movies.

The ratio of interface to total area combines two effects: changes in the number of neighbours a cell has, and changes in the size of the interface between neighbours. To disentangle these two, I measure the ratio of the interface area to total area of a cell, averaged over all neighbours. Writing this explicitly, for a cell with N neighbours, indexed by i, I measure

$$\Phi = \frac{1}{N} \sum_i \frac{A_i^{\mathrm{Int}}}{A^{\mathrm{Tot}}} \tag{5.2}$$

where A_i^{Int} is the interfacial area between the cell and neighbour i, and A^{Tot} is the total area of the cell. Plots of Φ for 4 WT rosettes (top two rows) and 3 β1-KO movies (bottom row) are shown in Fig. 5.23. These plots demonstrate that the increase in interfacial area in the WT movies is due to an increase in the number of neighbours each cell has.

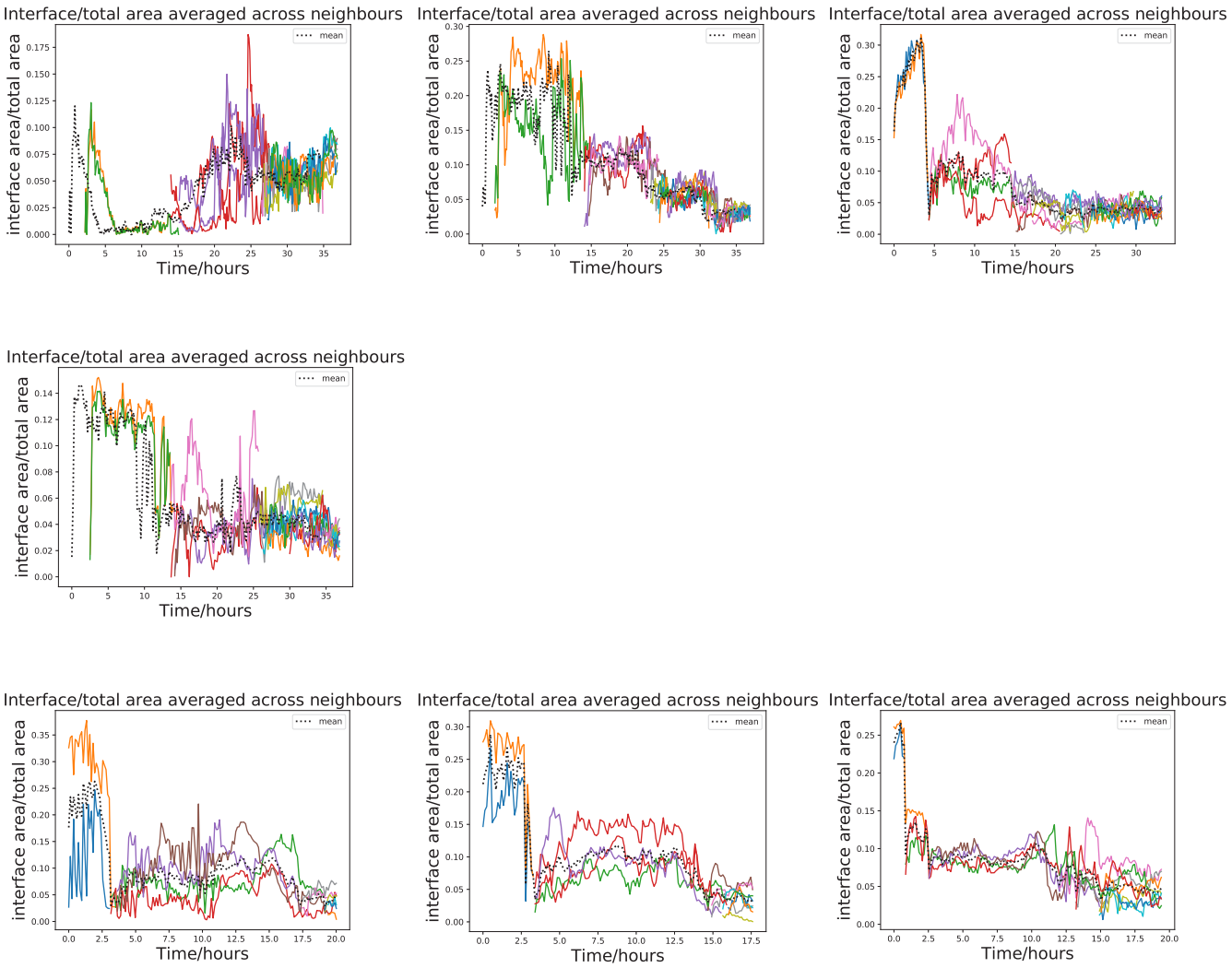

Figure 5.23: The ratio of interface area to total surface area, averaged over all neighbours. The top two rows are WT movies that form rosettes. The bottom row is β1-KOs.

The ratio Φ can be compared between WT and β1-KO movies at the two cell stage. This comparison is made for all two cell time points in Fig. 5.24. This figure demonstrates that β1-KOs tend to have a larger interface at the doublet stage.

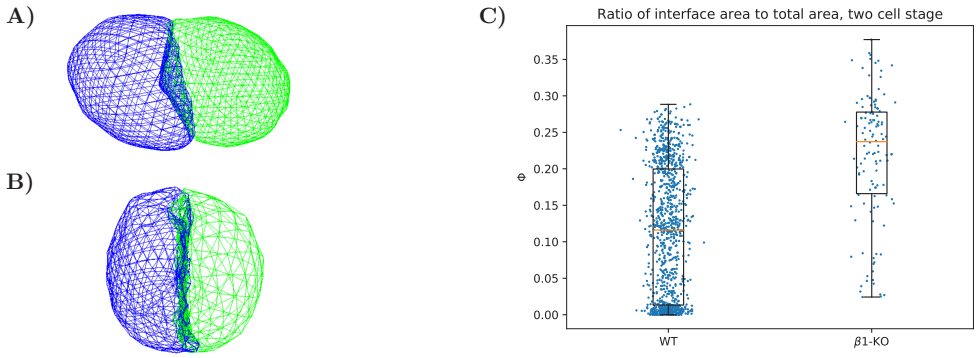

Figure 5.24: A) A typical example of a WT doublet. B) A typical example of a β1-KO doublet. C) The comparison of the ratio Φ, equal to the ratio of the interface area to total area of a cell, between WT and β1-KO movies.

5.2.7 Cell centres

The motion of the cell centres is plotted in Fig. 5.25 from the 6 cell stage onward, for representative examples of WT and β1-KO movies. Both examples demonstrate the dynamic nature of the aggregates. The cells are very mobile, as well as frequently changing shape and changing neighbours. The plots in Fig. 5.25 serve to illustrate the complex and noisy nature of the mESC system. The lack of a spherical, densely packed configuration is clear in the β1-KO example. More examples are shown in Fig. C.4. As well as highlighting the dynamic and stochastic nature of this system, these plots also highlight the lack of organised circular orbits observed in lumen forming aggregates of MDCK cells [206].

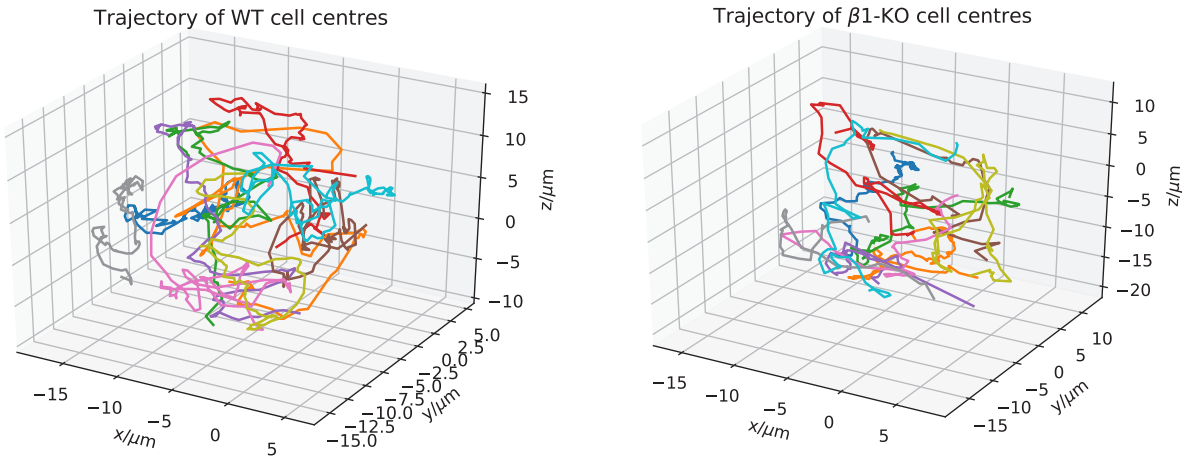

Figure 5.25: Representative examples of the cell centre trajectories from the 6 cell stage onward, for WT (left) and β1-KO (right) movies. The β1-KO movie is less compact and organised than the WT. Both plots demonstrate that the cells rearrange frequently.

5.2.8 Long axes

The long axis of a cell is defined as a line segment between the two most distant points on the cell surface. This is a variable with nematic symmetry, i.e. it has no front and back. It can be used as a measure of cell orientation. The long axis of a cell can be approximated by the long axis of its mesh, i.e. the line segment between the two mesh vertices that are furthest apart. An example of a segmented movie with overlayed long axes is shown in Fig. 5.26.

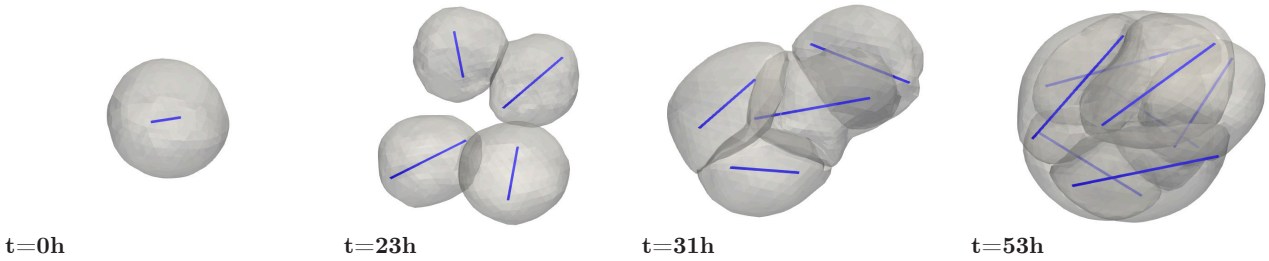

Figure 5.26: Stills from a segmented WT movie with long axes marked in blue.

The evolution of the distribution of long axes can be characterised by measuring their angular distribution with respect to the centre of the aggregate, as shown in Fig. 5.27. The evolution of the mean long axis angle (i.e. averaged over all cells in the aggregate) is shown for 4 WT movies that go from a single cell to a rosette in Fig. 5.28. The standard deviation of the long axis angle of these movies is shown in Fig. 5.29.

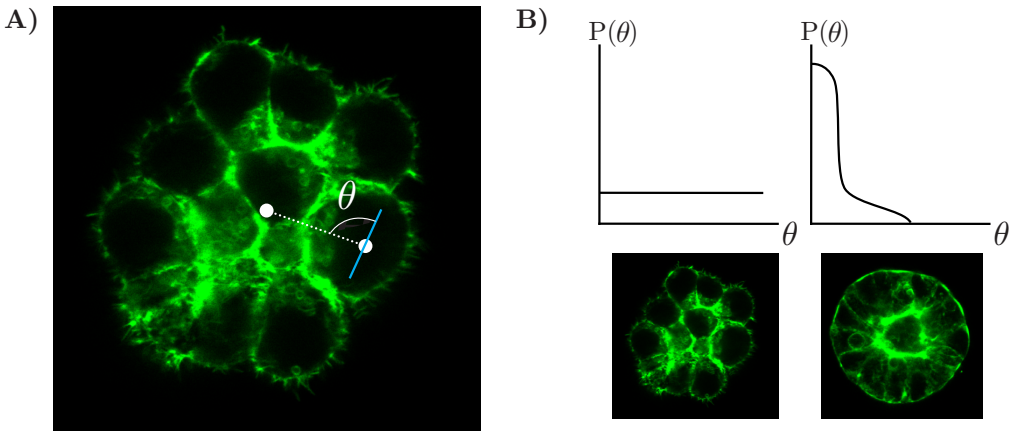

Figure 5.27: A schematic demonstrating the distribution of long angle axes. A) θ is defined as the angle between the long axis of the cell and the line connecting the centre of the cell with the centre of the aggregate. B) Schematic distributions for two aggregates. A random aggregate of cells will have an approximately uniform distribution, as shown on the left. A spheroid where the cells form a columnar epithelium, with the cell bodies elongated toward the centre, will have a narrower distribution peaked near 0, as shown on the right.

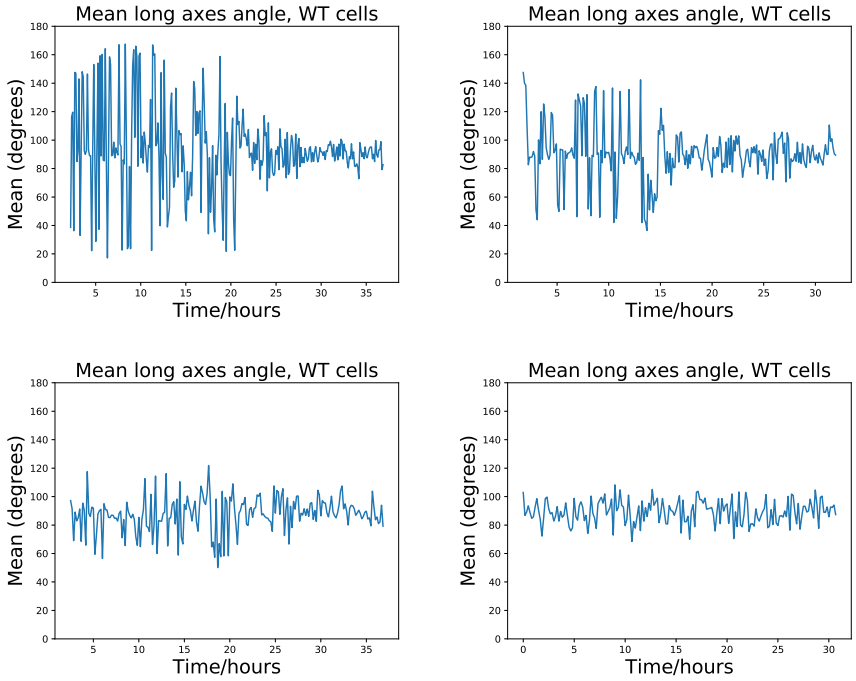

Figure 5.28: The evolution of the mean long axis angle of four movies that go from a single cell to a rosette.

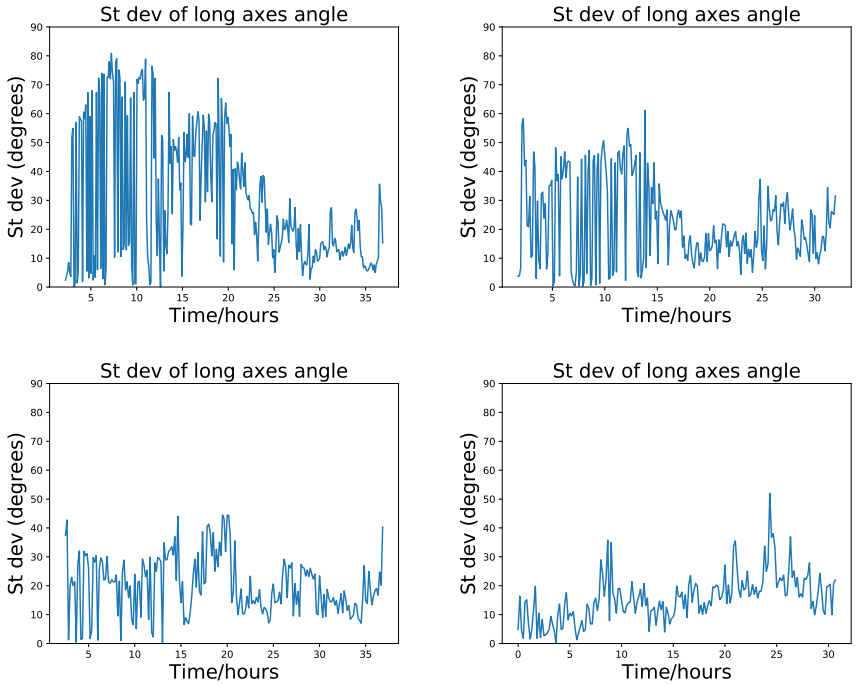

Figure 5.29: The evolution of the standard deviation of the long axis angle of four movies that go from a single cell to a rosette.

The mean and standard deviation of the long axis angle for three β1-KO movies is shown in Fig. 5.30 and Fig. 5.31, respectively. Qualitatively, WT cells grow into an ordered state, whereas β1-KOs grow into a disordered state. This is weakly on display in the long axis mean

and standard deviation plots. The WT mean angles either start at or transition to roughly 90°. In three of the four examples, there is also a decrease in the variation of the mean over time, and of the standard deviation between the first and second half of the movies. In contrast, the mean angle of the β1-KOs does not undergo any transition, varying between $\approx 60 - 120°$. In all three β1-KO examples, the standard deviation fails to decrease. More data is necessary to strongly support the claim that the WT movies undergo a transition from disordered to ordered state whereas the β1-KOs do not.

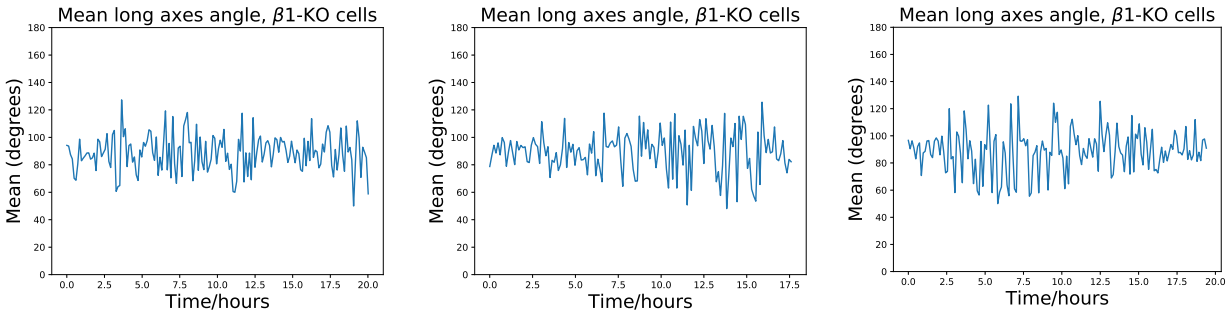

Figure 5.30: The evolution of the mean long axis angle of three β1-KO movies that fail to form rosettes.

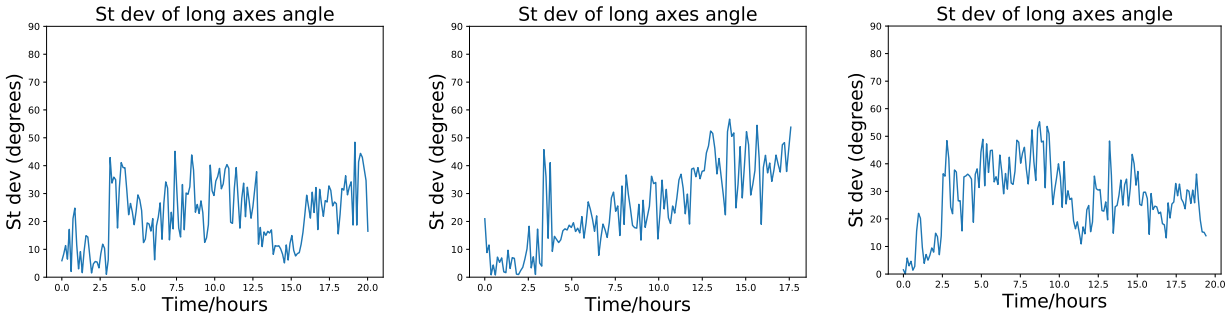

Figure 5.31: The evolution of the standard deviation of the long axis angle of three β1-KO movies that fail to form rosettes.

5.2.9 Polarity axes

For a cell with some scalar field, ϕ, defined on its surface (e.g. a chemical species number density), a polarity vector can be defined by

$$\mathbf{p} = \frac{1}{A} \oint dA \, \{\phi \hat{\mathbf{r}}\} \,, \tag{5.3}$$

where $\hat{r}_\alpha$ is a unit vector pointing from the centre of the cell to a point on the surface, and A is the total surface area of the cell. The integral is taken over the entire surface of the cell. As such, it is possible to measure a polarity vector from the fluorescence in a raw movie, assuming the fluorophore is attached to the chemical species of interest with a spatially uniform probability. However, in order to apply Eq. 5.3, systematic errors in the measurement of fluorescence intensity must be taken into account. Consider a movie, i.e. an array of intensity values, and a

set of vertices describing a time series of meshes, where the intensity values at the vertices are $\{\rho(x, y, z, t)\}$. The intensity curves in Fig. 5.32 are defined by

$$I_x(x') = \langle \rho(x = x', y, z, t) \rangle \tag{5.4}$$
$$I_y(y') = \langle \rho(x, y = y', z, t) \rangle \tag{5.5}$$
$$I_z(z') = \langle \rho(x, y, z = z', t) \rangle \tag{5.6}$$

where in the first line the average is taken over all y, z, and t, etc. In other words, Fig. 5.32 shows the fluorescence intensity as a function of x, y and z, averaged over all vertices in each x, y or z slice, and time averaged over a single WT movie. There is a clear bias in the z measurement: the fluorescence intensity at vertices in the upper half of the aggregate is higher than in the lower half. This is not unexpected, as the aggregate and the surrounding medium have some level of opacity. I assume the I_x and I_y curves are representative of the true signal. Consequently, I construct a scaling function, ϕ, by fitting an exponential to the ratio

$$\frac{I_x(r) + I_y(r)}{2I_z(r)} \tag{5.7}$$

where r is the distance away from the centre of the aggregate. An example of the above ratio, and the fitted scaling function, is shown in Fig. 5.33. I rescale the fluorescence intensities by $\phi(z)$. I.e., a movie $F(x, y, z, t)$, is scaled like $\phi(z)F(x, y, z, t)$. The curves described in Eq. 5.4-5.6 are shown for a scaled movie in Fig. 5.34. The z bias is removed.

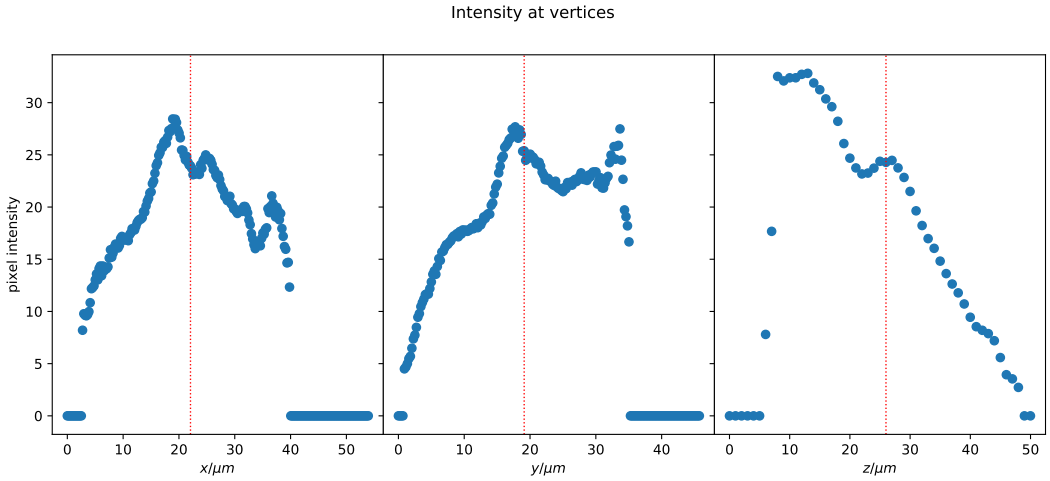

Figure 5.32: The intensity curves $I_x(x)$, $I_y(y)$ and $I_z(z)$ defined in Eq. 5.4-5.6. The time averaged centre of the aggregate is shown in red.

An alternative measure of the intensity bias in the z direction is the distribution of angles the polarity vector makes with the x, y, and z axes. A representative example from an unscaled movie is shown in Fig. 5.35. The polarity is strongly aligned with the z axis. The same distributions after scaling by ϕ are shown in Fig. 5.36, demonstrating that the z bias is significantly reduced. Further examples are shown in Appendix C.0.5.

Having corrected for z bias in the fluorescence intensities, polarity vectors can be calculated with Eq. 5.3. An example of a segmented WT E-cadherin movie with superposed polarity is shown in Fig. 5.37. In this, and all plots involving polarity, the arrow points from the basal to the apical domain. An example of a segmented β1-KO E-cadherin movie with superposed polarity is shown in Fig. 5.38. The WT polarities form a rosette, all pointing into the centre of

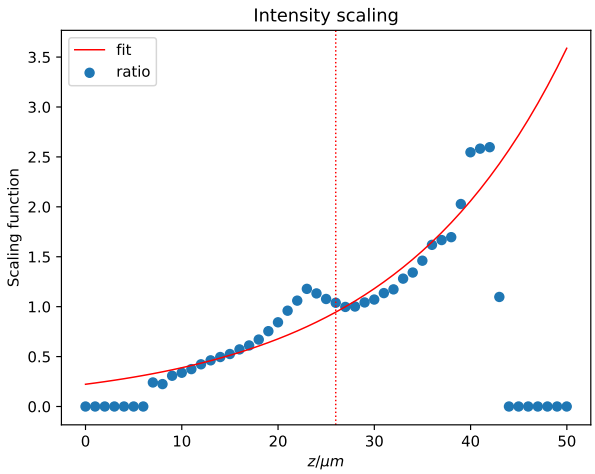

Figure 5.33: The intensity scaling function. In blue is the ratio in Eq. 5.7, and in red is the exponential curve fitted to the data points. The dashed red line marks the time averaged centre of the aggregate.

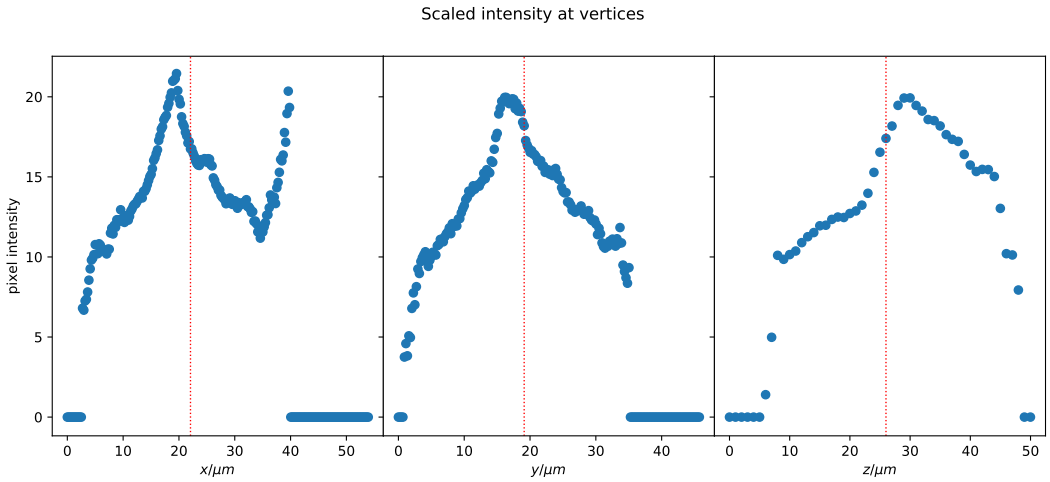

Figure 5.34: The intensity curves $I_x(x)$, $I_y(y)$ and $I_z(z)$ defined in Eq. 5.4-5.6, for a scaled movie. The time averaged centre of the aggregate is shown in red.

the aggregate. The β1-KO polarities do not. A polarity angle can be defined in the same way as with the long axes (see Fig. 5.27).

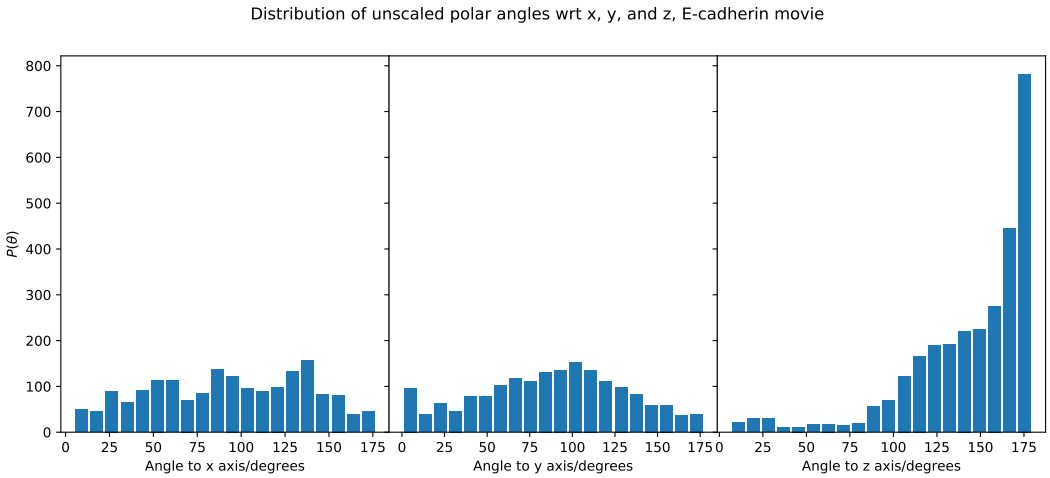

Figure 5.35: The distribution of angles between the polarity of an unscaled movie, measured by Eq. 5.3, and the x, y and z axes. There is a clear bias resulting in alignment with the z axis.

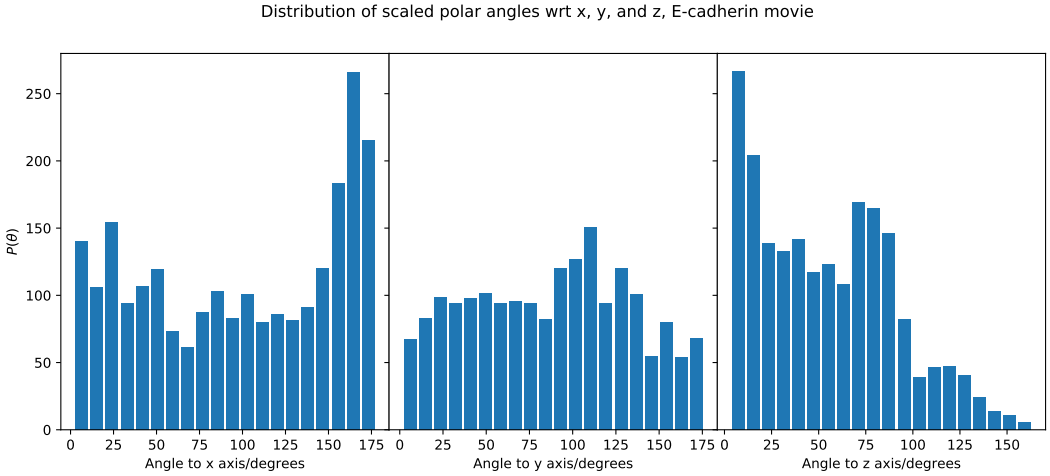

Figure 5.36: The distribution of angles between the polarity of a scaled movie, measured by Eq. 5.3, and the x, y and z axes. The z bias in Fig. 5.35 is gone.

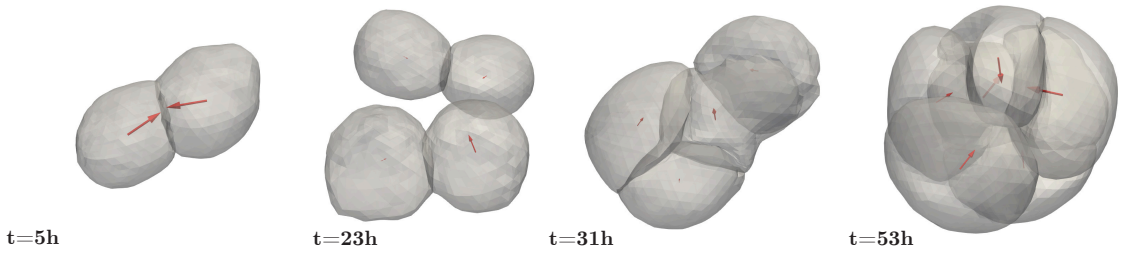

Figure 5.37: A segmented WT movie with E-cadherin polarity shown in red.

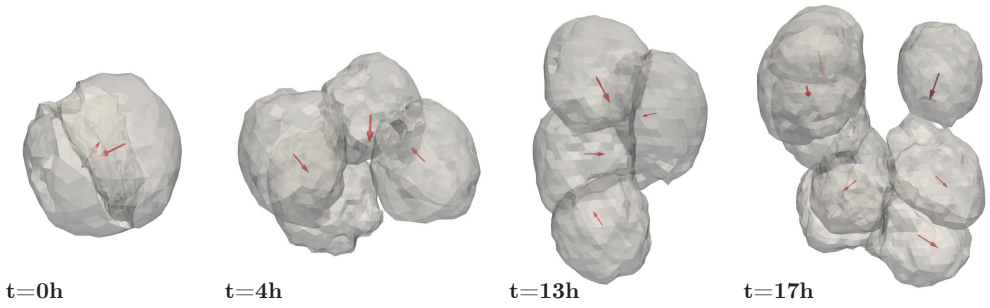

Figure 5.38: A segmented β1-KO movie with E-cadherin polarity shown in red.

A polarity angle can be defined with respect to the centre of the aggregate in the same way as the long axis angle described in Fig. 5.27. The evolution of this angle, averaged over all cells in the aggregate, is shown for 4 rosette forming WT movies in Fig. 5.39. The standard deviation of the polarity angle for the same movies is shown in Fig. 5.40. The mean and standard deviation of the polarity angle of 3 β1-KO movies are shown in Fig. 5.41, and Fig. 5.42. Both the mean and standard deviation of the β1-KOs increases near the end of the movies. This trend is absent in the WTs. It is difficult to observe any strong trends in the plots of the WT mean angle, however in 3 of the 4 examples the WT standard deviation either transitions from high to low values, or is initially low and stays that way. Much like the long axis angle, these plots weakly support my qualitative assertion that the WTs transition from a disordered to ordered state, whereas the β1-KOs fail to do so.

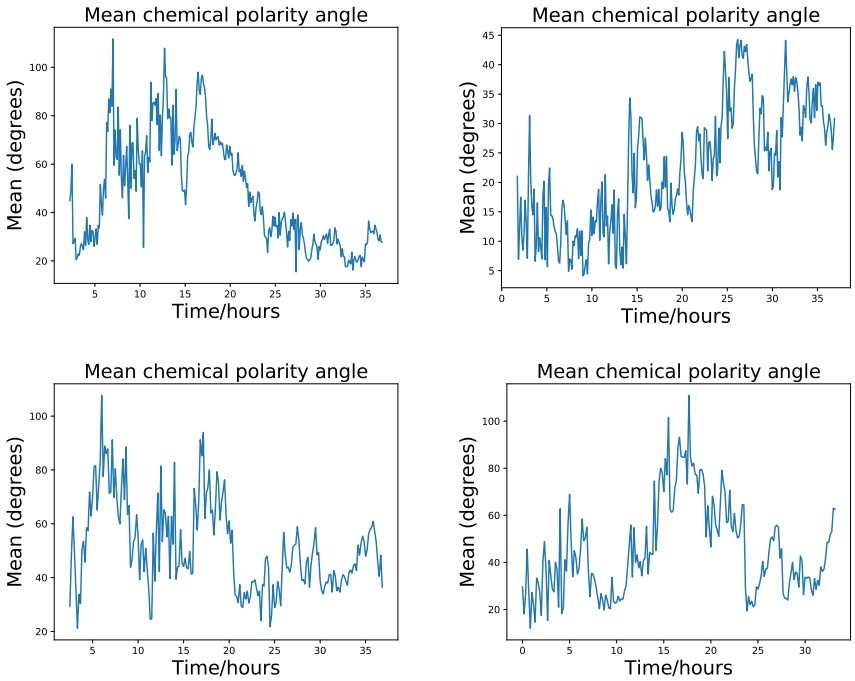

Figure 5.39: The evolution of the mean polar angle of four WT movies that go from a single cell to a rosette. The top two plots are E-cadherin movies, the bottom two are F-actin movies.

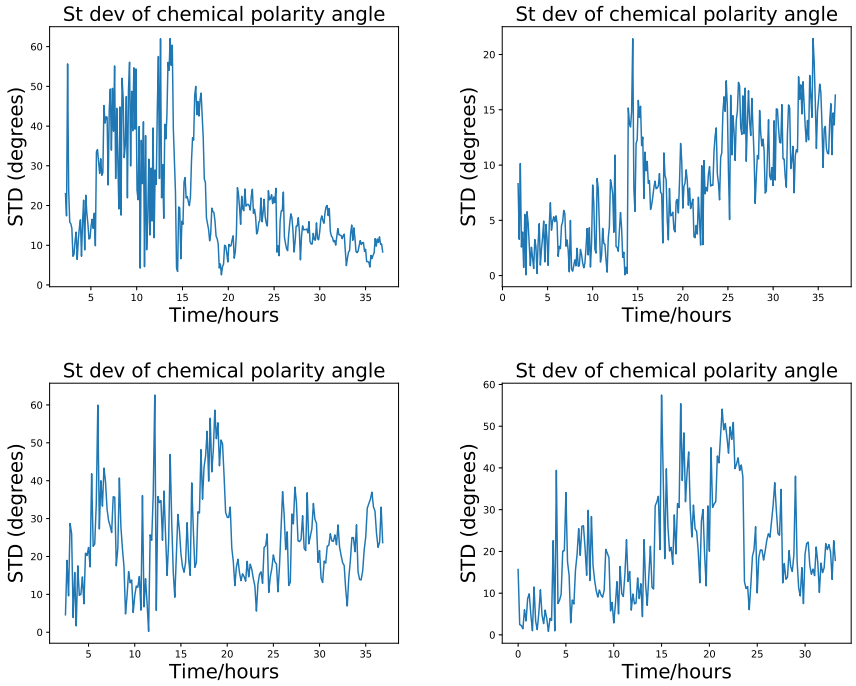

Figure 5.40: The evolution of the standard deviation of the polar angle of four movies that go from a single cell to a rosette. The top two plots are E-cadherin movies, the bottom two are F-actin movies.

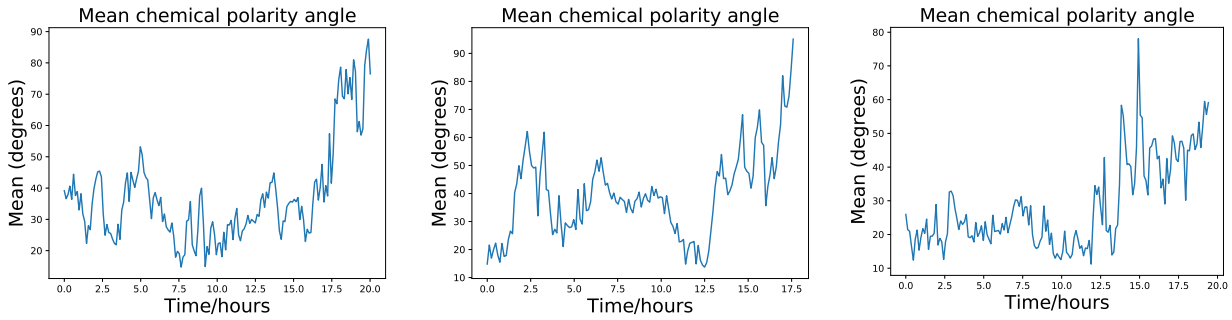

Figure 5.41: The evolution of the mean polar angle of three β1-KO movies that fail to form rosettes. All three are E-cadherin movies.

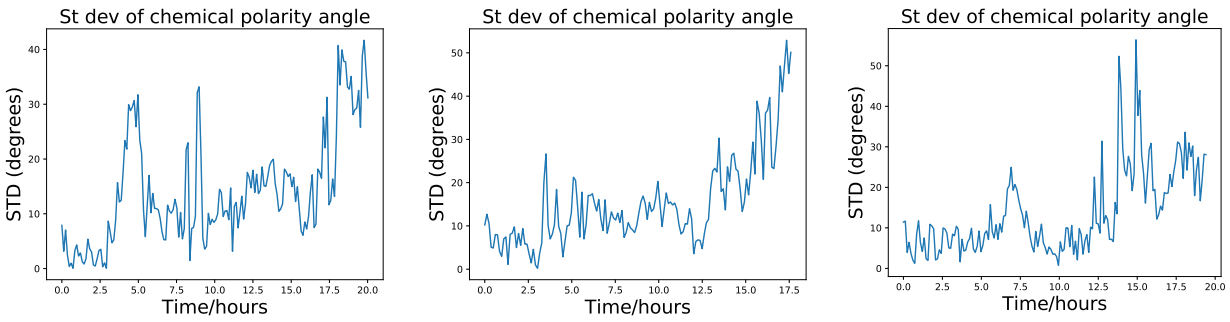

Figure 5.42: The evolution of the standard deviation of the polar angle of three β1-KO movies that fail to form rosettes. All three are E-cadherin movies.

5.2.10 The alignment of polarity with centre of mass connections

The relationship between polarity and the rearrangement of cells can be quantified with the angle, θ, between the polarity of a cell, and the line connecting the cell centre with the centre of its neighbour, as demonstrated in Fig. 5.43. The dynamics of θ are shown in Fig. 5.44 for an example WT movie where an extended configuration of cells transitions to a densely packed configuration. The trend is for angles greater than 90° to decrease, i.e. the polarity and centre of mass connection become more aligned as the cells rearrange.

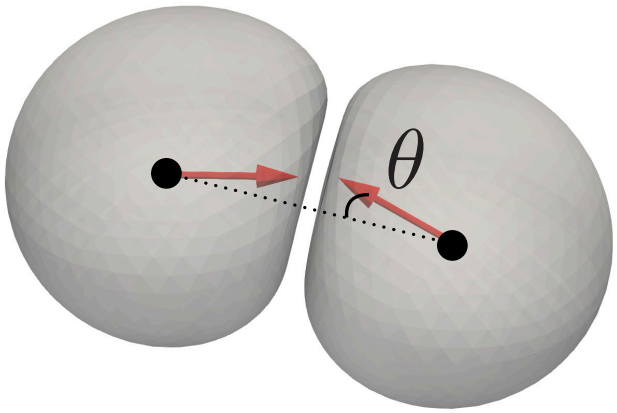

Figure 5.43: A schematic demonstrating the angle θ between the polarity of a cell, and the line connecting the centre of one cell to that of another. Low values of θ correspond to polarity aligned with the centre of mass connection.

As a concrete example of this process, consider the lower two cells in Fig. 5.45. At 6 hours, $\theta \approx 180°$ for the lower two cells, i.e. the polarity of the central cell is close to anti-parallel with the centre connection to the lower cell. At 10 hours, the cells have started to rearrange and θ decreases. By 15 hours, the cells have formed a ball, and $\theta \approx 45°$ for the left hand cell and its connection to the bottom cell.

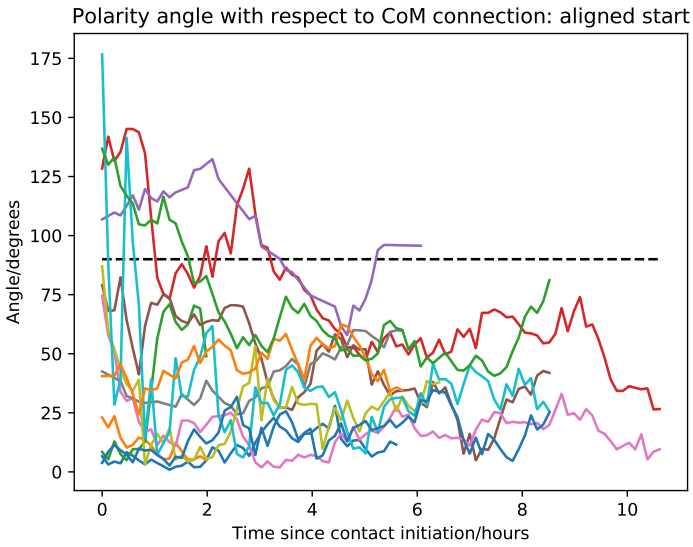

Figure 5.44: The angle between polarity and the line connecting neighbouring cell centres, for all neighbouring cells in a WT movie.

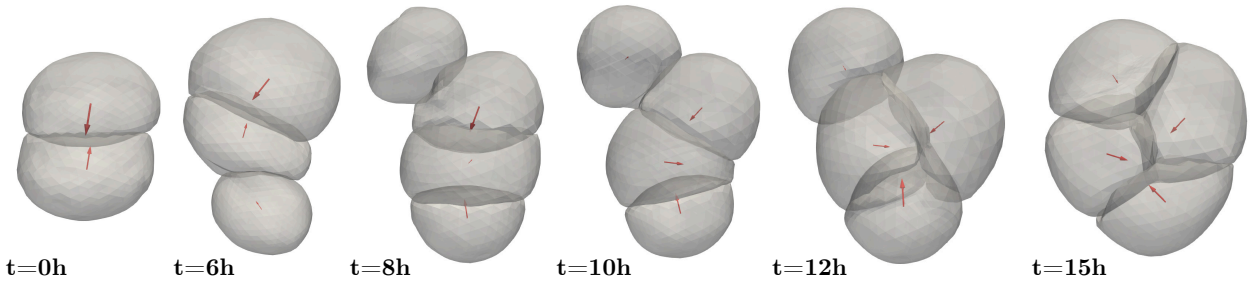

Figure 5.45: The segmented line to ball transition, with measured E-cadherin polarity in red.

How does θ evolve in the rest of my dataset? Measuring θ between all pairs of cells that come into contact with each other, across all WT and β1-KO movies, the trajectories can be categorised into 4 groups: those that start above 90° and end above 90°, those that start above 90° and end below, those that start below 90° and end above, and those that start start below 90° and end below. The proportions, and absolute numbers, of trajectories in each category for WT and β1-KOs are listed in Table 5.1. This summary shows that the majority of WT trajectories that start with $\theta > 90°$ transition to $\theta < 90°$. In contrast, the majority of β1-KO trajectories that start with $\theta > 90$ end with $\theta > 90$. This contrast reflects the failure of β1-KOs to transition to a densely packed rosette. Table 5.1 suggests an "error correction mechanism" that is absent in β1-KOs. Randomness in the orientation of cell divisions can place cells in an extended configuration away from the main body of the aggregate. In WT aggregates, this error is then corrected, and the cell brought into the densely packed structure. Such a correction does not take place in β1-KOs.

	WT	β1-KO	No. of WT trajectories	No. of β1-KO trajectories
$\theta > 90° \rightarrow \theta > 90°$	0.25	0.67	31	14
$\theta > 90° \rightarrow \theta < 90°$	0.75	0.33	94	7
$\theta < 90° \rightarrow \theta > 90°$	0.09	0.21	72	38
$\theta < 90° \rightarrow \theta < 90°$	0.91	0.79	753	141

Table 5.1

5.2.11 Summary of measurements

To summarise, the different growth dynamics of WT and β1-KO cells have been quantified by a number of variables. WT cells grow into aggregates that are densely packed, their cells undergo a transition from more to less spherical, and at late times they have high numbers of neighbours, organised long axes, and organised polarity vectors. The cells rearrange so as to decrease the angle between their polarity and the line connecting their centres to those of their neighbours. In contrast, β1-KO cells grow into extended aggregates, their cells do not change shape significantly, and at late times they have fewer neighbours, disorganised long axes, and disorganised polarity vectors. The cells do not reorganise to align their polarity with the line connecting their centre to that of their neighbours.

5.3 Summary

In this chapter I have described the methods used to quantify the movies resulting from mESC aggregate experiments performed by Ms. Weberling and Dr. Molé. I segmented the movies using the CNNs and active mesh plug-in developed by Dr. Smith. I then analysed the segmentations with a suite of Python analysis tools. This process has allowed me to make detailed measurements, at the single cell level, of the growth of mESC aggregates, for both WT and β1-KO cells. These measurements demonstrate the power of the segmentation and analysis pipeline developed by Dr. Smith and myself. The measurement of variables such as the number of neighbours each cell has, the size of cell-cell interfaces, or the trajectories of the cell centres, is hugely simplified by our mesh representation.

Chapter 6

A computational model of adhering cells

Computational models play a major role in biophysics, allowing researchers to study the behaviour of systems where analytic approaches are intractable (i.e. the vast majority of experiments). Three popular computational models of tissue mechanics are the Vertex Model, the Cellular Potts model, and the Phase Field Model. These three have been reviewed in Chapter 3. The cells in mESC aggregates are highly deformable, and pack together in dynamic 3D structures. Consequently, in order to accurately describe this system, and to be able to make quantitative comparisons with experiments, a new approach was necessary: one that could describe 3D cells with smooth surfaces, that could deform according to realistic dynamics, and that explicitly modelled adhesion forces.

6.1 The Spline Model: a 2D prototype

To address the mechanics of cellular aggregates, it was necessary to develop a computational model that was flexible with respect to the cells' geometry and topology, and explicitly included adhesion forces. Furthermore, in order to include the active surface physics described in Salbreux and Jülicher, we required the cell boundaries to have continuous second derivatives [164]. As a first step towards a general model, I developed the 2D Spline Model, so called because the cell boundaries are described as continuous spline curves.

6.1.1 An introduction to splines

A basis spline, or B-spline, of order d, is a parameterised curve $\mathbf{C}(u)$ of the form

$$\mathbf{C}(u) = \sum_{i}^{n} \mathbf{P}_i B_{i,d}(u), \tag{6.1}$$

where $u \in \mathbb{R}$, $\{B_{i,d}\}$ are the set of order d B-spline basis functions, and $\{\mathbf{P}_i\}$ are a set of n vectors, referred to as control points. The curve and all its derivatives up to $d-1$ are continuous [42]. $B_{i,d}$ are piecewise polynomials of order d. A 0^{th} order spline is simply the set of control points. A 1^{st} order spline is a linear interpolation between the control points. Higher order splines produce a smooth curve that approximately follows the control points, as shown in Fig. 6.1.

The parameterisation u is partitioned by an ordered set of "knots", $\{u_0, u_1, ..., u_m\}$ where $0 \leq u_i \leq 1$, and $m = n + d$. The basis functions can then be calculated recursively using the Cox-de Boor relation

$$\begin{aligned} B_{i,0}(u) &= 1 \quad u_i \leqslant u \leqslant u_{i+1} \\ &= 0 \quad \text{otherwise} \end{aligned} \tag{6.2}$$

$$B_{i,j}(u) = \frac{u - u_i}{u_{i+j} - u_i} B_{i,j-1}(u) + \frac{u_{i+j+1} - u}{u_{i+j+1} - u_{i+1}} B_{i+1,j-1}(u) \tag{6.3}$$

where $j = 1, 2, ..d$.

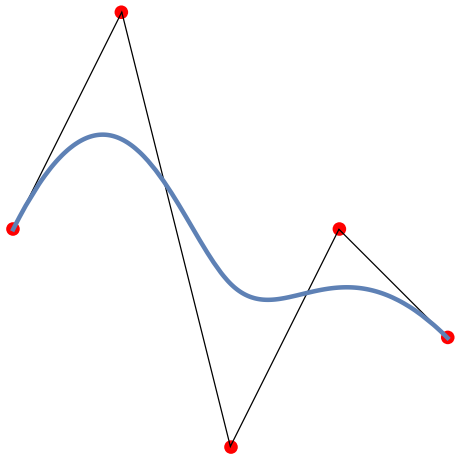

Figure 6.1: An example B-spline. The control points are shown in red, a linear interpolation between them in black, and the third order B-spline in blue.

$\mathbf{C}(u)$ has the desirable locality property that the position of the curve at any point is dependent on only the nearest $d+1$ control points. The "cardinal B-spline", $B_d^c(u)$, is constructed by selecting a uniformly spaced set of knots and applying the Cox-de Boor relation. Writing the 3rd order cardinal B-spline explicitly, we get

$$B_3^c(u) = \begin{cases} \frac{32u^3}{3} & 0 \leq u < \frac{1}{4} \\ \frac{1}{3}(-2)\left(48u^3 - 48u^2 + 12u - 1\right) & \frac{1}{4} \leq u < \frac{1}{2} \\ \frac{2}{3}\left(48u^3 - 96u^2 + 60u - 11\right) & \frac{1}{2} \leq u < \frac{3}{4} \\ \frac{1}{3}(-32)\left(u^3 - 3u^2 + 3u - 1\right) & \frac{3}{4} \leq u \leq 1 \\ 0 & \text{otherwise} \end{cases} \tag{6.4}$$

Using $B_d^c(u)$ it is possible to construct a closed curve

$$\mathbf{X}(u) = \sum_i^n \mathbf{P}_i B_{i,d}^p(u), \tag{6.5}$$

where $B_{i,d}^p(u)$, the periodic B-spline, is defined

$$B_{i,d}^p(u) = B_d^c\left(\frac{nu - (i-1)}{d+1}\right) \quad d < i < n - d + 1 \tag{6.6}$$

$$B_{i,d}^p(u) = B_d^c\left(\frac{nu - (i-1)}{d+1}\right) + B_d^c\left(\frac{nu - (i+n-1)}{d+1}\right) \quad 1 \leqslant i \leqslant d \tag{6.7}$$

$$B_{i,d}^p(u) = B_d^c\left(\frac{nu - (i-1)}{d+1}\right) + B_d^c\left(\frac{nu - (i-n-1)}{d+1}\right) \quad n - d + 1 \leqslant i \leqslant n \tag{6.8}$$

Intuitively, the periodic B-spline is constructed by wrapping d control points around the beginning/end of the curve. In the central region of the curve, a periodic spline is dependent on the control points in an identical way to an open spline, as described in Eq. 6.6. Near the beginning or end of the curve, the periodic spline combines control points from the beginning and end of the list of control points, as demonstrated in Eq. 6.7 and 6.8. An example of such a closed curve is shown in Fig. 6.2.

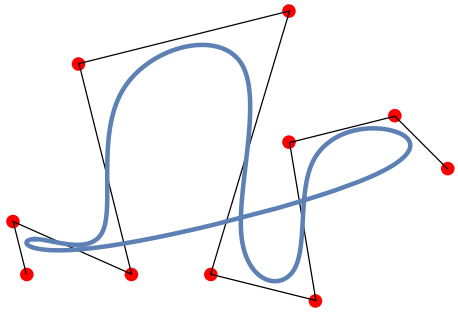

Figure 6.2: An example periodic B-spline. The control points are shown in red, a linear interpolation between them in black, and the third order periodic B-spline in blue.

6.1.2 Geometric properties of splines

Various geometric properties of the curve $\mathbf{X}(u)$ can be written in terms of $B^p_{i,d}$ and the control points. Note that from here on the subscript $d = 3$ on $B^p_{i,d}$ will be implicit. The length of the curve is given by

$$L = \int_0^L ds = \int_0^1 \frac{ds}{du} du. \tag{6.9}$$

The variable s is the proper length along the curve, whereas u is a parameterisation running from 0 to 1. The two are linked by

$$\begin{aligned} \frac{ds}{du} = |\partial_u \mathbf{X}| &= \left| \sum_{i=1}^{n} \mathbf{P}_i B_i^{p\prime}(u) \right| \\ &= \left[\sum_{i,j} \mathbf{P}_i \cdot \mathbf{P}_j B_i^{p\prime}(u) B_j^{p\prime}(u) \right]^{\frac{1}{2}}. \end{aligned} \tag{6.10}$$

The function

$$g_{\frac{1}{2}}(u) = \frac{ds}{du} = \left[\sum_{i,j} \mathbf{P}_i \cdot \mathbf{P}_j B_i^{p\prime}(u) B_j^{p\prime}(u) \right]^{\frac{1}{2}}, \tag{6.11}$$

is related to the metric $g(u)$ by $g(u) = \left(g_{\frac{1}{2}}(u)\right)^2$. Consequently, the length of the curve can be written

$$L = \int_{u=0}^{1} du \left[\sum_{i,j} \mathbf{P}_i \cdot \mathbf{P}_j B_i^{p\prime}(u) B_j^{p\prime}(u) \right]^{\frac{1}{2}}. \tag{6.12}$$

The area enclosed by the spline is given by

$$A = \frac{1}{2} \oint ds \mathbf{X}(s) \cdot \hat{\mathbf{n}}(s), \tag{6.13}$$

where $\hat{\mathbf{n}}(s)$ is the normal vector. Eq. 6.13 is the summation of triangular area elements with one side of length ds and one side of length $\mathbf{X}(s) \cdot \hat{\mathbf{n}}(s)$. The normal vector can be related to the tangent vector, $\hat{\mathbf{t}} = \partial_s \mathbf{X}$, by $n_\alpha = \epsilon_{\alpha\beta} t_\beta$, where $\epsilon_{\alpha\beta}$ is the Levi-Civita tensor. Consequently, the area is

$$A = \frac{1}{2} \epsilon_{\alpha\beta} \sum_{ij} P_{i\beta} P_{j\alpha} \left[\int_{u=0}^{1} B_i^{p\prime}(u) B_j^p(u) \right]. \tag{6.14}$$

Having written the length and area of the curve in terms of the spline basis functions and control points, it is now possible to construct a physical model of a cell with boundary $\mathbf{X}(u)$.

6.1.3 A physical model of a single cell

Let $\mathbf{X}(u)$ describe the boundary of a cell. The motion of the boundary is determined by the dynamics of the control points, which in the low Reynolds number limit read,

$$\gamma_p \frac{dP_\alpha^i}{dt} = f_\alpha^i = -\frac{\partial W}{\partial P_\alpha^i}, \tag{6.15}$$

where γ_p is a drag coefficient, and f_α^i is the force acting on the i^{th} control point. The effective work function, W, is

$$W = \frac{K}{2}(A - A_0)^2 + \gamma L, \tag{6.16}$$

where γ is the line tension of the boundary, and K is a bulk compressibility. A_0 is a preferred cell area. Eq. 6.15 and 6.16 are very similar to the description of a Vertex Model [5]. The Spline Model retains the computational efficiency of a Vertex Model in that the positions of a finite number of points are updated at each timestep, while allowing for a more flexible description of the cell boundary as a smooth curve.

There are two major simplifications inherent in this description of a cell. The various drag forces on the boundary of the cell, from the surrounding fluid, and internal cellular processes, are approximated as a single, constant drag coefficient on each control point, γ_p. Secondly, the role of pressure is overlooked, in favour of a phenomenological preference for an area A_0, with strength K.

6.1.4 Adhesion forces

A key goal of developing the Spline Model was to explicitly include adhesion forces, in contrast to the Vertex Model. In biological cells, adhesion forces are mediated by the formation of intercellular bonds between cadherin proteins, which obey a catch-bond force law [91] [24]. In order to avoid a complex and computationally expensive description of cadherin dynamics, adhesion forces are included in the Spline Model via the phenomenological Morse potential. For two particles separated by a distance r, the Morse potential is defined

$$u(r) = D(1 - e^{-a(r - r_m)})^2 - D, \tag{6.17}$$

with parameters D, a and r_m. The force between the particles is $f_\alpha^{\text{int}} = -\frac{du}{dr}$. The Morse potential, plotted in Fig. 6.3, results in long range attractive, and short range repulsive forces. As such, $u(r)$ describes both adhesion forces and steric repulsion between neighbouring cells. D determines the strength of the forces, a the width of the potential well, and r_m the minimum of the potential, i.e. the preferred distance between the two particles.

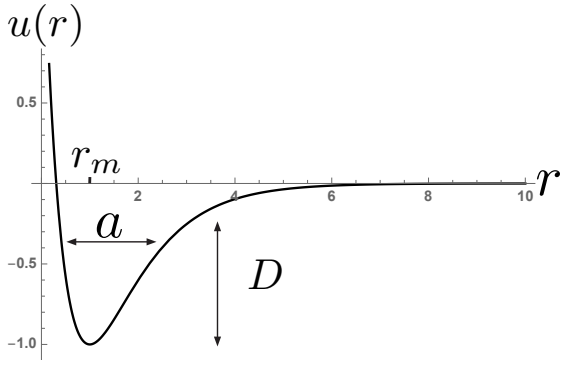

Figure 6.3: The Morse potential, with parameters labelled.

Consider two cells, with control points $\{\mathbf{P}_i\}$ and $\{\mathbf{Q}_i\}$, with boundaries

$$\mathbf{X}_1(u) = \sum_{i=1}^{n} \mathbf{P}_i B_i^p(u) \tag{6.18}$$

$$\mathbf{X}_2(u') = \sum_{j=1}^{n} \mathbf{Q}_j B_j^p(u'), \tag{6.19}$$

and point-wise interaction potential $u(r)$, where $r = |\mathbf{X}_1(u) - \mathbf{X}_2(u')|$. The force acting on control point $\mathbf{P}_i$ is

$$f_\alpha^i = -\int_0^L \int_0^L ds ds' \left\{ \frac{du(s,s')}{dP_\alpha^i} \right\} \tag{6.20}$$

$$= -\int_0^1 \int_0^1 d\nu d\nu' \left\{ g_{\frac{1}{2}}(\nu) g_{\frac{1}{2}}(\nu') \frac{2aD}{r} \left(e^{-a(r-r_m)} - e^{-2a(r-r_m)} \right) \sum_j \left[P_\alpha^j B_i^p(\nu) B_j^p(\nu) - Q_\alpha^j B_i(\nu) B_j(\nu') \right] \right\} \tag{6.21}$$

A set of adhering cells can be simulated by combining the internal forces described by Eq. 6.16 and the above adhesion force. However, there is a question of stability. Consider the doublet of cells shown in Fig. 6.4. The distance between the interfacial surfaces is $\approx r_m$, and the interaction potential is negligible outside of this region. Consequently, the effective work is

$$W = -DL_{\text{Int}}^2 + \sum_{i=1}^{2} \left\{ \frac{K}{2}(A^i - A_0)^2 + \gamma L_{\text{ECM}}^i + \gamma L_{\text{Int}} \right\}. \tag{6.22}$$

It becomes energetically favourable for the interface to grow indefinitely if $\gamma - DL_{\text{Int}} < 0$, i.e. the interface will buckle. Biological cell doublets demonstrate a wide variety of shapes, with large interfaces, without buckling. There are two realistic options for stabilising interfaces

in the Spline Model: including either elasticity, or bending rigidity, in the description of the cell boundary. The actin cortex is known to demonstrate both elasticity and bending rigidity [163]. We chose to include elasticity only. It is unphysical for the cortex to exhibit elasticity on timescales longer than the actin turnover time of approximately 10s, i.e. much shorter than the timescale of cell shape deformations. However, we made the decision to include elasticity and not bending rigidity for two reasons. Firstly, the extent to which the cell boundaries are elastic or rigid will have a secondary impact on the cell shapes, compared with the surface tension and adhesion strength. The main impact of elasticity or rigidity is to stabilise the buckling instability. Secondly, the 2D Spline Model is a prototype. Our goal in developing it was to demonstrate the plausibility of a model where cells had smooth boundaries and explicit adhesion forces. As such, simplicity and speed of development were prioritised over realism in this instance. Modelling the cell boundary as an elastic material has a further computational benefit in that it stops the control points getting too close together. Without elastic forces, gradients in the surface tension result in a flow of control points from regions of low tension to regions of high tension. Consequently, in regions of low tension, the spline has very few control points, with a resulting loss of fine control of the curve shape.

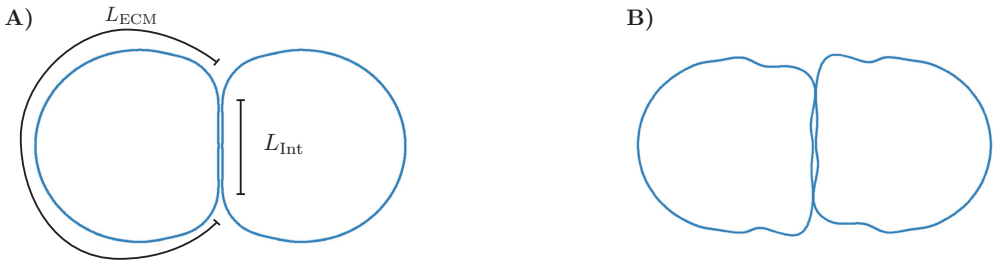

Figure 6.4: A) the geometry of a stable doublet, with the interfacial length L_{Int}, and length of boundary in contact with the ECM, L_{ECM}, labelled. B) the buckling instability that arises when $2\gamma - DL_{\mathrm{int}} < 0$.

6.1.5 An elastic cell boundary

The elastic energy of a curve parameterised by u is defined with respect to a reference state. This state is taken to be a curve of length L with uniformly spaced control points. The metric of the reference state is $g_0 = L^2$. The elastic energy of a curve with metric g is then

$$F_{\mathrm{el}} = \int_0^1 f_{\mathrm{el}} du = \int_0^1 du \left\{ \frac{\kappa\sqrt{g}}{2} \left(\frac{g - g_0}{g_0} \right)^2 \right\}, \tag{6.23}$$

where κ is the elastic constant. The elastic force on a control point is

$$f_{i\alpha} = -\frac{dF_{\mathrm{el}}}{dP_{i\alpha}} = -\int_0^1 du \left\{ 2P_{k\alpha} B_k^{p\prime}(u) B_i^{p\prime}(u) \left[\frac{\kappa\sqrt{g}}{g_0} \left(\frac{g - g_0}{g_0} \right) + \frac{\kappa}{4g^{\frac{1}{2}}} \left(\frac{g - g_0}{g_0} \right)^2 \right] \right\}. \tag{6.24}$$

6.1.6 Cell divisions

Cell divisions are included by choosing a random angle $\theta \in [0, 2\pi)$, and splitting the cell along a line through the centre with θ the angle of orientation to an arbitrary axis. New control points

are placed on either side of this line, separated by a distance r_m. The cell lifetime is chosen from a normal distribution, truncated at zero.

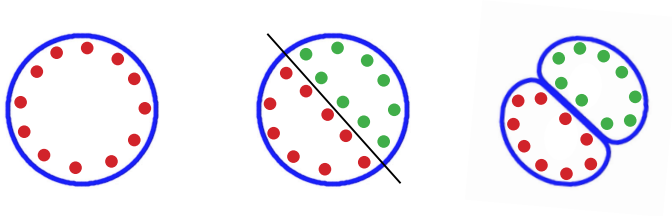

Figure 6.5: A schematic demonstrating the process of cell division. A random division line is selected, and new control points placed along either side of it. The two semi-circular cells are then allowed to relax.

6.1.7 Cell-cell intersection

The short range repulsive forces due to the Morse potential do not diverge as $r \to 0$. Consequently, it is possible for the cells to intersect. In order to push two cells apart when they have intersected, it is necessary to determine both the distance between two interacting points, and whether the cells are intersecting. Consider the force between two points on different cells, $\mathbf{x}^1$ and $\mathbf{x}^2$, separated by a distance r. It is necessary to determine whether $\mathbf{x}^2$ lies within the boundary of cell 1. This can be achieved by the method of ray casting: draw a straight line from $\mathbf{x}^2$ to infinity in any direction. Count how many times this line crosses the boundary of cell 1. If it crosses an even number of times, $\mathbf{x}^2$ lies outside of cell 1. If it crosses an odd number of times, $\mathbf{x}^2$ lies within cell 1.

6.1.8 Improving computational efficiency

Pairwise interactions

Consider a set of cells, the surfaces of which are discretised into a total of N points. Calculating interactions between all pairs of points requires $O(N^2)$ operations. This is the most costly process in each timestep of the Spline Model. We have introduced a number of methods to improve the efficiency of the calculation.

First, we approximate the force between any points separated by a distance $r > r_c$ to 0. The cut off r_c was typically chosen to be approximately $r_m + 3a$. Second, all points are assigned "grid coordinates" as well as their actual coordinates. Grid coordinates are a coarse discretisation of the 2D plane, where the size of a grid cell is taken to be r_c, as demonstrated in Fig. 6.6 [217]. If two points' x or y grid coordinates differ by more than 1 the interaction force between them is taken to be 0. The grid coordinates of every point are recalculated once at least one point has moved a distance $0.9r_c$. Evaluating the difference in grid coordinates is quicker than evaluating the true distance between points, and needs to be done only once between each recalculation of the grid. All pairwise distances must be calculated between points that lie within one grid cell of each other. We increase the efficiency of this calculation by storing the identity of nearest neighbours. If at time t a set of points $s = \{\mathbf{x}^i\}$ are within r_c of the point $\mathbf{x}^1$, at time $t + \Delta t$ we update s by conducting a search only over points that are in the vicinity of the points in s.

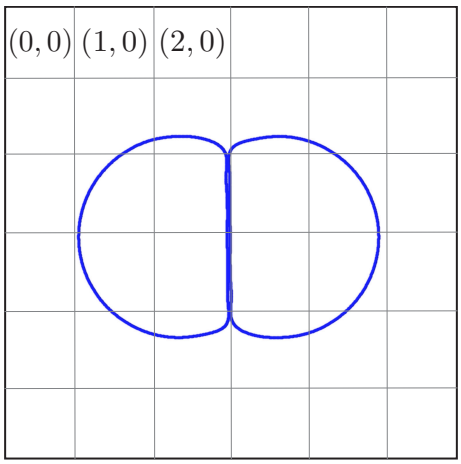

Figure 6.6: A schematic of the grid coordinate system, with cells $(0,0)$, $(1,0)$ and $(2,0)$ labelled. The system is divided into a coarse set of discrete cells. Interactions are only calculated between points that lie within one grid cell of each other.

Detecting interpenetration

The main drawback to ray tracing is that it is computationally inefficient. An exhaustive search over all the points in the discretised boundary of cell 1 is necessary to determine the crossing number of the ray. Calculating interactions between all points on all cell surfaces takes $O(N^2)$ operations, where N is the number of points in the system. Calculating a ray crossing number for each pair of points increases the number of operations to $O(N^3)$.

Instead of using ray tracing for all pairs of points, we instead use a heuristic measure of interpenetration for the majority of cases. We assume that in most instances the cells will be convex. In most cases where the cells do not interpenetrate, the vector between two points, $\mathbf{x}^1$ and $\mathbf{x}^2$ that lie within r^c of each other, lies within 90° of the outward normals at $\mathbf{x}^1$ and $\mathbf{x}^2$, i.e. the vector $\mathbf{x}^2 - \mathbf{x}^1$ is within 90° of the normal at $\mathbf{x}^1$, and the vector $\mathbf{x}^1 - \mathbf{x}^2$ lies within 90° of the normal at $\mathbf{x}^2$. This situation is demonstrated in Fig. 6.7 A. An example of when this measure fails is shown in Fig. 6.7 B. If $\mathbf{x}^2 - \mathbf{x}^1$ is within 90° of the normal at $\mathbf{x}^1$, and $\mathbf{x}^1 - \mathbf{x}^2$ is within 90° of the normal at $\mathbf{x}^2$, we consider the cells to be separated. This is the case in the vast majority of point pairs. If either condition fails, we check for interpenetration by ray tracing.

Parallelisation

We achieved further improvements to the speed of the code by using the shared memory parallel computing library OpenMP. OpenMP enables the creation of multi-threaded C++ programmes, i.e. programmes where multiple processing units can perform calculations on variables stored in shared memory. Such programmes benefit from the significant performance improvement afforded by parallelisation, while avoiding the complex programming obstacles of writing truly parallelised code with distributed memory. The simplicity of programming with OpenMP is demonstrated in the code snippet below, where adding a single line `pragma` command parallelises the for loop.

```
// Standard C++ for loop
for(int i=0; i<100; i++)
{
```

Figure 6.7: A schematic of the heuristic method of determining whether two cells interpenetrate. As demonstrated in A), if the vector $\mathbf{x}^2 - \mathbf{x}^1$ makes an angle less than 90°with the normal at $\mathbf{x}^1$, and vice versa, the two points are (probably) not interpenetrating. An example of when this method fails is shown in B).

```
        // Do something
}

// C++ for loop parallelised with OpenMP
#pragma omp parallel for private(i)
for(int i=0; i<100; i++)
{
        // Do something
}
```

Calculating the forces on N control points can be parallelised into up to N threads. The nodes of the Crick computing cluster can handle up to 32 threads, hence the performance benefits from OpenMP are significant.

To summarise, the 2D Spline Model consists of a set of cells, the boundaries of which evolve due to forces acting on their control points. The forces are the gradients of an effective work function, which contains line tension and bulk compressibility (Eq. 6.16), elasticity (Eq. 6.23), and adhesions (Eq. 6.21). The cells can divide by placing new control points along a randomly oriented division line. The evolution of the system is calculated with a fixed time step Euler integration routine, that makes use of the various performance improvement techniques detailed above.

6.2 Results of the 2D Spline Model

The steady state shape of a system of N_c cells is given by minimising the effective work

$$W = \sum_i^{N_c} \left\{ \frac{K}{2}(A - A_0)^2 + \gamma L + \int_0^1 du \left[\frac{\kappa\sqrt{g}}{2} \left(\frac{g - g_0}{g_0} \right)^2 \right] + \frac{1}{2} \int_0^1 d\nu \int_0^1 d\nu' \left[g_{\frac{1}{2}}(\nu) g_{\frac{1}{2}}(\nu') u(r(\nu, \nu')) \right] \right\}. \tag{6.25}$$

A dimensionless parameter, $\Xi = \frac{Da}{\gamma}$, can be constructed that controls the shape of the cell aggregate. The effect of varying Ξ on the shape of a doublet is shown in Fig. 6.8. At large Ξ,

adhesion forces dominate and the cells become more semi-circular. At low Ξ, surface tension dominates and the cells round up. As a rough measure of the computational efficiency of the Spline Model, each simulation in Fig. 6.8 took approximately 5 minutes to reach steady state on a personal laptop. Cell aggregates can be grown by starting with a single cell, and allowing repeated rounds of cell division. Such a simulation is shown in Fig 6.9. This simulation took approximately 10 hours on a node of the Crick computing cluster.

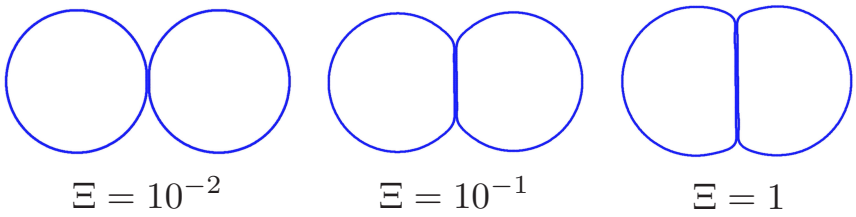

Figure 6.8: The effect of increasing Ξ. At low Ξ, surface tension dominates and the cells stay close to circular. At high Ξ, adhesion dominates and a large interface forms.

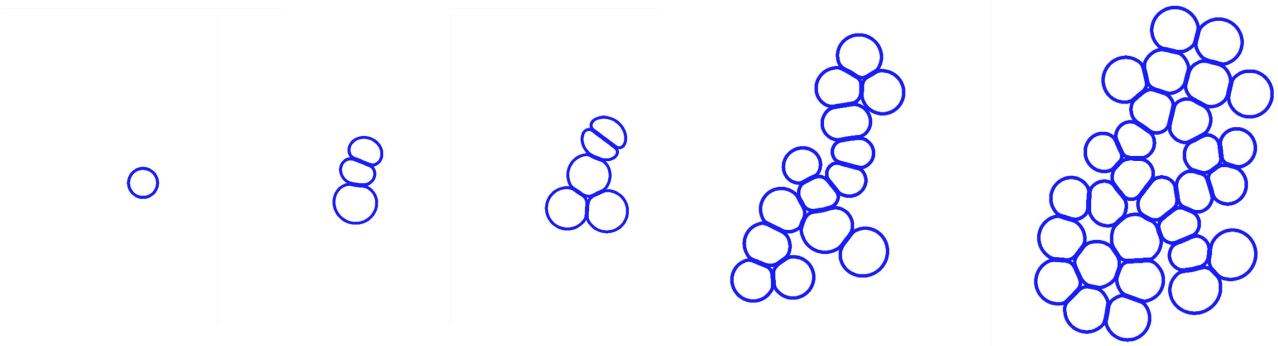

Figure 6.9: A single cell undergoing multiple rounds of cell divisions. Each cell doubles in area over its lifetime. The full list of parameters used is given in Appendix B.

Our goal with the 2D Spline Model was to test the efficacy of a new computational approach to tissue simulations: one that included smooth cell boundaries, while maintaining computational efficiency by only storing (and updating) a small number of points. Furthermore, we wished to explicitly include adhesion forces, and to do so in an efficient manner. We were successful in achieving these goals. In order to realistically model the behaviour of cell aggregates, and make quantitative comparisons between experiments and simulations, a 3D generalisation of the 2D Spline Model was necessary. This was provided by the work of Dr. Alejandro Torres-Sánchez, in the form of the Interacting Active Surfaces Model.

6.3 The Interacting Active Surfaces Model: a 3D Finite Elements Method cell simulation

The Interacting Active Surfaces (IAS) Model is a 3D description of cells that have surface tension, pressure, bending rigidity, and adhesion forces. It uses the Finite Elements Method

(FEM) to solve the dynamic equations determining the position and shape of the cells. The IAS Model was developed by Dr. Alejandro Torres-Sanchéz. I briefly outline the model here as it forms the basis of some of my work in the following chapter.

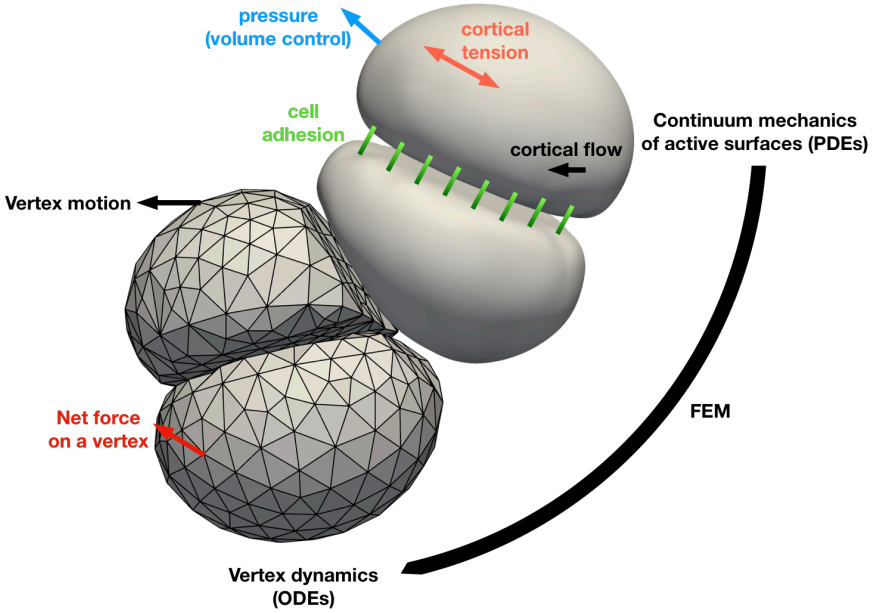

Figure 6.10: A schematic of the IAS Model. The mechanical equations of continuous active surfaces are discretised on a triangulated mesh, and solved using the Finite Elements Method. Reprinted with permission from the author, Dr. Torres-Sanchéz.

6.3.1 Mechanics of a single cell

In the IAS Model, the surface of a cell $\mathcal{S}$ is described by a function $x^\alpha(s^1, s^2, t)$, with coordinates s^1 and s^2. Note that in this section I will use superscript Greek indices for contravariant quantities and subscript for covariant quantities. The tangent plane to $\mathcal{S}$ is spanned by two basis vectors $\mathbf{e}_1$ and $\mathbf{e}_2$, defined by $e_i^\alpha = \partial_i x^\alpha$. The metric tensor on the surface can then be defined $g_{ij} = e_i^\alpha e_{j\alpha}$. The curvature tensor on the surface can be defined $C_{ij} = -(\partial_i e_j^\alpha) n_\alpha$, where the normal vector is $\mathbf{n} = (\mathbf{e}_1 \times \mathbf{e}_2)/|\mathbf{e}_1 \times \mathbf{e}_2|$. The dynamics of a single cell are given by the force balance equations (at low Reynolds number),

$$\nabla_j t^{ji} + f^i = 0, \tag{6.26}$$

$$-C_{ij} t^{ij} + f_n = 0. \tag{6.27}$$

t_{ij} is the tension tensor, and $f^\alpha = f^i e_i^\alpha + f_n n^\alpha$ are the external forces. The covariant derivative is defined for a vector v^b as $\nabla_a v^b = \partial_a v^b + \Gamma^b_{ac} v^c$, with Christoffel symbols $\Gamma^i_{jk} = e^i_\alpha \partial_j e^\alpha_k$. Eq. 6.26 describes the balance of forces tangential to the surface. Eq. 6.27 describes the balance of forces normal to the surface. Constitutive equations for the tension and external forces are needed in order to solve Eqs. 6.26 and 6.27. The tension can be written as a sum of active and viscous parts,

$$t^{ij} = t^{ij}_{\text{act}} + t^{ij}_{\text{vis}}. \tag{6.28}$$

The active part is written

$$t^{ij}_{\text{act}} = \gamma g^{ij} \tag{6.29}$$

where γ is an active tension generated by e.g. myosin. The viscous stress is

$$t^{ij}_{\text{vis}} = 2\eta v^{ij}, \tag{6.30}$$

where η is the viscosity, and $v_{ij} = \frac{1}{2}\partial_t g_{ij} = \frac{1}{2}\left((\partial_i v_\alpha)e^\alpha_j + (\partial_j v_\alpha)e^\alpha_i\right)$, where v_α is the velocity of the surface. The effect of bending rigidity can be combined with the external forces resulting in

$$f^i = -\mu v^i, \tag{6.31}$$

$$f_n = p + \kappa\left(\nabla^2 H + \frac{H-C}{2}\left(H^2 - 4K\right)\right). \tag{6.32}$$

The first equation describes friction with the surrounding medium, with friction coefficient μ. The second equation describes the forces in the normal direction due to internal cell pressure, and rigidity of the cell boundary with bending modulus κ. $H = C_{ij}g^{ij}$ is the total curvature, and $K = \det(C)\det(g^{-1})$ is the Gaussian curvature.

6.3.2 Cell-cell interactions

The interaction between two cells, $\mathcal{S}^I$ and $\mathcal{S}^J$, can be described by the free energy

$$F_{\text{int}}[\boldsymbol{x}^I, \boldsymbol{x}^J] = \sum_{I,J}\int_{\mathcal{S}^I}\int_{\mathcal{S}^J}\varphi^{IJ}\left(x^{IJ}\right)dS^I dS^J, \tag{6.33}$$

where $\varphi^{IJ}(x^{IJ})$ is the free energy density, and $x^{IJ} = ||\boldsymbol{x}^{IJ}||$ is the distance between two points on the two cells, with $\boldsymbol{x}^{IJ} = \boldsymbol{x}^I - \boldsymbol{x}^J$. Calculating $\delta F_{\text{int}}/\delta\boldsymbol{x}^I$, leads to an additional force and tension on cell I given by

$$f^{I,\text{int},\alpha} = -\sum_J\int_{\mathcal{S}^J}\frac{\partial\varphi}{\partial x^{IJ}}\frac{x^{IJ\alpha}}{x^{IJ}}dS_J, \tag{6.34}$$

$$\gamma^{I,\text{int}} = \sum_J\int_{\mathcal{S}^J}\varphi^{IJ}dS_J. \tag{6.35}$$

As with the 2D Spline model, interactions are modelled with the Morse potential,

$$\varphi(r) = D(1 - e^{-a(r-r_m)})^2 - D \tag{6.36}$$

6.3.3 Cell divisions

Cells divide in an analogous way to the 2D Spline Model. A division plane is selected with a random orientation, and the cell is cut along this plane. New surfaces are added to the two daughter cells parallel to this plane, and separated by the equilibrium distance of the Morse potential, r_m.

6.3.4 Summary

The velocity field on each cell surface is calculated by solving Eqs. 6.26 and 6.27 using the Finite Elements Method (more details are given in Appendix D). The positions of the mesh vertices are then updated using only the normal component of the velocity field, in order to avoid tangential distortions of the mesh.

6.4 Results of Interacting Active Surfaces

A dimensionless parameter, $\hat{D} = \frac{Da^2}{\gamma}$, can be constructed that controls the shape of cells in an aggregate. The effect of varying $\hat{D}$ on the shape of a doublet is shown in Fig. 6.11. At large $\hat{D}$, the adhesion forces dominate and the cells become more hemispherical. At small $\hat{D}$, surface tension dominates and the cells round up. This is analogous to the parameter Ξ in the 2D Spline Model.

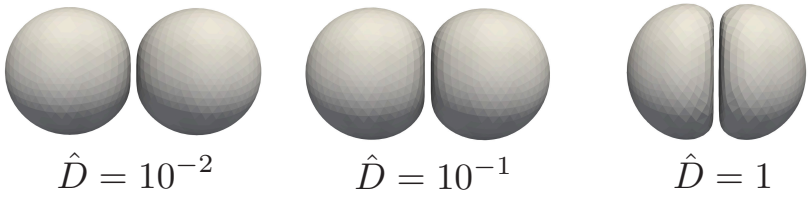

Figure 6.11: The effect of increasing $\hat{D}$. At low $\hat{D}$, surface tension dominates and the cells stay close to spherical. At high $\hat{D}$, adhesion dominates and a large interface forms.

6.4.1 Summary

The IAS Model was developed by Dr. Torres-Sanchéz. My own contribution has been to extend the model to polarised cells, the results of which are detailed in Chapter 7. As such, this section is necessarily brief. I have outlined the derivation and implementation of the IAS Model. I have also shown how the non-dimensional parameter $\hat{D}$ controls the ratio of interface to free area. At high $\hat{D}$ the cells have large interfaces, whereas at low $\hat{D}$ they have small interfaces. This behaviour is in agreement with the analogous 2D parameter Ξ.

Chapter 7

A computational model of the growth of mouse stem cell aggregates

In this chapter we use the novel computational methods developed in the previous chapter, the 2D Spline Model and the 3D Interacting Active Surfaces Model, to model the growth of mouse stem cell aggregates. My model does not include the opening of the lumen - we restrict ourselves to describing the deformation and rearrangement of the cells. Including the opening of the lumen would involve the further complexity of describing the flow of the surrounding fluid, and its interactions with the cell surface. Furthermore, once an aggregate has formed a rosette, with apicobasal polarity forming a hedgehog defect, and tight junctions at the apical domains making the central region impermeable to water, the subsequent opening of a lumen is unsurprising. As such, we decided that excluding the surrounding fluid from our model was an acceptable simplification.

7.1 Modelling

Disrupting polarity, as in the β1-KOs, disrupts morphogenesis. As such, in order to build a predictive model of rosette formation, I have taken the computational models described in Chapter 6, and modified them with the addition of a dynamic polarity vector that couples to the cell-cell adhesions.

7.1.1 Polarity dynamics

The orientation of the apicobasal polarity vector is determined by the sensing of collagen in the extra cellular matrix (*in vivo*) or matrigel (*in vitro*) by β1-integrin [216]. The effect of collagen sensing is to place the basal domain in contact with the external environment. Cell signalling and polarity establishment are complex process that are not fully understood. Attempting to model them explicitly would be challenging. As such, I propose the following phenomenological polarity dynamics:

$$\partial_t p_\alpha = -\frac{1}{\gamma_1}\frac{\partial F}{\partial p_\alpha} + \xi, \tag{7.1}$$

where γ_1 is a friction parameter, and ξ some noise. The free energy F is given by

$$F = \frac{\chi}{A}\int_S H(\hat{\mathbf{r}})\mathbf{p}\cdot\hat{\mathbf{r}}dA + \lambda(|\mathbf{p}|-1)^2, \tag{7.2}$$

where S is the surface of a cell, $\hat{\mathbf{r}}$ is a unit vector pointing from the centre of the cell to a point on the surface, and H is an indicator function that is 0 over any region of the cell that is in

contact with another cell, and 1 otherwise. The parameter χ determines how susceptible the cell is to the external signal of its surroundings, and λ describes the strength of the preference for a norm of 1. For simplicity, I set $\chi = \lambda = 1$. The form of F is chosen to approximate the behaviour of a cell sensing its environment. The integral in Eq. 7.2 acts as a weighted average of $\mathbf{p} \cdot \hat{\mathbf{r}}$ across the surface of the cell, with H the weights. Consequently, F is minimised when $\mathbf{p}$ lies anti-parallel to the regions of the surface where $H = 1$. In other words, F is minimised when the basal domain overlaps with the ECM. The second term in Eq. 7.2 favours $|\mathbf{p}| = 1$. This choice has been made based on the reasonable assumption that the cells have some favoured polarity state, and in the absence of any more detailed model for the dynamics of $|\mathbf{p}|$. The action of these polarity dynamics is demonstrated in Fig. 7.1. On the left, the apical domain points towards the interface, and the basal domain is in contact with the ECM. This is energetically favourable. The plot below shows the two parts of the integrand in Eq. 7.2, H and $\mathbf{p} \cdot \hat{\mathbf{r}}$. The correct positioning of the basal domain (negative part of $\mathbf{p} \cdot \hat{\mathbf{r}}$) in contact with the ECM (non-zero part of H) results in a negative integral. On the right, the apical domain is pointing towards the ECM, hence the basal domain is not in contact with the ECM. This is energetically unfavourable. The positive part of $\mathbf{p} \cdot \hat{\mathbf{r}}$ overlaps with the non-zero part of H, resulting in a positive integral.

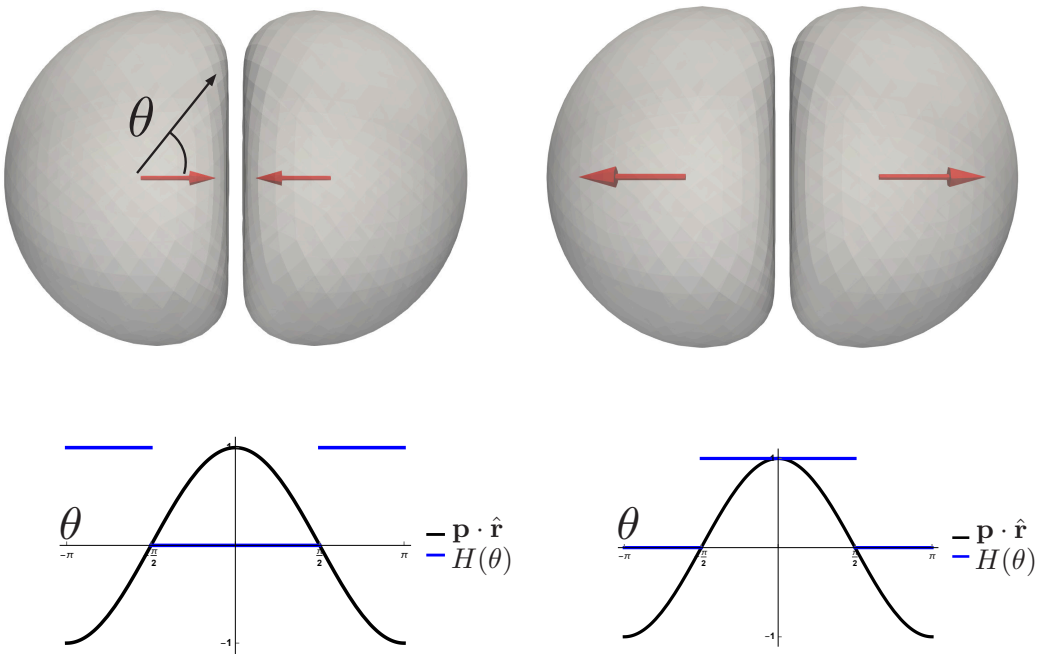

Figure 7.1: A schematic demonstrating the effect of the polarity free energy, Eq. 7.2, in two scenarios. On the left is the energetically favourable scenario with the basal domain in contact with the ECM. On the right is the unfavourable scenario with the basal domain pointing towards the interface.

7.1.2 Coupling between polarity and mechanics

Adhesions between cells are mediated by E-cadherin [91]. E-cadherin colocalises with the apical domain [175], hence I propose that apical adhesion forces are increased compared to the basal

domain. I achieve this by modifying the adhesion strength, D, according to

$$D(\theta) = \begin{cases} D & \text{if } \theta < \theta^* \\ D(1 - \Delta D) & \text{otherwise} \end{cases} \tag{7.3}$$

where θ is the angle between the polarity vector and a point on the cell surface, θ^* controls the width of the apical domain, and ΔD controls the difference between apical and basal adhesion strengths. Two interacting points on neighbouring cells at positions with angles θ_1 and θ_2 interact with a strength $D = \sqrt{D(\theta_1)D(\theta_2)}$. The effect of varying θ^* on interface size is demonstrated in Fig. 7.2.

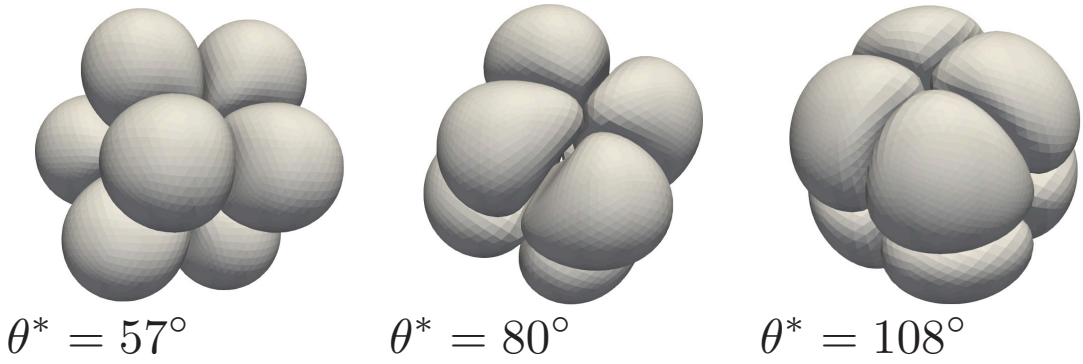

Figure 7.2: The effect of varying the apical angle, θ^*, on the size of cell-cell interfaces.

The coupling between polarity dynamics and adhesion forces described in Eq. 7.3 allows cells to crawl over each other. This effect is demonstrated in Fig. 7.3. In this simulation, a constant angular offset is artificially added to the polarity of one of the cells. This results in a net torque, and the doublet rotates.

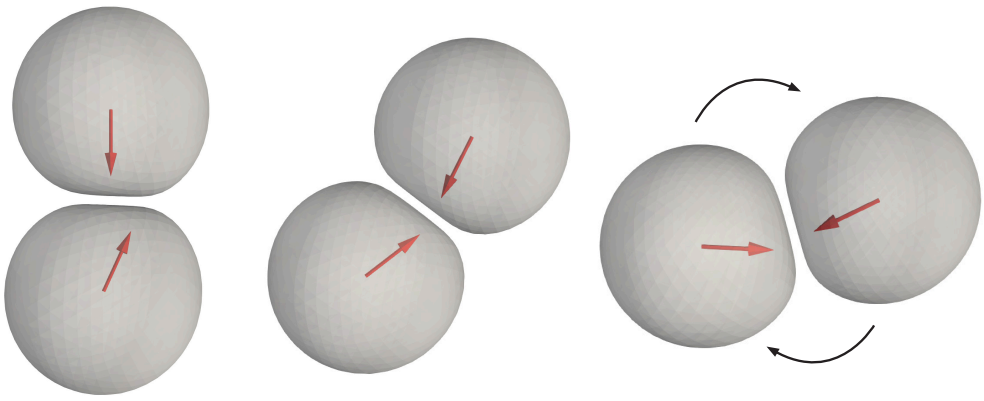

Figure 7.3: A constant angular offset is added to the polarity of the lower cell. This results in the doublet rotating.

In summary, the polarity evolves to point away from the ECM, as described in Eq. 7.1. Having established the apicobasal axis, the polarity couples to the cell mechanics by increasing

the adhesion forces in the apical domain, as described in Eq. 7.3. This model of polarity-adhesion coupling has the following parameters, in addition to those that determine the shape of the cells as described in Chapter 6:

- γ_1 - the drag on the polarity dynamics.
- ΔD - the difference in adhesion strength between apical and basal domains.
- θ^* - the size of the apical domain.
- ξ - the noise on the polarity dynamics.

We refer to the IAS Model with the addition of a polarity vector and polarity-adhesion coupling as the Polar IAS Model.

7.2 2D results

It is possible to draw qualitative comparisons between the 2D Spline Model and the experiments. There are two scenarios that are particularly interesting. First, the transition of a line of cells to a ball, as shown in Fig. 7.15. Implementing the adhesion dynamics described in Eq. 7.1, and the polarity-adhesion coupling described in Eq. 7.3, the Spline Model recapitulates the line to ball transition, as shown in Fig. 7.4.

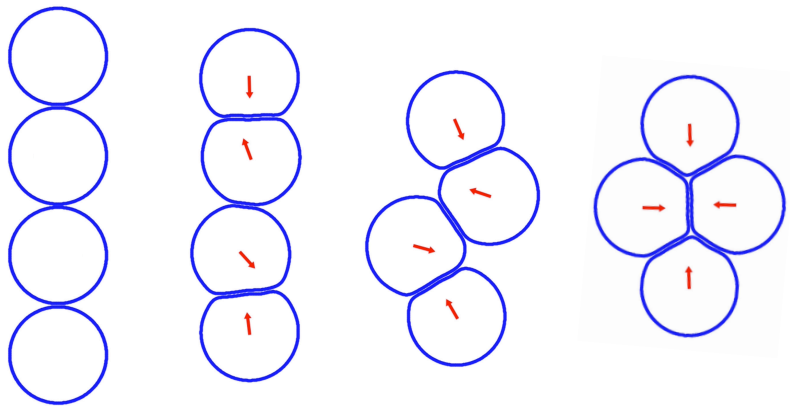

Figure 7.4: A line of cells reorganises into a "ball" in the 2D Spline Model. The apical polarity vector is shown in red, and evolves to position the basal domain in contact with the ECM according to Eq. 7.1. Adhesion forces are increased in the apical domain according to Eq. 7.3. The parameters used are listed in Appendix B.

The second scenario of interest is a single cell growing into a rosette. In the following simulations, the cells grow to double their initial area over their lifetime, in agreement with the experimental volume measurements shown in Fig. 5.8. Futhermore, the division angle is chosen from a normal distribution with mean 90°, and standard deviation 30°, approximating the experimental division angle distributions in Fig. 5.16. An example simulation of a single cell undergoing three rounds of division is shown in Fig. 7.5. Despite the random orientation

of divisions, the cells form a dense clump. To demonstrate the causal effect of the polarity-adhesion coupling, another simulation was run with $\Delta D = 0$ (isotropic adhesions). The result is shown in Fig. 7.6. The 8 cell aggregate is much more branched than the one in Fig. 7.5. More examples of such aggregates are shown in Fig. 7.7.

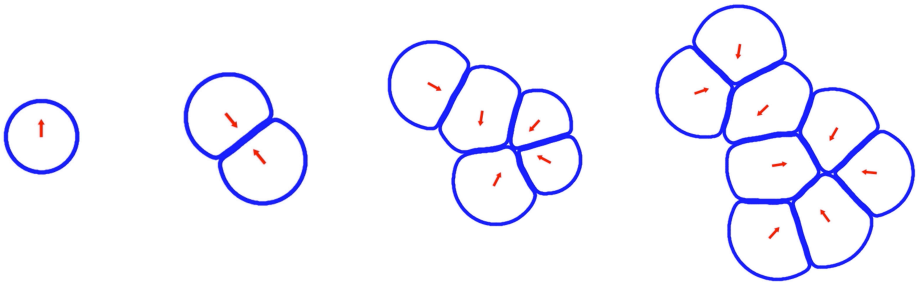

Figure 7.5: A single cell undergoes three rounds of division, resulting in a dense aggregate of cells. The parameters used are listed in Appendix B.

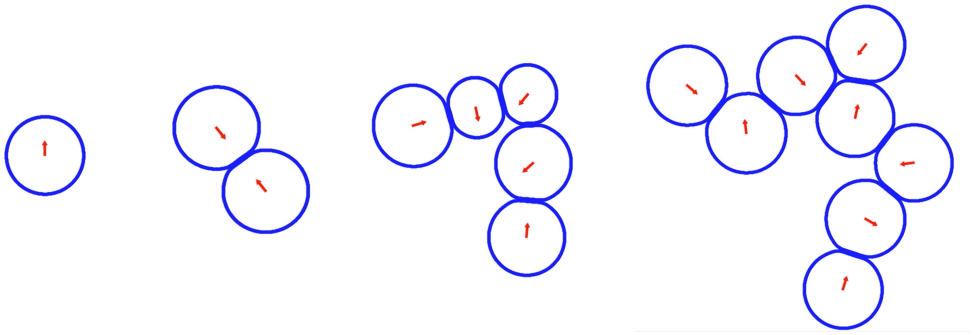

Figure 7.6: A single cell undergoes three rounds of division, with $\Delta D = 0$ (isotropic adhesions). The resulting structure is not densely packed. The parameters used are listed in Appendix B.

It is difficult to say whether the cells in the bottom right of the aggregate in Fig. 7.5 count as a rosette. It is more difficult to pack cells round a central point in 2D than in 3D, hence it is unreasonable to expect 8 or more cells to polarise towards a central point as is seen in the experiments. Although there is a clear difference in packing density between the aggregates with $\Delta D = 0.9$ and$\Delta D = 0$, as demonstrated in Fig. 7.7, we cannot make quantitative comparisons with experiments, due to the 2D nature of the Spline Model. In order to quantitatively address the mechanics of mESC aggregates, we turn to the 3D Polar IAS Model.

7.3 3D Results

7.3.1 Polarity dynamics

We are able to make quantitative comparisons between the polarity predicted by the steady state of Eq. 7.1, and that measured according to Eq. 5.3. In the experiment shown in Fig.

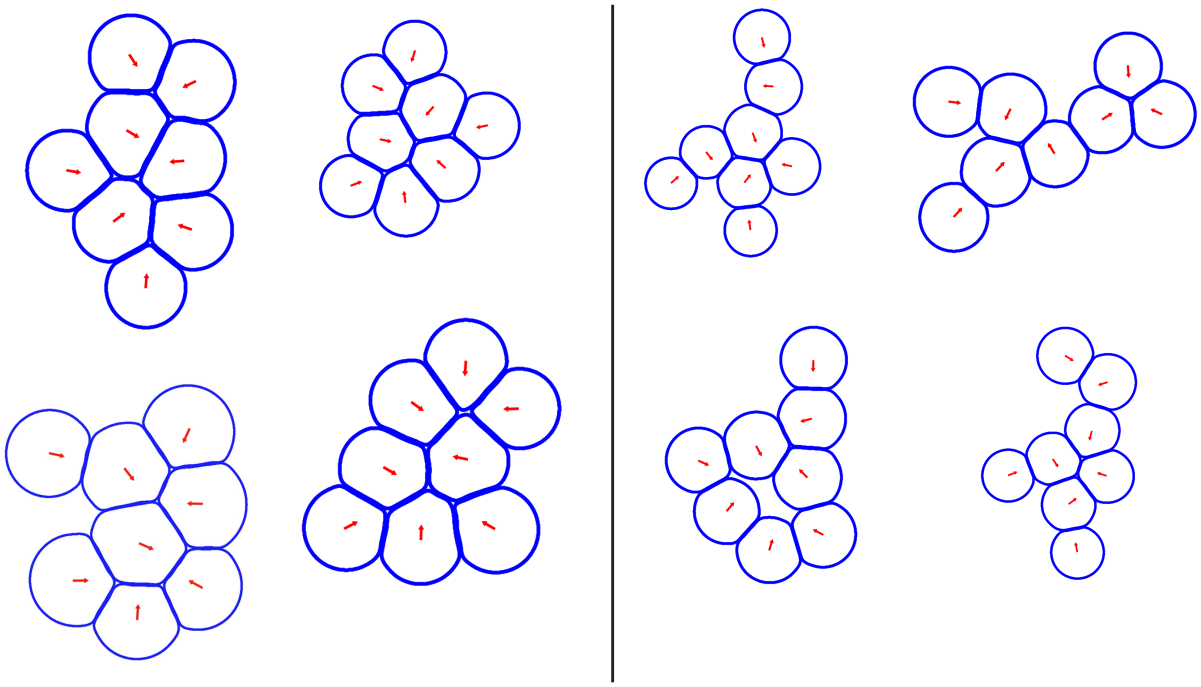

Figure 7.7: Examples of aggregates formed with $\Delta D = 0.9$ (left), and $\Delta D = 0$ (right). The parameters used are listed in Appendix B.

7.8, three cells form an approximate line. Consider the evolution of the polarity of the middle cell. The polarity is initially pointed upward. Then as the lower cell forms an interface with the middle cell, the polarity rotates to point sidewise. This motion is in agreement with the polarity dynamics described in Eq. 7.1 and 7.2. The cell is initially polarised upward because the lower region is exposed to ECM at the two cell stage. As the interface forms with the lower cell, the dominant ECM signal to the middle cell comes from the left hand side, hence the polarity rotates to point right. The angle between the measured polarity, and that predicted by the steady state of Eq. 7.1 is shown in Fig. 7.9. The left hand panel shows the relaxation of the polarity of the middle cell to the predicted value, after the disruption of cell division. The right hand panel shows the good agreement between measurement and prediction for all cells in the movie. Fig. 7.9 A) also demonstrates how the polarity dynamics are fast. Relaxation occurs on a timescale of roughly 10s of minutes.

How closely does the predicted polarity follow the measured polarity across my whole dataset? The predicted polarity vs measured polarity for a particular WT movie is shown in Fig. 7.10, demonstrating the correlation between the two. The Product Moment Correlation Coefficient, r, is calculated for each panel, according to the formula

$$r = \frac{\sum_i (x_i - \bar{x})(y_i - \bar{y})}{\sqrt{\sum_i (x_i - \bar{x})^2 \sum_i (y_i - \bar{y})^2}}, \tag{7.4}$$

for measured polarity components x_i, and predicted polarity components y_i. $\bar{x}$ is the mean of x_i, and similarly for y_i. More plots of the correlation between predicted and measured polarity are shown in Appendix E.1 - E.9.

Is there a significant difference in the correlation between measurement and prediction between WT and β1-KO cells? In Fig. 7.11, r is plotted for the x, y, and z components of all

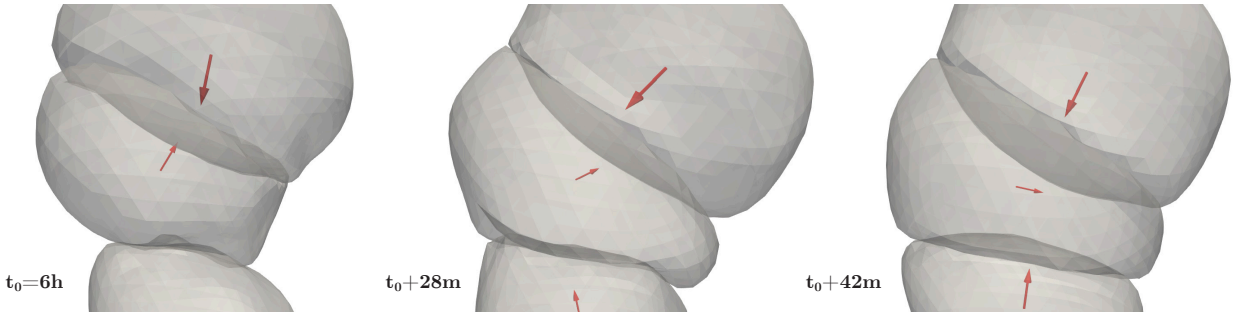

Figure 7.8: The polarity dynamics of the middle cell at the beginning of the three cell stage. Initially the polarity points towards the upper cell. As an interface is formed between middle and lower cells, the polarity of the middle cell rotates to point right. This is what is expected from the polarity model described in Eq. 7.1.

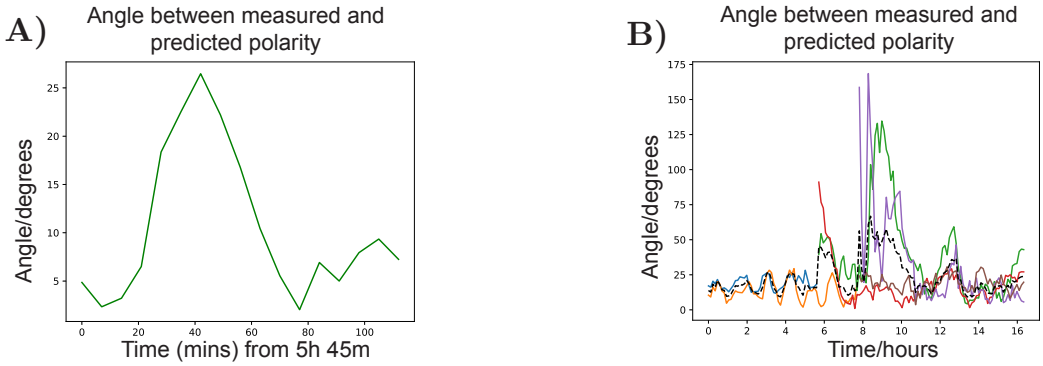

Figure 7.9: The angle between the measured and predicted polarity of the movie in Fig. 7.15. A) The angle of the polarity of the middle cell, over the time period shown in Fig. 7.8 when the middle polarity is rotating. B) The angle of the polarity of all cells in the movie. There is good agreement between measurement and prediction (i.e. an angle close to 0) except for the peaks at 6 hours and 8 hours. These correspond to two cell divisions.

the segmented movies. There is no significant difference between WT and β1-KOs. This is in agreement with unpublished work by the Zernicka-Goetz Group demonstrating the disruption of actomyosin polarity in β1-KOs, while E-cadherin polarity remains unaffected [209]. It is also noteworthy that the correlation between prediction and measurement for the F-actin movies is poor, as shown in Fig. 7.12. From this I conclude that the F-actin polarity is not well predicted by the position of the ECM. Visually, the F-actin polarity is weak, hence the orientation of the polarity vector will be dominated by noise. I propose that this leads to the poor correlation in Fig. 7.12, although I do not quantify this hypothesis here.

An alternative measure of how well the polarity predicted by Eq. 7.2 agrees with the measured polarity is the angle between the two. This angle is plotted for 3 WT and 3 β1-KO movies in Fig. 7.13. The mean value is around 50°, which raises the question: is this good? This is a subjective judgement. Aggregates of mESCs are a noisy and complex system. Furthermore, the model of polarity given in Eq. 7.2 is extremely simple, and with respect to the direction of the

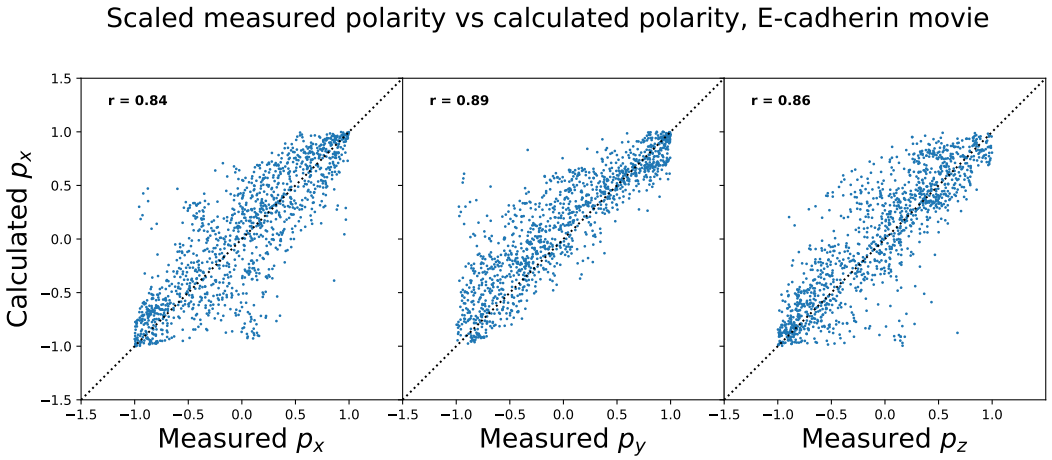

Figure 7.10: Measured vs predicted polarity for a WT movie. The x, y, and z components of each polarity vector are plotted against each other.

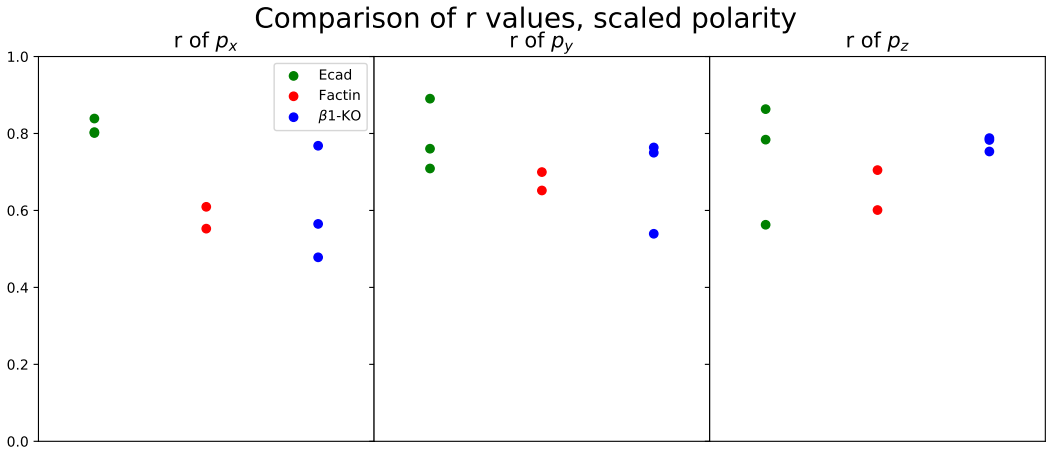

Figure 7.11: The Product Moment Correlation Coefficient values between measured and predicted polarity, in the x, y, and z directions, for WT E-cadherin (green), WT F-actin (red), and β1-KO E-cadherin (blue) movies. There is no significant difference between the three types of movie.

polarity, has no parameters. Consequently, I would be satisfied with any agreement between the model and experiments within $\approx 90°$.

7.3.2 Cell shapes

The cell shapes in Fig. 7.2 can be quantified using the tools described in Chapter 5. Measurements of the ratio of total interface area to free area, the ratio of interface area to free area averaged over neighbouring cells, and the sphericity are shown in Fig. 7.14, as these cells evolve from an initially spherical state placed at the vertices of a cube. For the WT movie shown in Fig. 5.6, these three variables are shown in Fig. 5.21 (top left), Fig. 5.23 (top left), and Fig. 5.10 (left), respectively. These plots give a final value of the ratio of total interface area to free area of approximately 0.45, a final value of the ratio of interface area to free area averaged over neighbours of approximately 0.06, and a final sphericity of approximately 0.85. The two experimental ratios of interface to free area lie between those for the $\theta^* = 80°$ and $\theta^* = 108°$

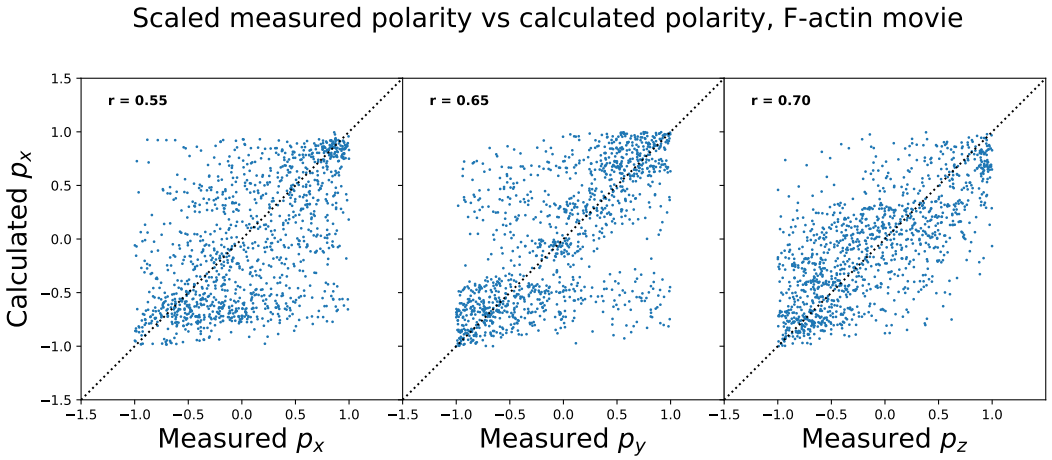

Figure 7.12: Measured vs predicted polarity for a WT F-actin movie. The x, y, and z components of each polarity vector are plotted against each other.

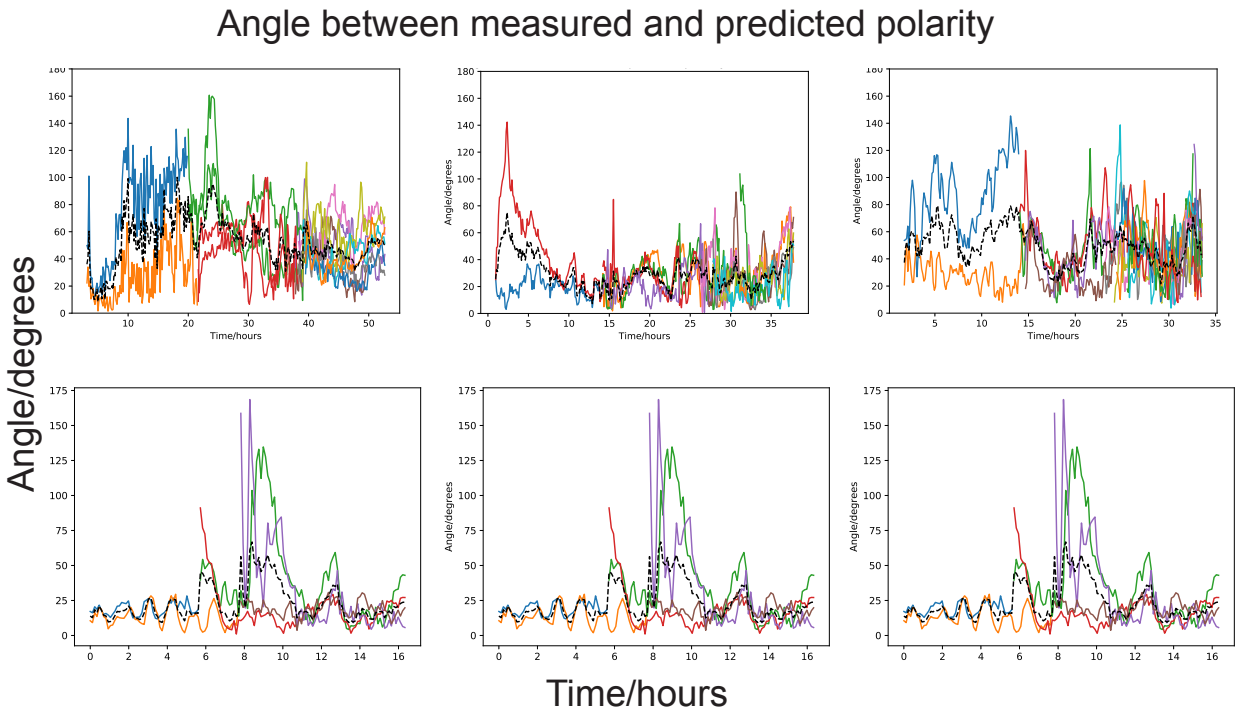

Figure 7.13: The angle between the measured and predicted polarity for 3 WT (top row) and 3 β1-KO (bottom row) movies. The mean is plotted as the dashed, black curve.

simulations. The experimental value of the sphericity is lower (i.e. more extreme) than that for the simulation with $\theta^* = 108°$. From these measurements I conclude that the Polar IAS Model can achieve cell shapes that are comparable to experiment.

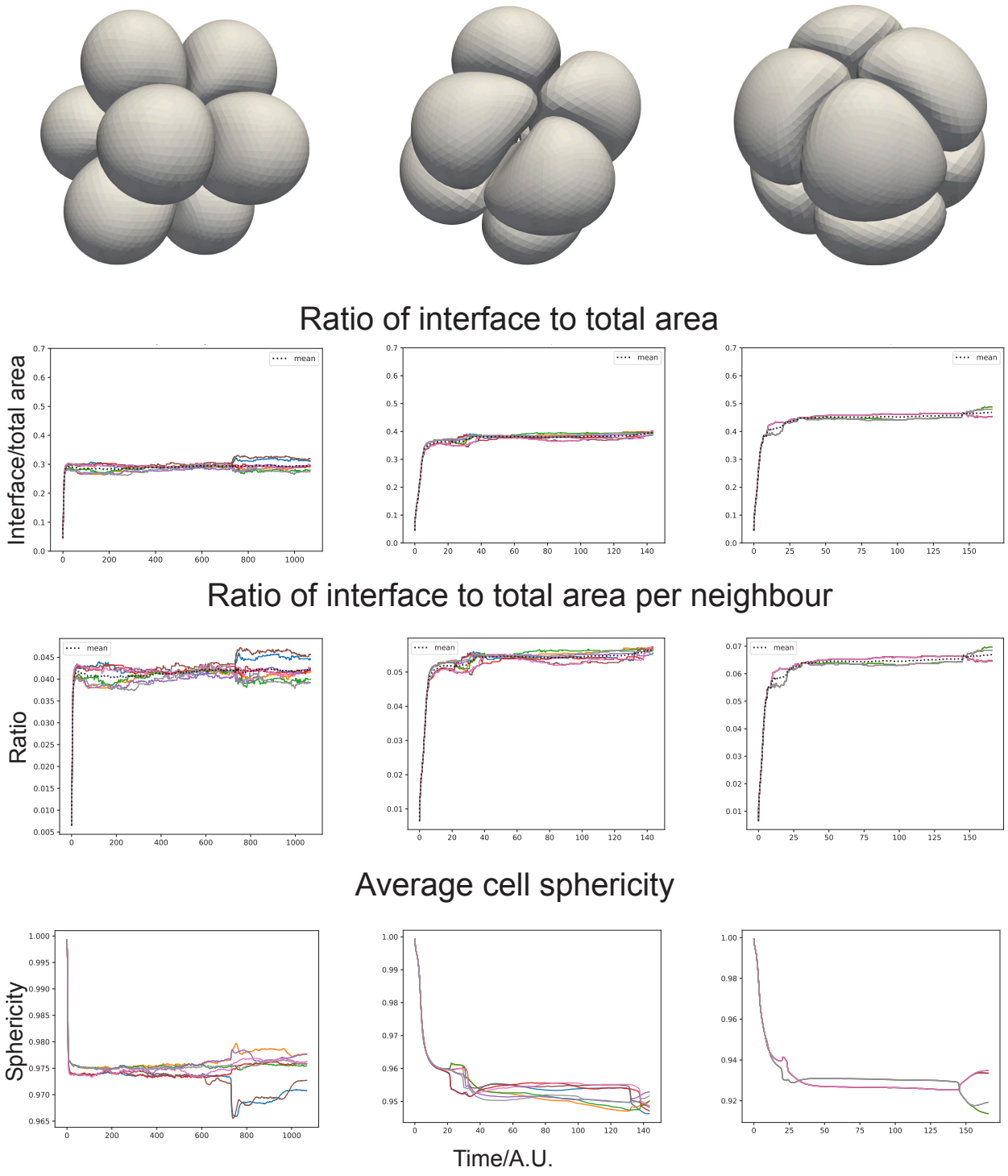

Figure 7.14: Quantification of the cell shapes in an 8 cell aggregate with $\theta^* = 57°$ (left column), $\theta^* = 80°$ (middle column), $\theta^* = 108°$ (right column). The cell shapes are quantified by measuring the ratio of total interfacial area to free area (top row), the ratio of interfacial area to free area averaged over all neighbouring cells (middle row), and the sphericity (bottom row).

7.3.3 The line to ball transition

Increased adhesion in an apical domain that is positioned away from the ECM allows cells in an extended configuration to transition into a compact configuration. Such transitions are necessary to ultimately achieve a rosette. The clearest example of such a configurational change is shown in Figure 7.15. In this movie, 2 cells divide so as to form an extended line of 4 cells. This line of cells then transitions into a compact ball-like configuration.

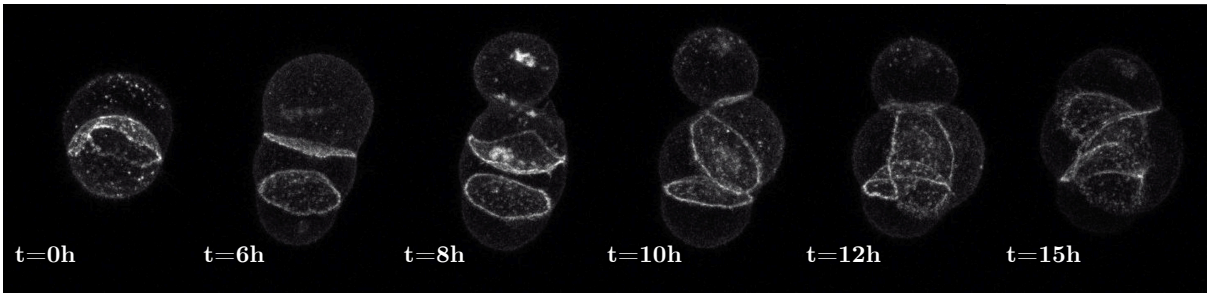

Figure 7.15: In this WT movie the cells divide into an extended line of four. They then undergo a transition from a line configuration into a densely packed ball.

Segmenting the above movie, it is possible to track the E-cadherin polarity as measured by Eq. 5.3. The result is shown in Fig. 7.16.

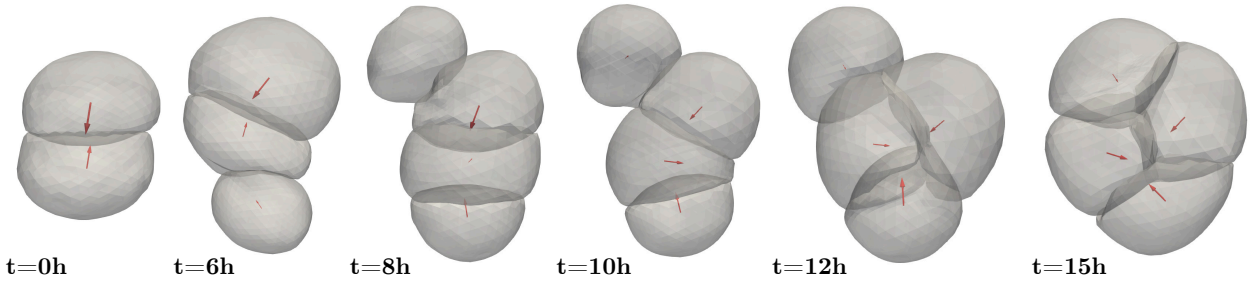

Figure 7.16: The segmented line to ball transition, with measured E-cadherin polarity in red.

By including the coupling between polarity and adhesion described in Eq. 7.3, the line to ball transition is recapitulated in my simulations, as shown in Fig. 7.17. In this simulation, I initialise the system as a line of 4 unpolarised, spherical cells.

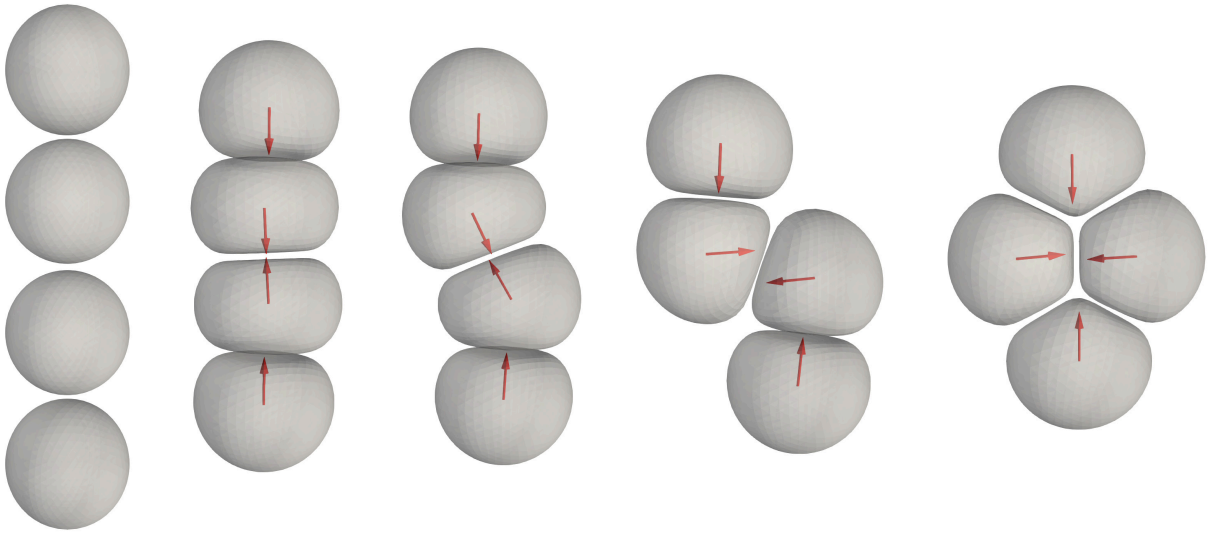

Figure 7.17: A simulation of the line to ball transition, recapitulating the behaviour in Fig. 7.16. The parameters used are listed in Appendix B.

The dynamics of both experiments and simulations can be quantified using the analysis tools developed in Chapter 5. The action of the polarity-adhesion coupling is to move the cells such that the line connecting their centres lies close to parallel/anti-parallel with their polarities. This can be quantified with the angle, θ, between the polarity of a cell, and the line connecting the cell centre with the centre of its neighbour, as demonstrated in Fig. 7.18 (repeating the measurement of Fig. 5.44). Typically θ does not reach zero, due to the presence of other cells, as demonstrated in the final structure in Fig. 7.17 for example. The dynamics of θ are shown in Fig. 7.19 for the experimental line to ball transition shown in Fig. 7.15 (left hand plot), and the line to ball simulation shown in Fig. 7.17 (right hand plot). The trend is for angles greater than 90° to decrease, i.e. the polarity and centre of mass connection become more aligned as the extended configuration transitions into a densely packed configuration.

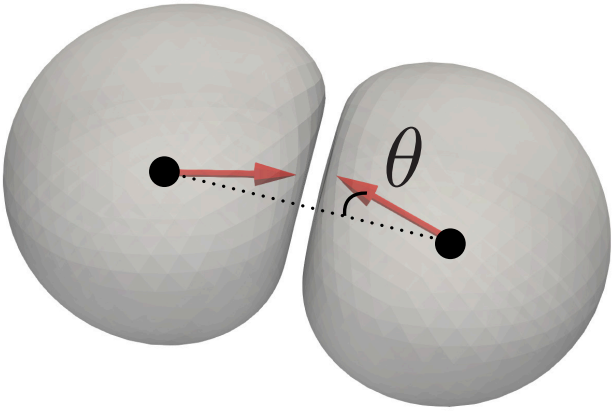

Figure 7.18: A schematic demonstrating the angle θ between the polarity of a cell, and the line connecting the centre of one cell to that of another. Low values of θ correspond to polarity aligned with the cell neighbour connection.

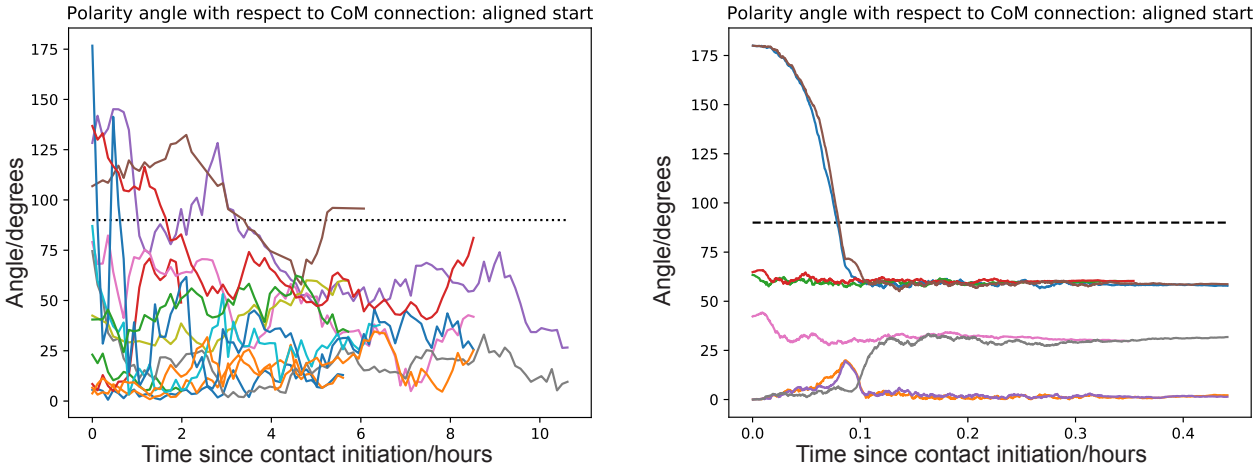

Figure 7.19: The dynamics of angles, θ, between polarity and cell neighbour connections, for all pairs of cells that come into contact with each other, in the experimental line to ball movie in Fig. 7.15 (left), and the simulation in Fig. 7.17 (right). The curves have been aligned to the time where the cells first come into contact. Different colours correspond to different cell pairs.

The causal link between polarity-adhesion coupling and the successful transition from a line to a ball is demonstrated by the control simulation shown in Figure 7.20. In this simulation, there is no coupling between polarity and adhesion, i.e. the adhesion forces are isotropic. The transition fails to occur.

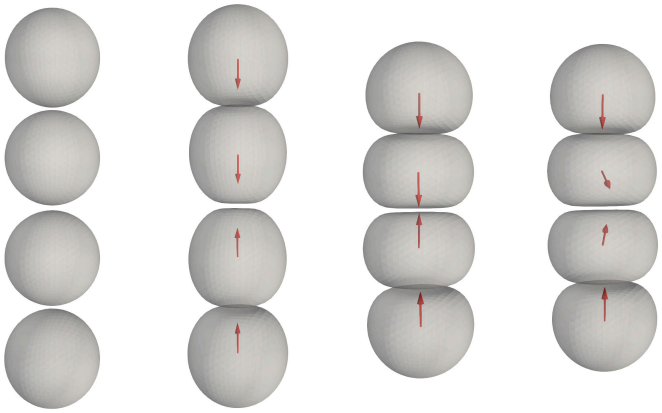

Figure 7.20: A simulation with no coupling between polarity and adhesion, i.e. $\Delta D = 0$ in Eq. 7.3. The transition to a ball does not occur. Note that the polarities become misaligned due to the noise term in Eq. 7.1.

When initialised in a line, the model displays a variety of behaviours depending on the adhesion strength, adhesion anisotropy, and noise. The different resulting configurations are shown in Figure 7.21 for a low level of noise, and in Figure 7.22 for a high level of noise. Although I do not rigorously categorise the behaviour of the model in different regions of parameter space, the two diagrams demonstrate some intuitive behaviour, as well as raising some unanswered questions. At low noise, it is to be expected that the cells will more easily get stuck in metastable states, i.e. the square arrangement at $D = 20$, $\Delta D = 0.5$, in Fig. 7.21. The separation of the line into two doublets at $D = 20$, $\Delta D = 0.9$ is a result of the fact that the middle cells polarise away from each other, resulting in very low adhesion forces at the centre of the line where their basal domains face each other. I do not have an explanation as to why, at $D = 15$, $\Delta D = 0.9$, the line configuration is metastable. In the high noise diagram, Fig. 7.22, when $\Delta D = 0.9$, the line transforms into a tetrahedron. This is to be expected from the point of view of the cells maximising their interfacial area, hence minimising their adhesion energy. What is more mysterious is why, when $\Delta D = 0.5$, the cells adopt a planar arrangement. I do not have an explanation for this.

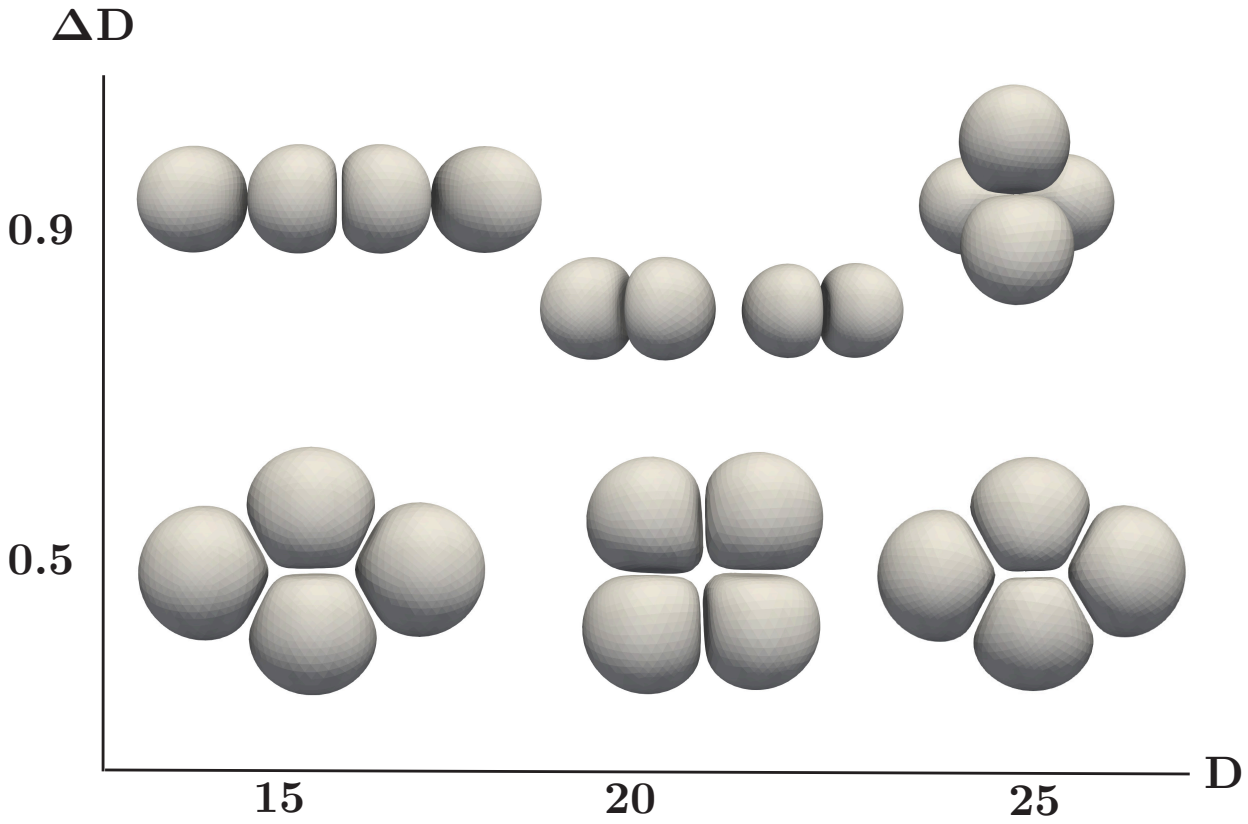

Figure 7.21: The shape diagram for an initial line of 4 cells, with low levels of noise.

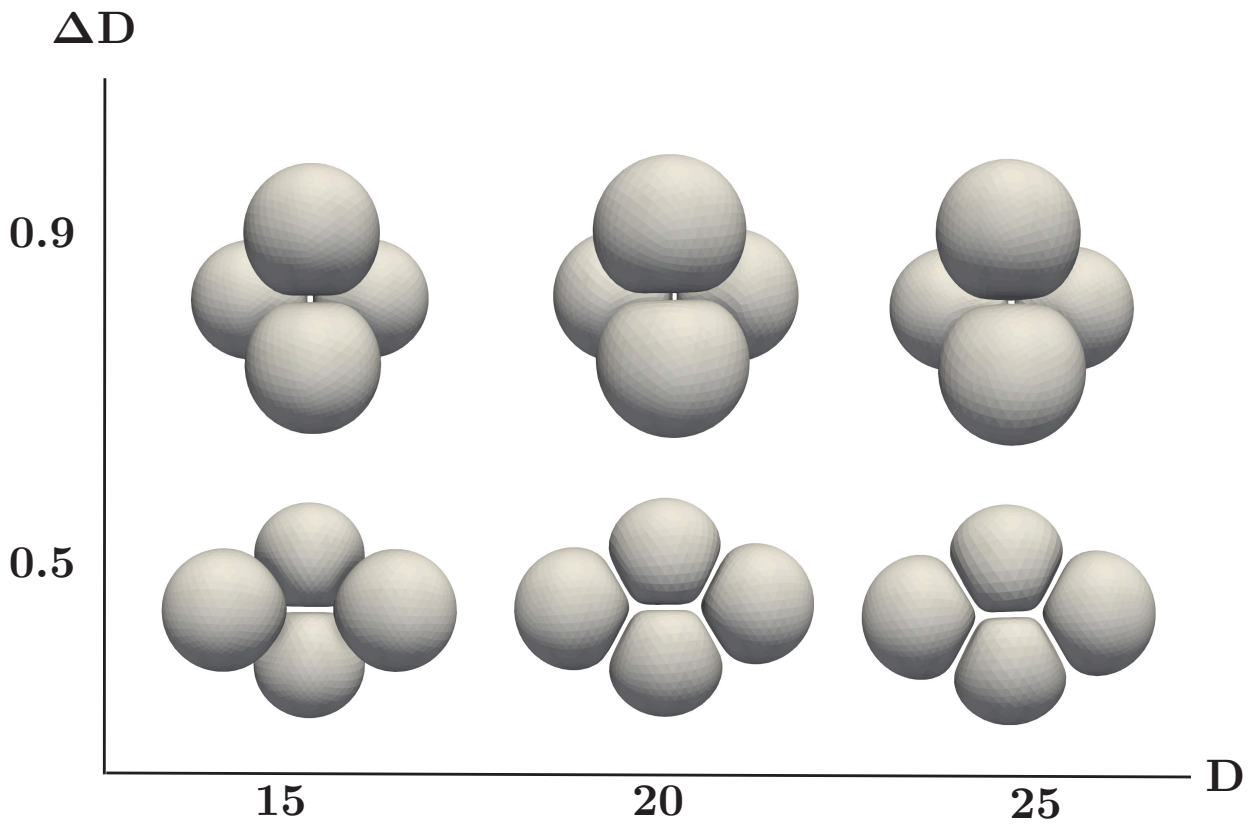

Figure 7.22: The shape diagram for an initial line of 4 cells, with high levels of noise.

To summarise, the polarity dynamics described in Eq. 7.1 recapitulate the behaviour of the experimental polarity, as measured by Eq. 5.3. By increasing the adhesion forces in the apical domain, as described in Eq. 7.3, I am able to recapitulate the line to ball transition observed experimentally. The movie shown in Fig. 7.15 is particularly useful for analysis as the cells divide into a line. This gives a very clear topological transition where the dynamics of polarity and cell rearrangements can be studied.

7.3.4 Further polarity-adhesion transitions

Polarity-adhesion coupling can transform a variety of initial conditions into densely packed aggregates resembling rosettes. In Fig. 7.23, a line of 8 unpolarised cells folds into a densely packed aggregate with all the cells polarised towards the centre. In Fig. 7.24, a grid of 8 unpolarised cells makes a similar transition.

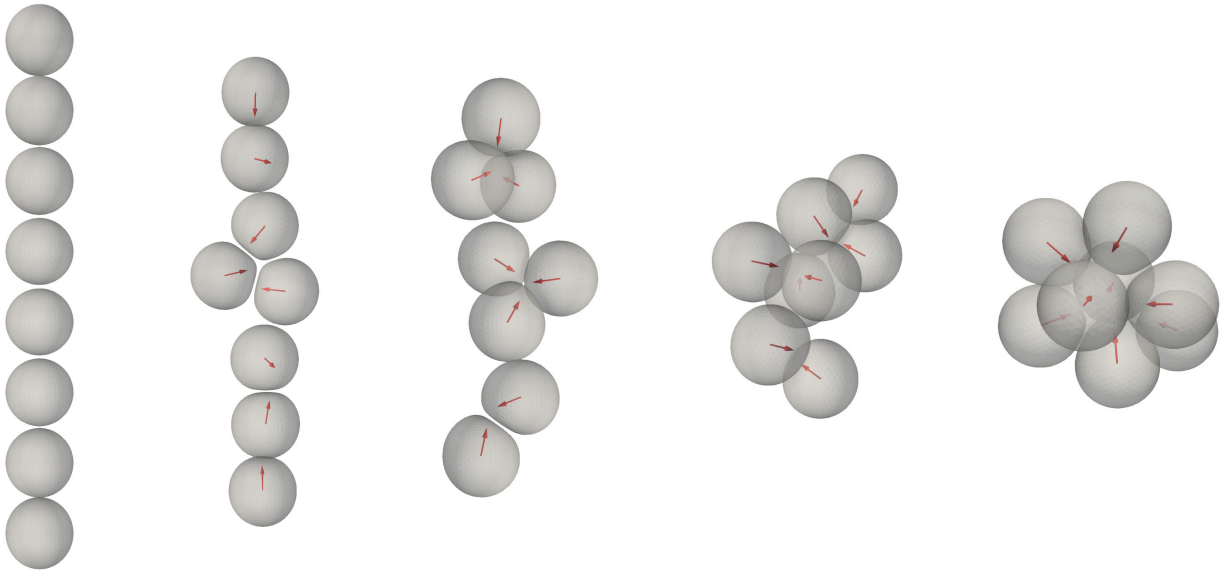

Figure 7.23: A line of 8 initially unpolarised cells transitions into a densely packed aggregate, reminiscent of a rosette.

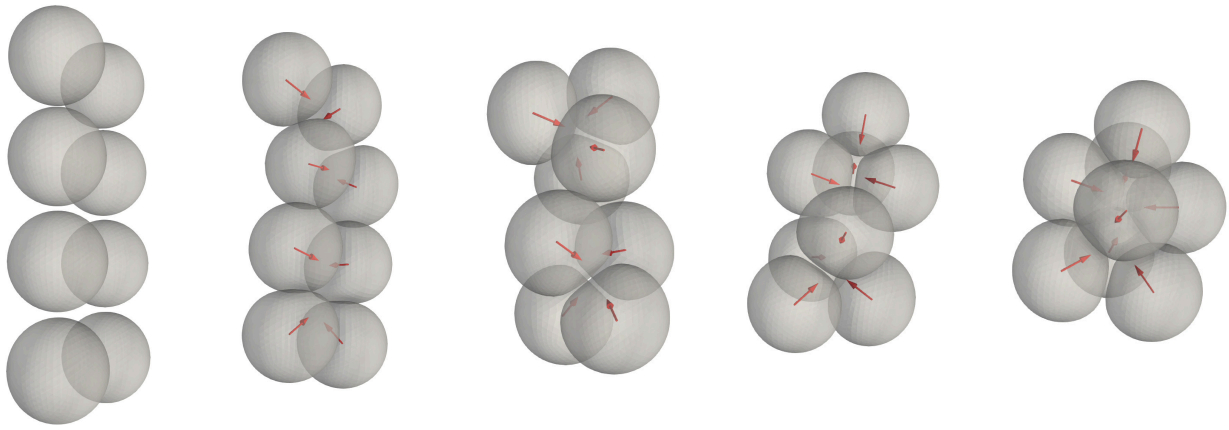

Figure 7.24: A 2×4 grid of 8 initially unpolarised cells transitions into a densely packed aggregate, reminiscent of a rosette.

The simulations shown in Fig. 7.23 and Fig. 7.24 can be quantified using the analysis tools of Chapter 5. The number of neighbours, mean polarity angle, and standard deviation of the polarity angle are shown for both simulations in Fig. 7.25. Similar to the WT experiments, and in contrast to the β1-KOs, the aggregates transition to a densely packed state where each cell has three or more neighbours. The polarity vectors start in an organised state (the line or grid), transition to disordered states, and finally reach a different ordered state, the rosette. These transitions can be observed in both polarity mean angle and standard deviation where the trajectories start at low values, increase to a maximum, then decrease again. The first half of these simulations is not comparable to the experiments, as they start with 8 cells, not 1. However, the second half, when the cells organise into a rosette is comparable. The decrease in the mean and standard deviation of the experimental polar angle can be observed in Fig. 5.39

and Fig. 5.40.

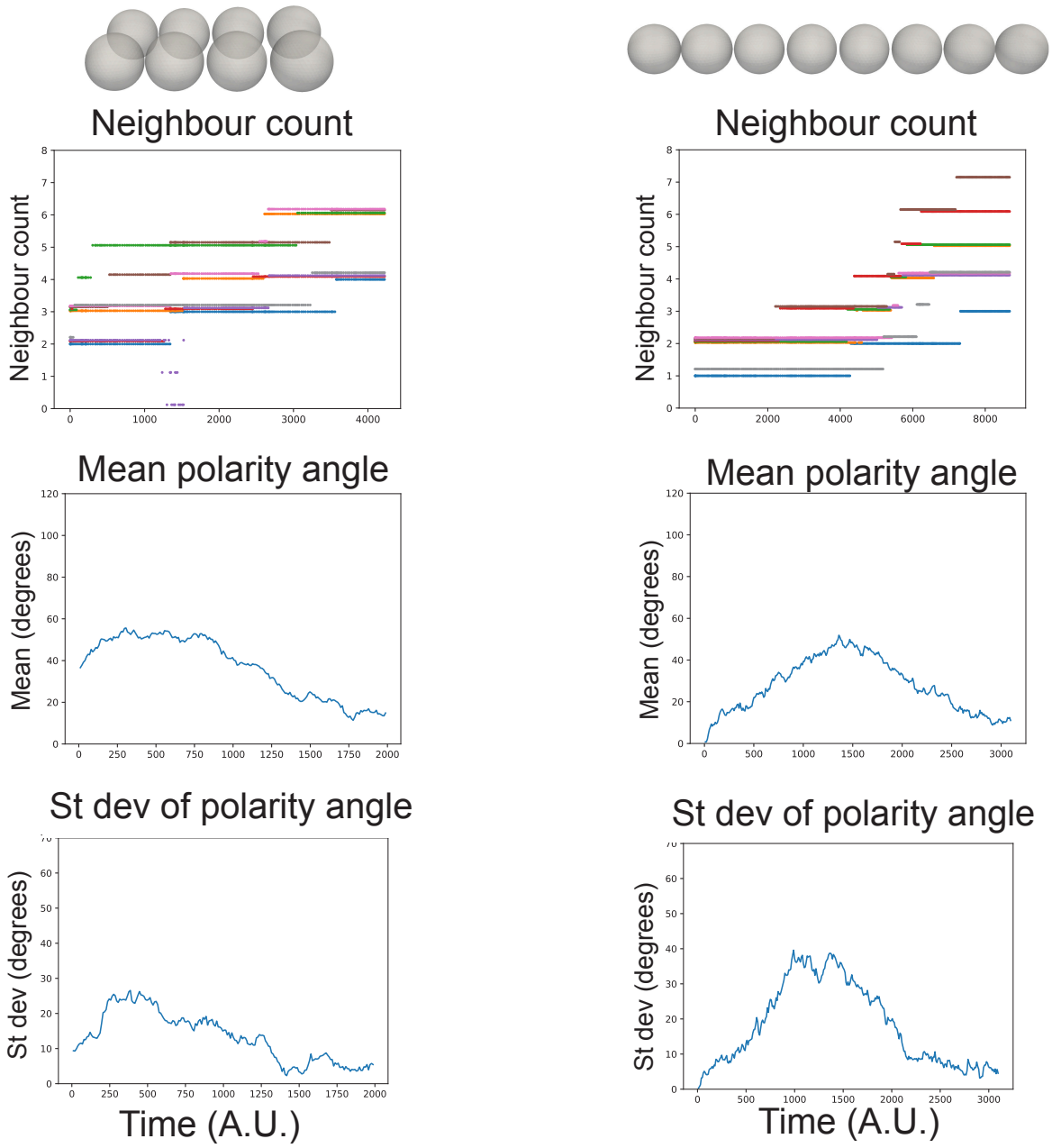

Figure 7.25: The number of neighbours, the mean polarity angle, and the standard deviation of the polarity angle, plotted for the two simulations above.

The mean and standard deviation of the long axis angle is shown in Fig. 7.26. These measurements do not show a transition to a final ordered state. This is because the simulation parameters are such that the cells remain close to spherical. Hence there is a large degree of randomness to the orientation of their long axes. The shapes of the cells are quantified in Fig. 7.27, where the ratio of total interfacial to free area, the ratio of interfacial area to free area averaged over neighbours, and the sphericity are plotted. The simulations have a ratio of total interfacial to free area of approximately 0.25 (compared with 0.45 for a WT movie), a

ratio of interfacial to free area averaged over neighbours of approximately 0.03 (compared with 0.05 for a WT movie), and a sphericity of approximately 0.99 (compared with 0.85 for a WT movie). The choice of parameters resulting in very spherical cells was a practical decision made to increase the speed of the simulations. Smaller interfaces result in faster code, as the interactions are the most computationally expensive part of the Polar IAS Model. The simulation in Fig. 7.23 took approximately 3 days to run, using 8 cores on the Crick computing cluster. I estimate computing a similar length of simulation time with $\theta^* = 108°$ would take at least a week. Furthermore, large interfaces are more robust to the buckling behaviour required to transition from a line to a ball, hence take even longer to simulate.

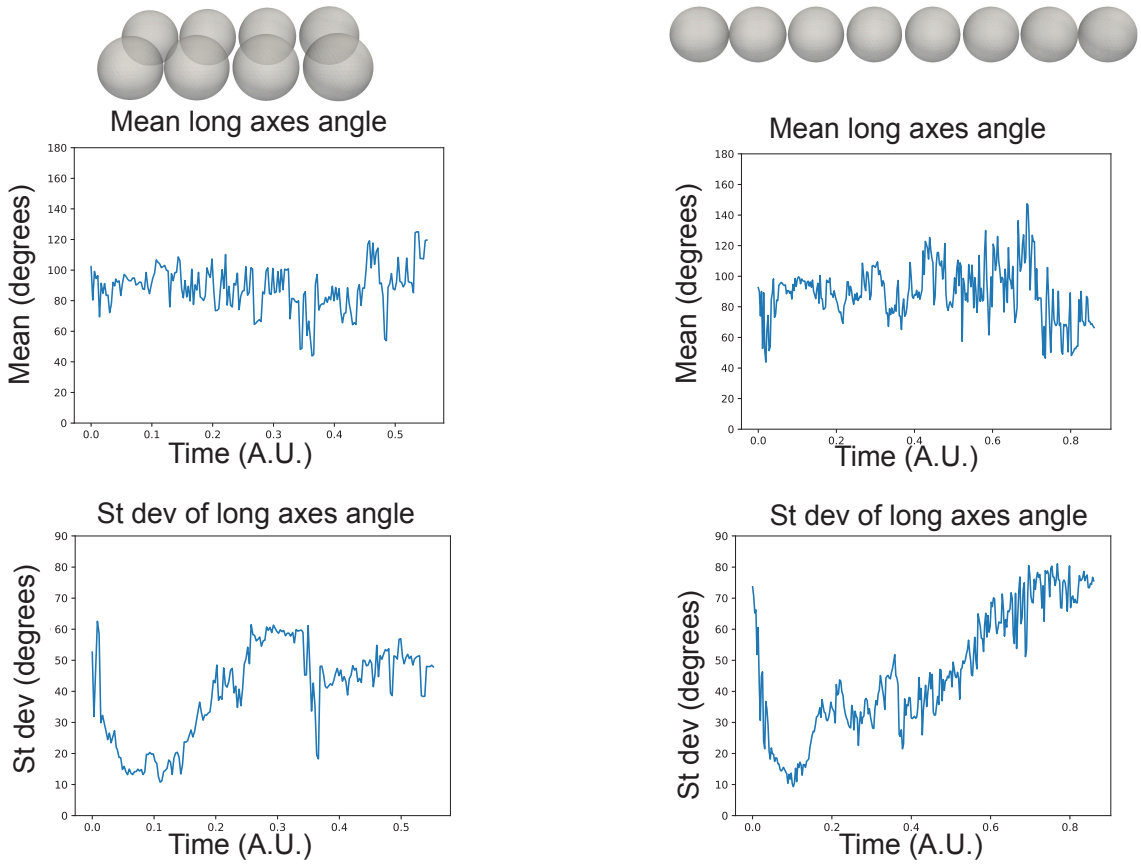

Figure 7.26: The mean long axis angle, and the standard deviation of the long axis angle, plotted for the two simulations above.

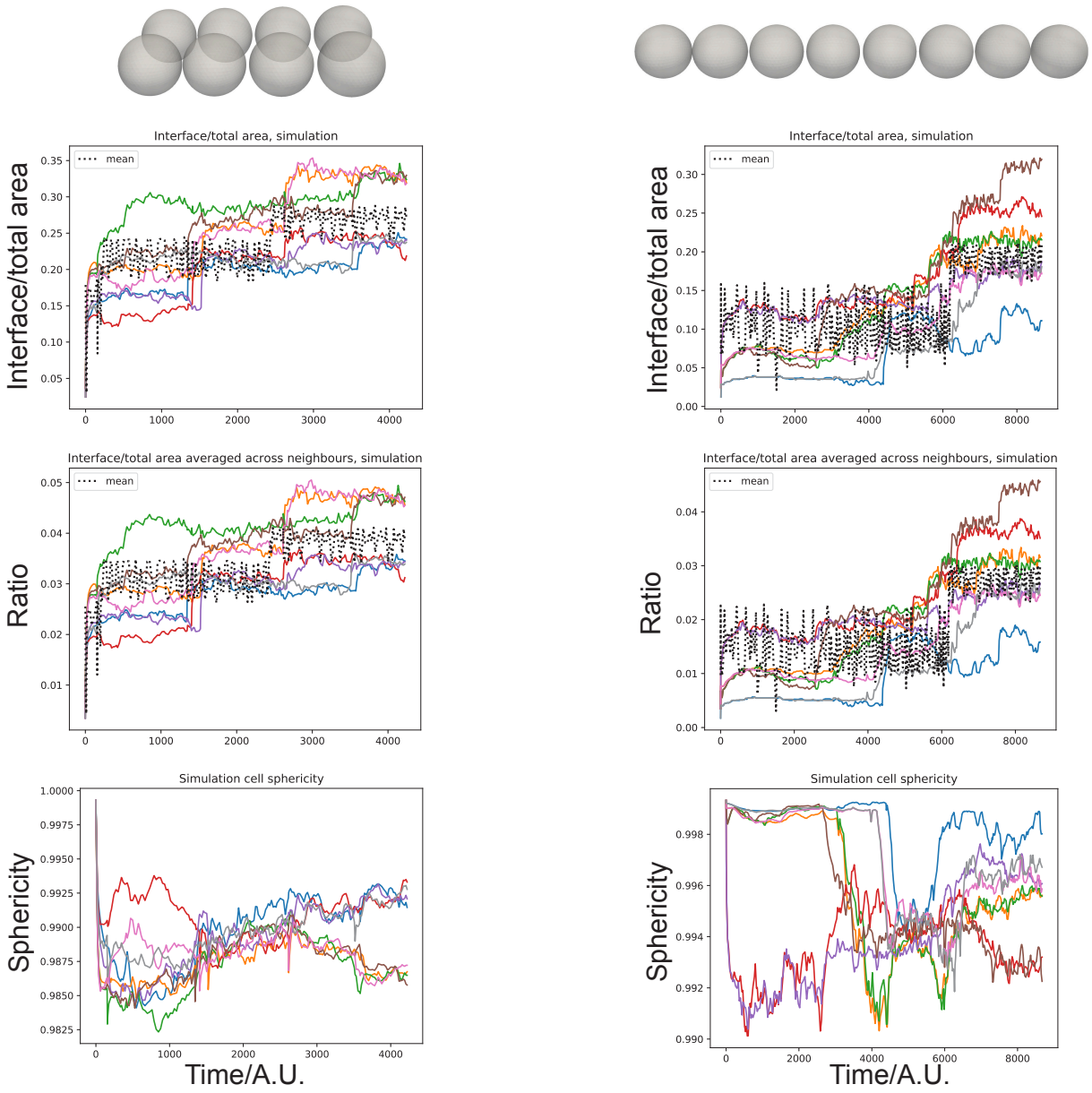

Figure 7.27: The ratio of total interfacial to free area, the ratio of interfacial to free area averaged over neighbours, and the sphericity, plotted for the two simulations above.

The evolution of the angle θ between cell polarity and cell neighbour connections is plotted for both simulations in Fig. 7.28. These plots show that θ trajectories that start above 90° tend to decrease. This is to be expected as a result of polarity-adhesion coupling, which drives the transition from an extended initial configuration to a rosette. This trend is in agreement with the experimental findings in Fig. 5.44 and Table 5.1.

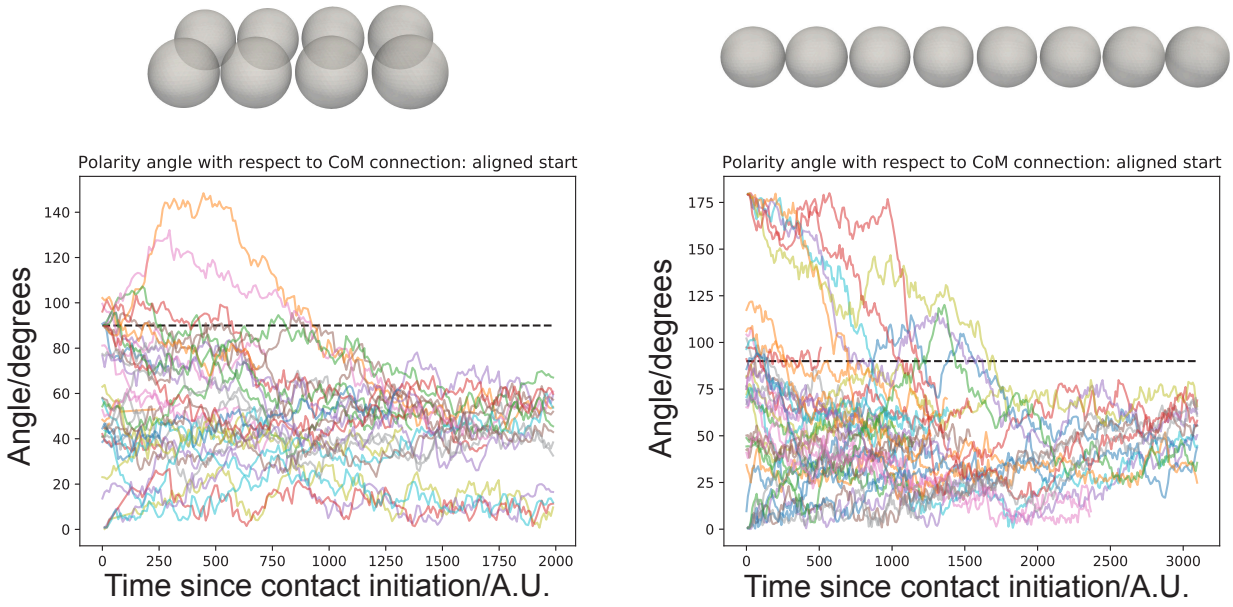

Figure 7.28: The angle between polarity and the connection between cell centres, plotted for all pairs of cells that come into contact in the above simulations. The trajectories have been aligned to the time at which contact is initiated between the cells.

7.4 Summary

In this chapter, I have developed a model of mESC aggregate growth. I hypothesise that the apicobasal polarity vector is positioned with the basal domain in contact with the ECM, and cell-cell adhesions are increased in the apical domain. I incorporate these mechanisms into the 2D Spline Model and 3D IAS Model. Using the Spline Model, I demonstrate in 2D that a line of 4 cells can transition into a ball. I also demonstrate that a single cell can grow into a densely packed aggregate with polarity-adhesion coupling, and into an extended structure without it.

In 3D, I demonstrate that there is a positive correlation between the polarity predicted by my model, and that measured from the experimental data. By allowing a set of 8 spherical cells, positioned at the vertices of a cube, to adhere and deform onto each other, I quantify the shape of cells in the Polar IAS Model. These measurements demonstrate quantitative agreement between the simulated and experimental cell shapes. I also demonstrate that a line of 4 cells can transition into a ball. Quantifying the dynamics of the angle between cell polarity and cell neighbour connections, I demonstrate a trend for this angle to decrease, in agreement with experiments. Finally, I demonstrate that both a line of 8 cells, and a 2×4 grid of cells, can transition into a dense aggregate, reminiscent of a rosette. Unlike the simulations where 8 cells are placed at the corners of a cube, the shapes of the cells in the line and grid simulations are dissimilar to experiments, as the shape parameters were chosen to minimise computing time. For example, the strength of the adhesion forces was chosen so that the cells form small interfaces, which reduces the number of pairwise calculations at each timestep. These 8 cell simulations also recapitulate the trend for the angle between polarity and neighbour connections to decrease.

These simulations recapitulate several aspects of the experiments. There are two key predictions. First, that the orientation of the polarity is set by where the cell is in contact with

the ECM. This is in agreement with the biological literature. This claim is born out by my analyses in the case of E-cadherin, but not F-actin. From my analysis it is not clear why the F-actin polarity is poorly predicted by the ECM. The second prediction is that adhesion forces are increased in the apical domain. This is a novel hypothesis that has not yet been suggested in the literature, however it does lead to cell and polarity rearrangements in agreement with the data. The extent to which this represents the true biological mechanism is discussed in Section 9.4.

Chapter 8

Conclusion

In this thesis I have studied the formation of fluid filled cavities in cellular systems, both in a general hydrodynamic theory, and with a specific study of the growth of mESC aggregates. In conducting this work I have developed, and then used, a novel theoretical description of pumping cells, as well as novel computational tools for the analysis and simulation of cellular systems.

8.1 The hydrodynamics of pumping cell aggregates

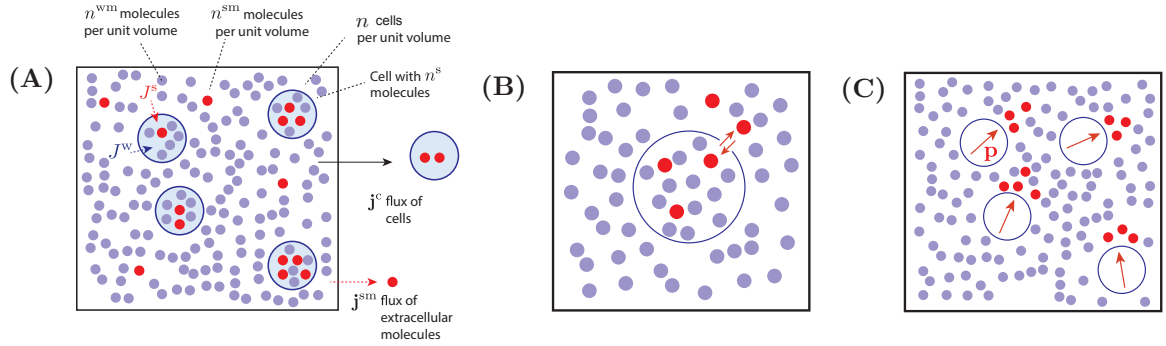

Figure 8.1: A) The system described by the hydrodynamic theory of pumping cells. B) The active transport of solutes across the cell membrane. C) Polar active pumping of solutes.

In the hydrodynamic theory I describe the system depicted in Fig. 8.1: a ternary fluid, consisting of cells in a background fluid of water and solutes. The cells can polarise, and actively transport solutes across their membranes. Within this theory I have studied various aspects of the equilibrium and non-equilibrium behaviour of the system. Driven by cell-cell adhesions, the system can undergo spinodal phase separation into a cell rich region (the tissue) and a cell poor region (a fluid filled cavity). This separation process occurs on a timescale of roughly 1 hour, which is plausible for developmental processes. In order to describe the dynamics of this system, I have derived constitutive equations for the various fluxes in the dynamic equations for cells, cell volumes, solutes, and polarity (the water having been removed by incompressibility). A tractable set of constitutive equations are derived by selecting a subset of couplings predicted by a fully symmetric Onsager theory.

I solve the dynamic equations in a number of situations. First, I show that a spherical shell of cells enclosing a fluid filled cavity reproduces the Young-Laplace Law with an active

surface tension. Second, in the limit of impermeable cells, I demonstrate the system undergoes diffusion with the diffusion constants linked to drag coefficients by the Maxwell-Stefan framework of multi-component diffusion. This analysis also predicts a percolation length for the fluid. Third, in the limit of infinitely permeable cells I recover the diffusion equation for solutes, as expected. Fourth, I consider the linear stability of cells that actively pump solutes across their membranes in order to maintain a target volume. This is shown schematically in Fig. 8.1 B). This volume control mechanism results in cell volume relaxation in response to an osmotic shock on timescales of roughly 10 minutes. Finally, I have demonstrated the existence of an instability due to active, polar pumping of the solutes by the cells. Active polar pumping is shown schematically in Fig. 8.1 C). The cells pump solutes into defects in their polarity field, water flows into these regions by osmosis, and cells are consequently forced out, forming a cavity. The system becomes unstable with respect to this mechanism at biologically plausible pumping rates.

These analyses demonstrate that the hydrodynamic theory makes realistic predictions for the behaviour of cellular aggregates in a range of biologically relevant scenarios.

8.2 Segmentation and analysis pipeline

I have been provided with a dataset consisting of 3D movies of growing mESC aggregates by the group of Prof. Zernicka-Goetz. The movies consist of either WT or β1-KO cells with either E-cadherin or F-actin fluorescently tagged. In order to extract meaningful insight from this dataset, I have developed and used a segmentation and analysis pipeline. Cell segmentation requires a number of steps. First, the raw movies are passed through Convolutional Neural Networks (CNNs) developed by Dr. Matthew Smith, and trained on manual segmentations produced by me. The CNNs calculate a distance transform from the original images. The value of the distance transform at any point is equal to the distance between that point and the nearest cell membrane. As such, the CNNs are applying a pixel-wise transformation. The training set consists of manually segmented 3D movies, of which each pixel is a training example. As such, the training set is sufficiently large to achieve good performance. Furthermore, as I segmented more and more movies by combining the CNNs and active mesh plug-in, I fed the completed segmentations back into the training set. The distance transform gives a simplified, noise free representation of the original image. Second, I segment the distance transforms using the active mesh FIJI plug-in described by Smith et al. [181]. This plug-in allows a 3D mesh to be deformed onto objects within a 3D image. Finally, I deform the distance transform meshes onto the cell membranes of the (blurred) original movies. The segmentations are stored in a 3D mesh format, i.e. as an object containing arrays of vertex coordinates, pairs of points that share an edge, and triplets of points that form a triangle.

These meshes are passed to a suite of Python analysis tools. With these tools I measure a range of variables about the meshes, e.g. volume, sphericity, number of neighbours, interfacial area, and long axis orientation, to name but a few. I also calculate a polarity vector by measuring the distribution of fluorescence on the surface of the cells. These meshes allow me to compare and contrast the growth of WT and β1-KO aggregates. Both cell types roughly double their volume over the cell cycle, and both have a bias in their division orientation towards tangential divisions. WT aggregates grow into structured rosettes whereas β1-KOs grow into loosely packed and disorganised aggregates. This is reflected in several of my quantifications. At late times, WT cells typically have 4 or more neighbours, whereas β1-KOs can have as few as 1. The angular distribution of WT cell long axes transitions to an organised state with the long axis angle $\approx 90^\circ$ (the angle is defined with respect to the radial direction of the aggregate

as described in Fig. 5.27). In contrast, the long axes of β1-KO cells remains disorganised. A similar transition occurs with the WT polarity angles tending to 0°, while the β1-KO polarity angles remain disorganised.

The segmentation and analysis pipeline developed by Dr. Smith and myself allows meaningful insight to be extracted from complex 3D + time data. I have used this pipeline to quantitatively describe the growth of WT mESC aggregates into organised rosettes, and the failure of rosette formation in β1-KOs.

8.3 Computational tissue mechanics

I have developed a novel 2D model of tissue mechanics where cell boundaries are described by periodic B-spline curves. The shape of this curve is determined by a set of control points. The cells evolve in time according to the steepest gradient descent of a free energy function combining surface tension, pressure, and pair-wise interaction forces. The interaction forces are mediated by a Morse potential that results in long range attractive and short range repulsive forces. The cells also experience tangential elastic forces. Including elastic effects stabilises cell-cell interfaces at high adhesion strengths, and stops tangential surface flows that cause the control points to bunch together. The Spline Model was inspired by the Vertex Model, but with several modifications designed to model non-epithelial cells. The flexibility of periodic B-splines allows the Spline Model to describe a wide range of cell shapes, not just approximate polygons. Furthermore, third order B-splines are continuous in their second derivative, which allows the Spline Model to be extended to include active torques [164]. Finally, by explicitly including adhesion forces between cells, the Spline Model is well placed to describe situations where cells are pulled apart or come together.

I use various techniques to increase the computational efficiency of the model. First, the number of pair-wise interactions calculated is reduced by using grid coordinates to segregate the system into macroscopic regions that do not interact. Second, within each grid cell, the calculation of pair-wise interactions is sped up by storing lists of nearest neighbours. Finally, I use the shared memory parallelisation library OpenMP to calculate the forces on different control points in parallel.

The cell shapes produced by the model can be controlled by varying the dimensionless parameter Ξ, as shown in Fig. 6.8. At high Ξ, adhesion forces dominate and the cells form large interfaces. At low Ξ, surface tension dominates and the cells are close to circular. The Spline Model is capable of simulating 10s of cells, as demonstrated in Fig. 6.9, where a single cell undergoes multiple rounds of division.

8.4 Modelling mESC aggregates

In order to model the growth of mESC aggregates I build upon the 3D Interacting Active Surfaces (IAS) Model of Dr. Torres-Sanchéz. The IAS Model is similar to the Spline Model in so much as the cells are described by a continuous surface over a discrete mesh. The cells experience forces from surface tension, pressure, and interactions mediated by a Morse potential. However, in contrast to the Spline Model, the cell surfaces are treated as a viscous fluid. Interfaces are stabilised with respect to adhesion induced buckling by the inclusion of bending rigidity. The mesh vertices are updated along the direction of the normal of the surface only,

to avoid tangential distortion of the mesh.

I modify the IAS Model by including a polarity vector associated to each cell, describing the apicobasal axis (specifically the direction from basal to apical domains). The polarity evolves in order to minimise the free energy described in Eq. 7.2. Typically this results in a polarity that is of norm 1 and with a basal domain maximally overlapping with the surrounding ECM. The polarity couples to the mechanics by decreasing the adhesion forces outside of the apical domain. The IAS Model with polar vector and polarity-adhesion coupling is referred to as the Polar IAS Model. This coupling generates torques between neighbouring cells, allowing them to rotate around each other. In 2D, the inclusion of polarity-adhesion coupling causes a line of cells to rearrange into a ball (Fig. 7.4), replicating a transition observed experimentally (Fig. 7.15). Polarity-adhesion coupling also results in 2D cell aggregates that are densely packed, as demonstrated in Fig. 7.7.

Using the image analysis tools developed in Chapter 5, quantitative comparisons can be drawn between experiments and the Polar IAS Model. I have compared the measured polarity of segmented movies with that predicted by the steady state of Eq. 7.1, and found a positive correlation in both WT and β1-KO E-cadherin movies, as shown in Fig. 7.10 and Fig. E.7, with typical correlation values of $r \approx 0.8$. Eq. 7.1 makes poorer predictions of the F-actin polarity, as shown in Fig. 7.12, with typical correlation values of $r \approx 0.6$.

In 3D, when 8 cells are placed at the vertices of a cube and allowed to deform onto each other, the resulting cell shapes are comparable to WT experiments, as quantified in Fig. 7.14. With polar-adhesion coupling, the Polar IAS Model reproduces the transition of a line of 4 cells to a ball, as shown in Fig. 7.17. The angle between polarity and cell neighbour connections tends to decrease, in agreement with WT experiments. Similar transitions, where a line of 8 cells, and a 2×4 grid of cells form rosettes, are shown in Fig. 7.23 and Fig. 7.24 respectively. In both cases, the polarity angles transition to an ordered state, replicating the behaviour of WT experiments. The cell shapes are dissimilar to those in the experiments, and the long axes do not organise into an ordered state. This is due to the model parameters being chosen to minimise computing time. Finally, the angle between polarity and neighbour connections also tends to decrease, again in agreement with WT experiments.

Chapter 9

Discussion

9.1 The hydrodynamics of pumping cell aggregates

With the hydrodynamic theory of pumping cells we set out to derive a theory that describes cells capable of moving material across their membranes, and to demonstrate that this could give rise to realistic cavity forming mechanisms. In this we have been successful. The derivation includes several simplifying assumptions. First, the number densities are all treated as smooth fields as a result of coarse-graining over volume elements much larger than the constituent particles. Such a description is only representative of systems containing large numbers of cells. We do not analyse the scale at which finite particle size effects begin to invalidate this smoothness assumption. Second, we derive constitutive equations using the Onsager theory of non-equilibrium thermodynamics, i.e. by writing the entropy production as a sum of pairs of thermodynamic fluxes and forces, and expanding the fluxes to linear order in the forces. This approach, being perturbative, is only valid close to equilibrium. Furthermore, in writing the entropy as an integral over a smooth entropy density field, we implicitly assume a condition of local equilibrium. This means that within each volume element the microscopic degrees of freedom relax quickly to thermodynamic equilibrium, and are slaved to hydrodynamic variables that evolve slowly, and vary over length scales much larger than a volume element. It is unlikely that a biological system will be close to equilibrium or satisfy local equilibrium.

Either or both simplifications, the assumption of smoothness and the use of Onsager theory, are ubiquitous in the field of active matter hydrodynamics [85] [99] [29] [89] [113]. In the case of the smoothness assumption, the ability to write down a theory in terms of differential equations, and hence to make use of the vast array of analytical and numerical tools developed to analyse differential equations, outweighs the disadvantage of restricting ourselves to large systems. The use of Onsager theory is more contentious, as cells are not close to equilibrium. One good argument in favour of Onsager theory is the lack of an alternative. We address the far from equilibrium nature of living systems by not simply using the full constitutive equations predicted by Onsager theory, and instead choosing particular couplings that we think will dominate based on physical arguments. A further disadvantage to Onsager theory is it gives no information as to the functional dependence of the coefficients on the state variables of the system. We address this, at least in the case of the diffusive fluxes, by using the Maxwell-Stefan framework. This framework allows us to relate diffusion constants to drag coefficients, for which we can predict the behaviour in certain limits.

Our theory is an addition to the existing field of active matter hydrodynamics. Kruse et al. derive the hydrodynamic equations of a polar active fluid [99], and Joanny et al. consider active multi component fluids [85]. In Ranft et al., hydrodynamic equations for a tissue are

derived, where the cells and ECM are treated as an elastic solid (in the absence of cell division), with permeating interstitial fluid [152]. Duclut et al. use the tissue model of Ranft et al. to model the growth of a lumen in a spherical shell of cells [53]. Our theory introduces several novel ideas. First, we apply the Maxwell-Stefan framework of multi component diffusion to a three component active fluid. This allows us to make reasonable arguments about how the diffusion constants depend on the volume fractions. Second, the solutes and water can move in and out of the cells. This is novel in itself, and also introduces the cell volume, internal solute number, and first moment of the internal solute distribution as dynamic variables. By explicitly describing membrane transport processes we can describe phenomena like cell volume control. Our theory allows the active pumping of solutes, and resultant osmotic flows, to be described in the hydrodynamic limit. Furthermore, these processes are described in a sufficiently simplified manner (e.g. including only one solute species) so that biologically realistic scenarios can be analysed analytically.

In what direction could this research be developed? There are several interesting options. First, there are values of the adhesion strength and pumping rate that result in the system being simultaneously unstable with respect to both spinodal phase separation and polar pumping. In the linear regime the evolution of the system will be dominated by whichever instability is faster. However, it would be interesting to study how the two instabilities would interact in the non-linear regime. This question has particular relevance given the recent experiments of Dumortier et al. [55]. In this work the mouse blastocoel cavity is shown to open when the pumping of fluid into the centre of the embryo by polarised cells overcomes cell-cell adhesions. This occurs by the opening of microlumens which then drain into one central lumen, as shown in Fig. 9.1, in a process reminiscent of the coarsening of domains by Ostwald ripening in binary fluid phase separation [205]. This scenario has strong parallels with the combination of spinodal and polar pumping instabilities in our hydrodynamic theory. The strong volume control limit, where the dynamics of the cell volume and internal solutes are eliminated by exploiting a separation of timescales, suggests itself as a simplified theory within which to study the interaction of both instabilities.

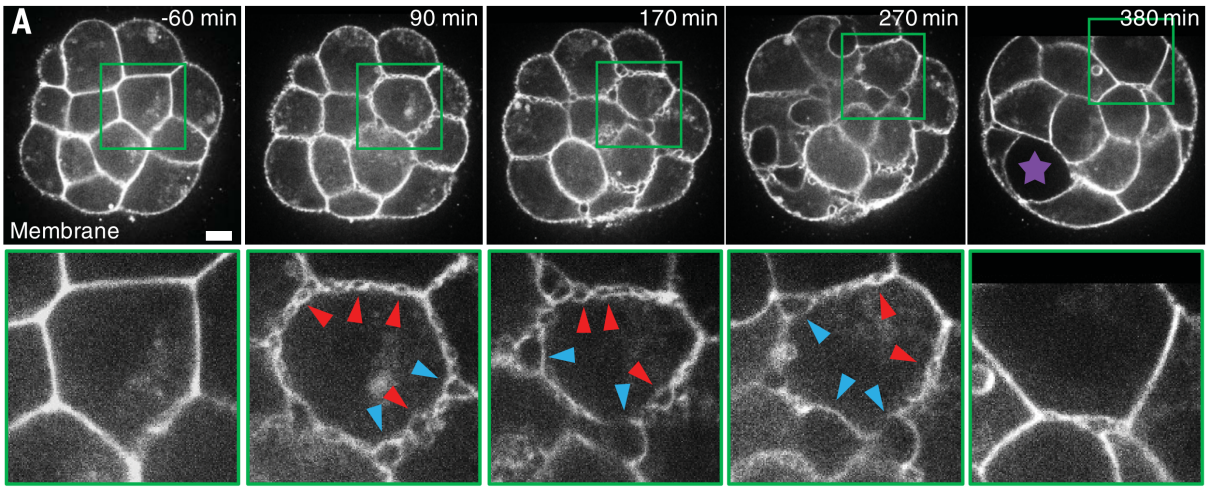

Figure 9.1: The formation of microlumens in the mouse blastocyst. The microlumens eventually drain into a single, large cavity (the purple star). This image is from Dumortier et al. [55].

One of the novelties of our theory is that the cells have a dynamic volume. This does not

significantly affect most of the calculations we perform. It would be interesting to find biological examples where spatial variation in the cell volume plays a major role, and model them with our theory. For example, in Ainslie et al., a population of small cells replaces a population of large cells in the fly abdomen [2].

A key simplification in our theory is only including a single solute species. In reality, there are many different solutes in cellular systems, e.g. ions, fats, and proteins, all differing dramatically in their size, charge, and biochemistry. It would be interesting to include a range of different solutes, thus describing the extra-cellular fluid as a polydisperse, as opposed to binary, fluid. This would also allow us to describe the electrochemical interactions of different ion species, for example in the exchange of sodium, potassium and calcium ions in various transmembrane pumps and channels.

Finally, the modelling of microbial communities would be a natural application of our theory. It would be very interesting to add some genetic dynamics on top of the spatial dynamics of the theory and study the evolution of spatially distributed populations of microbes. Our generic solute molecules could describe nutrients, drugs, viruses, or any other biomolecule that could impact the fitness of the microbes. This would combine ecological dynamics (e.g. the movement of populations) with evolutionary dynamics, and would be a continuum analogue to the discrete models of spatially distributed evolution in e.g. Dobramysl [48].

9.2 Segmentation and analysis pipeline

Our goal in developing the segmentation and analysis pipeline was to be able to convert 3D experimental movies into accurate segmentations, and from the segmentations measure physically relevant variables. Furthermore, we wanted to be able to do this in a reasonable amount of time, with a minimum of manual intervention. We have been successful in addressing the first goal. We can indeed take an experimental movie, segment it, and extract useful quantifications. The sort of measurements I have made, e.g. changes in the number of neighbours each cell has, the ratio of interfacial to free surface area, or the polarity resulting from an anisotropic distribution of fluorescence on the cell surface, would be very difficult to do without the tools Dr. Smith and I have built. I believe my segmentations to be accurate. It is difficult to quantify how accurate the segmentations are, as there is no "ground truth" with which to compare.

The second part of our goal was to be able to process a movie in a reasonable amount of time, and with a minimum of manual intervention. It takes me roughly 8 hours to segment a 300 frame movie of a single cell growing into 10 cells. With the aim of studying rosette formation in mESC aggregates, this does indeed count as a reasonable amount of time. However, to study larger structures, e.g. the embryonic organoids in Harrison et al., which consist of ≈ 100 cells, further work would be necessary to speed up the segmentation process [74]. Speeding up this process, and decreasing the amount of manual intervention need to go hand in hand. Currently, I place an initial guess of a mesh, deform it, then transplant the deformed mesh to the next frame where it serves as the new initial guess. It would not be hard to automate this process, with manual error correction. A nice aspect of the pipeline is that each finished segmentation is added to the training set of the neural networks. Consequently, the distance transforms are getting iteratively more accurate. This will reduce the amount of manual error correction necessary.

Beyond improvements to the software, improvements will have to be made to the imaging process if we are to apply these tools to larger structures, on longer timescales. The movies pro-

vided by Ms. Weberling and Dr. Molé were produced by confocal microscope. Consequently, the signal to noise ratio was often low, and the frame rate and movie length was limited by phototoxicity and bleaching. More advanced microscopy techniques, e.g. Selective Plane Illumination Microscopy (SPIM) [82], would greatly reduce the exposure of the sample to laser light. This would allow us to increase the signal to noise ratio, and take longer movies.

The segmentation and analysis pipeline tells us several things that we could not see by eye alone. Firstly, it allows us to quantify results that we could observe qualitatively in 2D slices or projections, e.g. measuring the actual volume of the cells over time, instead of just observing that they grow. Secondly, with the pipeline we can rule out observables that we might have expected to be informative based on qualitative analyses. For example, by eye we expected the sphericity of the cells to differ between WT and KO movies, but when quantified we found this to be untrue. Finally, we have performed measurements that could only be done with our pipeline. For example, calculating the polarity of a cell by integrating the fluorescence over its surface is a non-trivial calculation that would be very difficult to do without our novel tools.

9.3 Computational tissue mechanics

The vast majority of experimentally relevant tissue mechanics problems cannot be solved analytically. As such, there is a pressing need for realistic computational methods, with the competing demand that they must be efficient. The major inspiration for the 2D Spline Model (and to a lesser extent for Dr. Torres-Sanchéz's Interacting Active Surfaces Model) was the Vertex Model. The Vertex Model is a popular and effective model of epithelial dynamics, which achieves computational efficiency by describing cells with only a few points forming the vertices of polygons. In our work, we borrow the idea of describing cell boundaries with a few points, while changing two of the Vertex Model's assumptions, that cells are polygonal and confluent, in order to describe non-epithelial cells. By describing cell boundaries as continuous curves with sufficient smoothness, the Spline Model has the attractive capability of including active bending moments, which play an important role in the physics of active surfaces [81] [164] [197]. Furthermore, the Spline Model can describe a much broader range of cell morphologies. In replacing the confluent cells of the Vertex Model with separate cells that interact via adhesion and steric repulsion forces, we can model processes inaccessible to the Vertex Model, e.g. the separation of cells during cavity formation. However, interactions incur a major cost in that they are a pairwise operation, hence scale quadratically with the size of the system. A significant part of the development of the Spline Model was devoted to finding efficient ways to compute the interaction forces.

The resulting simulations successfully address the aims of the project. The Spline Model can simulate large numbers of interacting cells, with flexible morphologies, in a reasonable amount of time ($\approx$ 10 hours on a 32 core computing node). However, the model is less efficient than a similar Vertex Model, due to the costly calculation of pairwise interactions. The obvious next step in modelling cell aggregates was to build a 3D model. This was done by Dr. Torres-Sanchéz with the IAS Model. The IAS Model has similar design principles to the Spline Model, namely describing a smooth surface as the summation of basis functions over a set of discrete points. The cells experience adhesion and steric repulsion forces via a Morse potential, just like the Spline Model. The move from a confluent tissue to interacting cells pays dividends in 3D, where we are able to sidestep the major obstacle of 3D topological transitions. In fact, the need to avoid 3D topological transitions was one of the key motivations for the conception of the Spline Model.

I believe both the Spline Model and IAS Model have very broad applicability to problems in biophysics. Whether the Spline Model will be useful for modelling pseudo-2D systems (e.g. cell monolayers), or will mainly serve as a prototyping tool for simulations that will eventually be run in the IAS Model, remains to be seen. What work now needs to be done? The most important next step is to encourage uptake of our models by the biophysics community. This will be done by releasing our models as open source code, in conjunction with a publication (in preparation). We can maximise uptake by presenting the models in a format that is easy to use, and easy to modify. In addition to this, it is always beneficial to improve computational efficiency. Building techniques from the Spline Model, e.g. grid coordinates, or storing nearest neighbours, into the parallelised FEM framework of the IAS Model would speed up the 3D simulations. Another interesting extension to both models would be adding an explicit description of flows in the surrounding fluid, and concentration fields to the cell surfaces. This would allow the models to include signalling and pattern formation mechanisms described by reaction-diffusion equations.

9.4 Modelling mESC aggregates

Although biophysical models are greatly simplified representations of reality, when successful they allow us to identify a minimal set of mechanisms necessary to recapitulate experimentally observed phenomena. This is what we are trying to achieve in studying the growth of mESC aggregates. We have been successful in reproducing several aspects of mESC aggregate growth: apicobasal polarity dynamics, cell shape deformations, and cell rearrangements. We have also been able to use the analysis tools developed in Chapter 5 to make detailed, quantitative comparisons between simulations and experiments. This is an important achievement. However, a key goal of this project is to build a simulation that starts with a single cell, divides several times, and forms a rosette. I have not yet achieved this. Cell divisions have proven to be particularly challenging to model in 3D, as they are a large and rapid change in the cell shape. This results in large forces which either cause numerical errors, or an unfeasibly small time step. However, other than this practical difficulty, I believe I have all of the ingredients necessary to simulate a rosette. I have shown that the polarity dynamics that place the basal domain in contact with the ECM are believable, that the Polar IAS Model is capable of reproducing realistic cell shapes, and that polarity-adhesion coupling is capable of transforming an extended configuration of cells (e.g. a line of 8) into a rosette. Furthermore, the 2D simulations which do include cell division show a clear difference between compact aggregates with polarity-adhesion coupling, and extended aggregates without.

A further challenge remains in that even if I produce a simulation of a single cell growing into a rosette as a result of polarity-adhesion coupling, I will have demonstrated *a* mechanism. How do I then provide evidence that it is *the* mechanism that occurs in nature? Making a range of quantitative comparisons between the simulations and experiments, and reproducing the behaviour of perturbation experiments (e.g. the β1-KOs) are two important ways. Furthermore, I could make predictions about new experimental scenarios (e.g. mixing cells with differential adhesion strengths, a WT-KO chimera being one possibility) and compare these with experiments. Testing and eliminating alternative mechanisms (e.g. coupling between polarity and surface tension, or cells rearranging randomly) could also play an important role, however this comes with the challenge that there will always be alternative mechanisms to test.

Looking to the future, I hope that this project will demonstrate the utility of the Polar IAS Model, and the analysis pipeline, in building quantitative models of tissue mechanics. I would be excited to extend this work to the more complex embryonic organoids of Harrison et al. [74], and Sozen et al. [185]. In principle, the parallelised nature of the IAS Model will allow

it to model the roughly 100 cells in such aggregates. Gaining a quantitative, and causative, understanding of the self organisation of mESC aggregates will be greatly beneficial to the engineering of increasingly complex embryonic organoids.

9.5 Concluding remarks

In this thesis, I have summarised my efforts in studying the self organisation of cellular systems, with a particular emphasis on mESC aggregates. I hope I have made a small contribution to improving the state of the art in the fields of active matter hydrodynamics, image analysis and computational tissue mechanics. I also hope that my work demonstrates the utility of concepts from theoretical physics for understanding biological systems.

Appendix A

Hydrodynamics

Here I include details of calculations referred to in the main body of the text.

A.1 Linear stability of passive, apolar, impermeable cells

Impermeable cells are described by the limit $\Lambda^{\rm s} = \Lambda^{\rm sm,\xi} = \Lambda^{\rm w} = 0$. The passive limit corresponds to $\Delta\mu = 0$. The incompressibility condition is

$$\partial_\alpha u_\alpha = 0. \tag{A.1}$$

The force balance equation is

$$\partial_\beta \sigma^{\rm Tot}_{\alpha\beta} = 0 \tag{A.2}$$

$$\implies \partial^2_\alpha P = \partial^2_\alpha \partial_\beta v_\beta. \tag{A.3}$$

With appropriate boundary conditions this can be integrated to $P = \partial_\beta v_\beta$. The equilibrium pressure is given in Eq. 4.61 as

$$P^e = P^{\rm m} + kTnZ(\phi), \tag{A.4}$$

where we have set $K^{\rm c} = 0$. Hence, the hydrodynamic equations are

$$\frac{dn}{dt} = -\partial_\alpha(nv_\alpha) \tag{A.5}$$

$$\frac{dn^{\rm sm}}{dt} = -\partial_\alpha(n^{\rm sm} v^{\rm sm0}_\alpha) \tag{A.6}$$

$$\begin{aligned} v^{\rm sm,0}_\alpha =& \frac{v^{\rm c}(1-\phi)(\xi^{\rm sw}v^{\rm c} - \xi^{\rm s}v^{\rm s})}{\xi(\xi^{\rm s}\phi v^{\rm s} + v^{\rm c}\xi^{\rm sw}(1-\phi))}\left[n\partial_\alpha\mu + \phi\partial_\alpha(P-P^e) - \partial_\beta\tilde{\sigma}_{\alpha\beta}\right] \\ & - \frac{1-\phi}{n^{\rm sm}\left[\xi^{\rm sw}(1-\phi) + \xi^{\rm s}\phi\frac{v^{\rm s}}{v^{\rm c}}\right]}\left[n^{\rm sm}\partial_\alpha\mu^{\rm sm} + (1-\phi)\bar{\phi}^{\rm sm}\partial_\alpha(P-P^e)\right] \end{aligned} \tag{A.7}$$

$$\begin{aligned} v_\alpha =& -\frac{(1-\phi)}{n\xi}\left[n\partial_\alpha\mu + \phi\partial_\alpha(P-P^e) - \partial_\beta\tilde{\sigma}_{\alpha\beta}\right] \\ & + \frac{v^{\rm s}\phi(1-\phi)(\xi-\xi^{\rm s})}{\xi n\left[\xi^{\rm s}\phi v^{\rm s} + v^{\rm c}\xi^{\rm sw}(1-\phi)\right]}\left[n^{\rm sm}\partial_\alpha\mu^{\rm sm} + (1-\phi)\bar{\phi}^{\rm sm}\partial_\alpha(P-P^e)\right] \end{aligned} \tag{A.8}$$

The cell stress can be written

$$-\partial_\beta\sigma^c_{\alpha\beta} = n\partial_\alpha\mu + \phi\partial_\alpha(P-P^e) - \partial_\beta\tilde{\sigma}_{\alpha\beta} \tag{A.9}$$

$$= (1-\phi)kTz\partial_\alpha n + \phi\eta\partial_\alpha\partial_\beta v_\beta - \eta\partial^2_\beta u_\alpha - 2\eta\partial_\beta\tilde{v}_{\alpha\beta}. \tag{A.10}$$

The solute stress can be written

$$-\partial_\beta \sigma^s_{\alpha\beta} = n^{\rm sm}\partial_\alpha \mu^{\rm sm} + (1-\phi)\bar{\phi}^{\rm sm}\partial_\alpha(P-P^e) \tag{A.11}$$

$$= kT(1-\phi)\partial_\alpha \bar{n}^{\rm sm} + \phi^{\rm sm}\eta\partial_\alpha\partial_\beta v_\beta - kTz\phi^{\rm sm}\partial_\alpha n, \tag{A.12}$$

where the compressibility $z(\phi) = Z(\phi) + \phi Z'(\phi) = 2\phi\tilde{Z}' + \phi^2\tilde{Z}''$. Consequently, the divergences of the cell and solute flux are

$$\partial_\alpha j^{\rm sm}_\alpha = -D^{\rm s}(1-\phi)\partial^2_\alpha \bar{n}^{\rm sm} + D^{\rm s}z\phi^{\rm sm}\left\{1 + \frac{\xi^{\rm sw}v^{\rm c} - \xi^{\rm s}v^{\rm s}}{v^{\rm s}\xi}(1-\phi)\right\}\partial^2_\alpha n$$
$$+ \frac{D^{\rm s}\eta\phi^{\rm sm}}{kT}\left\{-1 + \frac{\xi^{\rm sw}v^{\rm c} - \xi^{\rm s}v^{\rm s}}{v^{\rm s}\xi}\left(\phi - \frac{4}{3}\right)\right\}\partial^2_\alpha\partial_\beta v_\beta \tag{A.13}$$

$$\partial_\alpha(nv_\alpha) = \frac{zkT}{\xi}\left\{-(1-\phi)^2 - \frac{v^{\rm s}n(\xi-\xi^{\rm s})D^{\rm s}\phi^{\rm sm}}{kT}\right\}\partial^2_\alpha n + \frac{D^{\rm s}v^{\rm s}n(1-\phi)(\xi-\xi^{\rm s})}{\xi}\partial^2_\alpha\bar{n}^{\rm sm}$$
$$+ \frac{\eta}{\xi}\left\{-(1-\phi)\left(\phi - \frac{4}{3}\right) + \frac{v^{\rm s}n(\xi-\xi^{\rm s})D^{\rm s}\phi^{\rm sm}}{kT}\right\}\partial^2_\alpha\partial_\beta v_\beta \tag{A.14}$$

These expressions can be simplified by noting

$$\frac{v^{\rm s}n(\xi-\xi^{\rm s})D^{\rm s}\phi^{\rm sm}}{kT} \simeq \frac{a^2}{r^2} \ll 1, \tag{A.15}$$

$$\frac{\xi^{\rm sw}v^{\rm c} - \xi^{\rm s}v^{\rm s}}{\xi v^{\rm s}} \simeq \frac{r^2}{a^2} \gg 1. \tag{A.16}$$

where a is the size of a solute, and r the size of a cell. Hence,

$$\partial_\alpha j^{\rm sm}_\alpha = -D^{\rm s}(1-\phi)\partial^2_\alpha\bar{n}^{\rm sm} + D^{\rm s}z\phi^{\rm sm}\frac{\xi^{\rm sw}v^{\rm c} - \xi^{\rm s}v^{\rm s}}{v^{\rm s}\xi}(1-\phi)\partial^2_\alpha n + \frac{D^{\rm s}\eta\phi^{\rm sm}}{kT}\frac{\xi^{\rm sw}v^{\rm c} - \xi^{\rm s}v^{\rm s}}{v^{\rm s}\xi}\left(\phi - \frac{4}{3}\right)\partial^2_\alpha\partial_\beta v_\beta \tag{A.17}$$

$$\partial_\alpha(nv_\alpha) = -\frac{zkT}{\xi}(1-\phi)^2\partial^2_\alpha n + \frac{D^{\rm s}v^{\rm s}n(1-\phi)(\xi-\xi^{\rm s})}{\xi}\partial^2_\alpha\bar{n}^{\rm sm} - \frac{\eta}{\xi}(1-\phi)\left(\phi - \frac{4}{3}\right)\partial^2_\alpha\partial_\beta v_\beta. \tag{A.18}$$

This brings us to the equations in the main body of the text.

A.2 Polar pumping instability

The hydrodynamic equations are

$$\frac{dn}{dt} = -\partial_\alpha(nv_\alpha) \tag{A.19}$$

$$\frac{dv}{dt} = \Lambda^{\mathrm{w}}\left(kT\left(\bar{n}^{\mathrm{s}}-\bar{n}^{\mathrm{sm}}\right)-kTn\tilde{Z}'(\phi)-f_0^{\mathrm{c}\prime}(v^{\mathrm{c}})+\frac{\Lambda^{\mathrm{wa}}}{\Lambda^{\mathrm{w}}}\Delta\mu\right)+v^{\mathrm{s}}\Lambda^{\mathrm{s}}kT\ln\frac{\bar{n}^{\mathrm{sm}}}{\bar{n}^{\mathrm{s}}}-v^{\mathrm{s}}\Lambda^{\mathrm{sa0}}(v^{\mathrm{c}}-v^{\mathrm{T}})\Delta\mu \tag{A.20}$$

$$\frac{dn^{\mathrm{s}}}{dt} = \Lambda^{\mathrm{s}}kT\ln\frac{\bar{n}^{\mathrm{sm}}}{\bar{n}^{\mathrm{s}}}-\Lambda^{\mathrm{sa0}}(v^{\mathrm{c}}-v^{\mathrm{T}})\Delta\mu \tag{A.21}$$

$$\frac{d\xi_\alpha}{dt} = \frac{\Lambda^{\mathrm{sm},\xi}kT}{\bar{n}^{\mathrm{sm}}}\left(\partial_\alpha\bar{n}^{\mathrm{sm}}-\frac{\xi_\alpha}{v^{\mathrm{c}\frac{2}{3}}}\right)-\frac{D^{\mathrm{s}}}{v^{\mathrm{c}\frac{2}{3}}}\xi_\alpha \tag{A.22}$$

$$\begin{aligned}\frac{dn^{\mathrm{sm}}}{dt} =& \partial_\alpha\left(-n^{\mathrm{sm}}v_\alpha^{\mathrm{sm0}}+\phi\Lambda^{\mathrm{sm},\xi}\left(\partial_\alpha\bar{\mu}^{\mathrm{sm}}+\frac{kT}{K\bar{n}^{\mathrm{sm}}v^{\mathrm{c}\frac{2}{3}}}\chi_\alpha\right)-\lambda^{\mathrm{sa0}}\Delta\mu nn^{\mathrm{sm}}p_\alpha\right)\\ &-\Lambda^{\mathrm{s}}nkT\ln\frac{\bar{n}^{\mathrm{sm}}}{\bar{n}^{\mathrm{s}}}+\Lambda^{\mathrm{sa0}}(v^{\mathrm{c}}-v^{\mathrm{T}})n\Delta\mu\end{aligned} \tag{A.23}$$

$$\frac{Dp_\alpha}{Dt} = -\frac{1}{\tau_p}p_\alpha-\beta p_\beta p_\beta p_\alpha+K\partial_\beta^2p_\alpha-\kappa\partial_\alpha n \tag{A.24}$$

$$\begin{aligned}v_\alpha^{\mathrm{sm},0} =& \frac{D^{\mathrm{s}}(\xi^{\mathrm{sw}}v^{\mathrm{c}}-\xi^{\mathrm{s}}v^{\mathrm{s}})}{\xi kT}\left[n\partial_\alpha\mu+h_\beta\partial_\alpha p_\beta+\phi\partial_\alpha(P-P^e)-\partial_\beta\tilde{\sigma}_{\alpha\beta}\right]\\ &-\frac{D^{\mathrm{s}}}{n^{\mathrm{sm}}kT}\left[n^{\mathrm{sm}}\partial_\alpha\mu^{\mathrm{sm}}+(1-\phi)\bar{\phi}^{\mathrm{sm}}\partial_\alpha(P-P^e)\right]\end{aligned} \tag{A.25}$$

$$\begin{aligned}v_\alpha =& -\frac{D(1-\phi)}{nkT}\left[n\partial_\alpha\mu+h_\beta\partial_\alpha p_\beta+\phi\partial_\alpha(P-P^e)-\partial_\beta\tilde{\sigma}_{\alpha\beta}\right]\\ &+\frac{D^{\mathrm{s}}v^{\mathrm{s}}(\xi-\xi^{\mathrm{s}})}{\xi kT}\left[n^{\mathrm{sm}}\partial_\alpha\mu^{\mathrm{sm}}+(1-\phi)\bar{\phi}^{\mathrm{sm}}\partial_\alpha(P-P^e)\right]\end{aligned} \tag{A.26}$$

It is convenient to construct the following equation

$$\begin{aligned}\frac{d}{dt}\left(n^{\mathrm{sm}}+nn^{\mathrm{s}}-\phi\partial_\alpha\xi_\alpha\right) =& -\partial_\alpha\left\{n^{\mathrm{sm}}v_\alpha^{\mathrm{sm0}}+\lambda^{\mathrm{sa0}}nn^{\mathrm{sm}}\Delta\mu p_\alpha-\frac{\phi D^{\mathrm{s}}}{v^{\mathrm{c}\frac{2}{3}}}\xi_\alpha+n^{\mathrm{s}}nv_\alpha\right\}\\ &+nv_\alpha\partial_\alpha n^{\mathrm{s}}+\partial_\alpha\xi_\alpha\partial_\beta(\phi v_\beta).\end{aligned} \tag{A.27}$$

In the limit of fast volume control, this becomes

$$\begin{aligned}\frac{d}{dt}\left(\bar{n}^{\mathrm{sm}}-\phi\ell^2\partial_\alpha^2\bar{n}^{\mathrm{sm}}\right) =& -\partial_\alpha\left\{n^{\mathrm{sm}}v_\alpha^{\mathrm{sm0}}+\lambda^{\mathrm{sa0}}nn^{\mathrm{sm}}\Delta\mu p_\alpha-\phi D^{\mathrm{s}}\partial_\alpha\bar{n}^{\mathrm{sm}}+n^{\mathrm{s}}nv_\alpha\right\}\\ &+nv_\alpha\partial_\alpha n^{\mathrm{s}}+\partial_\alpha\xi_\alpha\partial_\beta(\phi v_\beta).\end{aligned} \tag{A.28}$$

In the hydrodynamic limit gradients in $\bar{n}^{\mathrm{sm}}$ occur on length scales much larger than ℓ, so we can neglect the second term on the left. Perturbing about a steady state and truncating to linear order, the hydrodynamic equations then become

$$\partial_t\delta n = -n\partial_\alpha\delta v_\alpha \tag{A.29}$$

$$\partial_t\delta\bar{n}^{\mathrm{sm}} = -\partial_\alpha\left\{n^{\mathrm{sm}}\delta v_\alpha^{\mathrm{sm0}}+\lambda^{\mathrm{sa0}}nn^{\mathrm{sm}}\Delta\mu\delta p_\alpha-\phi D^{\mathrm{s}}\partial_\alpha\delta\bar{n}^{\mathrm{sm}}+n^{\mathrm{s}}n\delta v_\alpha\right\} \tag{A.30}$$

$$\partial_t\delta p_\alpha = \frac{-1}{\tau^{\mathrm{p}}}\delta p_\alpha+K\partial_\beta^2\delta p_\alpha-\kappa\partial_\alpha\delta n \tag{A.31}$$

Next we calculate the fluxes of cells and solutes. To linear order, the divergence of the cell stress is

$$-\partial_\beta \sigma^c_{\alpha\beta} = n\partial_\alpha \mu + \phi\partial_\alpha(P - P^e) - \partial_\beta \tilde{\sigma}_{\alpha\beta} \tag{A.32}$$

$$= (1-\phi)kTz\partial_\alpha n + \phi\eta\partial_\alpha\partial_\beta v_\beta - \eta\partial^2_\beta u_\alpha - 2\eta\partial_\beta \tilde{v}_{\alpha\beta}. \tag{A.33}$$

To linear order the divergence of the solute stress is

$$-\partial_\beta \sigma^s_{\alpha\beta} = n^{\mathrm{sm}}\partial_\alpha \mu^{\mathrm{sm}} + (1-\phi)\bar{\phi}^{\mathrm{sm}}\partial_\alpha(P - P^e) \tag{A.34}$$

$$= kT(1-\phi)\partial_\alpha \bar{n}^{\mathrm{sm}} + \phi^{\mathrm{sm}}\eta\partial_\alpha\partial_\beta v_\beta - kTz\phi^{\mathrm{sm}}\partial_\alpha n. \tag{A.35}$$

Note that we have neglected K^{c} as it does not affect the stability at low wave number. These expressions are identical to those in the impermeable cell calculation. Following the same steps as the impermeable cell calculation, we get, to linear order,

$$\begin{aligned}\partial_\alpha(n^{\mathrm{sm}} v^{\mathrm{sm0}}_\alpha) =& -D^{\mathrm{s}}(1-\phi)\partial^2_\alpha \bar{n}^{\mathrm{sm}} + D^{\mathrm{s}} z\phi^{\mathrm{sm}} \frac{\xi^{\mathrm{sw}} v^{\mathrm{c}} - \xi^{\mathrm{s}} v^{\mathrm{s}}}{v^{\mathrm{s}}\xi}(1-\phi)\partial^2_\alpha n \\ &+ \frac{D^{\mathrm{s}}\eta\phi^{\mathrm{sm}}}{kT}\frac{\xi^{\mathrm{sw}} v^{\mathrm{c}} - \xi^{\mathrm{s}} v^{\mathrm{s}}}{v^{\mathrm{s}}\xi}\left(\phi - \frac{4}{3}\right)\partial^2_\alpha \partial_\beta v_\beta \end{aligned} \tag{A.36}$$

$$n\partial_\alpha(v_\alpha) + n\ell_p^2\partial^2_\alpha\partial_\beta v_\beta = -\frac{zkT}{\xi}(1-\phi)^2\partial^2_\alpha n + \frac{D^{\mathrm{s}} v^{\mathrm{s}} n(1-\phi)(\xi - \xi^{\mathrm{s}})}{\xi}\partial^2_\alpha \bar{n}^{\mathrm{sm}}, \tag{A.37}$$

where $\ell_p^2 = \frac{\eta v^{\mathrm{c}}}{\xi\phi}(1-\phi)\left(\phi - \frac{4}{3}\right)$ is the permeation length. Fourier transforming in space like so, $\delta\tilde{n} = \frac{1}{\sqrt{2\pi}}\int e^{-i\mathbf{q}\cdot\mathbf{r}}\delta n d\mathbf{r}$, $\delta\tilde{n}^{\mathrm{sm}} = \frac{1}{\sqrt{2\pi}}\int e^{-i\mathbf{q}\cdot\mathbf{r}}\delta\bar{n}^{\mathrm{sm}} d\mathbf{r}$, $\delta\tilde{\rho} = \frac{1}{\sqrt{2\pi}}\int e^{-i\mathbf{q}\cdot\mathbf{r}}\delta\partial_\alpha p_\alpha d\mathbf{r}$, perturbing about a steady state, and truncating to linear order, we get

$$\partial_t\delta\tilde{n} = \frac{1}{1-\ell_p^2 q^2}\left\{-zD(1-\phi)^2 q^2\delta\tilde{n} + D^{\mathrm{s}} v^{\mathrm{s}} n(1-\phi)\left(\frac{\xi^s}{\xi} - 1\right)q^2\delta\tilde{n}^{\mathrm{sm}}\right\} \tag{A.38}$$

$$\begin{aligned}\partial_t\delta\tilde{n}^{\mathrm{sm}} =& -\left\{D^{\mathrm{s}} + \frac{(Aq^2 + n^{\mathrm{s}}n)}{n - n\ell_p^2 q^2}\frac{D^{\mathrm{s}} v^{\mathrm{s}} n(1-\phi)(\xi - \xi^{\mathrm{s}})}{\xi}\right\}q^2\delta\tilde{n}^{\mathrm{sm}} \\ &+ \left\{B + \frac{Aq^2 + n^{\mathrm{s}}n}{n - n\ell_p^2 q^2} zD(1-\phi)^2\right\}q^2\delta\tilde{n} + \lambda^{\mathrm{sa0}} n n^{\mathrm{sm}}\Delta\mu\delta\tilde{\rho}\end{aligned} \tag{A.39}$$

$$\partial_t\delta\tilde{\rho} = -\frac{1}{\tau^{\mathrm{p}}}\delta\tilde{\rho} - Kq^2\delta\tilde{\rho} + \kappa q^2\delta\tilde{n}. \tag{A.40}$$

The polarity relaxation timescale $\tau^{\mathrm{p}} = \frac{\gamma_1}{\alpha}$, and the modified Frank constant $K = \frac{K^{\mathrm{p}}}{\gamma_1}$. For readability, we have introduced the constants $A = \frac{D^{\mathrm{s}}\eta\phi^{\mathrm{sm}}(\xi^{\mathrm{sw}} v^{\mathrm{c}} - \xi^{\mathrm{s}} v^{\mathrm{s}})}{kTv^{\mathrm{s}}\xi}\left(\phi - \frac{4}{3}\right)$, and $B = D^{\mathrm{s}} z\phi^{\mathrm{sm}}(1-\phi)\frac{\xi^{\mathrm{sw}} v^{\mathrm{c}} - \xi^{\mathrm{s}} v^{\mathrm{s}}}{v^{\mathrm{s}}\xi}$. At $\lambda^{\mathrm{sa0}} = 0$, the system has three negative eigenvalues. One corresponds to the relaxation dynamics of the polarity field. The other two correspond to the diffusion of cells and solutes. As λ^{sa0} increases, one of the diffusion eigenvalues becomes positive. However, at $q^2 = 0$, both diffusion eigenvalues remain zero. Consequently this system of equations has a Type II instability at high λ^{sa0}, hence we can consider the behaviour at small q^2. Truncating to lowest order in q^2, we get

$$\partial_t\delta\tilde{n} = -zD(1-\phi)^2 q^2\delta\tilde{n} + D^{\mathrm{s}} v^{\mathrm{s}} n(1-\phi)\left(\frac{\xi^s}{\xi} - 1\right)q^2\delta\tilde{n}^{\mathrm{sm}} \tag{A.41}$$

$$\partial_t\delta\tilde{n}^{\mathrm{sm}} = -\left\{1 - n^{\mathrm{s}} n v^{\mathrm{s}}(1-\phi)\left(\frac{\xi^{\mathrm{s}}}{\xi} - 1\right)\right\}D^{\mathrm{s}} q^2\delta\tilde{n}^{\mathrm{sm}} + \left\{B + n^{\mathrm{s}} zD(1-\phi)^2\right\}q^2\delta\tilde{n} + \lambda^{\mathrm{sa0}} n n^{\mathrm{sm}}\Delta\mu\delta\tilde{\rho} \tag{A.42}$$

$$\partial_t\delta\tilde{\rho} = -\frac{1}{\tau^{\mathrm{p}}}\delta\tilde{\rho} - Kq^2\delta\tilde{\rho} + \kappa q^2\delta\tilde{n}. \tag{A.43}$$

Substituting a trial solution of the form $\delta\tilde{n}(\mathbf{q},t) = e^{\lambda t}\delta\tilde{n}(\mathbf{q})$, etc., these equations can be written as the eigenvalue problem

$$\lambda \begin{pmatrix} \delta\tilde{n} \\ \delta\tilde{n}^{\mathrm{sm}} \\ \delta\tilde{\rho} \end{pmatrix} = \begin{pmatrix} a & b & 0 \\ c & d & e \\ f & 0 & g \end{pmatrix} \begin{pmatrix} \delta\tilde{n} \\ \delta\tilde{n}^{\mathrm{sm}} \\ \delta\tilde{\rho} \end{pmatrix}, \tag{A.44}$$

where the elements of the matrix can be read from Eq. A.41 - A.43. The eigenvalues are given by the roots of the characteristic polynomial

$$\begin{aligned} P(\lambda) &= bef + (g-\lambda)(ad - bc - (a+d)\lambda + \lambda^2) && \text{(A.45)} \\ &= bef + Q(\lambda) && \text{(A.46)} \\ &= 0. && \text{(A.47)} \end{aligned}$$

A positive eigenvalue exists for $-bef < Q(0)$. This condition is equivalent to

$$\lambda^{\mathrm{sa0}}\Delta\mu > \left(\frac{1}{\tau^{\mathrm{p}}} + Kq^2\right)\frac{\Phi}{\kappa} \tag{A.48}$$

where

$$\begin{aligned} \Phi = \frac{z(\phi)}{v^{\mathrm{s}}n^2 n^{\mathrm{sm}}\left(\frac{\xi^{\mathrm{s}}}{\xi}-1\right)}\Bigg\{ & D(1-\phi)\left[1 - n^{\mathrm{s}}nv^{\mathrm{s}}(1-\phi)\left(\frac{\xi^{\mathrm{s}}}{\xi}-1\right)\right] \\ & - v^{\mathrm{s}}n\left(\frac{\xi^{\mathrm{s}}}{\xi}-1\right)\left[D^{\mathrm{s}}\phi^{\mathrm{sm}}(1-\phi)\left(\frac{\xi^{\mathrm{sw}}v^{\mathrm{c}} - \xi^{\mathrm{s}}v^{\mathrm{s}}}{\xi v^{\mathrm{s}}}\right) + n^{\mathrm{s}}D(1-\phi)^2\right]\Bigg\}. \end{aligned} \tag{A.49}$$

A.2.1 Numerical evaluation of the pumping instability

This expression can be related to an approximate solute pumping rate per cell by considering the pumping flux j_α^{p} in response to a step function tissue boundary. Neglecting the Frank term, the polarity dynamics are $\partial_t p_\alpha = \frac{-1}{\tau^{\mathrm{p}}}p_\alpha - \frac{\kappa}{v}\partial_\alpha\phi$. The polarity, $\bar{p}$, induced by a 1D tissue boundary that goes from $\phi \approx 1$ to $\phi \approx 0$ across a length scale of one cell is

$$\bar{p} = \frac{\kappa\tau^{\mathrm{p}}}{v^{\mathrm{c}\frac{4}{3}}}. \tag{A.50}$$

The flux of solutes pumped by a single cell is $\sigma|\mathbf{j}^p| = \sigma\lambda^{\mathrm{sa0}}\Delta\mu n n^{\mathrm{sm}}\bar{p} = N^{\mathrm{p}}$, where σ is the cross sectional area of the cell. Hence,

$$N^{\mathrm{p}} = \frac{\pi\lambda^{\mathrm{sa0}}\Delta\mu n n^{\mathrm{sm}}\kappa\tau^{\mathrm{p}}}{v^{\mathrm{c}\frac{2}{3}}}. \tag{A.51}$$

To evaluate N^{p} we use the following parameter values

Parameter	Value
v^{c}	$10^{-15}\,\mathrm{m}^3$
v^{s}	$10^{-29}\,\mathrm{m}^3$
D	$10^{-14}\,\mathrm{m}^2\,\mathrm{s}^{-1}$
D^{s}	$10^{-10}\,\mathrm{m}^2\,\mathrm{s}^{-1}$
η^{w}	$10^{-3}\,\mathrm{Pa\,s}$

Furthermore we take $\xi^{\mathrm{s}} = 3\xi$, $\xi = 6\pi\eta^{\mathrm{w}} v^{\mathrm{c}\frac{1}{3}}$, and $\xi^{\mathrm{sw}} = 6\pi\eta^{\mathrm{w}} v^{\mathrm{s}\frac{1}{3}}$. For the volume fractions we use $\phi = 0.5$, $\phi^{\mathrm{sm}} = 0.1$, $\bar{\phi}^{\mathrm{s}} = \frac{n^{\mathrm{s}} v^{\mathrm{s}}}{v} = 0.1$. For the incompressibility factor, we take $z = 0.1$, where $z = 0$ is the boundary of spinodal stability. Consequently, the boundary of stability in the limit $|\mathbf{q}| \to 0$ is

$$N^{\mathrm{p}} > \frac{\pi n n^{\mathrm{sm}} \Phi}{v^{\mathrm{c}\frac{2}{3}}} \approx 10^9\,\mathrm{s}^{-1}. \tag{A.52}$$

Appendix B

Parameter sets

B.1 The 2D Spline Model

Note that the parameter values for the 2D Spline Model were chosen for demonstration purposes only, hence are in some cases wildly unphysical.

B.1.1 Simulation in Fig. 6.8

Parameter	Value
K	$0.1\,\mathrm{kg\,\mu m^{-2}\,s^{-2}}$
A_0	$6.5 \times 10^3\,\mathrm{\mu m^2}$
γ	$10,\ 100,\ 1000\,\mathrm{kg\,\mu m\,s^{-2}}$
κ	$5 \times 10^{-2}\,\mathrm{kg\,\mu m\,s^{-2}}$
D	$5\,\mathrm{kg\,s^{-2}}$
a	$1.84\,\mathrm{\mu m^{-1}}$
r_m	$1.9\,\mathrm{\mu m}$

B.1.2 Simulation in Fig. 6.9

Parameter	Value
K	$0.1\,\mathrm{kg\,\mu m^{-2}\,s^{-2}}$
A_0	$6.5 \times 10^3\,\mathrm{\mu m^2}$
γ	$1\,\mathrm{kg\,\mu m\,s^{-2}}$
κ	$5 \times 10^{-2}\,\mathrm{kg\,\mu m\,s^{-2}}$
D	$2\,\mathrm{kg\,s^{-2}}$
a	$2\,\mathrm{\mu m^{-1}}$
r_m	$4\,\mathrm{\mu m}$

B.1.3 Simulation in Fig. 7.4

Parameter	Value
K	$0.1\,\mathrm{kg\,\mu m^{-2}\,s^{-2}}$
A_0	$6.5 \times 10^3\,\mu\mathrm{m}^2$
γ	$1\,\mathrm{kg\,\mu m\,s^{-2}}$
κ	$5 \times 10^{-2}\,\mathrm{kg\,\mu m\,s^{-2}}$
D	$2\,\mathrm{kg\,s^{-2}}$
a	$2\,\mu\mathrm{m}^{-1}$
r_m	$4\,\mu\mathrm{m}$
ΔD	0.9
θ^*	$\frac{\pi}{4}$ rad

B.1.4 Simulation in Fig. 7.5

Parameter	Value
K	$0.1\,\mathrm{kg\,\mu m^{-2}\,s^{-2}}$
A_0	$6.5 \times 10^3\,\mu\mathrm{m}^2$
γ	$1\,\mathrm{kg\,\mu m\,s^{-2}}$
κ	$5 \times 10^{-2}\,\mathrm{kg\,\mu m\,s^{-2}}$
D	$2\,\mathrm{kg\,s^{-2}}$
a	$2\,\mu\mathrm{m}^{-1}$
r_m	$4\,\mu\mathrm{m}$
ΔD	0.9
θ^*	$\frac{\pi}{4}$ rad

B.1.5 Simulation in Fig. 7.7

Parameter	Value
K	$0.1\,\mathrm{kg\,\mu m^{-2}\,s^{-2}}$
A_0	$6.5 \times 10^3\,\mu\mathrm{m}^2$
γ	$1\,\mathrm{kg\,\mu m\,s^{-2}}$
κ	$5 \times 10^{-2}\,\mathrm{kg\,\mu m\,s^{-2}}$
D	$2\,\mathrm{kg\,s^{-2}}$
a	$2\,\mu\mathrm{m}^{-1}$
r_m	$4\,\mu\mathrm{m}$
ΔD	0.9, 0
θ^*	1.4 rad

B.1.6 Simulation in Fig. 7.17

Parameter	Value
$\hat{D}$	0.56
ΔD	0.5
θ^*	45°

Appendix C

Quantification of mESC aggregate growth

Here I list plots of the various variables detailed in Chapter 5, for all movies in my segmented dataset. This consists of 6 WT movies, 4 of which form rosettes, and 3 β1-KO movies.

C.0.1 Cell volume

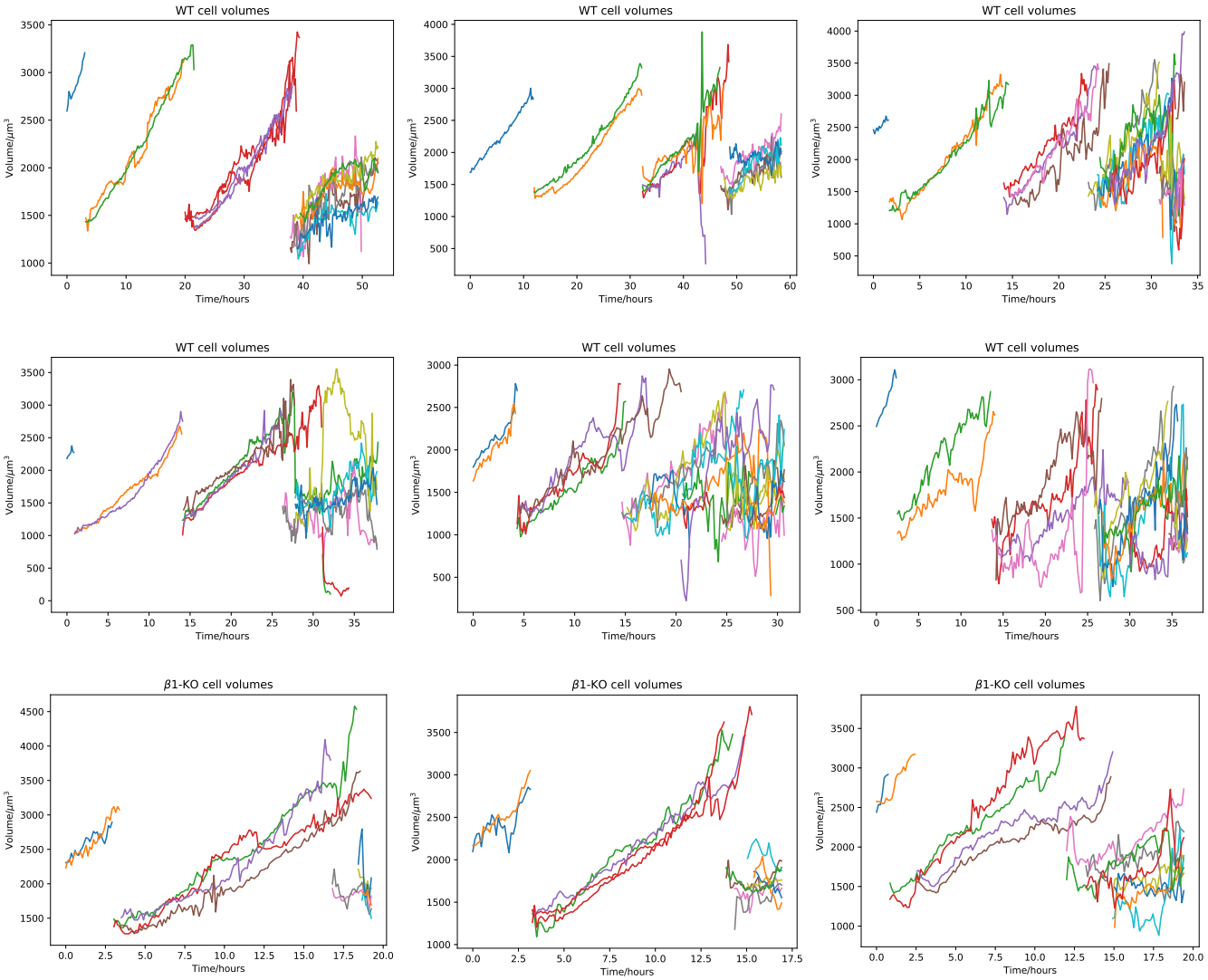

Figure C.1

C.0.2 Sphericity

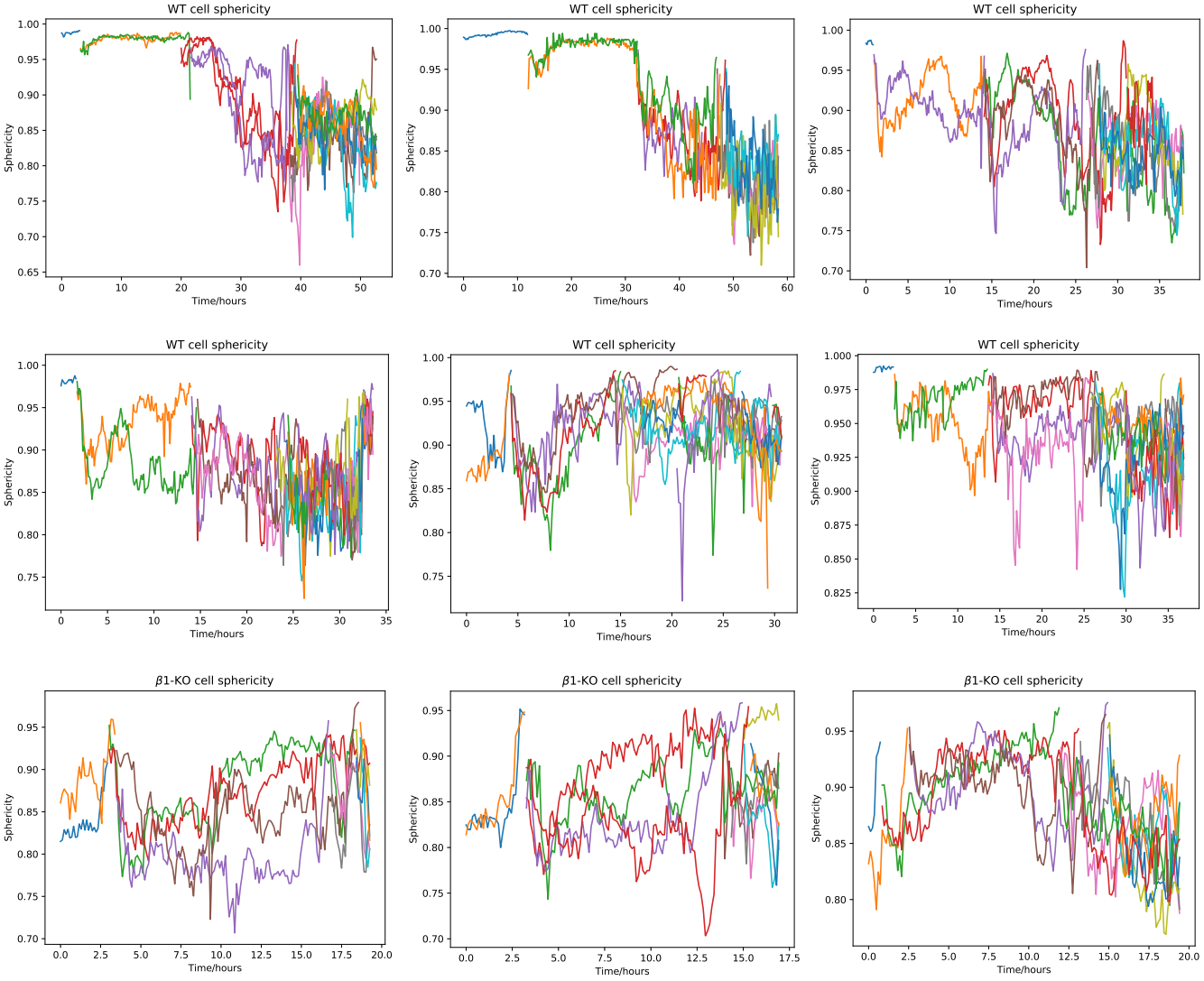

Figure C.2

C.0.3 Neighbour count

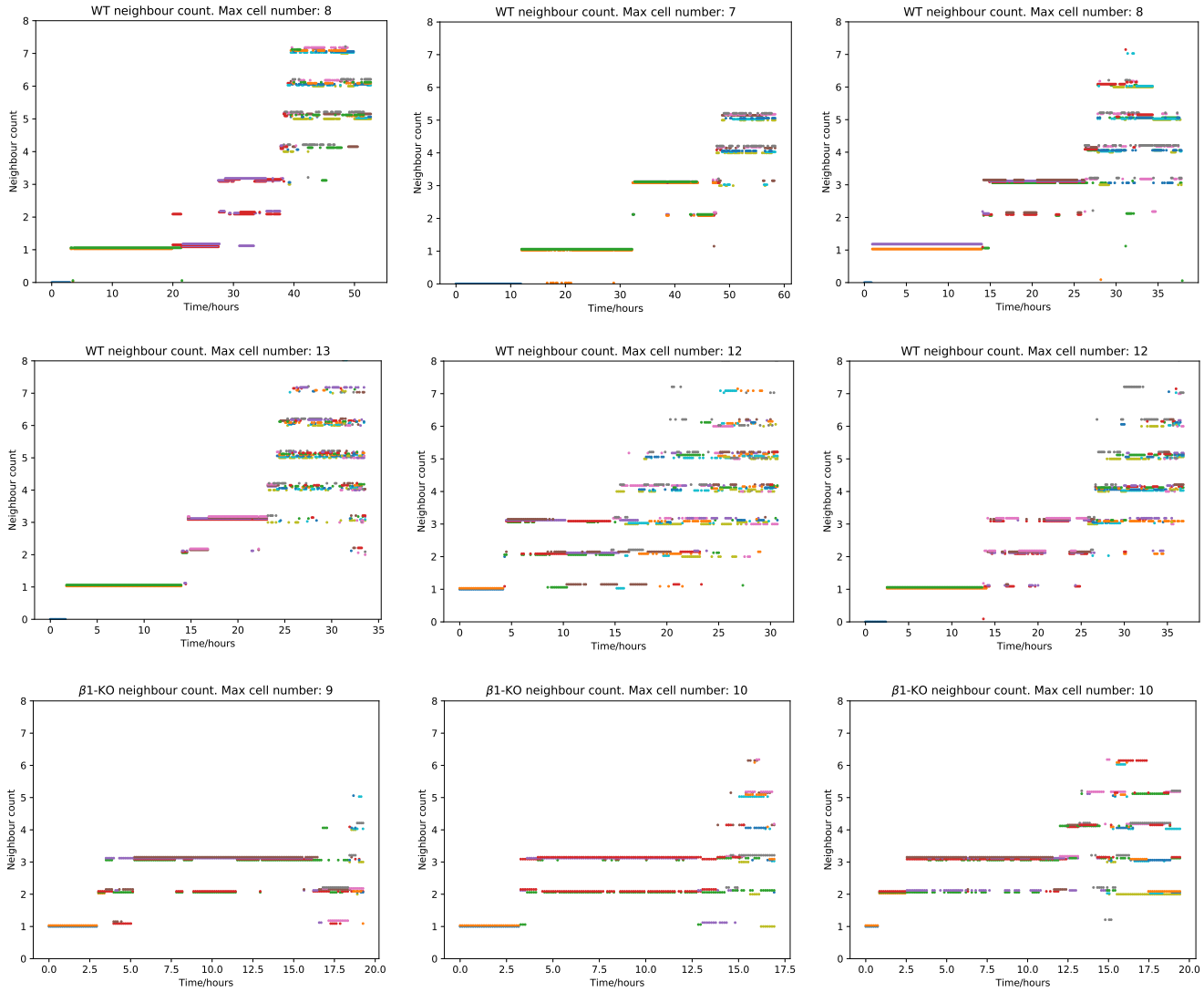

Figure C.3

C.0.4 Cell centres

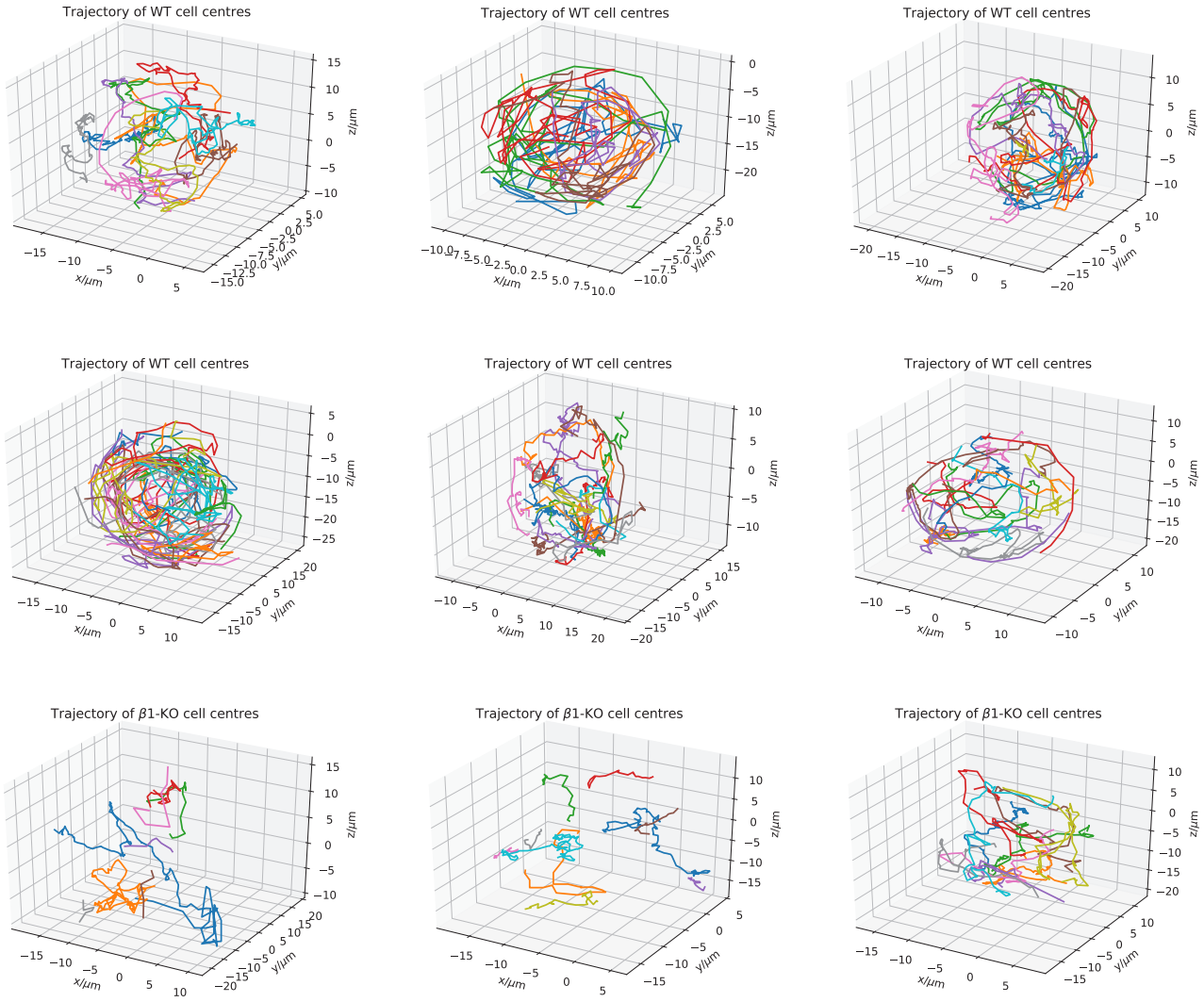

Figure C.4

C.0.5 Polar angle distribution

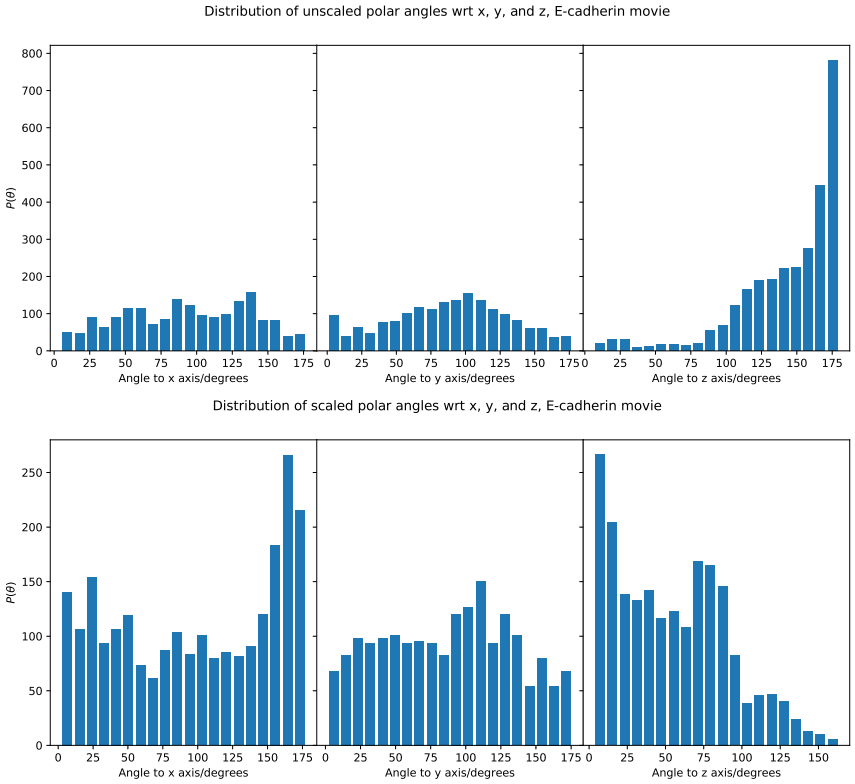

Figure C.5

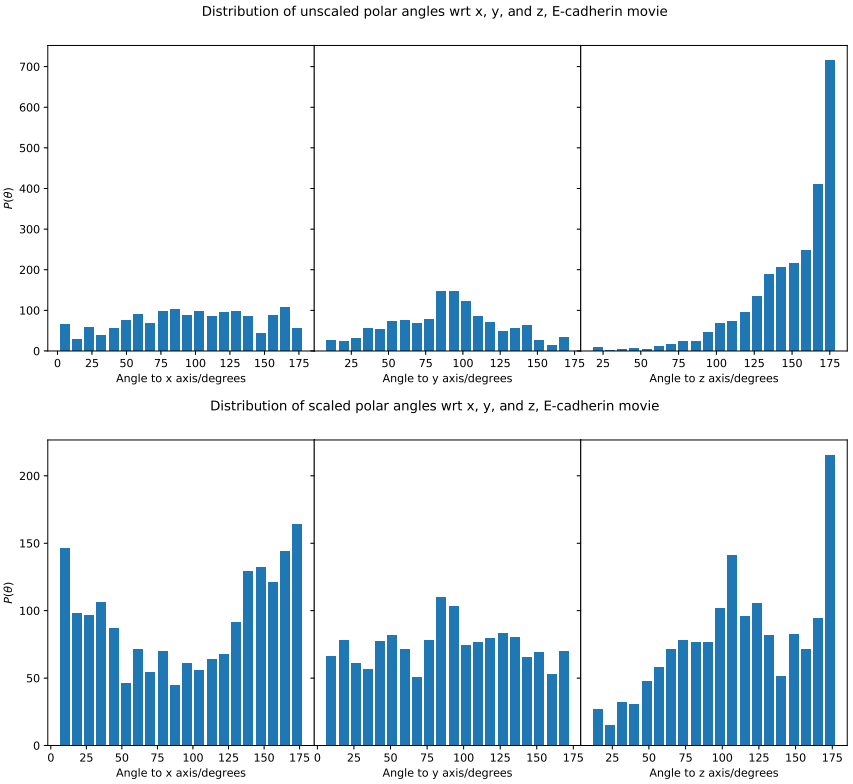

Figure C.6

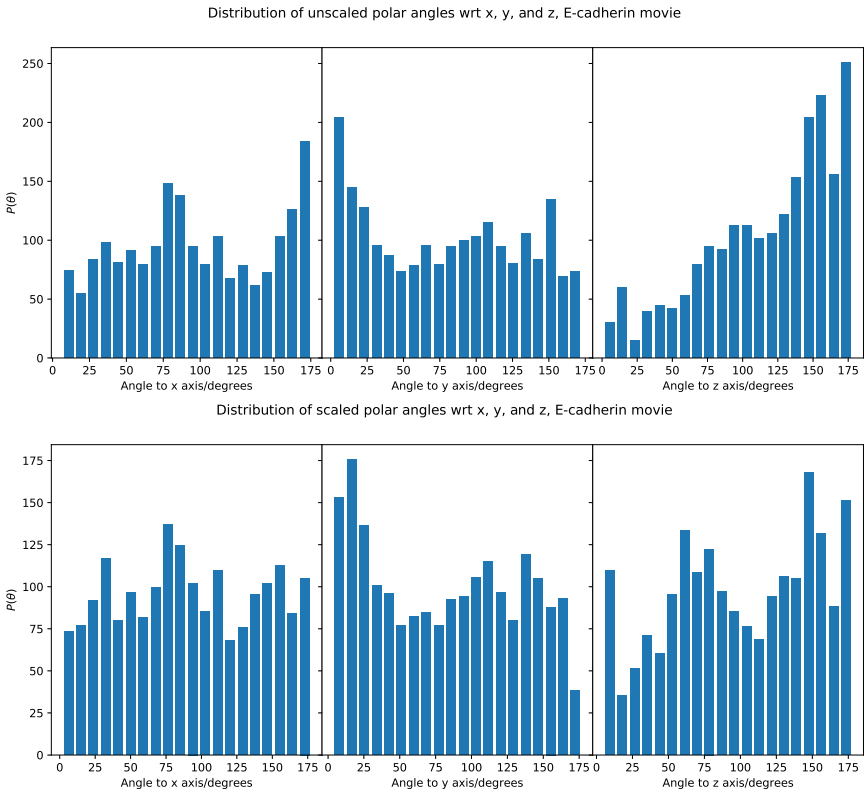

Figure C.7

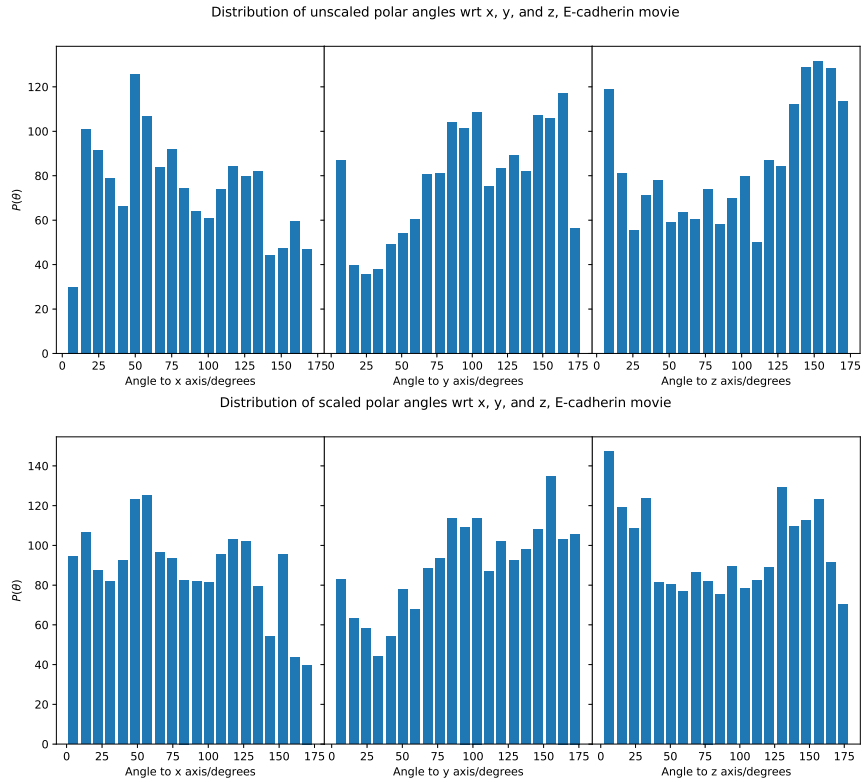

Figure C.8

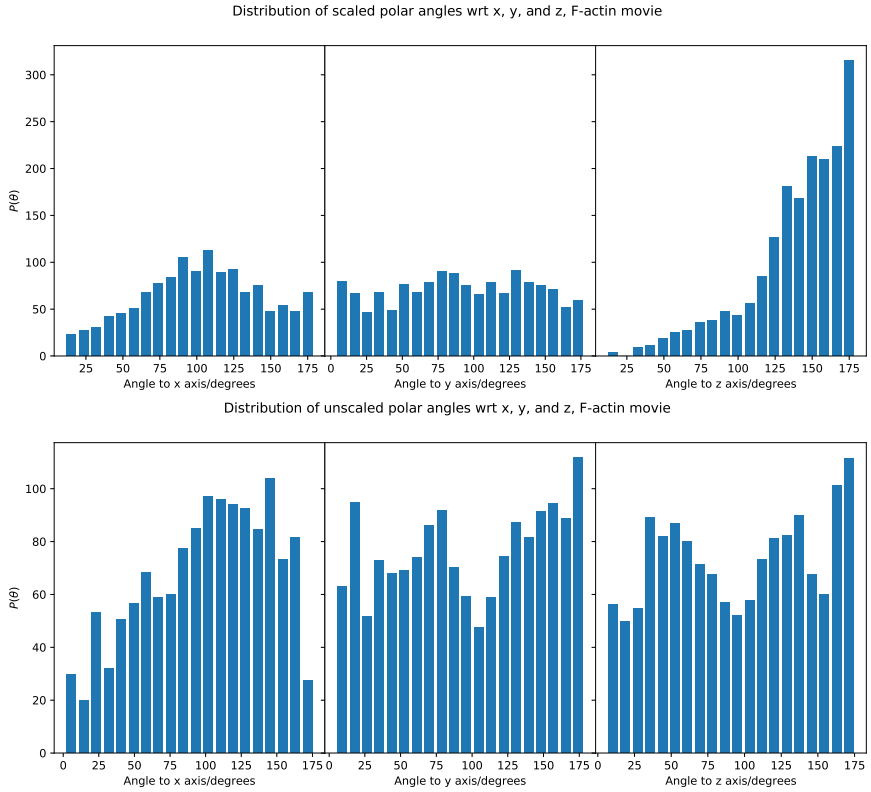

Figure C.9

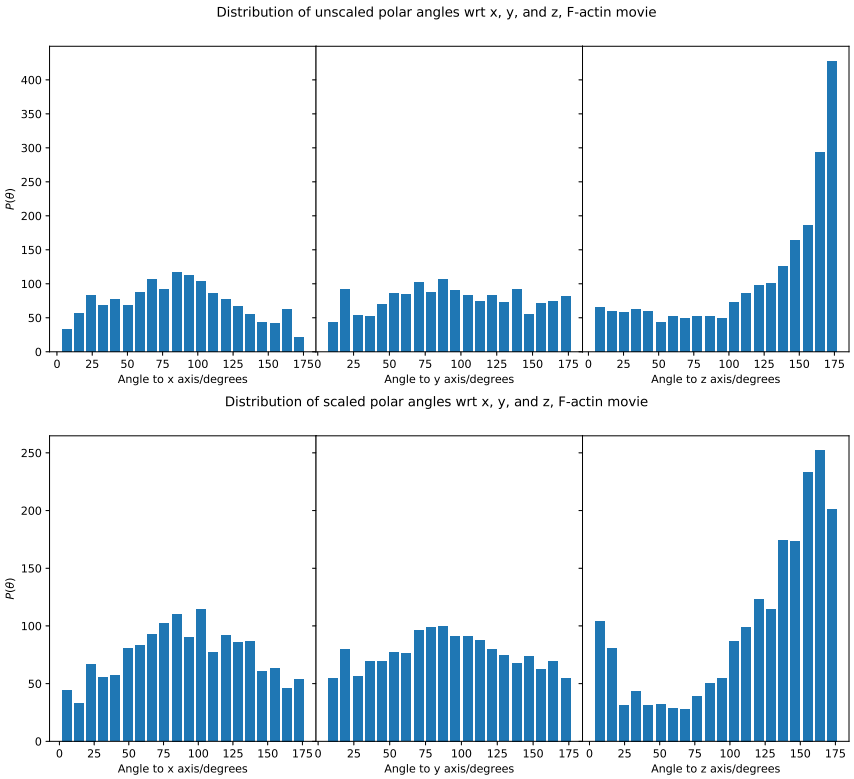

Figure C.10

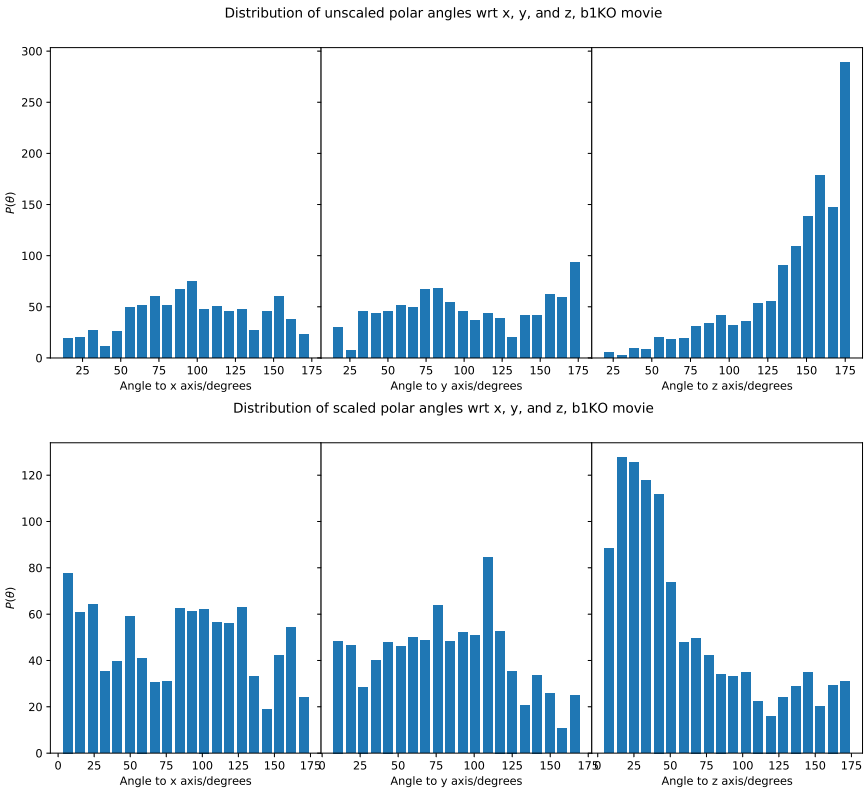

Figure C.11

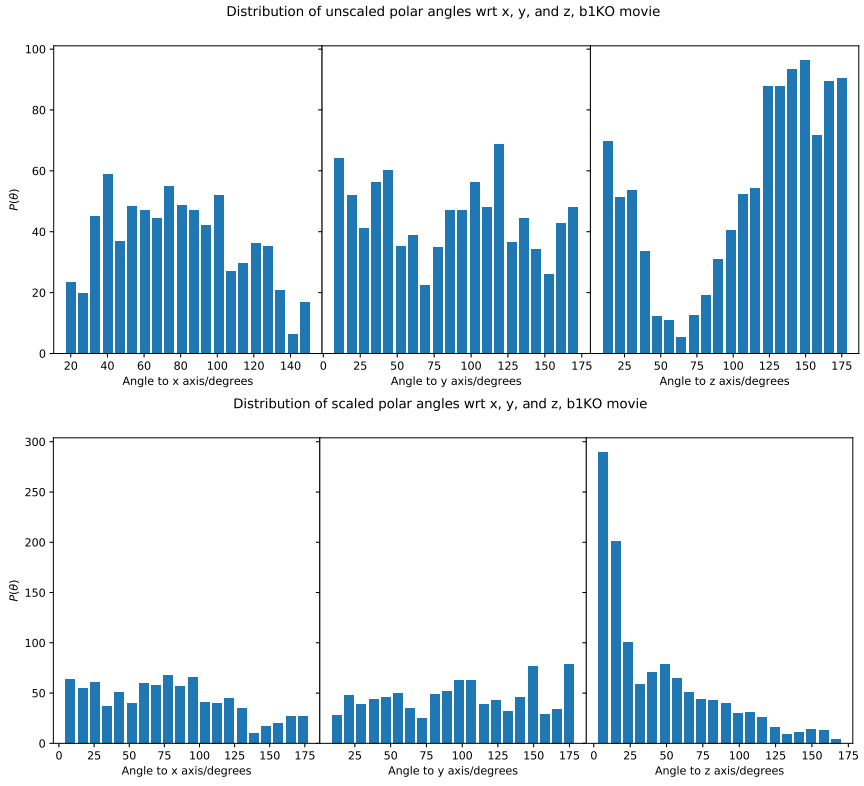

Figure C.12

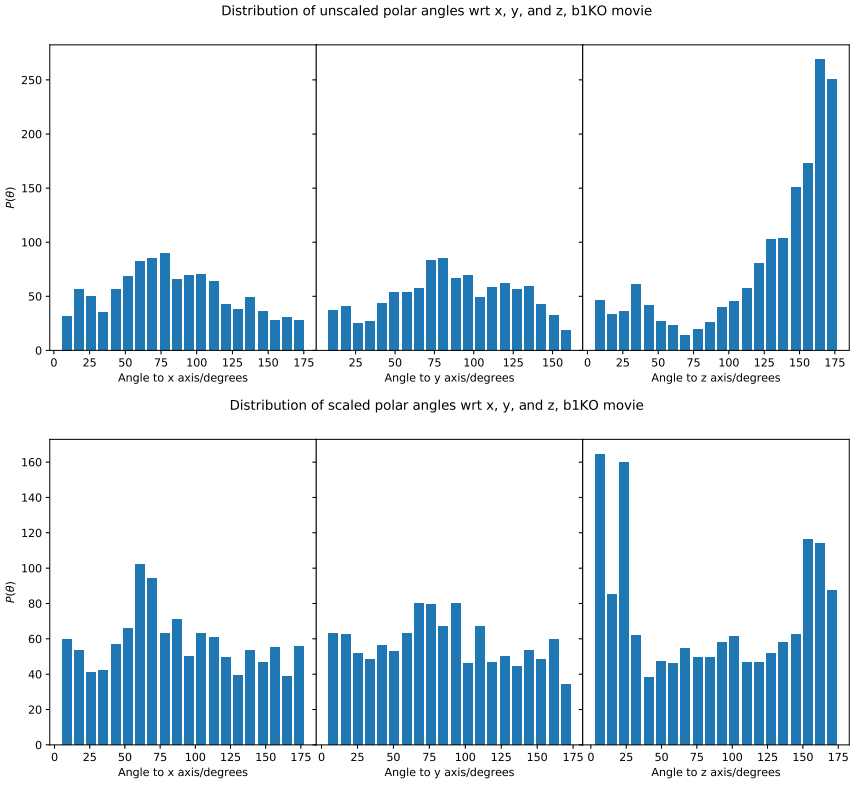
Distribution of unscaled polar angles wrt x, y, and z, b1KO movie
P(θ)
Angle to x axis/degrees
Angle to y axis/degrees
Angle to z axis/degrees
Distribution of scaled polar angles wrt x, y, and z, b1KO movie
P(θ)
Angle to x axis/degrees
Angle to y axis/degrees
Angle to z axis/degrees

Figure C.13

Appendix D

Computational methods

D.1 The Finite Element Method

The Finite Element Method (FEM) is a method of finding approximate solutions to partial differential equations. I will describe the method in the context of solving the Poisson equation. Our goal is to find a solution, u, that satisfies

$$\nabla^2 u = f, \tag{D.1}$$

on some domain, Ω, with Neumann boundary conditions, $\nabla u \cdot \boldsymbol{\nu} = q$, on some subset of the boundary of the domain, $\partial\Omega_N$, with normal $\boldsymbol{\nu}$, and Dirichlet boundary conditions on the rest of the boundary, $\partial\Omega_D$. Instead of solving this problem, FEM aims to solve a "weak form" of the problem, i.e. finding some u that satisfies

$$v\nabla^2 u = vf, \tag{D.2}$$

for all v in a set of test functions $\{v\}$, where $v = 0$ on $\partial\Omega_D$. Integrating by parts over Ω, we get

$$\int_\Omega v\nabla^2 u dV = \int_\Omega v f dV \tag{D.3}$$

$$-\int_\Omega \nabla v \cdot \nabla u dV + \int_{\partial\Omega_N} vq dS = \int_\Omega v f dV. \tag{D.4}$$

A function can be approximated over a discretised domain by interpolating with a set of basis functions, like so

$$u^{\text{approx}}(\mathbf{x}) = \sum_I N_I(\mathbf{x}) u_I, \tag{D.5}$$

where $\{N_I\}$ are the basis functions, and $\{u_I\}$ are the values of the function at discrete points. In our case we discretise the surface of a cell with a triangular mesh, defining the u_I at the vertices. We take as basis functions the so called tent functions,

$$N_1 = 1 - \xi_1 - \xi_2, \tag{D.6}$$

$$N_2 = \xi_1, \tag{D.7}$$

$$N_3 = \xi_2, \tag{D.8}$$

where ξ_i are coordinates running along two sides of each triangle. The Galerkin FEM is where we choose $\{N_I\}$ as the test functions. Making this substitution in Eq. D.4, we get

$$-\sum_J \int_\Omega \nabla N_I \cdot \nabla N_J dV u_J = \int_\Omega N_I f dV - \int_{\partial\Omega_N} N_I q dS. \tag{D.9}$$

Eq. D.9 is a linear problem of the form $A_{IJ}u_J = b_I$, which can be solved by standard numerical methods. As the mesh size is decreased, u^{approx} tends to a solution of the Poisson Equation [13]. Similar steps are used to discretise and solve the force balance equations for the surface of a cell in the Interacting Active Surfaces Model.

Appendix E

Modelling mESC aggregates

Here I list further plots referred to in the main text.

E.0.1 Measured vs predicted polarity: WT E-cadherin movies

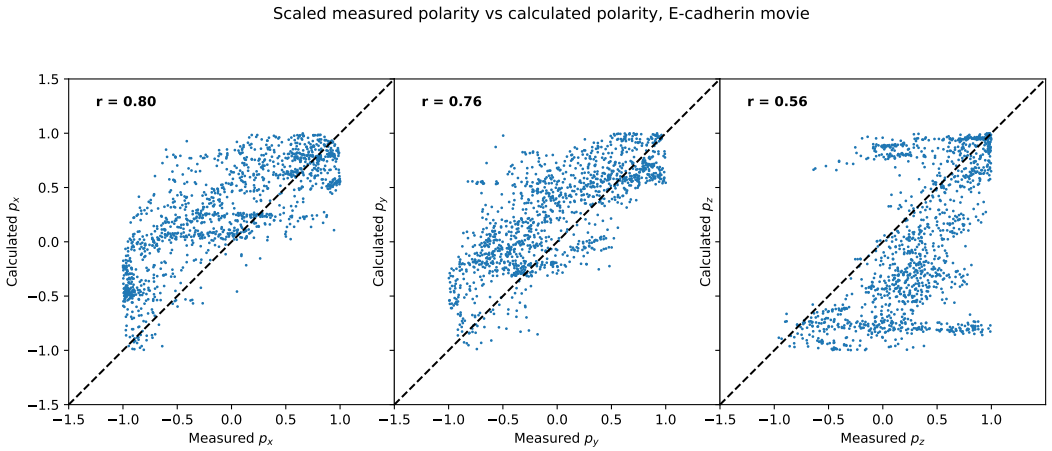

Figure E.1: Measured vs predicted polarity for a WT E-cadherin movie. The x, y, and z components of each polarity vector are plotted against each other.

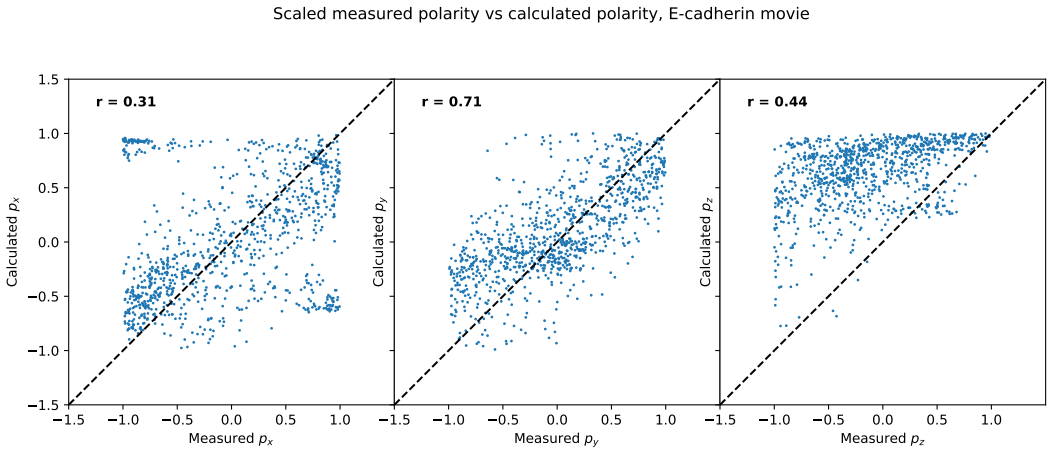

Figure E.2: Measured vs predicted polarity for a WT E-cadherin movie. The x, y, and z components of each polarity vector are plotted against each other.

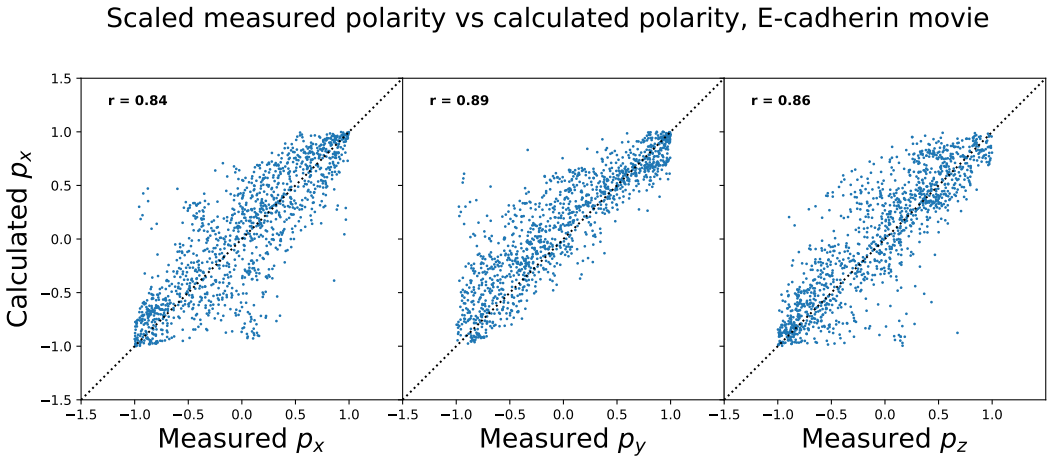

Figure E.3: Measured vs predicted polarity for a WT E-cadherin movie. The x, y, and z components of each polarity vector are plotted against each other.

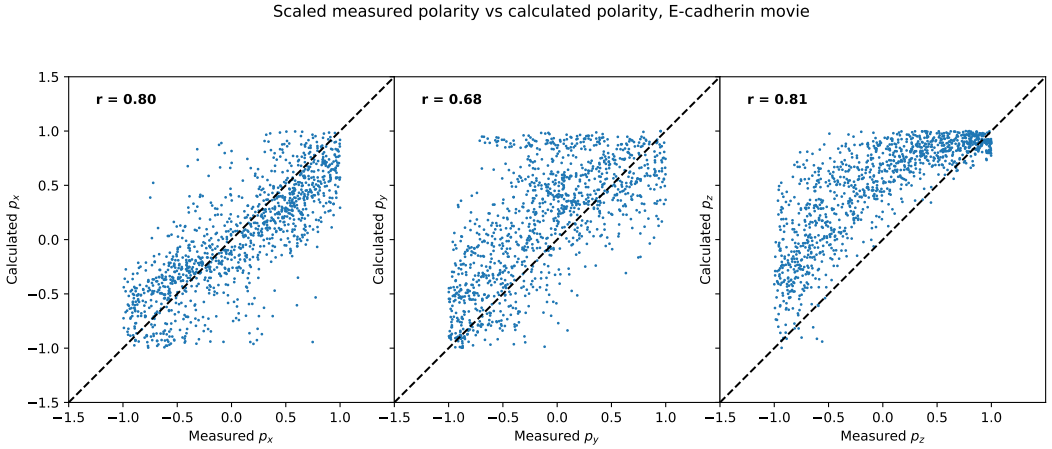

Figure E.4: Measured vs predicted polarity for a WT E-cadherin movie. The x, y, and z components of each polarity vector are plotted against each other.

E.0.2 Measured vs predicted polarity: β1-KO E-cadherin movies

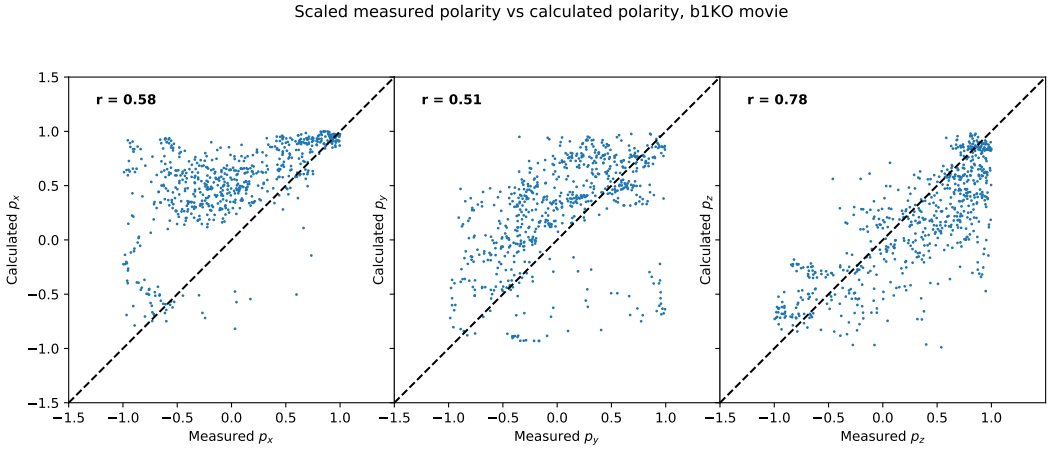

Figure E.5: Measured vs predicted polarity for a β1-KO E-cadherin movie. The x, y, and z components of each polarity vector are plotted against each other.

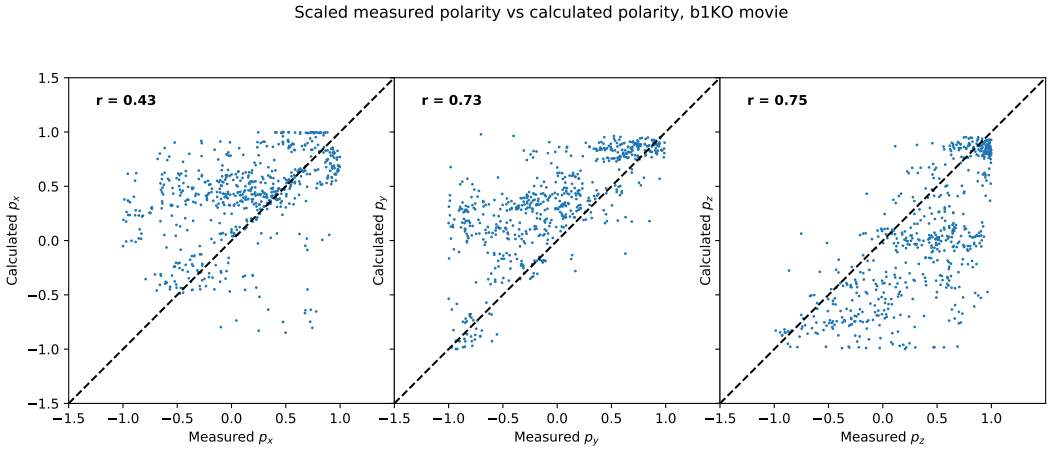

Figure E.6: Measured vs predicted polarity for a β1-KO E-cadherin movie. The x, y, and z components of each polarity vector are plotted against each other.

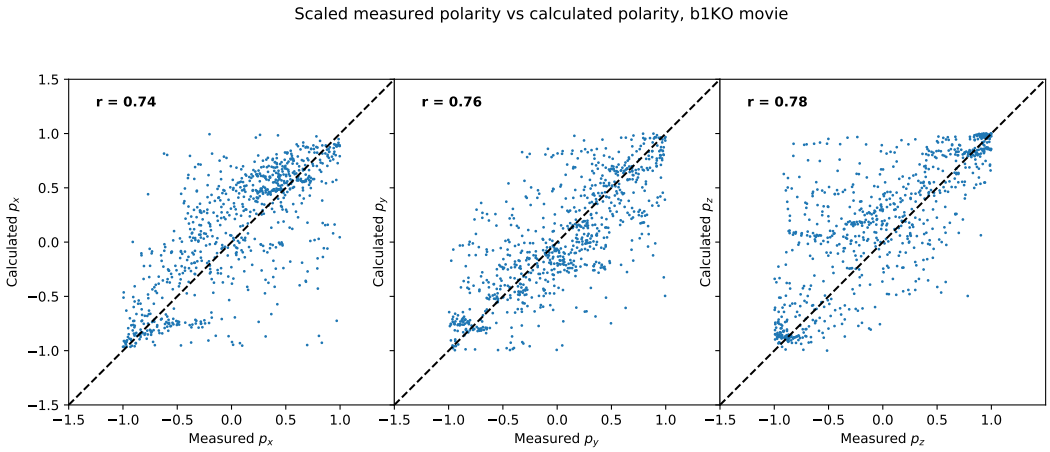

Figure E.7: Measured vs predicted polarity for a β1-KO E-cadherin movie. The x, y, and z components of each polarity vector are plotted against each other.

E.0.3 Measured vs predicted polarity: WT F-actin movies

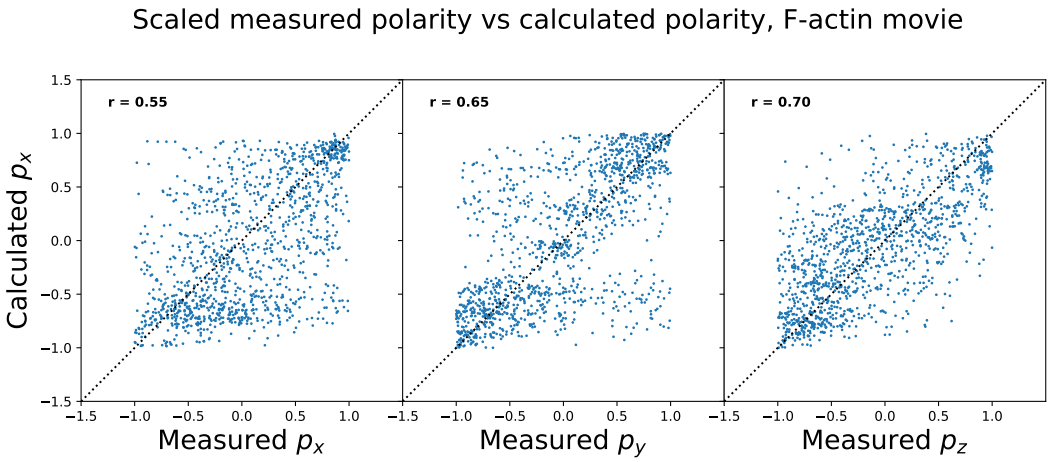

Figure E.8: Measured vs predicted polarity for a F-actin movie. The x, y, and z components of each polarity vector are plotted against each other.

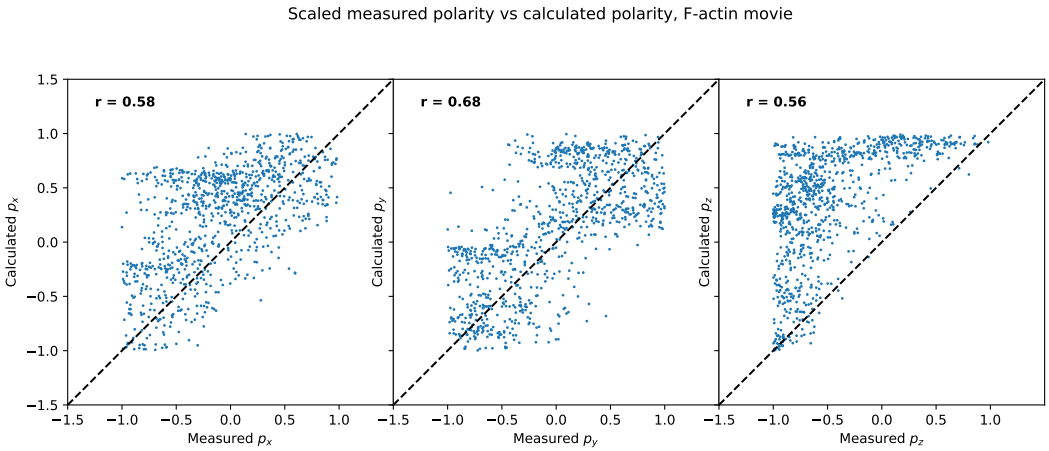

Figure E.9: Measured vs predicted polarity for a F-actin movie. The x, y, and z components of each polarity vector are plotted against each other.

Bibliography

[1] D. G. Aarts, M. Schmidt, and H. N. Lekkerkerker. Direct Visual Observation of Thermal Capillary Waves. *Science*, 304(5672):847–850, 2004.

[2] A. P. Ainslie, J. R. Davis, J. J. Williamson, A. Ferreira, A. Torres-Sanchez, A. Hoppe, F. Mangione, M. B. Smith, E. Martin-Blanco, G. Salbreux, and N. Tapon. ECM remodeling and spatial cell cycle coordination determine tissue growth kinetics. *bioRxiv*, 2020.

[3] M. Akiyama, M. Nonomura, A. Tero, and R. Kobayashi. Numerical study on spindle positioning using phase field method. *Physical Biology*, 16, 2019.

[4] G. P. Alexander, B. G. G. Chen, E. A. Matsumoto, and R. D. Kamien. Colloquium: Disclination loops, point defects, and all that in nematic liquid crystals. *Reviews of Modern Physics*, 84(2):497–514, 2012.

[5] S. Alt, P. Ganguly, and G. Salbreux. Vertex models: from cell mechanics to tissue morphogenesis. *Philosophical Transactions of the Royal Society of London B: Biological Sciences*, 372(1720), 2017.

[6] J. Anderson. Colloid Transport By Interfacial Forces. *Annual Review of Fluid Mechanics*, 21(1):61–99, 1989.

[7] M. P. Applebey. The Viscosity of Salt Solutions. *Journal of the Chemical Society, Transactions*, 97:2000–2025, 1910.

[8] S. Asakura and F. Oosawa. Interaction between Particles Suspended in Solutions. *Journal of Polymer Science*, 33:183–192, 1958.

[9] A. Attanasi, A. Cavagna, L. Del Castello, I. Giardina, A. Jelic, S. Melillo, L. Parisi, O. Pohl, E. Shen, and M. Viale. Emergence of collective changes in travel direction of starling flocks from individual birds' fluctuations. *Journal of the Royal Society Interface*, 12(108), 2015.

[10] S. Auer and D. Frenkel. Suppression of crystal nucleation in polydisperse colloids due to increase of the surface free energy. *Nature*, 413:711–713, 2001.

[11] A. E. Bailey, W. C. Poon, R. J. Christianson, A. B. Schofield, U. Gasser, V. Prasad, S. Manley, P. N. Segre, L. Cipelletti, W. V. Meyer, M. P. Doherty, S. Sankaran, A. L. Jankovsky, W. L. Shiley, J. P. Bowen, J. C. Eggers, C. Kurta, T. Lorik, P. N. Pusey, and D. A. Weitz. Spinodal decomposition in a model colloid-polymer mixture in microgravity. *Physical Review Letters*, 99(20):1–4, 2007.

[12] J. A. Barker and D. Henderson. What is "liquid" ? Understanding the states of matter. *Reviews of Modern Physics*, 48(4):588–664, 1976.

[13] K. Bathe. *Finite Element Procedures*. K.J. Bathe, Watertown, MA, 2 edition, 2014.

[14] C. Bechinger, R. Di Leonardo, H. Löwen, C. Reichhardt, G. Volpe, and G. Volpe. Active particles in complex and crowded environments. *Reviews of Modern Physics*, 88(4):1–50, 2016.

[15] I. Bedzhov, S. J. Graham, C. Y. Leung, and M. Zernicka-Goetz. Developmental plasticity, cell fate specification and morphogenesis in the early mouse embryo. *Philosophical Transactions of the Royal Society B: Biological Sciences*, 369(1657), 2014.

[16] I. Bedzhov and M. Zernicka-Goetz. Self-organizing properties of mouse pluripotent cells initiate morphogenesis upon implantation. *Cell*, 156(5):1032–1044, 2014.

[17] G. J. Beitel and M. A. Kransnow. Genetic control of epithelial tube size in the Drosophila tracheal system. *Development*, 127(15):3271–3282, 2000.

[18] E. Betzig, G. H. Patterson, R. Sougrat, O. W. Lindwasser, S. Olenych, J. S. Bonifacino, M. W. Davidson, J. Lippincott-Schwartz, and H. F. Hess. Imaging intracellular fluorescent proteins at nanometer resolution. *Science*, 313(5793):1642–1645, 2006.

[19] T. Biben and J. P. Hansen. Phase separation of asymmetric binary hard-sphere fluids. *Physical Review Letters*, 66(17):2215–2218, 1991.

[20] C. Bielmeier, S. Alt, V. Weichselberger, M. La Fortezza, H. Harz, F. Jülicher, G. Salbreux, and A. K. Classen. Interface contractility between differently fated cells drives cell elimination and cyst formation. *Current Biology*, 26(5):563–574, 2016.

[21] P. Blakeley, N. M. E. Fogarty, I. Valle, S. E. Wamaitha, T. X. Hu, K. Elder, P. Snell, L. Christie, P. Robson, K. K. Niakan, P. Blakeley, N. M. E. Fogarty, I. Valle, S. E. Wamaitha, T. X. Hu, K. Elder, P. Snell, L. Christie, P. Robson, and K. K. Niakan. Defining the three cell lineages of the human blastocyst by single-cell RNA-seq. *Development*, 142(20):3613, 2015.

[22] D. Bothe and P. Druet. On the structure of continuum thermodynamical diffusion fluxes – A novel closure scheme and its relation to the Maxwell-Stefan and the Fick-Onsager approach. *arXiv*, pages 1–50, 2020.

[23] J. R. Bowman. Distillation of an Indefinite Number of Components. *Industrial & Engineering Chemistry*, 41(9):2004–2007, 1949.

[24] C. D. Buckley, J. Tan, K. L. Anderson, D. Hanein, N. Volkmann, W. I. Weis, W. J. Nelson, and A. R. Dunn. The minimal cadherin-catenin complex binds to actin filaments under force. *Science*, 346(6209), 2014.

[25] C. Cadart, L. Venkova, P. Recho, M. C. Lagomarsino, and M. Piel. The physics of cell-size regulation across timescales. *Nature Physics*, 2019.

[26] M. D. Cahalan, H. Wulff, and K. G. Chandy. Molecular properties and physiological roles of ion channels in the immune system. *Journal of Clinical Immunology*, 21(4):235–252, 2001.

[27] J. W. Cahn. On Spinodal Decomposition. *Acta Metallurgica*, 9:795–801, 1961.

[28] J. W. Cahn and J. E. Hilliard. Free energy of a nonuniform system. I. Interfacial free energy. *The Journal of Chemical Physics*, 28(2):258–267, 1958.

[29] A. C. Callan-Jones and F. Jülicher. Hydrodynamics of active permeating gels. *New Journal of Physics*, 13, 2011.

[30] N. F. Carnahan and K. E. Starling. Equation of state for nonattracting rigid spheres. *The Journal of Chemical Physics*, 51(2):635–636, 1969.

[31] C. Casagrande, P. Fabre, E. Raphaël, and M. Veyssié. Janus beads: Realization and behaviour at water/oil interfaces. *Europhysics Letters*, 9(3):251–255, 1989.

[32] M. E. Cates and E. Tjhung. Theories of binary fluid mixtures: From phase-separation kinetics to active emulsions. *Journal of Fluid Mechanics*, 836:P1, 2018.

[33] C. P. Chen, S. Posy, A. Ben-Shaul, L. Shapiro, and B. H. Honig. Specificity of cell-cell adhesion by classical cadherins: Critical role for low-affinity dimerization through β-strand swapping. *Proceedings of the National Academy of Sciences of the United States of America*, 102(24):8531–8536, 2005.

[34] T. Chou, K. Mallick, and R. K. Zia. Non-equilibrium statistical mechanics: From a paradigmatic model to biological transport. *Reports on Progress in Physics*, 74(11), 2011.

[35] N. Christodoulou, C. Kyprianou, A. Weberling, R. Wang, G. Cui, G. Peng, N. Jing, and M. Zernicka-Goetz. Sequential formation and resolution of multiple rosettes drive embryo remodelling after implantation. *Nature Cell Biology*, 20(11):1278–1289, 2018.

[36] S. Ciliberto. Experiments in Stochastic Thermodynamics: Short History and Perspectives. *Physical Review X*, 7(2):16–21, 2017.

[37] J. Clerk Maxwell. On the Dynamical Theory of Gases. *Philosophical Transactions of the Royal Society of London*, 157:49–88, 1867.

[38] E. Coucouvanis and G. R. Martin. Signals for death and survival: A two-step mechanism for cavitation in the vertebrate embryo. *Cell*, 83(2):279–287, 1995.

[39] M. C. Cross and P. C. Hohenberg. Pattern formation outside of equilibrium. *Reviews of Modern Physics*, 65(3):851–1112, 1993.

[40] P. Curie. Sur la symétrie dans les phénomènes physiques, symétrie d'un champ électrique et d'un champ magnétique. *Journal de Physique (Paris)*, 1894.

[41] D. Dan, C. Mueller, K. Chen, and J. A. Glazier. Solving the advection-diffusion equations in biological contexts using the cellular Potts model. *Physical Review E*, 72(4):1–10, 2005.

[42] C. de Boor. On Calculating with B-Splines. *Journal of Approximation Theory*, 6:50–62, 1972.

[43] P. G. de Gennes. Dynamics of fluctuations and spinodal decomposition in polymer blends. II. *The Journal of Chemical Physics*, 72(9):4756–4763, 1980.

[44] P. G. de Gennes, F. Brochard-Wyart, and D. Quere. *Capillarity and Wetting Phenomena: Drops, Bubbles, Pearls, Waves*. Springer, 2004.

[45] P. G. de Gennes and J. Prost. *The Physics of Liquid Crystals*. Oxford University Press, 2nd edition, 1993.

[46] S. R. de Groot and P. Mazur. *Non-equilibrium thermodynamics*. Dover Publications Inc., New York, 1962.

[47] S. K. Dey, H. Lim, S. K. Das, J. Reese, B. C. Paria, T. Daikoku, and H. Wang. Molecular cues to implantation. *Endocrine Reviews*, 25(3):341–373, 2004.

[48] U. Dobramysl, M. Mobilia, M. Pleimling, and U. C. Tauber. Stochastic population dynamics in spatially extended predator-prey systems. *Journal of Physics A: Mathematical and Theoretical*, 51(6), 2018.

[49] A. V. Dobrynin and L. Leibler. Theory of polydisperse multiblock copolymers. *Macromolecules*, 30(16):4756–4765, 1997.

[50] G. Duclos, R. Adkins, D. Banerjee, M. S. Peterson, M. Varghese, I. Kolvin, A. Baskaran, R. A. Pelcovits, T. R. Powers, A. Baskaran, F. Toschi, M. F. Hagan, S. J. Streichan, V. Vitelli, D. A. Beller, and Z. Dogic. Topological structure and dynamics of three-dimensional active nematics. *Science*, 367(6482):1120–1124, 2020.

[51] G. Duclos, C. Erlenkämper, J.-F. Joanny, and P. Silberzan. Topological defects in confined populations of spindle-shaped cells. *Nature Physics*, 13(September 2016):1–6, 2016.

[52] G. Duclos, C. Erlenkämper, J. F. Joanny, and P. Silberzan. Topological defects in confined populations of spindle-shaped cells. *Nature Physics*, 13(1):58–62, 2017.

[53] C. Duclut, N. Sarkar, J. Prost, and F. Jülicher. Fluid pumping and active flexoelectricity can promote lumen nucleation in cell assemblies. *Proceedings of the National Academy of Sciences of the United States of America*, 116(39):19264–19273, 2019.

[54] E. Dulos, J. Boissonade, J. J. Perraud, B. Rudovics, and P. De Kepper. Chemical morphogenesis: Turing patterns in an experimental chemical system. *Acta Biotheoretica*, 44(3-4):249–261, 1996.

[55] J. G. Dumortier, M. Le Verge-Serandour, A. F. Tortorelli, A. Mielke, L. De Plater, H. Turlier, and J. L. Maître. Hydraulic fracturing and active coarsening position the lumen of the mouse blastocyst. *Science*, 365(6452):465–468, 2019.

[56] K. Edashige, S. Ohta, M. Tanaka, T. Kuwano, D. M. Valdez, T. Hara, B. Jin, S. I. Takahashi, S. Seki, C. Koshimoto, and M. Kasai. The role of aquaporin 3 in the movement of water and cryoprotectants in mouse morulae. *Biology of Reproduction*, 77(2):365–375, 2007.

[57] R. G. Edwards, P. C. Steptoe, and J. M. Pubdy. Fertilization and cleavage in vitro of preovulator human oocytes. *Obstetrical and Gynecological Survey*, 26(4):287–288, 1971.

[58] Y. Elani, R. V. Law, and O. Ces. Vesicle-based artificial cells as chemical microreactors with spatially segregated reaction pathways. *Nature Communications*, 5:1–5, 2014.

[59] R. Farhadifar, J. C. Röper, B. Aigouy, S. Eaton, and F. Jülicher. The influence of cell mechanics, cell-cell interactions, and proliferation on epithelial packing. *Current Biology*, 17(24):2095–2104, 2007.

[60] E. Fischer-Friedrich, A. A. Hyman, F. Jülicher, D. J. Muller, and J. Helenius. Quantification of surface tension and internal pressure generated by single mitotic cells. *Scientific Reports*, pages 4–11, 2014.

[61] M. E. Fisher. Renormalization group theory: Its basis and formulation in statistical physics. *Reviews of Modern Physics*, 70(2):653–681, 1998.

[62] P. J. Flory. Thermodynamics of High Polymer Solutions. *The Journal of Chemical Physics*, 51, 1942.

[63] N. M. E. Fogarty, A. McCarthy, K. E. Snijders, B. E. Powell, N. Kubikova, P. Blakeley, R. Lea, K. Elder, S. E. Wamaitha, D. Kim, V. Maciulyte, J. Kleinjung, J.-S. Kim, D. Wells, L. Vallier, A. Bertero, J. M. A. Turner, and K. K. Niakan. Genome editing reveals a role for OCT4 in human embryogenesis. *Nature*, 550:67–73, 2017.

[64] D. Frenkel and A. A. Louis. Phase separation in binary hard-core mixtures: An exact result. *Physical Review Letters*, 68(22):3363–3365, 1992.

[65] M. L. Gardel, M. T. Valentine, J. C. Crocker, A. R. Bausch, and D. A. Weitz. Microrheology of entangled f-actin solutions. *Physical Review Letters*, 91(15):8–11, 2003.

[66] R. L. Gardner. Investigation of cell lineage and differentiation in the extraembryonic endoderm of the mouse embryo. *Journal of Embryology and Experimental Morphology*, 68:175–198, 1982.

[67] S. L. Giandomenico, S. B. Mierau, G. M. Gibbons, L. M. Wenger, L. Masullo, T. Sit, M. Sutcliffe, J. Boulanger, M. Tripodi, E. Derivery, O. Paulsen, A. Lakatos, and M. A. Lancaster. Cerebral organoids at the air-liquid interface generate diverse nerve tracts with functional output. *Nature Neuroscience*, 22(4):669–679, 2019.

[68] D. J. Giesen, C. J. Cramer, and D. G. Truhlar. Entropic contributions to free energies of solvation. *Journal of Physical Chemistry*, 98(15):4141–4147, 1994.

[69] J. A. Glazier and F. Graner. Simulation of the differential adhesion driven rearrangement of biological cells. *Physical Review E*, 47(3):2128–2154, 1993.

[70] N. W. Goehring, P. K. Trong, J. S. Bois, D. Chowdhury, E. M. Nicola, A. A. Hyman, and S. W. Grill. Polarization of PAR Proteins by Advective Triggering of a Pattern-Forming System. *Science*, 334(November):1137–1142, 2011.

[71] P. Gómez-Gálvez, P. Vicente-Munuera, A. Tagua, C. Forja, A. M. Castro, M. Letrán, A. Valencia-Expósito, C. Grima, M. Bermúdez-Gallardo, Ó. Serrano-Pérez-Higueras, F. Cavodeassi, S. Sotillos, M. D. Martín-Bermudo, A. Márquez, J. Buceta, and L. M. Escudero. Scutoids are a geometrical solution to three-dimensional packing of epithelia. *Nature Communications*, 9(1):1–14, 2018.

[72] F. Graner and J. A. Glazier. Simulation of biological cell sorting using a two-dimensional extended Potts model. *Physical Review Letters*, 69(13):2013–2016, 1992.

[73] M. Grosell. Intestinal anion exchange in marine fish osmoregulation. *Journal of Experimental Biology*, 209(15):2813–2827, 2006.

[74] S. E. Harrison, B. Sozen, N. Christodoulou, C. Kyprianou, and M. Zernicka-Goetz. Assembly of embryonic and extraembryonic stem cells to mimic embryogenesis in vitro. *Science*, 356(6334):eaal1810, 2017.

[75] R. Hartmann, P. K. Singh, P. Pearce, R. Mok, B. Song, F. Díaz-Pascual, J. Dunkel, and K. Drescher. Emergence of three-dimensional order and structure in growing biofilms. *Nature Physics*, 15(3):251–256, 2019.

[76] A. Hashimoto, A. Nagao, and S. Okuda. Topological graph description of multicellular dynamics based on vertex model. *Journal of Theoretical Biology*, 437:187–201, 2018.

[77] K. Hashimoto, H. Fujimoto, and N. Nakatsuji. An ECM substratum allows mouse mesodermal cells isolated from the primitive streak to exhibit motility similar to that inside the embryo and reveals a deficiency in the T/T mutant cells. *Development*, 100(4):587–598, 1987.

[78] J. W. Hindley, Y. Elani, C. M. McGilvery, S. Ali, C. L. Bevan, R. V. Law, and O. Ces. Light-triggered enzymatic reactions in nested vesicle reactors. *Nature Communications*, 9(1):3–8, 2018.

[79] A. L. Hodgkin and A. F. Huxley. A Quantitative Description of Membrane Current and its Application to Conduction and Excitation in Nerve. *The Journal of Physiology*, 117:500–544, 1952.

[80] P. C. Hohenberg and B. Halperin. Theory of dynamic critical phenomena. *Reviews of Modern Physics*, 49(3):435–479, 1977.

[81] S. Höhn, A. R. Honerkamp-Smith, P. A. Haas, P. K. Trong, and R. E. Goldstein. Dynamics of a Volvox embryo turning itself inside out. *Physical Review Letters*, 114(17):1–5, 2015.

[82] J. Huisken and D. Y. Stainier. Selective plane illumination microscopy techniques in developmental biology. *Development*, 136(12):1963–1975, 2009.

[83] E. T. Jaynes. The Minimum Entropy Production Principle. *Annual Review of Physical Chemistry*, 31:579–601, 1980.

[84] S. W. Jin, D. Beis, T. Mitchell, J. N. Chen, and D. Y. Stainier. Cellular and molecular analyses of vascular tube and lumen formation in zebrafish. *Development*, 132(23):5199–5209, 2005.

[85] J. F. Joanny, F. Jülicher, K. Kruse, and J. Prost. Hydrodynamic theory for multicomponent active polar gels. *New Journal of Physics*, 9, 2007.

[86] J. F. Joanny, K. Kruse, J. Prost, and S. Ramaswamy. The actin cortex as an active wetting layer. *European Physical Journal E*, 36(5), 2013.

[87] P. Jop, A. Petrosyan, and S. Ciliberto. Work and dissipation fluctuations near the stochastic resonance of a colloidal particle. *Europhysics Letters*, 81(5), 2008.

[88] F. Jülicher, S. W. Grill, and G. Salbreux. Hydrodynamic theory of active matter. *Reports on Progress in Physics*, 81:1–29, 2018.

[89] F. Jülicher and J. Prost. Generic theory of colloidal transport. *European Physical Journal E*, 29(1):27–36, 2009.

[90] D. Karig, K. Michael Martini, T. Lu, N. A. DeLateur, N. Goldenfeld, and R. Weiss. Stochastic Turing patterns in a synthetic bacterial population. *Proceedings of the National Academy of Sciences of the United States of America*, 115(26):6572–6577, 2018.

[91] P. Katsamba, K. Carroll, G. Ahlsen, F. Bahna, J. Vendome, S. Posy, M. Rajebhosale, S. Price, T. M. Jessell, A. Ben-Shaul, L. Shapiro, and B. H. Honig. Linking molecular affinity and cellular specificity in cadherin-mediated adhesion. *Proceedings of the National Academy of Sciences of the United States of America*, 106(28):11594–11599, 2009.

[92] A. R. Kay and M. P. Blaustein. Evolution of our understanding of cell volume regulation by the pump-leak mechanism. *Journal of General Physiology*, 151(4):407–416, 2019.

[93] A. Kicheva, P. Pantazis, T. Bollenbach, Y. Kalaidzidis, T. Bittig, F. Jülicher, and M. González-Gaitán. Kinetics of morphogen gradient formation. *Science*, 315(5811):521–525, 2007.

[94] J. G. Kirkwood, R. L. Baldwin, P. J. Dunlop, L. J. Gosting, and G. Kegeles. Flow equations and frames of reference for isothermal diffusion in liquids. *The Journal of Chemical Physics*, 33(5):1505–1513, 1960.

[95] R. Koningsveld and A. J. Staverman. Liquid-liquid phase separation in multicomponent polymer solutions. III. Cloud-point curves. *Journal of Polymer Science Part A-2: Polymer Physics*, 6(2):349–366, 1968.

[96] T. Koromila and A. Stathopoulos. Broadly expressed repressors integrate patterning across orthogonal axes in embryos. *Proceedings of the National Academy of Sciences of the United States of America*, 114(31):8295–8300, 2017.

[97] M. Krupa, E. Mazur, K. Szczepańska, K. Filimonow, M. Maleszewski, and A. Suwińska. Allocation of inner cells to epiblast vs primitive endoderm in the mouse embryo is biased but not determined by the round of asymmetric divisions (8->16- and 16->32-cells). *Developmental Biology*, 385(1):136–148, 2014.

[98] K. Kruse, J. F. Joanny, F. Jülicher, J. Prost, and K. Sekimoto. Asters , Vortices , and Rotating Spirals in Active Gels of Polar Filaments. *Physical Review Letters*, 92(7), 2004.

[99] K. Kruse, J. F. Joanny, F. Jülicher, J. Prost, and K. Sekimoto. Generic theory of active polar gels: A paradigm for cytoskeletal dynamics. *European Physical Journal E*, 16(1):5–16, 2005.

[100] M. A. Lancaster and J. A. Knoblich. Organogenesis in a dish: Modeling development and disease using organoid technologies. *Science*, 345(6194), 2014.

[101] L. D. Landau. *Collected Papers of L. D. Landau*. Pergamon, first edition, 1965.

[102] L. D. Landau and E. M. Lifshitz. *Statistical Physics*. Elsevier Butterworth-Heinemann, third edition, 1980.

[103] L. D. Landau and E. M. Lifshitz. *Fluid Mechanics*. Pergamon, 2nd edition, 1987.

[104] G. R. Lázaro, I. Pagonabarraga, and A. Hernández-Machado. Phase-field theories for mathematical modeling of biological membranes. *Chemistry and Physics of Lipids*, 185:46–60, 2015.

[105] H. N. Lekkerkerker, W. C. Poon, P. N. Pusey, A. Stroobants, and P. B. Warren. Phase behaviour of colloid + polymer mixtures. *Europhysics Letters*, 20(6):559–564, 1992.

[106] H. N. Lekkerkerker and A. Stroobants. On the spinodal instability of highly asymmetric hard sphere suspensions. *Physica A: Statistical Mechanics and its Applications*, 195(3-4):387–397, 1993.

[107] H. N. W. Lekkerkerker, W. C. K. Poon, P. N. Pusey, A. Stroobants, and P. B. Warren. Phase-Behavior of Colloid Plus Polymer Mixtures. *Europhysics Letters*, 20(6):559–564, 1992.

[108] S. L. Lewis and P. P. Tam. Definitive endoderm of the mouse embryo: Formation, cell fates, and morphogenetic function. *Developmental Dynamics*, 235(9):2315–2329, 2006.

[109] M. L. Li, J. Aggeler, D. A. Farson, C. Hatier, J. Hassell, and M. J. Bissell. Influence of a reconstituted basement membrane and its components on casein gene expression and secretion in mouse mammary epithelial cells. *Proceedings of the National Academy of Sciences of the United States of America*, 84(1):136–140, 1987.

[110] L. A. Lowery and H. Sive. Strategies of vertebrate neurulation and a re-evaluation of teleost neural tube formation. *Mechanisms of Development*, 121(10):1189–1197, 2004.

[111] B. Lubarsky and M. A. Krasnow. Tube morphogenesis: Making and shaping biological tubes. *Cell*, 112(1):19–28, 2003.

[112] A. Manninen. Epithelial polarity - Generating and integrating signals from the ECM with integrins. *Experimental Cell Research*, 334(2):337–349, 2015.

[113] M. C. Marchetti, J. F. Joanny, S. Ramaswamy, T. B. Liverpool, J. Prost, M. Rao, and R. A. Simha. Hydrodynamics of soft active matter. *Reviews of Modern Physics*, 85(3):1143–1189, 2013.

[114] A. F. Marée, A. Jilkine, A. Dawes, V. A. Grieneisen, and L. Edelstein-Keshet. Polarization and movement of keratocytes: A multiscale modelling approach. *Bulletin of Mathematical Biology*, 68(5):1169–1211, 2006.

[115] J. Marston. Planetary Atmospheres as Nonequilibrium Condensed Matter. *Annual Review of Condensed Matter Physics*, 3(1):285–310, 2012.

[116] W. Marth, S. Praetorius, and A. Voigt. A mechanism for cell motility by active polar gels. *Journal of the Royal Society Interface*, 12(107), 2015.

[117] P. Mazur. Mesoscopic nonequilibrium thermodynamics; Irreversible processes and fluctuations. *Physica A: Statistical Mechanics and its Applications*, 274(3):491–504, 1999.

[118] M. Merkel, R. Etournay, M. Popović, G. Salbreux, S. Eaton, and F. Jülicher. Triangles bridge the scales: Quantifying cellular contributions to tissue deformation. *Physical Review E*, 95(3):1–24, 2017.

[119] N. D. Mermin. The topological theory of defects in ordered media. *Reviews of Modern Physics*, 51(3):591–648, 1979.

[120] N. D. Mermin and H. Wagner. Absence of ferromagnetism or antiferromagnetism in one- or two-dimensional isotropic Heisenberg models. *Physical Review Letters*, 17(22):1133–1136, 1966.

[121] A. Meroni, A. Pimpinelli, and L. Reatto. On the entropy of mixing of a binary mixture of hard spheres. *The Journal of Chemical Physics*, 87(6):3644–3646, 1987.

[122] D. G. Miller. Thermodynamics of irreversible processes. *Chemical Reviews*, 60(1):15–37, 1960.

[123] D. G. Miller. Explicit relations of velocity correlation coefficients to Onsager lij's, to experimental quantities, and to infinite dilution limiting laws for binary electrolyte solutions. *Journal of Physical Chemistry*, 85(9):1137–1146, 1981.

[124] D. G. Miller, V. Vitagliano, and R. Sartorio. Some comments on multicomponent diffusion: Negative main term diffusion coefficients, second law constraints, solvent choices, and reference frame transformations. *Journal of Physical Chemistry*, 90(8):1509–1519, 1986.

[125] Z. G. Mills, W. Mao, and A. Alexeev. Mesoscale modeling: Solving complex flows in biology and biotechnology. *Trends in Biotechnology*, 31(7):426–434, 2013.

[126] H. Morita, S. Grigolon, M. Bock, S. F. Krens, G. Salbreux, and C. P. Heisenberg. The Physical Basis of Coordinated Tissue Spreading in Zebrafish Gastrulation. *Developmental Cell*, 40(4):354–366.e4, 2017.

[127] J. E. Morral and J. W. Cahn. Spinodal decomposition in ternary systems. *Acta Metallurgica*, 19(10):1037–1045, 1971.

[128] S. A. Morris, S. Grewal, F. Barrios, S. N. Patankar, B. Strauss, L. Buttery, M. Alexander, K. M. Shakesheff, and M. Zernicka-Goetz. Dynamics of anteriorposterior axis formation in the developing mouse embryo. *Nature Communications*, 3:673, 2012.

[129] S. A. Morris, R. T. Teo, H. Li, P. Robson, D. M. Glover, and M. Zernicka-Goetz. Origin and formation of the first two distinct cell types of the inner cell mass in the mouse embryo. *Proceedings of the National Academy of Sciences of the United States of America*, 107(14):6364–6369, 2010.

[130] S. P. Muench, J. Trinick, and M. A. Harrison. Structural divergence of the rotary ATPases. *Quarterly Reviews of Biophysics*, 44(3):311–356, 2011.

[131] A. Mulero, C. A. Galán, and F. Cuadros. Equations of state for hard spheres. A review of accuracy and applications. *Physical Chemistry Chemical Physics*, 3(22):4991–4999, 2001.

[132] I. Muševič, M. Škarabot, U. Tkalec, M. Ravnik, and S. Žumer. Two-dimensional nematic colloidal crystals self-assembled by topological defects. *Science*, 313(5789):954–958, 2006.

[133] S. A. Mutch, P. Kensel-Hammes, J. C. Gadd, B. S. Fujimoto, R. W. Allen, P. G. Schiro, R. M. Lorenz, C. L. Kuyper, J. S. Kuo, S. M. Bajjalieh, and D. T. Chiu. Protein quantification at the single vesicle level reveals that a subset of synaptic vesicle proteins are trafficked with high precision. *Journal of Neuroscience*, 31(4):1461–1470, 2011.

[134] T. Nagai and H. Honda. A dynamic cell model for the formation of epithelial tissues. *Philosophical Magazine Part B*, 81(7):699–719, 2001.

[135] S. Najem and M. Grant. Phase-field model for collective cell migration. *Physical Review E*, 93(5):1–5, 2016.

[136] C. Nardini, E. Fodor, E. Tjhung, F. van Wijland, J. Tailleur, and M. E. Cates. Entropy production in field theories without time-reversal symmetry: Quantifying the non-equilibrium character of active matter. *Physical Review X*, 7(2):1–20, 2017.

[137] D. R. Nelson. Toward a Tetravalent Chemistry of Colloids. *Nano Letters*, 2(10):1125–1129, 2002.

[138] S. B. Nissen, S. Rønhild, A. Trusina, and K. Sneppen. Theoretical tool bridging cell polarities with development of robust morphologies. *eLife*, pages 1–25, 2018.

[139] M. Nonomura. Study on Multicellular Systems Using a Phase Field Model. *PLoS ONE*, 7(4):1–9, 2012.

[140] S. Okuda, Y. Inoue, and T. Adachi. Three-dimensional vertex model for simulating multicellular morphogenesis. *Biophysics and Physicobiology*, 12:13–20, 2015.

[141] S. Okuda, T. Miura, Y. Inoue, T. Adachi, and M. Eiraku. Combining Turing and 3D vertex models reproduces autonomous multicellular morphogenesis with undulation, tubulation, and branching. *Scientific Reports*, 8(1):1–15, 2018.

[142] S. Okuda, K. Unoki, M. Eiraku, and K.-i. Tsubota. Three-dimensional deformation mode of multicellular epithelial tube under tension and compression tests. *Journal of Biomechanical Science and Engineering*, 13(4):1–9, 2018.

[143] L. Onsager. Reciprocal Relations In Irreversible Processes I. *Physical Review*, 37, 1931.

[144] R. O'Rahilly. Early human development and the chief sources of information on staged human embryos. *European Journal of Obstetrics and Gynecology and Reproductive Biology*, 9(4):273–280, 1979.

[145] J. T. G. Overbeek. Microemulsions, A Field at the Border Between Lyophobic and Lyophilic Colloids. *Faraday Discussions of the Chemical Society*, 65, 1978.

[146] P. Pearce, B. Song, D. J. Skinner, R. Mok, R. Hartmann, P. K. Singh, H. Jeckel, J. S. Oishi, K. Drescher, and J. Dunkel. Flow-Induced Symmetry Breaking in Growing Bacterial Biofilms. *Physical Review Letters*, 123(25):258101, 2019.

[147] C. Pérez-González, R. Alert, C. Blanch-Mercader, M. Gómez-González, T. Kolodziej, E. Bazellieres, J. Casademunt, and X. Trepat. Active wetting of epithelial tissues. *Nature Physics*, 15(1):79–88, 2019.

[148] J. L. Podolski and T. L. Steck. Length distribution of F-actin in Dictyostelium discoideum. *Journal of Biological Chemistry*, 265(3):1312–1318, 1990.

[149] M. Popović, A. Nandi, M. Merkel, R. Etournay, S. Eaton, F. Jülicher, and G. Salbreux. Active dynamics of tissue shear flow. *New Journal of Physics*, 19(3), 2017.

[150] J. Prost, F. Jülicher, and J.-f. Joanny. Active gel physics. *Nature Physics*, 11(February):131–139, 2015.

[151] S. Ramaswamy. The mechanics and statistics of active matter. *Annual Review of Condensed Matter Physics*, 1(1):323–345, 2010.

[152] J. Ranft, J. Prost, F. Jülicher, and J.-F. Joanny. Tissue dynamics with permeation. *European Physical Journal E*, 35(46), 2012.

[153] J. Raspopovic, L. Marcon, L. Russo, and J. Sharpe. Digit patterning is controlled by a Bmp-Sox9-Wnt Turing network modulated by morphogen gradients. *Science*, 566 {VN} -(6196):10–15, 2014.

[154] M. Renner, M. A. Lancaster, S. Bian, H. Choi, T. Ku, A. Peer, K. Chung, and J. A. Knoblich. Selforganized developmental patterning and differentiation in cerebral organoids. *The EMBO Journal*, 36(10):1316–1329, 2017.

[155] A.-C. Reymann, F. Staniscia, A. Erzberger, G. Salbreux, and S. W. Grill. Cortical flow aligns actin filaments to form a furrow. *eLife*, 5:e17807, 2016.

[156] J. M. Ritchie and R. B. Rogart. Density of sodium channels in mammalian myelinated nerve fibers and nature of the axonal membrane under the myelin sheath. *Proceedings of the National Academy of Sciences of the United States of America*, 74(1):211–215, 1977.

[157] W. P. Robinson, D. E. McFadden, I. J. Barrett, B. Kuchinkal, M. S. Peñaherrera, H. Bruyère, R. G. Best, D. A. Pedreira, S. Langlois, and D. K. Kalousek. Origin of amnion and implications for evaluation of the fetal genotype in cases of mosaicism. *Prenatal Diagnosis*, 22(12):1076–1085, 2002.

[158] O. Ronneberger, P. Fischer, and T. Brox. U-Net: Convolutional Networks for Biomedical Image Segmentation. *Medical Image Computing and Computer-Assisted Intervention (MICCAI)*, 9901:234–241, 2016.

[159] P. Rouw, A. Woutersen, B. Ackerson, and C. De Kruif. Adhesive hard sphere dispersions. *Physica A: Statistical Mechanics and its Applications*, 156(3):876–898, 1989.

[160] E. Ruckenstein and J. C. Chi. Stability of microemulsions. *Journal of the Chemical Society, Faraday Transactions 2: Molecular and Chemical Physics*, 71:1690–1707, 1975.

[161] M. J. Rust, M. Bates, and X. Zhuang. Stochastic optical reconstruction microscopy (STORM) provides sub-diffraction-limit image resolution. *Nature Methods*, 3(10):793–795, 2006.

[162] N. Saito. Concentration Dependence of the Viscosity of High Polymer Solutions I. *Journal of the Physical Society of Japan*, 5(1):4–8, 1950.

[163] G. Salbreux, G. Charras, and E. Paluch. Actin cortex mechanics and cellular morphogenesis. *Trends in Cell Biology*, 22(10):536–545, 2012.

[164] G. Salbreux and F. Jülicher. Mechanics of active surfaces. *Physical Review E*, 96, 2017.

[165] G. Salbreux, J. Prost, and J. F. Joanny. Hydrodynamics of cellular cortical flows and the formation of contractile rings. *Physical Review Letters*, 103(5):1–4, 2009.

[166] N. Sarkar, J. Prost, and F. Jülicher. Field induced cell proliferation and death in a model epithelium. *New Journal of Physics*, 21(4), 2019.

[167] T. Sato, R. G. Vries, H. J. Snippert, M. Van De Wetering, N. Barker, D. E. Stange, J. H. Van Es, A. Abo, P. Kujala, P. J. Peters, and H. Clevers. Single Lgr5 stem cells build crypt-villus structures in vitro without a mesenchymal niche. *Nature*, 459(7244):262–265, 2009.

[168] M. G. Saunders and G. A. Voth. Coarse-Graining Methods for Computational Biology. *Annual Review of Biophysics*, 42(1):73–93, 2013.

[169] T. B. Saw, A. Doostmohammadi, V. Nier, L. Kocgozlu, S. Thampi, Y. Toyama, P. Marcq, C. T. Lim, J. M. Yeomans, and B. Ladoux. Topological defects in epithelia govern cell death and extrusion. *Nature*, 544(7649):212–216, 2017.

[170] J. Schnakenberg. Network theory of microscopic and macroscopic behavior of master equation systems. *Reviews of Modern Physics*, 48(4):571–585, 1976.

[171] U. Seifert. Stochastic thermodynamics of single enzymes and molecular motors. *European Physical Journal E*, 34(3), 2011.

[172] U. Seifert. Stochastic thermodynamics, fluctuation theorems and molecular machines. *Reports on Progress in Physics*, 75(12), 2012.

[173] U. Seifert. Stochastic thermodynamics: From principles to the cost of precision. *Physica A: Statistical Mechanics and its Applications*, 504:176–191, 2018.

[174] M. N. Shahbazi, A. Jedrusik, S. Vuoristo, G. Recher, A. Hupalowska, V. Bolton, N. M. E. Fogarty, A. Campbell, L. G. Devito, D. Ilic, Y. Khalaf, K. K. Niakan, S. Fishel, and M. Zernicka-Goetz. Self-organization of the human embryo in the absence of maternal tissues. *Nature Cell Biology*, 18(6):700–8, 2016.

[175] M. N. Shahbazi, A. Scialdone, N. Skorupska, A. Weberling, G. Recher, M. Zhu, A. Jedrusik, L. G. Devito, L. Noli, I. C. MacAulay, C. Buecker, Y. Khalaf, D. Ilic, T. Voet, J. C. Marioni, and M. Zernicka-Goetz. Pluripotent state transitions coordinate morphogenesis in mouse and human embryos. *Nature*, 552(7684):239–243, 2017.

[176] S. Shankar and M. C. Marchetti. Hydrodynamics of Active Defects: From Order to Chaos to Defect Ordering. *Physical Review X*, 91(4):41047, 2019.

[177] K. Sharp and F. Matschinsky. Translation of Ludwig Boltzmann's paper "on the relationship between the second fundamental theorem of the mechanical theory of heat and probability calculations regarding the conditions for thermal equilibrium". *Entropy*, 17(4):1971–2009, 2015.

[178] M. P. Sheetz, J. E. Sable, and H. G. Döbereiner. Continuous membrane-cytoskeleton adhesion requires continuous accommodation to lipid and cytoskeleton dynamics. *Annual Review of Biophysics and Biomolecular Structure*, 35:417–434, 2006.

[179] B. I. Shraiman. Mechanical feedback as a possible regulator of tissue growth. *Proceedings of the National Academy of Sciences of the United States of America*, 102(9):3318–3323, 2005.

[180] M. B. Smith. Unpublished work, reproduced with permission.

[181] M. B. Smith, A. Chaigne, and E. K. Paluch. An active contour ImageJ plugin to monitor daughter cell size in 3D during cytokinesis. *Methods in Cell Biology*, 137:323–340, 2017.

[182] M. B. Smith, H. Li, T. Shen, X. Huang, E. Yusuf, and D. Vavylonis. Segmentation and tracking of cytoskeletal filaments using open active contours. *Cytoskeleton*, 67(11):693–705, 2010.

[183] P. Sollich. Predicting phase equilibria in polydisperse systems. *Journal of Physics: Condensed Matter*, 14:79–117, 2002.

[184] E. H. Sondheimer. The Kelvin relations in thermo-electricity. *Proceedings of the Royal Society of London. Series A. Mathematical and Physical Sciences*, 234(1198):391–398, 1956.

[185] B. Sozen, G. Amadei, A. Cox, R. Wang, E. Na, S. Czukiewska, L. Chappell, T. Voet, G. Michel, N. Jing, D. M. Glover, and M. Zernicka-goetz. Self-assembly of embryonic and two extra-embryonic stem cell types into gastrulating embryo-like structures. *Nature Cell Biology*, 20(August), 2018.

[186] B. Sozen, A. L. Cox, J. De Jonghe, M. Bao, F. Hollfelder, D. M. Glover, and M. Zernicka-Goetz. Self-Organization of Mouse Stem Cells into an Extended Potential Blastoid. *Developmental Cell*, 51(6):698–712.e8, 2019.

[187] I. Steinbach. Phase-Field Model for Microstructure Evolution at the Mesoscopic Scale. *Annual Review of Materials Research*, 43(1):89–107, 2013.

[188] C. D. Stern, editor. *Gastrulation: From cells to embryos*. Cold Spring Harbor Laboratory Press, 2004.

[189] Q. P. Su, W. Du, Q. Ji, B. Xue, D. Jiang, Y. Zhu, J. Lou, L. Yu, and Y. Sun. Vesicle Size Regulates Nanotube Formation in the Cell. *Scientific Reports*, 6(January):1–11, 2016.

[190] A. Szabó and R. M. H. Merks. Cellular Potts Modeling of Tumor Growth, Tumor Invasion, and Tumor Evolution. *Frontiers in Oncology*, 3(April):1–12, 2013.

[191] P. Tabeling, G. Zocchi, and A. Libchaber. An experimental study of the Saffman-Taylor instability. *Journal of Fluid Mechanics*, 177(3):67–82, 1987.

[192] M. Takasato, P. X. Er, M. Becroft, J. M. Vanslambrouck, E. G. Stanley, A. G. Elefanty, and M. H. Little. Directing human embryonic stem cell differentiation towards a renal lineage generates a self-organizing kidney. *Nature Cell Biology*, 16(1):118–126, 2014.

[193] D. W. Thompson. *On Growth and Form*. Cambridge University Press, 1st edition, 1917.

[194] E. Tjhung, C. Nardini, and M. E. Cates. Cluster Phases and Bubbly Phase Separation in Active Fluids: Reversal of the Ostwald Process. *Physical Review X*, 8(3):31080, 2018.

[195] H. Tompa. Phase relationships in polymer solutions. *Transactions of the Faraday Society*, 45:1142–1152, 1949.

[196] J. Toner and Y. Tu. Long-range order in a two-dimensional dynamical XY model: How birds fly together. *Physical Review Letters*, 75(23):4326–4329, 1995.

[197] A. Torres-Sanchez, D. Millan, and M. Arroyo. Modelling fluid deformable surfaces with an emphasis on biological interfaces. *Journal of Fluid Mechanics*, 872:218–271, 2019.

[198] D. C. Tosteson and J. F. Hoffman. Regulation of cell volume by active cation transport in high and low potassium sheep red cells. *The Journal of General Physiology*, 44:169–194, 1960.

[199] D. R. Tree, L. F. Dos Santos, C. B. Wilson, T. R. Scott, J. U. Garcia, and G. H. Fredrickson. Mass-transfer driven spinodal decomposition in a ternary polymer solution. *Soft Matter*, 15(23):4614–4628, 2019.

[200] A. M. Turing. The chemical basis of morphogenesis. *Philosophical Transactions of the Royal Society B: Biological Sciences*, 237:37–72, 1952.

[201] W. van Saarloos and P. C. Hohenberg. Pulses and Fronts in the Complex Ginzburg-Landau Equation near a Subcritical Bifurcation. *Physical Review Letters*, 64(7):749–752, 1990.

[202] J. H. Van't Hoff. The role of osmotic pressure in the analogy between solutions and gases (translation). *Journal of Membrane Science*, 100:39–44, 1995.

[203] T. Vicsek, A. Czirok, E. Ben-Jacob, I. Cohen, and O. Shochet. Novel type of phase transition in a system of self-driven particles. *Physical Review Letters*, 75(6):1226–1229, 1995.

[204] B. Vincent, J. Edwards, S. Emmett, and R. Croot. Phase separation in dispersions of weakly interacting particles in solutions of non-adsorbing polymer. *Colloids and Surfaces*, 31:267–298, 1988.

[205] P. W. Voorhees. The Theory of Ostwald Ripening. *J. Stat. Phys.*, 38(1/2):231–252, 1985.

[206] H. Wang, S. Lacoche, L. Huang, B. Xue, and S. K. Muthuswamy. Rotational motion during three-dimensional morphogenesis of mammary epithelial acini relates to laminin matrix assembly. *Proceedings of the National Academy of Sciences of the United States of America*, 110(1):163–168, 2013.

[207] H. Wang and G. Oster. Energy transduction in the F1 motor of ATP synthase. *Nature*, 396(6708):279–282, 1998.

[208] C. A. Weber, D. Zwicker, F. Jülicher, and C. F. Lee. Physics of active emulsions. *Reports on Progress in Physics*, 82(6):064601, 2019.

[209] A. Weberling, M. Mole, M. N. Shahbazi, and M. Zernicka-Goetz. Unpublished work, reproduced with permission.

[210] R. Wittkowski, J. Stenhammar, and M. E. Cates. Nonequilibrium dynamics of mixtures of active and passive particles. *Physical Review E*, – to be s:1–17, 2017.

[211] R. Wittkowski, A. Tiribocchi, J. Stenhammar, R. J. Allen, D. Marenduzzo, and M. E. Cates. Scalar $\phi(4)$ field theory for active-particle phase separation. *Nature Communications*, 5:4351, 2014.

[212] L. Wolpert. Positional information and the spatial pattern of cellular differentiation. *Journal of Theoretical Biology*, 25(1):1–47, 1969.

[213] L. A. Woolf and K. R. Harris. Velocity correlation coefficients as an expression of particle-particle interactions in (electrolyte) solutions. *Journal of the Chemical Society, Faraday Transactions 1: Physical Chemistry in Condensed Phases*, 74:933–947, 1978.

[214] N. J. Yang and M. J. Hinner. Site-Specific Protein Labeling: Methods and Protocols. *Methods in Molecular Biology*, pages 29–53, 2015.

[215] W. T. Yeh and H. Y. Chen. Hydrodynamics of stratified epithelium: Steady state and linearized dynamics. *Physical Review E*, 93(5):1–15, 2016.

[216] W. Yu, A. Datta, P. Leroy, L. E. O'Brien, G. Mak, T. S. Jou, K. S. Matlin, K. E. Mostov, and M. M. Zegers. β1-integrin orients epithelial polarity via Rac1 and laminin. *Molecular Biology of the Cell*, 16(2):433–445, 2005.

[217] X. Yu, K. Q. Pu, and N. Koudas. Monitoring k-nearest neighbor queries over moving objects. *Proceedings of the 21st International Conference on Data Engineering*, pages 631–642, 2005.

[218] M. Zernicka-Goetz, S. A. Morris, and A. W. Bruce. Making a firm decision: Multifaceted regulation of cell fate in the early mouse embryo. *Nature Reviews Genetics*, 10(7):467–477, 2009.